# Analytical Methods, Correlative Microscopy and Software Tools for Quantitative Single Molecule Localization Microscopy

THÈSE N$^{O}$ 6726 (2015)

PRÉSENTÉE LE 21 AOÛT 2015
À LA FACULTÉ DES SCIENCES ET TECHNIQUES DE L'INGÉNIEUR
LABORATOIRE DE BIOLOGIE À L'ÉCHELLE NANOMÉTRIQUE
PROGRAMME DOCTORAL EN BIOTECHNOLOGIE ET GÉNIE BIOLOGIQUE

ÉCOLE POLYTECHNIQUE FÉDÉRALE DE LAUSANNE

POUR L'OBTENTION DU GRADE DE DOCTEUR ÈS SCIENCES

PAR

Arun SHIVANANDAN

acceptée sur proposition du jury:

Prof. S. Maerkl, président du jury
Prof. A. Radenovic, Prof. I. Sbalzarini, directeurs de thèse
Prof. A. Diaspro, rapporteur
Prof. J.-B. Sibarita, rapporteur
Prof. D. Suter, rapporteur

ÉCOLE POLYTECHNIQUE
FÉDÉRALE DE LAUSANNE

Suisse
2015

# Abstract

Conventional Fluorescent Microscopy (FM), an inalienable tool for biologists due to its ability to perform high contrast imaging of specific molecular species or cellular structures at conditions close to their natural environment, is fundamentally limited in its resolving power in space to about 200nm due to the diffraction of light. Prominent among the new technologies that can get around the diffraction limit are Single Molecule Localization Microscopy (SMLM) techniques, such as PhotoActivated Localization Microscopy (PALM) and STochastic Optical Reconstruction Microscopy(STORM). SMLM has hence been used to address several biological problems, including those involving quantitative studies, such as molecular counting, membrane protein organization and single molecule/organelle co-localization.

There are a number of possible sources of imaging errors in SMLM which can significantly impact such studies, and have to be accounted for so as quantitative SMLM can become a stable, accurate microscopy tool in biology. This thesis provides a rigorous review of such sources of error. They include labeling artifacts, a limited detection efficiency of label molecules(of about 40-60% in PALM, e.g.,) and an uncertainty in localization in the range of 20-50nm, among others. Also, the SMLM readout is different from conventional FM, primarily consisting of a set of molecular point localizations rather than direct images for which standard quantification tools in bio-imaging are designed. Accurate and precise quantitative imaging with SMLM requires analytical, experimental and software tools that address such issues, and this thesis contributes towards it.

We describe analytical methods that accounts for two major sources of errors in analysis of membrane protein organization with SMLM. We model limited detection efficiency as independent subsampling of the set of label molecules. We then use a theoretical property of commonly used second order properties in quantitative SMLM, such as Ripley's $K$-function, $L(r) - r$ function and the Pair Correlation Function (PCF), to show that they are invariant to such subsampling. We derive expressions for their stochastic estimators due to subsampling, and characterize the errors using simulations. The results can be extended to co-localization analysis as well. We then describe a method that estimate the true locations of points given the observed ones in clusters. We characterize the relative Mean Squared Error of the combined approach, and find that it can significantly reduce the errors in quantification. We apply these methods on data on clustering due to photoblinking of individual fluorophores, and data with redundant labeling. We then study the theoretical properties of a function that has been proposed as an estimator of cluster size. We also describe a method to identify the cluster model from data.

SMLM provides single molecule resolution images of specific molecular species. Atomic Force Microscopy( AFM), on the other hand, provides nonspecific, high resolution spatial profile information. Correlative AFM-SMLM can provide not only validation of SMLM, but also the complementary information so obtained can be used to design innovative experiments. We describe in vitro imaging of actin filaments with an AFM-SMLM correlative tool, that could provide information about sources of imaging inhomogeneity in SMLM. The tool were also used to image live mammalian cells, and can be used to obtain nanoscale information about mechanical properties of cells and also as a tool for nanomanipulation.

Co-localization is a common spatial interaction quantification method used in biological imaging. It is possible to use tools from spatial statistics to obtain better statistical power on tests of spatial interaction, compared to conventional co-localization measures. Such tools can also handle SMLM data better, since they work on point patterns rather than images. We describe an ImageJ/Fiji plugin that implements a spatial statistics framework that extends the concept of co-localization, by means of a model based on Gibbs function of interaction potentials. We describe the application of this software on both confocal microscopy data of virus-endosomes, and SMLM data on GPCR protein-clathrin.

## Keywords

quantitative microscopy, optical super-resolution, single molecule localization microscopy, palm/storm, ripley k-function, pair correlation function, co-localization, spatial interaction,membrane proteins, imagej/fiji, correlative microscopy, image analysis

# Résumé

L'objectif de ma thèse est d'établir une analyse quantitative de données provenant de la technique dite "de Single Molecule Localisation Microscopie (SMLM)". Cette technique donne des images de haute spécificité de protéine dans des conditions proches de leurs conditions naturelles. SMLM permet également d'aller au delà de la limite de diffraction jusqu'a une résolution de l'ordre de la molécule unique.

Cependant, cette technique possède plusieurs sources d'erreur, ce qui en limite son utilité pour des mesures quantitatives.

Dans cet exposé, nous effectuons une enquête quantitative rigoureuse des sources d'erreur liées à la technique de SMLM. Ensuite, nous présentons une série de projets ayant pour but commun l'établissement d'une méthode de correction des différentes sources d'erreur décrites auparavant.

Ces projets sont les suivant: 1) Etablissement d'une méthode quantitative d'analyse pour corriger les erreurs introduites par l'efficacité de détection limitée et la précision de localisation. Ces deux points sont inhérents à la technique de SMLM. Cette méthode permet de caractériser l'organisation spatiale des protéines membranaires. 2) Proposition d'un outil de microscopie corrélative SMLM-AFM (Atomic Force Microscopy), pour valider les données de SMLM avec des données AFM de haute résolution et caractériser leurs différentes sources d'erreur. Les informations complémentaires obtenues par cet outil microscopique peuvent être utilisées en vue d'expériences innovantes. 3) Développement d'un logiciel de déduction de paramètres d'interaction spatiale à partir des données de microscopie de couleur double, y compris SMLM. Ce logiciel a été conçu comme un plugin open source pour ImageJ / Fiji.

## Mots-clés

microscopie quantitative,interaction spatiale, les protéines membranaires, Imagej / Fiji, microscopie corrélative, analyse d'image, palm, storm, smlm

# Acknowledgements

Eventful four years! This thesis work started in Zurich, thrived in Lausanne, and ended, well, informally in Montpellier. It started in a Theoretical Computer Science group and ended in a Experimental Physics group. It started and ended with the reading of books on Spatial Statistics, however passed through a few optical instruments manuals and imaging protocols on the way. I would like to thank the people who helped me during the PhD, either professionally or personally.

I would like to start by thanking my primary supervisor Aleksandra Radenovic. She was always fully supportive of initiatives from my side. The regular meetings with her gave direction to the work and ensured progress. She was always positive about collaborations, and this certainly helped me with my work. I also appreciate her patience regarding my experimental skills.

I would also like to thank my co-supervisor Ivo Sbalzarini. While our work together was limited to the initial part of the PhD, Ivo's positive energy, breadth and intelligence have been inspiring. He gives full freedom to the students. His communication abilities, written and spoken , are also very inspiring, and I could learn much from him.

I would also like to thank my jury members Profs. Alberto Diaspro, Jean-Baptiste Sibarita and David Suter for kindly reading and critiquing my work.

So much of the good in this thesis would not have happened without the help from colleagues and collaborators. My collaboration with Jayakrishnan Unnikrishnan was extremely fruitful, and I learned so much by working with him. He's really a genius, and that too with such a calm and cool demeanor.

Discussions with Hendrik Deschout helped me immensely – most certainly professionally, and often personally. The number of important concepts he has clarified to me is in dozens. I am extremely grateful to have had Paolo Annibale help me with the basics of optics and microscopy. That is in addition to having his own work to follow-up on, the themes explored in this thesis was hugely influenced by the results of his PhD. I was blessed to have the kind and cool Lely Feletti as a trainer of basic molecular and cell biology techniques. I also want to thank my collaborators Georg Fantner and Pascal Odermatt. It was a pleasure to work with Radek Jankele, and to have known him as a person. His motivation regarding research was contagious.

That much on the professional side. But I would not have survived it without the kindness, love and camaraderie of colleagues, friends and family. This list include Floriano Traversi, Fabrizia Dutto, Pencho Yordanov, Ramona Sorecau, Natalie Emch, Swati Krishnan, Daniel Toth, Hamed Hasani, Marie Didier, Asia Andrzejka Naveen, Dilu Mathew, Federico Corradi, Tushant Singh, Daria Krasnozhon, Adrien Allain, Saheer Babu and so many others, in no

particular order. Special thanks to my colleagues Jiandong Feng, Ke Liu, Michael Graf, Lorenz Steinbock and Roman Bulushev. All of them helped me in some way or the other.

Also thanks to my age old friends, with whom while contacts were sporadic, were always in my mind: Dileep MK, Amr Najjar, Arun IB, Rahul Devassy, Anil Chorppath. I would like to thank Prof. Sibi Chacko, and Anish Mampetta, for motivating me to take up research, and to Kerala Shasthra Sahitya Prishad (KSSP) for instilling that wonder and love of science and nature, which will never go away!

And lastly, to my family: my mother, father and sister, who were with me in sun and in shadows, and to my beloved life partner Rakhi, and my little girl Zoya, for being so nice and kind with me...

Dedicated to my mother

*It is very easy to answer many of these fundamental biological questions; you just look at the thing!... Make the microscope one hundred times more powerful, and many problems of biology would be made very much easier. [...] the biologists [...] would prefer that to the criticism that they should use more mathematics.*

– Richard Feynman, *There's Plenty of Room at the Bottom* (1959)

*The aim of science is not to open the door to infinite wisdom, but to set a limit to infinite error.*

– Bertolt Brecht, *Life of Galileo* (1938)

# Note on content

Chapters 2, 3, 5, 6 and Appendix A consist of content reproduced verbatim (except for minor format uniformization) respectively from the following sources:

1. A. Shivanandan, H. Deschout, M. Scarselli, and A. Radenovic. Challenges in quantitative Single Molecule Localization Microscopy. *FEBS Lett*, 588(19):3595–3602, 2014
2. A. Shivanandan, J. Unnikrishnan, and A. Radenovic. Accounting for limited detection efficiency and localization precision in cluster analysis in Single Molecule Localization Microscopy. *PLOS ONE*, 10(3):e0118767, 2015
3. P. D. Odermatt, A. Shivanandan, H. Deschout, R. Jankele, A. P. Nievergelt, L. Feletti, M. W. Davidson, A. Radenovic, and G. E. Fantner. High resolution correlative microscopy: Bridging the gap between Single Molecule Localization Microscopy and Atomic Force Microscopy. *Nano Lett*, 2015. *Published.*
4. A. Shivanandan, A. Radenovic, and I. F. Sbalzarini. MosaicIA: an ImageJ/Fiji plugin for spatial pattern and interaction analysis. *BMC Bioinformatics*, 14(1):349, 2013
5. H. Deschout, A. Shivanandan, P. Annibale, M. Scarselli, and A. Radenovic. Progress in quantitative Single Molecule Localization Microscopy. *Histochem Cell Biol*, 142(1): 5–17, 2014a.

This also explains the variation in flow and style between the chapters, and the redundancy in information.

# Contents

# List of Figures

# List of Tables

# Chapter 1

# Introduction

## 1.1 Diffraction limit and Single Molecule Localization Microscopy

Fluorescent microscopy (FM) has been fundamentally important to biology. It allows the imaging of a specific component of interest, e.g., a protein, by attaching a fluorescent label to it, thus creating a high contrast with its background, in an environment close to natural conditions. This technology has been routinely used for quantitative studies of sub-cellular processes in live cells, in multi-color and 3D – in fact, -omics scale single molecule resolution data have been available (e.g. Taniguchi et al., 2010).

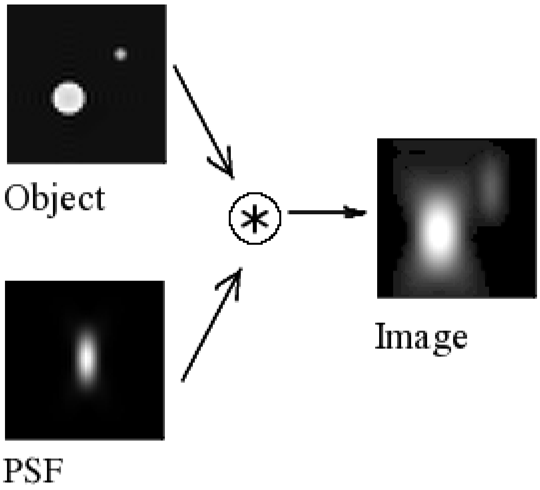

**Figure 1.1.** Image formation: convolution by Point Spread Function
Longitudinal (XZ) central slice of a 3D image acquired by a fluorescence microscope. The Object in the sample is convolved with the PSF of the microscope, resulting in the diffraction limited Image. Source: Wikimedia Commons.

However, the technology is plagued by a fundamental problem with optical imaging, related to the physical nature of light – since the light wave undergoes diffraction during its interaction with the objective, the imaging of an object in the sample results in an image which is a convolution of that object and the Point Spread Function (PSF) of the microscope (Figure 1.1) (Hell, 2007, and references therein). The PSF is theoretically described by an Airy disc model(Figure 1.2), and is often approximated by a Gaussian function whose width depends on the wavelength of light and the aperture of the objective used. For the

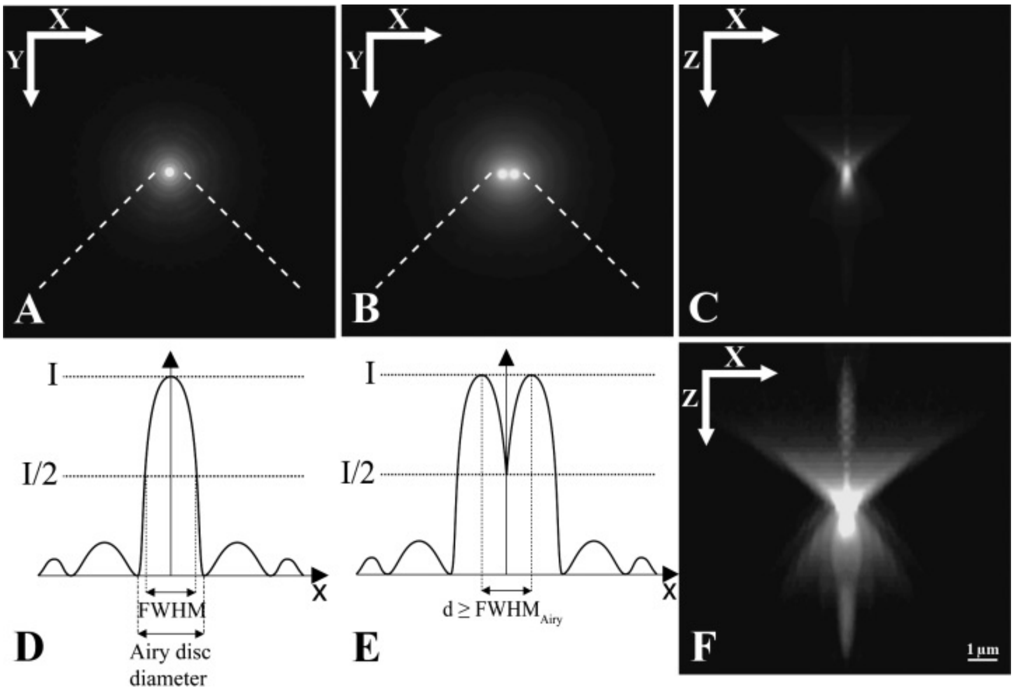

**Figure 1.2.** The Point Spread Function and resolution limit.
An image of a point is not a point but a pattern of diffracted light (A–C) Two-dimensional diffraction patterns of the centres of 170-nm green fluorescent beads seen through a wide-field microscope. (D) and (E) Corresponding fluorescence intensity curves traced along a line passing through the centre of the beads in (A) and (B), respectively (I being the maximum intensity). (F) Three-dimensional projection of the z-stack representing the diffraction pattern of the fluorescent bead seen from the side. (A) and (D) Note the concentric light rings around the Airy disc of a single fluorescent bead. The Airy disc is the first light patch in this diffraction pattern. Two characteristic dimensions may describe the bell-shaped curve: 1, Airy disc diameter, which is the distance between the two points where the first light ring extinguishes; 2, full width at half maximum (FWHM), which is directly related to resolutions. (B) and (E) Diffraction pattern of two beads. Two objects are resolved if their corresponding intensity curves at I/2 are distinct. The critical distance d between the centres of the intensity curves defines the lateral resolution (x, y) of the optical system. It is equal to FWHM. (C) Three-dimensional projection of a z-series of a fluorescent bead seen from the side (x, z) representing the diffraction pattern of the same fluorescent bead. Note that the axial resolution (z) of an optical system is not as good as the lateral resolution (x, y). Figure and caption from Bolte and Cordelières (2006). Reproduced with permission from John Wiley and Sons.

typical wavelengths used in FM (e.g., in the case of Green Fluorescent Protein, GFP, $\approx$ 500nm) and the typically available high aperture sizes ($\approx$ 1.49), the Full Width Half Maximum (FWHM) of this PSF is about 200nm – if there are multiple objects which fall within this scale, they cannot be identified separately, and hence, this is known as the diffraction limit of light (Figure 1.2). Alternative definitions of the limit, such as the Abbe resolution limit, exist (Bolte and Cordelières, 2006). Conventional FM (in modalities such as Wide Field and Confocal), therefore, has a resolution limited by diffraction of light.

In the cell, however, various components are of a much smaller size. E.g., the diameter of actin filaments is 8nm, whereas that of microtubules is 25nm. A large number of organelles and sub-cellular structures, from clathrin coated pits involved in endocytosis to nuclear pore complexes, have a size less than the diffraction limit. Most of membrane proteins are distributed in sub-micrometer clusters, whose sizes can often be below diffraction limit. To study these structures and their function, FM needs to go beyond the diffraction limit.

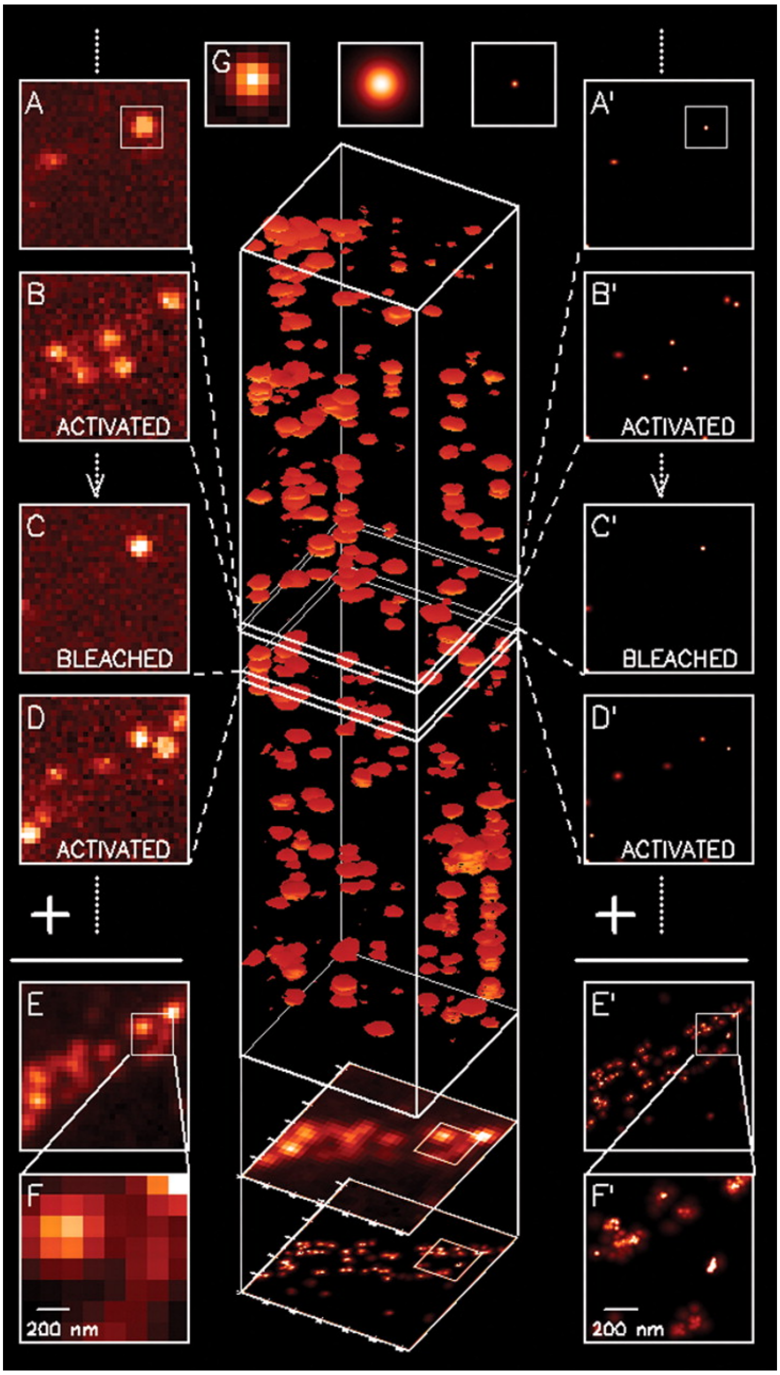

**Figure 1.3.** PALM concept: OFF-ON-localize cycles
**A,C** The fluorophores are mostly in the OFF state, except for the fiducial marker. **B,D** A sparse set is activated and imaged. **A′,B′,C′,D′** Localized positions. **E,E′** Conventional and PALM images. From Betzig et al. (2006). Reprinted with permission from AAAS.

While the diffraction limit is fundamental, a number of far-field microscopic modalities have been developed that can get around it. These optical Super-Resolution (SR) techniques include STimulated Emission Depletion (STED) Microscopy (Hell and Wichmann, 1994), Structured Illumination Microscopy (SIM) (Gustafsson, 2000, 2005), and a set of modalities that can be categorized under the umbrella term Single Molecule Localization Microscopy (SMLM), such as PhotoActivated Localization Microscopy (PALM) (Betzig et al., 2006), STochastic Optical Reconstruction Microscopy (STORM) (Rust et al., 2006) and Fluorescent PALM (FPALM) (Hess et al., 2006). The general idea for getting around the diffraction limit barrier is to use additional optical characteristics or states, so as to distinguish fluorescent molecules that fall within a diffraction region (Betzig, 1995; Hell and Wichmann, 1994; Hell, 2007). PALM/FPALM uses photoactivable/photoswitchable fusion protein approach for labeling, whereas STORM uses organic dyes. SMLM techniques have an advantage over the other SR techniques, in that it can offer single molecule resolution.

Briefly, SMLM modalities use the possibility of imaging multiple frames of only a sparse subset of well separated molecules in the field of view per frame, so that none of them fall within a diffraction limited region of another(Figure 1.3). This is achieved by the exploitation of additional states of the fluorophore apart from ON and OFF states. E.g., the fluorescent protein mEos2, which can be imaged by exciting it with 488nm light (called 'green' form), exhibits different photophysical properties if shined with 405nm light – it converts into a 'red' form, and becomes excitable with 561nm light. This 'photoactivation' property can be used for selecting only a sparse subset of molecules per frame, by using a low intensity 405nm activation, and its Poisson statistics. Once a molecule in the ON state is imaged, its position can be estimated, with an estimation error known as localization uncertainty, given by an error model.

The theory to estimate the true location from the imaged PSF has been described in Thompson et al. (2002), and later updated in Mortensen et al. (2010). The main contributors to measurement error are:

1. a limited signal i.e., count of collected photons $N$ (Figure. 1.4),
2. loss of information due to discrete imaging, i.e. having a finite pixel size $a$, and
3. a non-negligible mean background signal of $b^2$.

The variance of the least squared Gaussian fit estimator can be expressed in closed form, and is given by

$$\sigma_{loc}^2 = \frac{\sigma_a^2}{N}\left(\frac{16}{9} + \frac{8\pi\sigma_a^2 b^2}{Na^2}\right), \tag{1.1}$$

where $\sigma_a^2 = \sigma_{PSF}^2 + \frac{1}{12}a^2$, $\sigma_{PSF}^2$ is the variance of the 2D Gaussian PSF model. $\sigma_{loc}$ is often referred to as localization precision. The Full Width at Half Maximum (FWHM) value is given by $2.35\sigma_{loc}$.

Mortensen et al. (2010) further describes a maximum likelihood estimator, which is the optimal unbiased estimator. Other approaches, such as sparse-signal recovery based on compressed sensing, have also been proposed (e.g. Zhu et al. (2012)).

SMLM is in principle does not have a fundamental spatial resolution limit, its resolving power of a single molecule instead is limited in practice by the signal, i.e. number of photons collected from a fluorophore, and the background, with a typical value between 20nm-50nm (FWHM) for an experiment, thus filling the resolution gap between short range techniques such as Förster Resonence Energy Transfer (FRET) and conventional FM. For a sample with multiple molecules, the sampling rate of the underlying ultrastructure also becomes important in defining the overall resolving power (Shroff et al., 2008; Nieuwenhuizen et al., 2013). SMLM technologies have been used to address a large range of biological problems, and a brief overview of it can be found in Section 2.2, with a focus on biological applications. A detailed review with a focus on quantitative applications can be found in Appendix A.

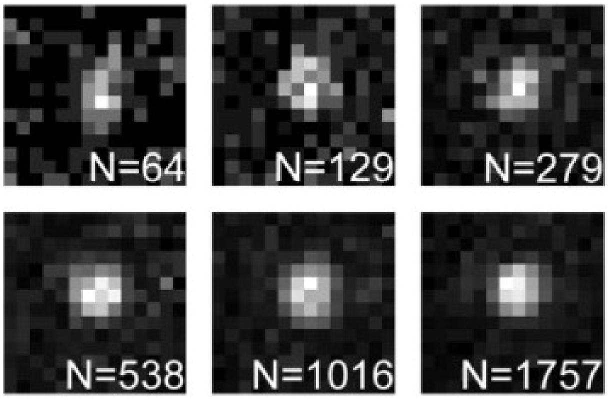

**Figure 1.4.** Effect of collected photon count on PSF image.
Images of a fluorescent bead, with varying photon count estimates. The larger counts result from accumulating an increasing number of images. Note the difference in signal quality, proportional to photon count. From Thompson et al. (2002). Reproduced with permission from Elsevier.

## 1.2 Quantitative SMLM

Quantification in biology involves a wide range of approaches: it can mean something as straightforward as correlation or co-localization (Bolte and Cordelières, 2006), or it can involve mathematical modeling and identification at different scales and coarseness – biophysical, systems biological, etc (e.g., De Jong, 2002). Some studies, such as molecular counting, are inherently quantitative. On the other hand, even the most descriptive of studies could possibly gain from accurate and precise quantification, as inference based on visual inspection could be misleading, as exemplified by the optical illusion in Figure 1.5. Inference based on manual/visual approaches are prone to sampling biases, do not account for random chances and systematic errors, possess a limited detection range, and are typically not systematic and objective. Its effectiveness in case of non-binary, or not ″obviously″ qualitative differences in output is limited. Also, as the throughput of the experiments increase, visual or manual approaches simply are not practical. These reasons apply for SMLM, perhaps in higher magnitudes, especially if single molecule level studies are intended.

As explained in the previous section, SMLM has an inherent non-trivial computational component, even in its most non-quantitative application. In its basic form, SMLM involves simple estimation algorithms – the signal from single molecules must be identified with image filters, and then fit to models of PSFs, by least square or maximum likelihood approaches, and then the estimated point locations rendered by some algorithm.

Performing quantitative studies with SMLM, however, requires more complicated analysis tools. SMLM has been typically used for three types of quantitative studies: single molecule counting, studies of the structured spatial organization of proteins, and co-localization(an elaborate review can be found in Section 2.2 and Appendix A). Quantitative studies with SMLM involves accounting for a number of issues that are inherent to the technique.

The following list, while not exhaustive, collates many of the issues involved in the application of SMLM to biology, and especially, quantitative studies. The list focuses on PALM, while they are applicable to STORM in different magnitudes. Section 2.3 reviews these in detail (also see Appendix A). They include:

1. Labeling errors and artifacts. This is a challenge that SMLM shares in part with conventional FM, however in higher magnitude, due to higher resolution and sparse imag-

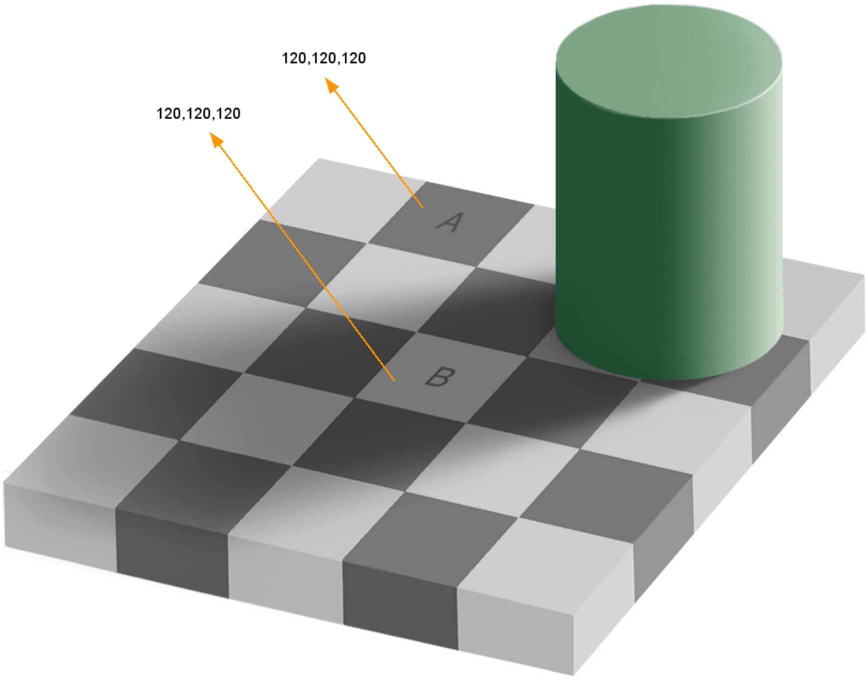

**Figure 1.5.** Visual inference can be decieving: an optical illusion
The intensity values at the squares A and B in the 2D image are the same (the RGB triplets are shown). Yet, they might give the illusion that they have different colors. Source: Wikimedia Commons.

ing. In addition to the issues associated with the expression of fusion protein (such as overexpression *vs* endogeneous), there could be imperfect or non-homogeneous labeling, as well as artifacts introduced due to non-negligible label size. Often, the features appearing in the PALM image cannot be distinguished from the artifacts due to labeling errors(Figure 1.6). Section 2.3.1 provides a brief overview of this problem.

2. Fluorophore photoconversion efficiency, or detection efficiency of about 40-60%, i.e., only a fraction of the label molecules in the sample turn fluorescent (Annibale et al., 2012; Puchner et al., 2013; Durisic et al., 2014b). This might affect all major quantification studies with SMLM, including counting, cluster analysis and co-localization. Section 2.3.2 provides a brief overview.

3. Localization uncertainty of 20-50nm FWHM (Section 2.3.3). A large number of systems imaged with SMLM have a length scale in the same order. This could be significant in quantitative studies, especially on a single molecule level.

4. Quantification tools. The readout from SMLM is quite unlike typical imaging systems – standard SMLM produces a list of coordinates of localizations, along with their localization uncertainties, and not directly an image. The rendering of these localizations as an image could be done in multiple ways, each with its own limitations and information loss (Section 2.3.7). The representation and quantification of these, especially considering the systematic issues such as blinking and limited detection efficiency, could be a complicated problem. The sparse localizations – a point pattern – finds a readily accessible toolset in the field of spatial statistics and spatial point patterns. Customizing the spatial statistics framework for the specific questions in SMLM is one task, having user friendly software that does these is another.

5. Fluorophore blinking (Section 2.3.4). The same fluorophore is often imaged in multi-

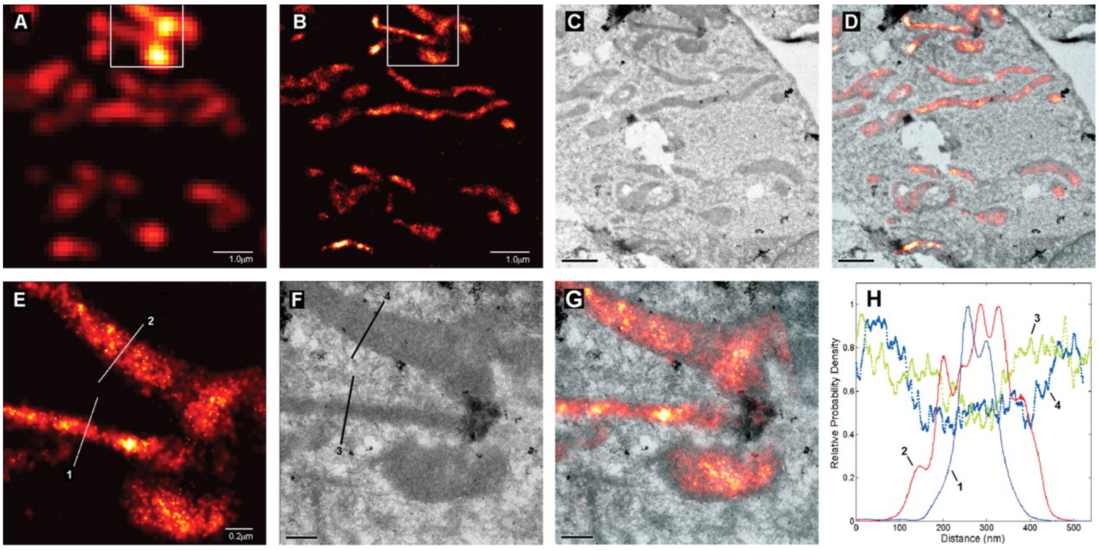

**Figure 1.6.** TEM-PALM correlative microscopy: non-homogeneous labeling
Images are of mitochondria in a cryo-prepared thin section from a COS-7 cell expressing dEosFP-tagged cytochrome-C oxidase import sequence. **A** diffraction limited image **B** PALM image **C** TEM image **D** PALM-TEM overlay **E,F,G** zoom in and **H** line profile. The non-homogeneities in the PALM signal can be observed in **E,G**, which is not reflected in the TEM image. From (Betzig et al., 2006). Reprinted with permission from AAAS.

ple frames, and often reappear after going OFF in a few frames. It could be difficult to identify such multiple appearances to the same fluorophore, possibly resulting in appearance of false clusters, or wrong molecular counts.

6. Sample drift(Section 2.3.5). SMLM involves imaging of multiple frames, in the range of 1000-100000, taking a time in the range of several minutes. The sample drift, due to thermal and vibrational energy, could be as high as 100nm, producing significant image artifacts.
7. Fixation artifacts(Section 2.3.6). Due to a long imaging time, live cell imaging is difficult, and a large number of SMLM studies were done on fixed samples, focusing on structure and not dynamics. However, fixation could produce artifacts – e.g., different molecules could be getting fixed at different times, affecting the configuration.
8. Optical aberrations and registration problem. This could especially be an issue in two color or correlative imaging. More details can be found in Section A.4.

It is in this context that the contribution of this thesis lies.

## 1.3 Contribution and structure of the thesis

The focus area of this thesis is the development of methods for quantitative SMLM. As mentioned above and detailed in Chapter 2, the technology has several sources of errors, such as a limited detection efficiency and localization precision, and also errors due to imperfect labeling, limiting its utility for accurate and precise measurements, especially for quantitative studies. For example, for PALM, the detection efficiency and localization uncertainty in the range of 40-60% and 20-50nm (FWHM) respectively can significantly affect quantitative analysis. For accurate and precise quantification, the analysis methods need to account for these errors. Such errors also point to the need of correlative microscopic tools, for validation and error calibration, apart from the obvious complementary utilities offered by both techniques. Also, the novel structure of data – coordinates of localizations along with their localization errors rather than images – also require new analysis software. This thesis consists of three different but related projects addressing this context – a set of analysis techniques, software and an experimental tool. The next sections briefly introduce the work presented in this thesis.

### Analysis methods for accurate quantitative SMLM

SMLM has been commonly used to investigate the spatial organization of membrane proteins. However, the above mentioned errors inherent in SMLM can affect quantitative studies. We developed analysis methods that account for some of these errors.

In the SMLM field, quantification of spatial structure of membrane protein clusters is often done by means of spatial summary statistics functions of second-order properties, such as the Ripley $K$-function, $L(r) - r$ function and the Pair Correlation Function (PCF) (Section A.3 and 3.4.1). They have several advantages over other empirical characterization methods: they are either parameter independent or only mildly dependent, can detect interactions at multiple spatial scales, and can work with both dense and sparse point patterns – features that make them advantages over other empirical, parameter dependent methods, such as clustering using a clustering algorithm followed by analysis of clusters.

To account for limited detection efficiency, we modeled limited detection efficiency as a case of spatial subsampling or $p$-thinning. This allowed us to use the known property of these second-order summary statistics functions, which says that they functions are invariant to independent spatial subsampling or $p$-thinning. The result is also applicable to co-localization measures based on these functions.

We also developed analytical solutions for the mean and variance of these subsampled estimators, as a function of true points and the subsampling ratio. The analytical methods are shown to agree well with results from simulation studies. We characterized the bias and the relative variance of the subsampled functions based on simulations, and found that they are relatively low for a large class of cluster conditions. We also demonstrated the applicability of these methods to SMLM data, by 1) adding errors artificially and 2) applying the methods on redundant labeling data.

We also describe an estimation framework for the true locations of the localizations in clusters that account for the localization uncertainty. It estimates true locations given the observed points in clusters and the localization error model. The derivation for Gaussian shaped clusters are provided, which can also be used for cluster shapes that are approximately Gaussian. The framework provides the formulation in the case of other cluster shapes. We describe a method to identify the cluster models empirically in Section. We applied this method on SMLM data from photoblinking caused clusters.

The error due to the combined approach – true location estimation and second-order characterization based on summary statistics – was characterized for a variety of cluster conditions. They were found to significantly reduce the error in quantification. Our approach, among the first in the SMLM literature to tackle these sources of errors in analysis, paves way to more accurate quantitative SMLM.

Also, we analyzed the theoretical properties of an estimator of cluster size that has been described in microscopy literature. Conflicting reports have appeared in the literature about the relation of this estimator, defined as $r_a = \arg\max_r L(r) - r$, to the true cluster size. Our study clarifies this with mathematical rigor, and provides a cautionary note to its use.

### SMLM-AFM correlative microscopy

Since Atomic Force Microscopy (AFM) provides high resolution spatial profile of the imaging area, it can be used as a validation and error estimation tool for SMLM imaging. Additionally, since SMLM and AFM provides complementary information, correlative microscopy involving the two can provide a useful tool for biologists. E.g., it can be used for accurate study of diffusion, since high resolution spatial profiles can be obtained from AFM; or say, studies on cell morphology and its link to specific proteins. AFM's ability to provide information about mechanical properties of bio-structures, and its possible utility as a nanomanipulation tool, can also be used to design innovative experiments.

For such applications, the combined tool must work with glass substrates, and in the presence of fluid, so as to be close to natural conditions, and to obtain optimal optical properties. We imaged actin filaments *in vitro* by means of a STORM-AFM correlative microscopy tool in glass/fluid, and also developed a simple algorithm to perform overlay of the SMLM and AFM images. We found that the height of the filaments correlate with the localization density, and the source of localization inhomogeneties can be partially identified to bundling of actin filaments. The tool also was used to image bacterial and live mammalian cells, in the AFM-PALM modality.

### ImageJ plugin for spatial interaction analysis

In this work, we implemented a software in the popular ImageJ platform to perform spatial interaction inference for dual-color microscopy. The method involved the extention of the traditional nearest neighbor-threshold based co-localization method, so as to increase the detection power of interaction, by modeling spatial interactions between objects (such as proteins, cells etc) by means of a spatial Gibbs function which accepts various "interaction potential" shapes along with the traditional threshold function. The framework also consists of hypothesis tests for interaction. The software works with both images as well as coordinates of points, forming an ideal analysis tool for SMLM data. We describe the application of this software on both confocal microscopy and SMLM data.

### Thesis organization

The organization of the thesis is as follows. Chapter 2 consists of a review of the applications of quantitative SMLM to biological problems, and the challenges in performing accurate quantitative SMLM. This chapter acts as a more detailed introduction, and sets the ground for the research work described in this thesis. Chapter 3 consists of development of analytical techniques to perform cluster analysis, after accounting for limited detection efficiency and localization precision. Chapter 4 develops the ideas in Chapter 3 further, with some theoretical studies and extensions, and applications on real data. Chapter 5 describes the correlative AFM-SMLM microscopic tool, that can not only provide validation of SMLM data, but also perform innovative experiments utilizing the complementary readouts. Chapter 6 consists of a software framework that extends the traditional co-localization measure to a spatial interaction measure, and that works with both point locations as well as images. Chapter 7 concludes the thesis, by providing a summary and outlook.

# Chapter 2

# Challenges in quantitative single molecule localization microscopy

*This is a verbatim copy of a peer reviewed publication: A. Shivanandan, H. Deschout, M. Scarselli, and A. Radenovic. Challenges in quantitative Single Molecule Localization Microscopy.* FEBS Lett, *588(19):3595–3602, 2014. Reprinted with permission from Elsevier.*

## Abstract

Single molecule localization microscopy (SMLM), which can provide up to an order of magnitude improvement in spatial resolution over conventional fluorescence microscopy, has the potential to be a highly useful tool for quantitative biological experiments. It has already been used for this purpose in varied fields in biology, ranging from molecular biology to neuroscience. In this review article, we briefly review the applications of SMLM in quantitative biology, and also the challenges involved and some of the solutions that have been proposed. Due to its advantages in labeling specificity and the relatively low over-counting caused by photoblinking when photo-activable fluorescent proteins (PA-FPs) are used as labels, we focus specifically on Photo-Activated Localization Microscopy (PALM), even though the ideas presented might be applicable to SMLM in general. Also, we focus on the following three quantitative measurements: single molecule counting, analysis of protein spatial distribution heterogeneity and co-localization analysis.

## 2.1 Introduction

With the invention of single molecule localization microscopy (SMLM) (Betzig et al., 2006; Rust et al., 2006; Hess et al., 2006), it has become possible to extend the advantages of fluorescence microscopy beyond its diffraction limited spatial resolution of about 200 nm. This provides the possibility of resolving organelles or even single molecules with an order of magnitude better resolution, in multiple color channels and in 2D as well as 3D. Recent reviews on the updates on the technology and its uses can be found in (Oddone et al., 2014; Klein et al., 2014). SMLM can potentially be used for quantitative measurements (Gould et al., 2012; Deschout et al., 2014a), e.g., in counting the number of molecules of a protein specie (Lando et al., 2012), and stoichiometry estimation of protein complexes (Renz et al., 2012; Nan et al., 2013; Gunzenhäuser et al., 2012), characterizing the spatial distribution of a protein specie (Scarselli et al., 2012; Greenfield et al., 2009; Rossy et al., 2013; Sengupta et al., 2011), estimating the co-localization or co-clustering between organelles and also singlemolecules (SM) (Annibale et al., 2012; Pertsinidis et al., 2013; Lehmann et al., 2011; Sherman et al., 2011), estimating the relative positions of various components in a protein complexwith high precision (Szymborska et al., 2013; Loschberger et al., 2012), and estimating the diffusion coefficients by means of single particle tracking (SPT) in a dense sample (Manley et al., 2008; Persson et al., 2013). Two basic variants of SMLM are Photo-Activated Localization Microscopy (PALM) and STochastic Optical Reconstruction Microscopy (STORM). The former uses fluorescent proteins for labeling (called photo-activable fluorescent proteins, PA-FPs), whereas the latter uses organic dyes. Since the usage of fusion proteins used in PALM provides comparatively high specificity labeling as against immunolabeling (the typical labeling technique used for STORM), and since the phenomenon of photoblinking for PA-FPs is minimal (as against the photo-switchable organic dyes used in STORM, which typically blink 10 times or more before irreversible photobleaching (Dempsey et al., 2011)), PALM appears to be better suited for quantitative studies, and for this reason forms the focus of this article even though many of the ideas presented are applicable to SMLM in general. Yet, quantitative analysis with PALM is plagued by several sources of errors (Deschout et al., 2014a; Wang et al., 2014), including that of a limited detection efficiency of label molecules in the range of 40–60% (Annibale et al., 2012; Durisic et al., 2014b), a localization uncertainty in the order of 20–50 nm (Thompson et al., 2002; Mortensen et al., 2010), overcounting in the range of 100to reappearance of label molecules due to photoblinking (Sengupta et al., 2011; Annibale et al., 2010, 2011a; Lee et al., 2012), errors in labeling, a sample drift in the order of 50–100 nm (Betzig et al., 2006; Geisler et al., 2012) and in the case of multi-color imaging, registration errors (Annibale et al., 2012).

This review is divided into two parts. The application of SMLM has brought new discoveries in varied biological fields such as cell biology, neuroscience, microbiology and molecular genetics. First, we provide a bird's eye view of the applications of quantitative SMLM in these fields, focusing on the biological perspective. Then, with the help of cartoon figures, we explore in detail the challenges that are present in the use of SMLM, and specifically PALM, for quantitative experiments. We focus specifically on three specific quantitative applications of PALM: single molecule counting, analysis of protein spatial distribution heterogeneity and co-localization analysis. We also provide a brief summary of the methods that have been presented in the field to resolve the challenges presented.

## 2.2 Quantitative SMLM and biology

The possibility to quantify the number of proteins within biological assemblies and to characterize the protein spatial distribution has permitted to determine protein stoichiometry and distribution in signaling complexes. As a demonstration of this aspect, some groups, including ours, have analyzed the existence of protein aggregates such as oligomers and clusters for signaling receptors as G protein-coupled receptors (GPCRs), asialoglycoprotein receptors and RAS signaling molecules (Renz et al., 2012; Nan et al., 2013; Scarselli et al., 2013).

For the $\beta 2$ adrenergic receptors, by means of quantitative cluster analysis, we found that the receptors are partially organized in mini-clusters only in the cardiomyocytes like-cells but not in other cell lines, and these oligomers are not lipid raft related but depend on actin cytoskeleton integrity (Figure 2.1) (Scarselli et al., 2012; Ianoul et al., 2005). Importantly, this conclusion was quite different from a similar report that was obtained using a different method named near-field scanning optical microscopy (NSOM) (Ianoul et al., 2005), as a demonstration of a better precision of PALM over other techniques. Receptor oligomers were not affected by the addition of different ligands, indicating that the receptor is already pre-associated before activation and is not related to receptor basal activity. In contrast, in a study by Renz et al. that made use of quantitative single molecule counting, it

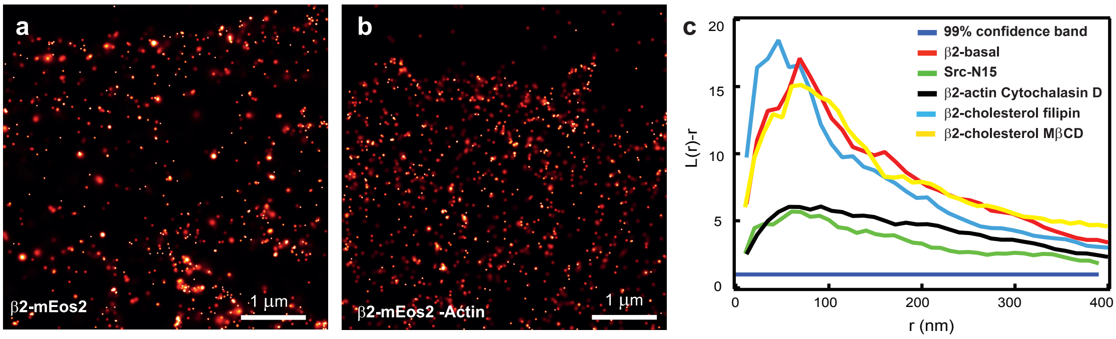

**Figure 2.1.** PALM images and cluster analysis of $\beta$2-mEos2 on the plasma membrane of H9C2 cells after cholesterol sequestration or actin microfilament disruption.
(a–b) PALM images in total internal reflection fluorescence geometry of $\beta$2-mEos2 on the plasma membrane of fixed H9C2 cells in basal condition (a), and after actin cytoskeleton disruption (b). (c) The degree of clustering for the experiments shown was determined by Ripley's $K$-function analysis and $L(r)$–$r$ function that displays the magnitude of deviations from a random distribution as positive y values (normalized to 99% confidence interval). Data are representative of experiments that were repeated at least three times. Cholesterol inactivation was obtained by preincubating cells with filipin for 30 min at the concentration of 12 lg/ml or MbDC with a preincubation of 30 min at the concentration of 5 mM, while actin microfilaments disruption was performed by preincubating for 30 min with cytochalasin D at the concentration of 2 $\mu M$.

was shown that assembly of asialoglycoprotein receptors into homo- and hetero-oligomeric structures is dictated by exogenous ligands leading to the internalization of one receptor complex over another complex (Renz et al., 2012). In this case, the authors used quantitative PALM together with ensemble Förster Resonance Energy Transfer (FRET) imaging. This experimental strategy has demonstrated the strong synergy that exists between these two different techniques combining the powerful sensitivity of FRET to detect receptor proximity with the capability to obtain direct visualization of receptor oligomers with PALM. A similar approach was also successfully applied to study another strategic protein in the RAS signaling, named RAF (Nan et al., 2013). By means of cluster analysis, the authors showed how RAF exists between an inactive monomeric state in the cytosol and a multimeric condition at the cell membrane when activated. Together, these results confirmed the importance of dimers and oligomers formation in RAF signaling, even though the precise biological role of these different multimeric states is yet to be determined.

Another relevant consequence of the introduction of SMLM has been a better definition of biological structures in the nanometer range. This has been particularly true in the neuroscience field whereas the morphology of neurons composed by dendritic spines and synapses is not perfectly suitable for confocal microscopy. For example, imaging presynaptic and postsynaptic scaffolding proteins in glomeruli of the mouse olfactory bulb using STORM, Dani et al. showed distinct punctate patters that were not resolved by conventional fluorescence image (Dani et al., 2010). They quantified various morphological parameters, and were able to distinguish the presynaptic Bassoon and postsynaptic Homer1 clusters. In this line of research, another group studied, by means of cluster analysis, the postsynaptic density (PSD) organization in live rat hippocampal neurons (MacGillavry et al., 2013). PALM was able to localize scaffolding nanodomains of PSD-95 enriched preferentially of AMPA receptors compared to NMDA receptors. This post-synaptic architecture could be relevant for the amplitude of postsynaptic currents, suggesting the mechanism of PSD in regulating the strength and plasticity of the glutamatergic transmission. For the optimization of cell morphology measurements in living cells using Single-Particle Tracking PALM, it has been shown using Monte-Carlo simulations how some technical parameters such as the length of the excitation pulse can influence the imaging of spine and spine neck morphology in living neurons, making them erroneously thinner when imaged using a longer excitation pulse (Frost et al., 2012).

SMLM was also applied to study exocytosis in different cell types, such as chromaffin cells. In PC12 cells, PALM was able to determine the size of clathrin coated pits during reuptake of vesicular acetylcholine transporters (Sochacki et al., 2012). In contrast to what was found with confocal microscopy, Bar-On et al. used PALM to demonstrate that syntaxin1 and SNAP-25 clusters have a weak co-localization in PC12 cells (Bar-On et al., 2012). Additionally, PALM helped to establish that clustered SNARE proteins are not involved in large dense core vesicles (LDCV) in the fusion process (Yang et al., 2012).

Another field in biology that has received attention for SMLM is microbiology, in particular for the study of bacteria and viruses. Because of the size of these microorganisms, the super resolution methods are suitable for revealing the details of their sub-cellular structures. For example, Ptacin et al. (2010), studying the partitioning (Par) apparatus that guides centromere segregation, were able to determine the ParA and ParB dynamics, suggesting that retracting ParA fibers are critical for this phenomenon. SMLM also has shown its applicability in providing new details into viral infection. Using dSTORM, Pereira et al. (2012) were able to visualize and quantify the distribution of structural proteins of the human immunodeficiency virus type 1 (HIV-1) before and after infection of lymphoid cells . Another work on the same theme was able to determine the distribution of the integrase enzyme (IN) of HIV in infected cells in the cytosol and in the nucleus, and to characterize its morphology (Lelek et al., 2012). The authors used a different version of the PALM technique, called FlAsH-PALM, where proteins are tagged with small tetracysteine motifs and the fluorescein arsenical helix binder.

Finally, super-resolution microscopies have opened a door in a deeper understanding of the chromosome organization and genome mapping. Wang et al. determined nucleoid-associated proteins distribution in live Escherichia coli cells (Wang et al., 2011), while another group was able to label 91 out of a total of 107 reference sites on a 180 kb human BAC gene with a 100 bp resolution (Baday et al., 2012). DNA mapping with such resolution offers new potentials to uncover genetic variance and to facilitate medical diagnosis in genetic diseases.

## 2.3 Challenges

In this section, we review the critical challenges that are present in using SMLM, and specifically PALM, for quantitative measurements. While the challenges presented might be applicable to different types of quantification measures, we focus specifically on single molecule counting, analysis of protein spatial distribution heterogeneity and co-localization analysis. Before proceeding further, we note that it is possible that the image processing and localization algorithms used can also introduce errors in quantification, however this is treated in detail elsewhere (Deschout et al., 2014b; Small and Stahlheber, 2014). A brief introduction to the quantitative measures being mentioned can be found in (Deschout et al., 2014a; Gould et al., 2012).

### 2.3.1 Labeling errors

In SMLM, typically, the label tag can either be a fluorescent protein (FP) or an organic dye. In the former case, the labeling is usually done by means of overexpression, i.e. introduction

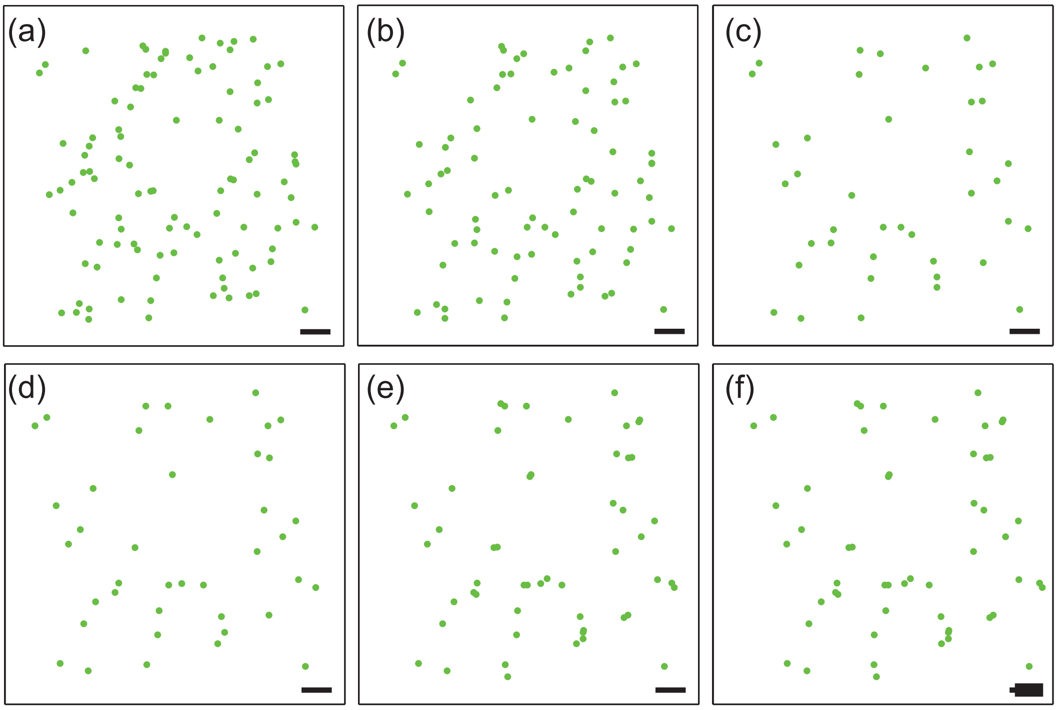

**Figure 2.2.** Illustration of the influence of several sources of error on single molecule counting with PALM.
The green dots represent the positions of single protein molecules (a), the positions of label molecules (b), and point localizations with step by step addition of different errors (c, d, e, f). The number of positions *nloc* is determined for each case. (a) There are 100 molecules that are spatially distributed at random (*nloc* = 100). (b) The fluorescent label is removed 5 nm from the molecule in a random direction and there is an 80% probability that a molecule is labeled (*nloc* = 81). (c) There is a 60% probability that a fluorescent label is activated and detected (*nloc* = 40). (d) The localization uncertainty is equivalent to sampling from a normal distribution with a standard deviation of 10 nm centered on the position of the fluorescent label (*nloc* = 40). (e) At a random time point within 10 s after deactivation, there is a 40% probability that the fluorescent label is again activated and localized with a 10 nm uncertainty (*nloc* = 54). (f) There is a 0.05 nm/s drift from left to right during an acquisition time that is 1000 s (*nloc* = 54). It should be noted that in certain situations it is possible that due to drift the molecule count may be affected since the area of imaging changes over time. The scale bars represent 100 nm.

to the cell of a plasmid with a vector consisting of the fusion of the sequences corresponding to the protein of interest and that of the fluorescent protein. In the latter case, the most typical labeling approach is immunolabeling, i.e., the dye is attached to the protein by means of antibodies. In this review we stick to PALM and hence labeling with PA-FPs, while noting that it is well known that the immunolabeling approach is more prone to labeling errors, including unspecific labeling.

In the case of labeling by means of overexpression, the protein expressed from the plasmid will exist in the cell along with those expressed endogenously. Since the latter is not fluorescent, this creates obvious limitations to quantification studies. One can get around this limitation by means of either knocking out the corresponding genes from the chromosome and thus making sure that only the overexpressed protein is present, or by introducing the fusion vector in the chromosome itself (“knock in”). In both cases, and especially the former, the effect on cell functioning might be profound.

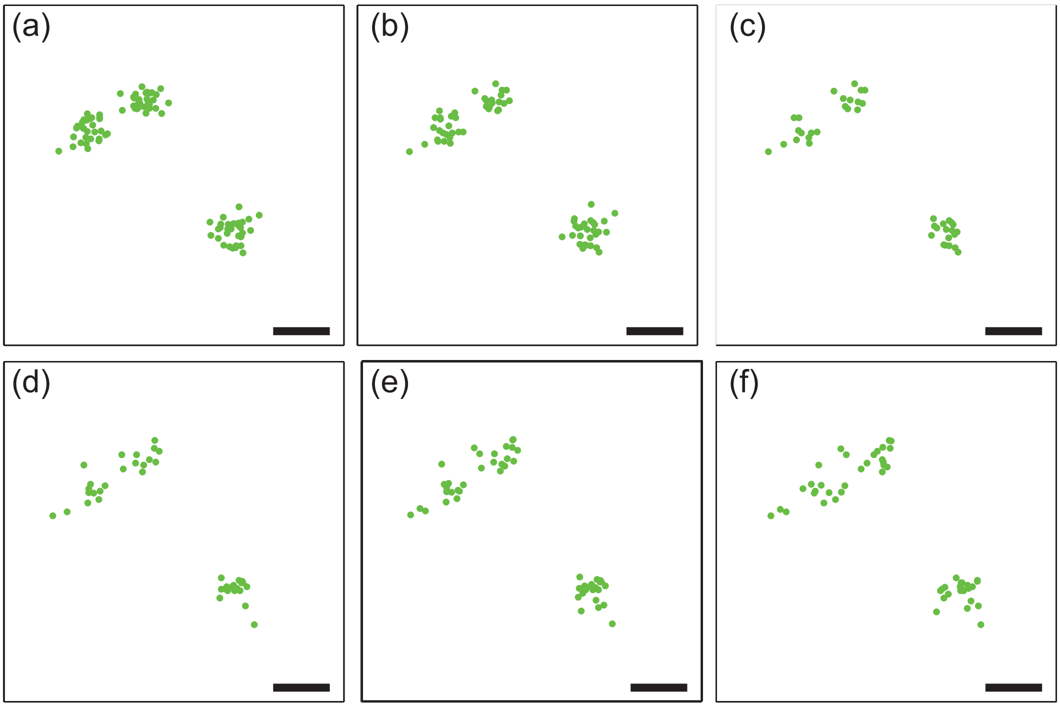

**Figure 2.3.** Illustration of the influence of several sources of error on cluster analysis with PALM.
The green dots represent the positions of single protein molecules (a), the positions of label molecules (b), and point localizations with step by step addition of different errors (c, d, e, f). The standard deviation of the position coordinates in each of the 3 clusters is calculated, and the average value $r$ over the 3 clusters is determined. (a) There are three normally distributed clusters that contain each 30 molecules ($r$ = 18.3 nm). (b) The fluorescent label is removed 5 nm from the molecule in a random direction and there is an 80% probability that a molecule is labeled ($r$ = 18.5 nm). (c) There is a 60% probability that a fluorescent label is activated and detected ($r$ = 17.9 nm). (d) The localization uncertainty is equivalent with sampling from a normal distribution with a standard deviation of 10 nm centered on the position of the fluorescent label ($r$ = 21.2 nm). It may be noted that the observed variance of the cluster can be estimated as the sum of the variance of the actual cluster and the localization uncertainty distribution, subject to sampling errors etc. (e) At a random time point within 10 s after deactivation, there is a 40% probability that the fluorescent label is again activated and localized with a 10 nm uncertainty ($r$ = 21.6 nm). (f) There is a 0.05 nm/s drift from left to right during an acquisition time that is 1000 s ($r$ = 25.3 nm). The scale bars represent 100 nm.

It must be noted that it is the fluorescent tag that is imaged, and not the protein of interest itself. If the tag is a PA-FP, it typically has a size of about 4 nm, and is attached to the protein of interest by means of an amino acid linker of length of up to 5 nm and hence the imaged structure can be off from the true structure by the vector sum of these quantities, in general in a random direction. This can introduce key errors in distance based studies, for example co-localization studies where the proteins of interest are physically co-localizing, whereas the FPs that label them might appear further apart, depending on their orientation within the labeled structure. Similarly, protein clusters will appear enlarged. Steric hindrance effects and label oligomerization can also complicate labeling accuracy. Also, in PALM experiments, typically a cell to be imaged is selected based on certain criteria – e.g. if the labeling is done properly, is sufficiently bright, and displays the expected morphology. This selection can be a source of sampling bias. High-throughput PALM that can image

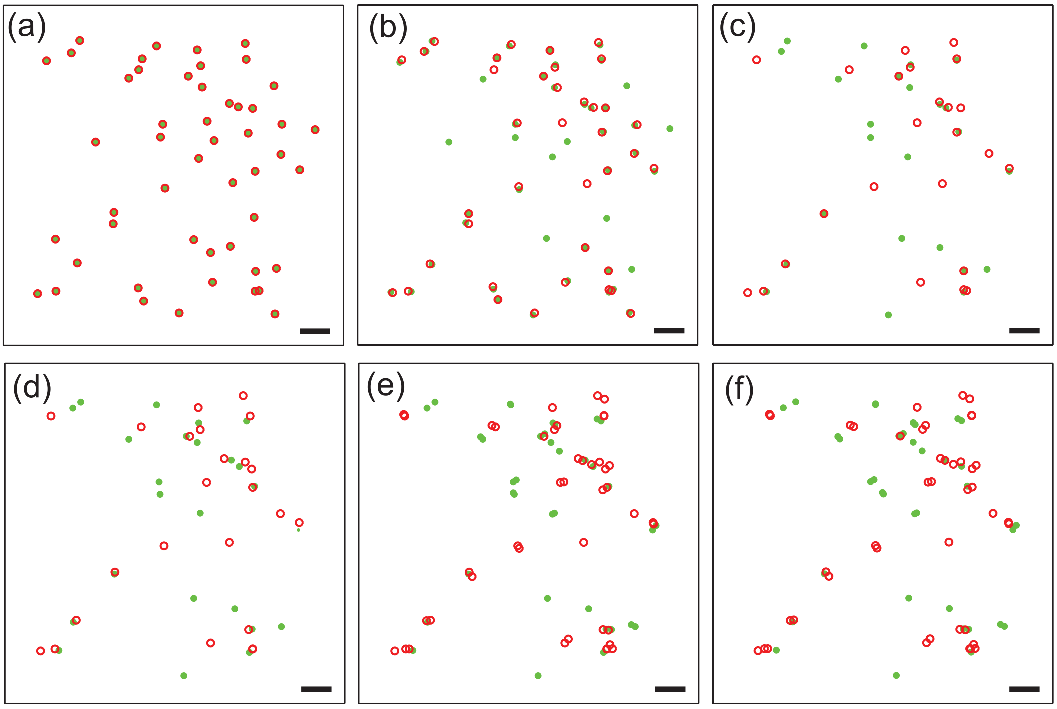

**Figure 2.4.** Illustration of the influence of several sources of error on co-localization analysis with dual-color PALM.
The green dots and red circles represent the positions of single protein molecules (a), the positions of label molecules (b), and point localizations with step by step addition of different errors (c, d, e, f) in the green and red channel respectively. The number of molecule pairs *ncoloc* that are within 10 nm distance from each other is determined for each case. (a) There are 50 pairs of green and red molecules that are separated 1 nm from each other in a random direction (*ncoloc* = 50). (b) The fluorescent label is removed 5 nm from the molecule in a random direction and there is an 80% probability that a molecule is labeled (*ncoloc* = 28). (c) There is a 60% probability that a fluorescent label is activated and detected (*ncoloc* = 10). (d) The localization uncertainty is equivalent with sampling from a normal distribution with a standard deviation of 10 nm centered on the position of the fluorescent label (*ncoloc* = 2). (e) At a random time point within 10 s after deactivation, there is a 40% probability that the fluorescent label is again activated and localized with a 10 nm uncertainty (*ncoloc* = 9). (f) There is a 0.05 nm/s drift from left to right during an acquisition time that is 1000 s (*ncoloc* = 9). It should be noted that drift might significantly affect the estimated colocalization in many cases, unlike in this case. The scale bars represent 100 nm.

hundreds of cells at the same time offers a solution to this problem (Holden et al., 2014).

The impact of both incomplete labeling as well as the distance between the protein molecule of interest and the FP molecule is shown in Figures 2.2a–b, 2.3a–b, and 2.4a–b for the three quantitative measures under discussion: counting, clustering and co-localization, respectively.

### 2.3.2 Detection efficiency

Since using FPs as label involves the complications associated with protein expression, errors in this step – misfolding, incomplete maturation etc. – can lead to the production of label molecules that are not fluorescent. Because of this reason, in the case of the conventional GFP, typically only 80% of the molecules that are present in the sample can be imaged (Ulbrich and Isacoff, 2007). In the case of PA-FPs, the fraction is even lower, due to incomplete photo-conversion. In the case of the relatively bright PA-FP mEos2, this fraction is about 60%, and for several other PA-FPs it can be as low as 40% (Durisic et al., 2014b; Annibale et al., 2012).

This can directly affect counting studies, as the number of counted molecules can be underestimated by the same fraction (Figure 2.2c). Other quantification measures might also be affected – for example, in the case of SM co-localization, assuming that the used co-localization measure is linearly related to the detection efficiency, the co-localization will be underestimated by a fraction $xy$, where $x$ is the detection efficiency in one channel, and $y$ in the other, leading to an underestimate of as low as 20% for commonly used PA-FP pairs (Figure 2.4c) (Annibale et al., 2012). However, in practice, the effect of limited detection efficiency on cluster (Figure 2.3c) and co-localization analysis is not well explored.

It is possible to use the obtained count as a lower bound (after correcting for blinking artifacts) for the counting. In the specific case of identifying protein complex stoichiometry by means of counting the photobleaching steps, a model that accounted for detection efficiency by a binomial model was found to provide accurate results (Renz et al., 2012; Ulbrich and Isacoff, 2007; Durisic et al., 2014b). A similar approach, of incorporating the detection efficiency in a model for the ratio between monomers and dimers, has been reported (Nan et al., 2013). Others have attempted to first characterize the relative detection efficiency of fusion protein pairs, and using it to estimate the stoichiometry for a target system (Renz et al., 2012).

### 2.3.3 Localization uncertainty

Each photon from the emitter molecule provides a sample of the PSF from the molecule. Based on these samples, single molecule localization algorithms provides an estimate for the position of the fluorescent molecule. This estimate is prone to uncertainties due to multiple reasons, predominated by limited sampling, i.e., by the limited number of photons obtained from the molecule. The resulting uncertainty in estimation can be quantified (Thompson et al., 2002; Mortensen et al., 2010), and assuming a Gaussian model for the uncertainty, is known to mainly vary inversely proportional to the square root of photon count collected $N$, i.e., $\sigma_{loc} \propto \frac{\sigma_{PSF}}{\sqrt{N}}$, where $\sigma_{loc}$ is the standard deviation of the Gaussian uncertainty model, and $\sigma_{PSF}$ that of the Gaussian approximation of the point spread function. Since the photon count typically collected from a PA-FP molecule is less than 1000, the precision rloc obtained is worse than 7 nm in the best cases, dropping to as low as 20 nm in practice, depending on the FP used, resulting in a full width half maximum (FWHM) resolution of 16–50 nm. Also, the assumption of isometric emitters is not necessarily true in practice, and the errors resulting from dipole orientation can be up to 40 nm (Deschout et al., 2014b; Enderlein et al., 2006; Stallinga and Rieger, 2010; Engelhardt et al., 2011).

With careful imaging and analysis, i.e. by ensuring that the imaged molecules within a frame are spatially separated enough so that the localization algorithms can correctly identify them, it is possible to minimize the effect of localization uncertainty on counting measures (Figure 2.2d). However, in the case of clustering and co-localization measures, this can cause a major impact (Figure 2.3d and 2.4d). For example, assuming that the localization estimation is approximately equivalent to sampling from a Gaussian distribution as mentioned above, centered at the true location of the emitter molecule, a cluster of molecules imaged in this way will appear enlarged, and hence the estimated cluster parameters will be affected (Figure 2.3d).

If a Gaussian error model can describe the uncertainty in position localization, the estimated distance between two point localizations is described by a non-Gaussian distribution (specifically, a function of modified Bessel functions of order zero) (Churchman et al., 2006).

If the true distance between two points is zero, and if the points are localized with an uncertainty as described above, then the estimated distance from the localizations will be greater than zero (Ruprecht et al., 2010). For example, if the localization precision for both points is 40 nm each, the estimated distance could be as high as 125 nm with a non-negligible probability (Ruprecht et al., 2010). Therefore, it is important to consider the effect of localization precision while performing quantitative analysis.

### 2.3.4 Blinking

The ideal fluorophore for counting will remain in the dark state until it is activated, and then will remain in the bright state emitting a large enough number of photons before photobleaching irreversibly, so that it does not reappear again in the bright state during imaging, resulting in overcounting. However, it has been observed that most available fluorescent proteins including GFP (Dickson et al., 1997), and the PA-FPs (Annibale et al., 2010; McEvoy et al., 2012), reappear after going to a long lived dark state from a bright state (called "blinking" behavior). Typical average values of reappearance is close to 1 for the commonly used fluorophore mEos2, but it can be a few times higher for a significant fraction of imaged molecules. In either case it will result in overcounting (Figure 2.3e), however if the molecule blinks multiple times it can also result in apparent clustering, forming artifacts amongst true physical clusters (Figure 2.3e). Photoblinking artifacts can also lead to false positives in the case of co-localization, depending on the co-localization measure used (Figure 2.4e).

It has been reported that the observed distribution for the time between the multiple appearances of a fluorophore (off time, $t_{off}$) can be fit to a single or double exponential distribution (Annibale et al., 2010, 2011b; Lee et al., 2012) . The average values of $t_{off}$ are comparatively on a much smaller scale compared to the imaging time of a PALM experiment, and hence on a spatial–temporal plot of the localizations, they appear as clusters. Therefore, by grouping together localizations that form these clusters, it is possible to correct for blinking artifacts (Annibale et al., 2011b; Lee et al., 2012; Annibale et al., 2011a). Lando et al. used a Kalman filtering approach to correct for the artifacts (Lando et al., 2012), whereas Sengupta et al. have used a pair correlation based approach that is focused on the specific case of cluster analysis (Sengupta et al., 2011). The latter approach works by separating the artifact clusters due to blinking from the true protein clusters by means of a model based on pair correlation function.

### 2.3.5 Drift

Since an SMLM experiment typically involves imaging 1000s of frames, due to temperature changes, air currents, mechanical vibrations etc., the sample might drift during the imaging time, in both lateral and axial direction. Since different subsets of molecules are imaged in different frames, drift can cause artifacts in SMLM imaging (Figure 2.2f, 2.3f, and 2.4f). Basic efforts to minimize sources of drift, such as temperature stabilization and the use vibration-damping optical tables, are essential. Drift in the axial direction can be controlled by means of closed-loop feedback system that moves the sample stage in order to counteract the motion of sample (Annibale et al., 2012; Pertsinidis et al., 2010). Even then, lateral drift in the nanometer scale seems to be difficult to avoid (Figure 2.2f, 2.3f and 2.4f) (Annibale et al., 2012; Geisler et al., 2012).

A common method to correct for sample drift is to insert fiducial markers in the sample, for example very bright fluorescent beads of 100 nm diameter (Betzig et al., 2006). Assuming that the fiducial marker does not move within the sample, and since the marker appears in all frames, the drift of the marker can be estimated, and the protein localizations corrected accordingly. To make sure that the correct sample drift is estimated, it is better to use multiple fiducial markers in the same sample, and the overall drift estimated from their individual drifts. However: (1) having multiple fiducials too close to the structure to be imaged will affect imaging and (2) the multiple fiducials might show different drift patterns, either due to movement within the sample or due to the variability of drift within the sample, and the overall drift estimation from them can be complicated.

In the case of imaging samples that have a clear structure, such as actin filaments or microtubules (as opposed to say, a sample with molecules distributed randomly in space), the subsets of localizations from adjacent frames lumped together might be correlated to each other throughout the imaging time. In this case, the information present in the correlation can be used to correct for drift. Multiple methods have been suggested to perform this correction (Geisler et al., 2012; Mlodzianoski et al., 2011).

### 2.3.6 Fixation artifacts

The long imaging time required for an SMLM experiment, necessitated by the need of imaging 1000s of frames, makes the use of SMLM for live cell imaging complicated. The use of fast imaging (Jones et al., 2011), including that of sCMOS cameras (Huang et al., 2013), and deconvolution based image processing algorithms (Zhu et al., 2012) that allow higher density of imaged molecules per frame, have resulted in major improvements in this direction. However, the long imaging time is not an issue in the case of fixed samples, and most of the quantitative applications of PALM were done on them.

In the case of analysis that quantifies protein spatial distributions, or co-localization, it is important that the fixation preserves the protein configuration at the time of fixation. However, it has been found that after applying the fixative, different molecules get fixed at different time (Annibale et al., 2012; Tanaka et al., 2010). This means that the protein configuration is affected by fixation. Further studies are required to fully understand the effect of fixation artifacts on such quantitative studies.

### 2.3.7 Representation

SMLM experiments, after processing the raw data, provide a set of point localizations (estimates of the actual positions of the fluorescent tags) along with the estimated localization precision. Representing such information in an image format is a challenge, as merely representing the estimated locations as points is akin to overestimating the information available. Therefore the localization precision has also to be taken into consideration.

In the initial PALM papers (Betzig et al., 2006), the researchers represented the data by means of a 'probability map', an image obtained by summing together Gaussian distributions corresponding to the localization uncertainty model estimated for each point localization, centered at the estimated localization. Such a representation involves loss in information. If $x_A, x_B, ...$ are true point locations of imaged molecules $A, B, ...$, then SMLM provides estimates of these locations $\hat{x}_A, \hat{x}_B, ...$ along with the error in estimation $\sigma_A, \sigma_B, ...$ In other words, probabilistic information about locations of individual molecules – $P(A), P(B), ...$ – is available. In the case of a probabilitymaprepresentation, the available information is reduced to $P(A + B + ...)$, that is, there is information loss. However, it is possible to use the probability map as a worst case image.

Histogram based representation is another alternative that has been suggested. In this method, the estimated localizations are binned together. However, no information about estimation error is provided in this representation, and hence the method overestimates the available resolution. Additionally, binning can introduce artifacts to the representation and analysis, therefore the binning size must be carefully chosen.

Baddeley et al. have proposed alternative methods based on quad-tree and Delaunay triangulations (Baddeley et al., 2010). However, all such representations also involve a loss of information compared to the raw results provided by SMLM. By the same reasoning, for quantitative analysis it is best to work with all the available information, i.e. the estimated locations and localization precision.

For analysis, researchers often select the localizations with the best precision for analysis, so as to obtain a more precisely localized structure. Such techniques can provide significant improvement in resolution (Pertsinidis et al., 2013). However, since such a selection is a case of spatial sampling, the effect of it on analysis techniques must be addressed. The situation is more complicated if the distribution of localization precision in space is not homogeneous, since the selection then will be skewed. Such situations are possible due to non-homogeneous illumination, local variations in pH and even intermolecular interactions. Adequate precautions and controls must be done so as to ensure that artifacts are not created due to the use of a cut-off on localization precision.

## 2.4 Conclusion

In this article, we have presented a broad overview of the applications of SMLM in quantitative microscopy in varied fields of biology. We have also reviewed the various challenges that are present in using SMLM for quantitative measurements, with a focus on PALM, along with a brief review of the solutions that have been presented in the literature. Through cartoon figures, we have presented how the various errors that are present in the technique affect the three main ways SMLM data have been quantified: counting, cluster analysis and co-localization. We conclude that there is a critical need for accounting for these sources of errors, in order to achieve accurate and precise quantitative measurements. Furthermore, some of the challenges remain unsolved, and need novel solutions, both analytical and experimental.

# Chapter 3

# Accounting for limited detection efficiency and localization precision in SMLM

*This is a verbatim copy of an open access peer reviewed publication: A. Shivanandan, J. Unnikrishnan, and A. Radenovic. Accounting for limited detection efficiency and localization precision in cluster analysis in Single Molecule Localization Microscopy.* PLOS ONE, *10(3):e0118767, 2015.*

## Abstract

Single Molecule Localization Microscopy techniques like PhotoActivated Localization Microscopy, with their sub-diffraction limit spatial resolution, have been popularly used to characterize the spatial organization of membrane proteins, by means of quantitative cluster analysis. However, such quantitative studies remain challenged by the techniques' inherent sources of errors such as a limited detection efficiency of less than 60%, due to incomplete photo-conversion, and a limited localization precision in the range of $10 - 30$nm, varying across the detected molecules, mainly depending on the number of photons collected from each. We provide analytical methods to estimate the effect of these errors in cluster analysis and to correct for them. These methods, based on the Ripley's $L(r) - r$ or Pair Correlation Function popularly used by the community, by providing a more accurate and precise quantification of protein spatial organization, can facilitate potentially breakthrough results in quantitative biology.

## 3.1 Introduction

The spatial organization of most membrane proteins as sub-micrometer spatial clusters might be a key property affecting their functionality (Sieber et al., 2007; Lang and Rizzoli, 2010; Hartman and Groves, 2011). The characteristics of these microdomains, such as the number of proteins per cluster, cluster size and density, are heterogeneous in general, depending on the specific cell type, protein, lipid, cell cycle and environmental conditions. The possible mechanisms of cluster formation include compartmentalization due to enrichment in lipid rafts (Simons and Ikonen, 1997), protein-protein interactions (Sieber et al., 2007) and physical barriers created by actin cytoskeleton (Lillemeier et al., 2006). Various biological functions, for example signalling (Hartman and Groves, 2011; Lang and Rizzoli, 2010), might be facilitated by clustering. Accurate and precise imaging and quantitative characterization of the spatial microdomain parameters are important tools that can aid these studies.

The membrane proteins can be imaged at unprecedented length-scales, and with high specificity and contrast and in their natural environment, using single molecule localization microscopic (SMLM) techniques like PhotoActivated Localization Microscopy(PALM) (Betzig et al., 2006; Hess et al., 2006). Other SMLM techniques like STochastic Optical Reconstruction Microscopy (STORM) (Rust et al., 2006) also are promising, although, due to the high specificity provided by PALM originating from the genetic tagging of the protein under study with the fluorescent label, and the relatively lower blinking rate of the Photo-Activable Flourescent Proteins (PA-FPs) and the resulting reduction in the number of repeated localizations of the same fluorophore molecule, we focus on the application of PALM for quantitative analysis, while noting that the methods provided might be applicable to STORM as well. The technique has been popularly used for quantitative analysis of spatial organization of membrane proteins (Williamson et al., 2011; Sengupta et al., 2011; Lillemeier et al., 2009; Pertsinidis et al., 2013; Scarselli et al., 2012). Such studies typically also involve the use of cluster analysis methods for quantification.

However, the quantitative analysis of membrane organization with PALM has several sources of errors that can significantly limit its utility (Deschout et al., 2014a; Shivanandan et al., 2014; Annibale et al., 2012; Durisic et al., 2014a; Annibale et al., 2011b; Lee et al., 2012; Mortensen et al., 2010; Thompson et al., 2002; Sengupta et al., 2011). The most critical sources of these errors are: a) multiple localizations of the same label molecule due to fluorophore blinking (Annibale et al., 2011b; Lee et al., 2012) b) inability to image all the label molecules, due to a limited detection efficiency of typically 40%-60%, resulting from inherent errors like imperfect fluorescent protein folding, maturation and photo-conversion (Annibale et al., 2012; Durisic et al., 2014a) c) localization uncertainty, or the error in the estimation of the position of the label molecule due to the limited number of photons collected from them, commonly represented by the localization precision in the range of 10-30nm (Mortensen et al., 2010; Thompson et al., 2002). All of these can possibly cause significant variations in quantitative analysis( (Annibale et al., 2012, 2011b; Durisic et al., 2014a; Lee et al., 2012; Deschout et al., 2014a; Shivanandan et al., 2014), also Figure 3.4). Additionally, the finite label and linker size, stage drift and effects due to fixed dipole orientation of the emitter molecules can affect the accuracy and precision of localizations (Engelhardt et al., 2011; Stallinga and Rieger, 2010; Shivanandan et al., 2014). These sources of errors are applicable to other SMLM techniques like STORM, though in different magnitudes.

Several methods have been proposed to account for the multiple appearances due to blinking (Annibale et al., 2011b; Lee et al., 2012; Annibale et al., 2011a; Sengupta et al., 2011). However, the other two sources of error, the subsampling due to limited detection efficiency, and the effect of localization uncertainty on measured cluster properties, remain problematic. A method has been proposed to account for localization uncertainty in analysis (Nan et al., 2013), however, in the context of very small clusters (typically upto tetramers) and low molecular density, and based on simulations. Currently, several of the cluster analysis studies based on PALM perform the analysis and comparisons of estimated cluster properties without accounting for these satisfactorily, possibly resulting in inaccurate results (Figure 3.41).

In this work, we focus on these two problems. Based on a well-known result from spatial statistics, we demonstrate that the commonly used tools for cluster analysis such as Ripley's $K$ function, $L(r) - r$ function and the related Pair Correlation Function (PCF) are invariant to random subsampling, and hence, within limits, are unaffected by limited detection efficiency. We then provide a method to estimate true fluorophore locations from the localizations appearing in clusters, and to correct for errors due to localization uncertainty. These estimated true locations can be used to estimate the true Ripley's $L(r) - r$ function or the PCF, and thus provide better estimates of true cluster parameters.

Before proceeding further, we note that, while the methods discussed in the paper are focussed on the $L(r) - r$ function, they should be applicable to the PCF as well (Methods in Section 3.4). We also note that the result on invariance to random subsampling property applies to the bivariate versions of the $K$, $L(r) - r$ and PCF functions (called Cross Correlation Function or CCF), and hence on related co-localization measures (Sengupta et al., 2011).

## 3.2 Results

### 3.2.1 Accounting for limited detection efficiency

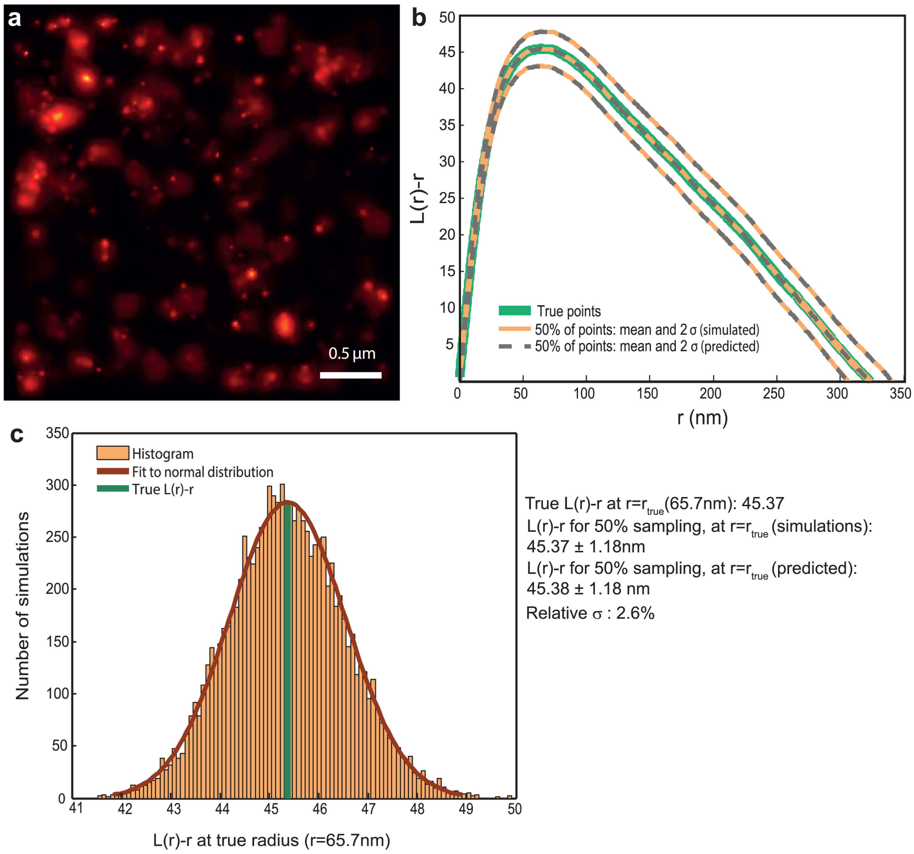

**Figure 3.1.** Ripley's $L(r) - r$ function is invariant to random subsampling.
(a) Probability map representation of a PALM image of $\beta 2-$adrenergic receptor molecules labeled with mEos2 on the plasma membrane of HeLa cells, post agonist addition. Density: 650 molecules/$\mu m^2$. (b) $L(r) - r$ functions for the true and subsampled points, estimates for the latter obtained from both simulations and the analytical method presented. Continuous green: Ripley $L(r) - r$ function $L_{true}(r) - r$ corresponding to the points in (a). Orange: mean and $2\sigma$ bounds of $L(r) - r$ functions corresponding to 10000 realizations of random sampling 50% of the points in (a). Broken lines: the mean and $2\sigma$ bounds corresponding to 50% subsampling, predicted by the analytical method presented. It can be seen that the mean values obtained from both simulations and analytical method coincide with $L_{true}(r) - r$ , and that the $2\sigma$ curves obtained from the simulations and the analytical method coincide. (c) Histogram of $L(r) - r$ of the subsampled realizations at $r = r_{true}$, where $r = r_{true}$ is the cluster radius corresponding to the maxima of the $L_{true}(r) - r$ function. It can be seen that it follows a normal distribution, with the fit parameters similar to that obtained from the analytical method. $r_{true}$ is also plotted (dark green). The relative standard deviation ($\sigma/\mu$, i.e, $\frac{\sigma_{subsampled}}{L_{true}(r)-r}$) at $r = r_{true}$ is 2.6% for 50% subsampling.

We consider the situation when the phenomenon of limited detection efficiency in a PALM experiment can be modelled as a case of random, independent, homogeneous subsampling of the label molecules present in the sample. Such a model is valid if the effect of limited detection efficiency, i.e., whether a flourophore that is present in the field of view is imaged or not, is independent of its spatial location. In the case of spatial homogeneity in illumination and environmental conditions such as pH, and in the absence of inter-fluorophore molecule interactions, this assumption is reasonable.

We then use the result from spatial statistics that analytically shows that the $L(r) - r$ function is invariant to random subsampling of the underlying point pattern (Møller and Waagepetersen, 2004)(Methods in Section 3.4, Figure 3.1). The result arises from the fact that, in the event of subsampling, both the numerator and the denominator of these measures gets scaled similarly and hence they cancel out, on average(details in Methods, Section 3.4).

Due to the stochasticity involved in random subsampling, the $L(r) - r$ function corresponding to the subsampled point pattern (i.e localizations corresponding to the detected molecules), called $L_{subsampled}(r) - r$, will also be a stochastic quantity (and a PALM experiment provides one realization of the subsampling). For a stationary point pattern, the $L_{subsampled}(r) - r$ at any point $r$ can be approximately modeled as a random variable with a normal distribution centered around a mean value; this mean $L_{subsampled}(r) - r$ provides an unbiased estimate for $L_{true}(r) - r$ as per the result above. We provide an analytical method to exactly compute the standard deviation of the $K$ distribution of the subsampled points at each point $r$, and approximately compute that of $L(r) - r$ (called $\sigma_{subsampling}$), given the true set of points (Figure 3.1, Methods in Section 3.4, Figure 3.5) and the sampling ratio.

We empirically characterized the $\sigma_{subsampling}$ corresponding to various cluster and subsampling conditions, by means of simulated points (Figure 3.6). Simulated clustered point patterns were created for varying cluster density (total number of clustered points in the area under analysis, conditions tested: 10, 100 and 1000 $\mu m^{-2}$), cluster size ($\sigma$ of Gaussian, 10,30,50 and 100) and number of points per cluster (10 and 100). The effect of sampling ratios of 20%, 40%, 60% and 80% were tested. In all the clustering conditions tested, the ratio of $\sigma_{subsampling}$ to the $L_{true}(r) - r$ at $r = r_{true}$, called relative standard deviation, $r_{true}$ corresponding to the point $r$ in which $L_{true}(r) - r$ is maximum, remained less than .25 for 60% sampling, with most conditions having a value less than .15. For several of the cluster conditions, the ratio obtained was less than .1 even for 20% sampling. The characterization for smaller clusters (dimers and tetramers) can be found in Figure 3.7, with similar results (ratio less than .15 for 60% sampling).

Since the $r$ value corresponding to the maxima of $L(r) - r$ function can provide an estimate of the cluster radius, the invariance property of $L(r) - r$ could also be useful for its accurate estimation (Figure 3.2).

It should be noted that in this work, subsampling is assumed to be spatially homogeneous. Apart from assuming that the limited detection efficiency due to physical phenomena is spatially homogeneous, it also assumes that the errors during the computation of localization estimation are also spatially homogeneous; e.g., the phenomena of higher number of missed localizations in denser regions due to overlapping Point Spread Functions is minimal. It is also important for accurate and precise estimation of the $L(r) - r$ functions that the effect of sampling errors is not significant. Therefore, in the case of very few clustered points in the area of analysis, it is important to validate the applicability by means of simulations.

### 3.2.2 Estimating true point locations in the presence of localization error

We propose a method that estimates the true fluorophore locations from imaged localizations that appear in clusters, accounting for localization uncertainty. Spatial clusters tend to

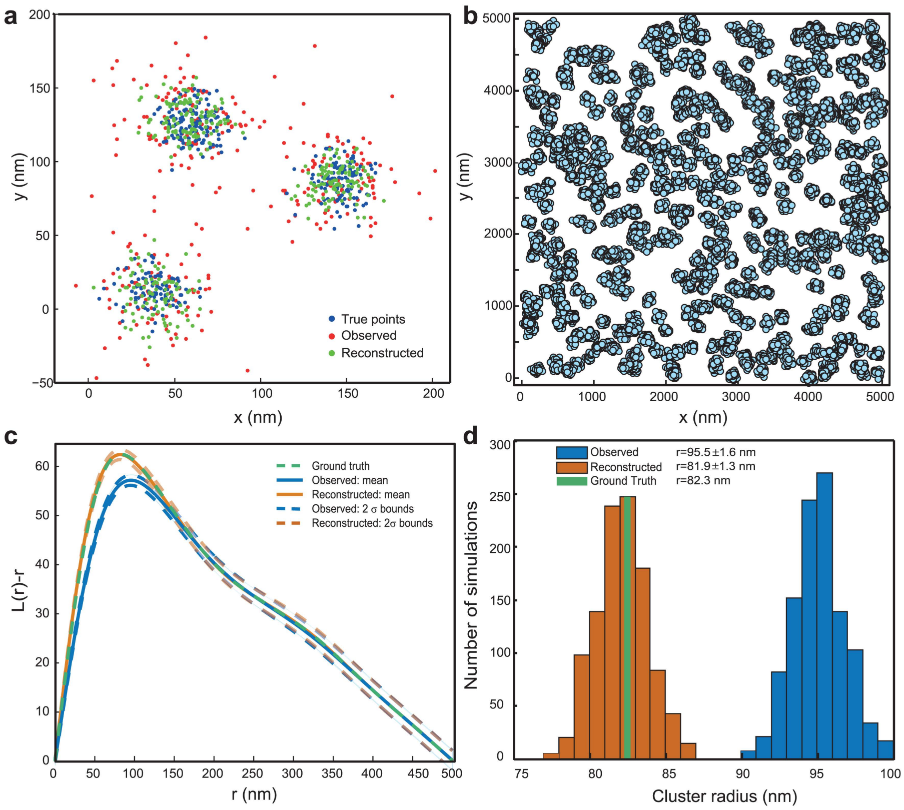

**Figure 3.2.** Reconstruction of true point locations from noisy observations. (a) Demonstrative example of reconstruction method. The true (blue), observed (red) and reconstructed (green) locations, in the case of 3 Gaussian clusters with average cluster standard deviation of 10nm observed with an average localization uncertainty ($\sigma$) of 17nm. It can be seen that the observed clusters (average $\sigma \approx$ 22nm) are enlarged with respect to the true clusters, and the reconstructed clusters are closer to the true ones. (b,c,d): Example of estimation of true cluster properties from simulations of clustered points with limited detection efficiency and localization errors added. (b) Ground truth: simulated membrane protein cluster. Each cluster is assumed to be Gaussian shaped ( $\sigma =$ 30nm), with 40 points on average. The overall density in the area of analysis is 760 molecules/$\mu m^2$. The true points are observed with a limited detection efficiency of 50% and a mean localization precision of 18nm. (c) Ripley $L(r) - r$ functions corresponding to true points (green), mean and $2\sigma$ envelopes for 1000 simulations of observed data (cyan) and reconstructions from them (orange). (d) Histograms of cluster radius estimated from the maxima of $L(r) - r$ curves in (c), for the observed data (cyan) and the reconstructions (orange), with the value corresponding to the ground-truth (green). It can be seen that the reconstructed values ($81.9 \pm 1.3$ nm) are very close to the ground-truth (82.3 nm), compared to the observed values ($95.5 \pm 1.6$nm).

appear more dispersed and hence enlarged, when the localizations involve measurement error (uncertainty). Thus naïve estimates of Ripley's $L(r) - r$ function that ignore localization uncertainties are biased even when the uncertainties are unbiased (Figure 3.4). However, the amount of enlargement for a given cluster can be predicted as a function of the precisions of all localizations. We show that if the precisions of all localizations are known, the true position corresponding to each localization in an observed cluster can be estimated (Methods in Section 3.4, Figure 3.2). A model for localization precision based on the photon count can generally be identified (Mortensen et al., 2010; Thompson et al., 2002) and can be used for this estimation, even though such models ignore other sources of estimation errors (finite label and linker size and orientation, stage drift, fixed emission dipole orientation). Hence such models should be considered as a lower bound for localization error.

These position estimates, obtained after correcting for the enlargement of the cluster due to localization uncertainty, can be used for more accurate cluster analysis, whether by means of exploratory tools like the $L(r) - r$ or PCF functions presented in this paper, or through clustering by means of algorithms like DBSCAN (Ester et al., 1996) followed by estimation of each cluster's properties (Deschout et al., 2014a).

In the case of using tools such as $K$, $L(r) - r$ or PCF, the property of invariance to random subsampling presented in the paper can correct for limited detection efficiency as well (Figure 3.2).

The methods are validated by simulations (Figure 3.2, 3, Figure 3.8). For a simulated clustered point pattern with a density of 760 points $\mu m^{-2}$ and with a true cluster radius of 82.3nm, while observation with an average localization precision of 18nm and a subsampling of 50% provided a cluster radius of $95.5 \pm 1.6$ nm, the reconstruction and estimation with the presented method provided a radius of $81.9 \pm 1.3$ nm. Characterization of the accuracy and precision of the reconstruction method for different cluster and error conditions can be found in Figure 3.3. Details of the simulations used in the paper can be found in Methods(Section 3.4). It should be noted that the reconstruction method is crucially dependent on the clustering of the localization data into appropriate shapes. A discussion of sources of error in reconstruction, especially that due to errors in clustering, can be found in Text S1. Example reconstruction by setting observed PALM data as true points, and involving the errors due to clustering, can be found in Figure 3.8. An example application of the method on a previously published cluster analysis data (Scarselli et al., 2012) can be found in Figure 3.9, where the $L(r) - r$ curve corresponding to the reconstructed points gives a measure of the possible deviation from that of the observed ones, due to the effect of limited localization precision. As expected, the cluster radius estimated for the reconstructed points(97.5 nm) was found to be 11.5 nm lower than one for the observed points(109 nm) that neglects the influence of limited localization precision.

We also provide an analytical method to exactly compute the mean $L(r) - r$ function corresponding to uncertain localizations, as a function of the true point locations and localization precisions of all points (Methods in Section 3.4, Figure 3.10). For a given PALM experiment, this method and the method to compute the variance due to subsampling can be used along with simulations of true points to compute the limits of minimum detection efficiency and localization precision permissible for a given target accuracy.

## 3.3 Discussion

It can be seen from the figures that we have successfully demonstrated the applicability of invariance to subsampling property to PALM data, and the estimation of the variance of subsampling and the reconstruction aspects of the method perform well, with the reconstruction method providing significant reductions in estimation error. The method is simple to implement, and an implementation in MATLAB is provided. The advantages of the method include the fact that it is based on Ripley's $L(r) - r$ function or Pair Correlation Function, methods that are very popular in the field. It can also be easily coupled with other methods that solve the problem of overcounting due to photoblinking, using models based on the PCF (Sengupta et al., 2011). The invariance to random subsampling property applies also to co-localization analysis with two-color $L(r) - r$ function or Cross Correlation Function, where the problem of limited detection efficiency involves the multiplicative propagation of errors. The reconstruction method can also be used independently of $L(r) - r$ or PCF functions. The methods' applicability is not limited to PALM or SMLM, the invariance

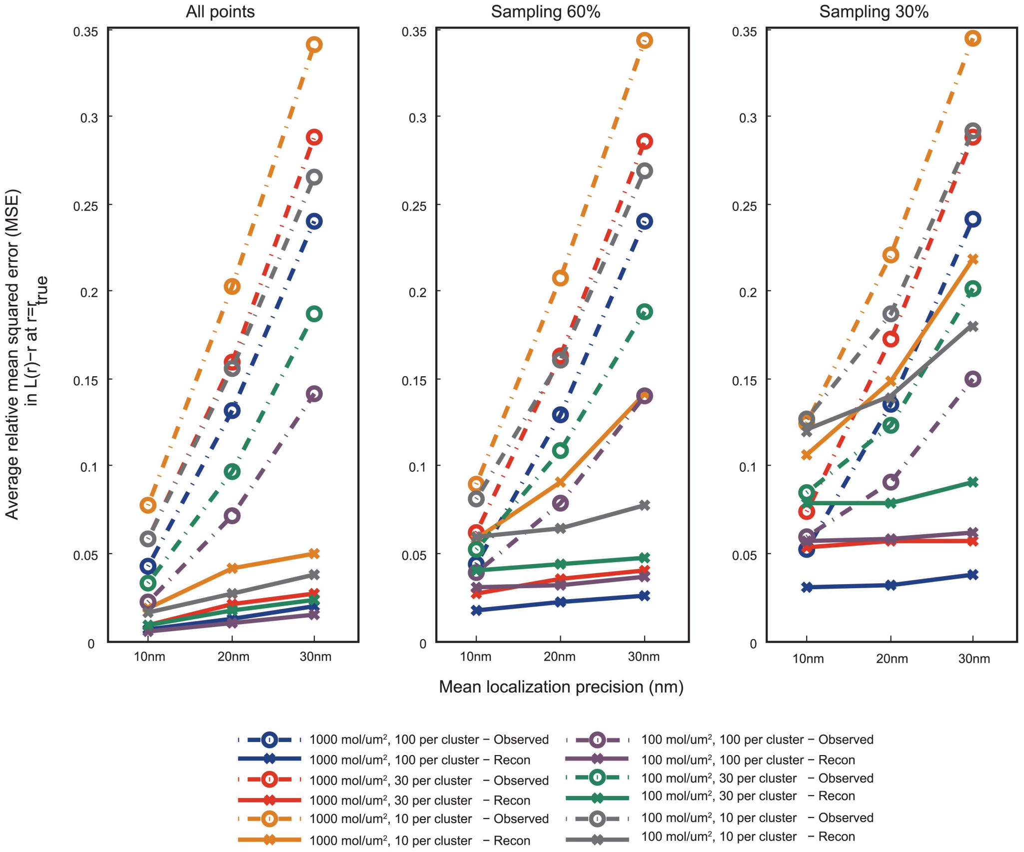

**Figure 3.3.** Characterization of error in $L(r) - r$ for observed and reconstructed points to that corresponding to true points, at $r = r_{true}$, based on simulated point patterns.
The simulations were done as described in Methods( Section 3.4). Cluster size ($\sigma$) of true point pattern: 30nm. The observed points were obtained from true points by applying localization errors with mean localization precision 10, 20 and 30nm, and sampling rates of 30%, 60% and 100% ( 40 realizations per condition). The reconstructed points were obtained from these points by means of the methods presented in the paper. The mean squared error in $L(r) - r$ between the ones corresponding to realizations of the observed/reconstructed points and the true points is computed at $r = r_{true}$, the true cluster radius estimated from the maxima of $L_{true}(r) - r$, and is then divided by $L_{true}(r) - r$ to make it relative. The relative MSE is averaged over 10 realizations of point patterns corresponding to the same cluster conditions. Broken lines: error rate corresponding to observed points, Solid lines: corresponding to reconstructed points. It can be seen that the reconstruction method provides significant reduction in error for sampling rates of 60% and 100% for all clustering conditions. The reduction in error remains significant even for 30% sampling, except for the case when the average number of points in a cluster is only 10, in which case also there is considerable improvement.

property might as well be applicable to Electron Microscopy based analysis of membrane proteins, where the immunolabelling of the ultrastructure involves major subsampling. We believe the method, by providing solutions for several important sources of error in SMLM, has the potential to form an invaluable tool for the community.

## 3.4 Methods

### 3.4.1 Invariance of $L(r) - r$ function and PCF to random subsampling

For a stationary spatial point pattern defined in two-dimensional space, Ripley's $K$-function is defined (Møller and Waagepetersen, 2004; Baddeley, 2008) as

$$K(r) = \frac{1}{\lambda}\mathsf{E}[M(r)] \tag{3.1}$$

where $\lambda$ is the spatial density (average number of points per unit area), and $M(r)$ is the number of extra events within distance $r$ of a randomly chosen event. Ripley's $L$ function is then defined as

$$L(r) = \sqrt{\frac{K(r)}{\pi}}. \tag{3.2}$$

For points that are distributed in space with complete spatial randomness, i.e. without forming any special organization such as clustering, $\mathsf{E}[M(r)] = \pi\lambda r^2$, and hence $L(r) - r = 0$. In the case of clustered point pattern, $L(r) - r > 0$ and in the case of anti-clustered (regularity), $L(r) - r < 0$. In the case of clustering, the magnitude of $L(r) - r$ gives a sense of the degree of clustering ('cluster strength') compared to a point pattern distributed uniformly at random with the same density, and can be used for comparisons in relative clustering between point patterns. The $r$ value corresponding to the maxima of $L(r) - r$ gives a measure of the average cluster radius. We note that other measures based on the $L(r) - r$ function to estimate the cluster radius are available (Kiskowski et al., 2009) , and the methods proposed in this work are independent of the specific measure used. Pair Correlation Function (PCF, represented by $g(r)$) is a closely related measure, in that $K(r)$ is the integral of $2\pi r g(r)$. We also note that the radius estimate obtained is an ensemble measure, and may not reflect the variability within the individual cluster radii of various clusters in the area of analysis.

A well-known result (Baddeley, 2008; Møller and Waagepetersen, 2004) in spatial statistics states the following. When a process is *randomly subsampled* by a factor $\alpha$, by means of independent Bernoulli trials with probability $\alpha$, the intensity $\lambda$, gets reduced to $\alpha\lambda$. Simultaneously $\mathsf{E}[M(r)]$ also gets multiplied by a factor $\alpha$ (see (Møller and Waagepetersen, 2004) for a proof), and hence $K(r)$ remains invariant to random subsampling. Similar argument holds for Pair Correlation Function (PCF) (Baddeley, 2008; Møller and Waagepetersen, 2004) and $L(r) - r$.

### 3.4.2 Exact computation of variance of $K$-function due to random subsampling

In practice the $K$-function is estimated using the following expression

$$K(r) = \frac{\sum_{i \neq j} \mathcal{I}\{\|X_i - X_j\| \leq r\}/N}{N/A} \tag{3.3}$$

where the numerator is an estimate for the expected value in Eq. (3.1) and the denominator is an estimate for the intensity $\lambda$. Here $N$ is the total number of points in the area under analysis, $A$ is the total area, and $X_1, X_2, \ldots, X_N$ are the positions of the points, represented as vectors in $\Re^2$, and $\mathcal{I}\{E\}$ is the indicator function of an event $E$, taking the value 1 if the event $E$ occurs and 0 otherwise.

Suppose the point pattern is randomly subsampled with a probability $\alpha$. Then the estimate of the $K$ function obtained from the subsampled point pattern is given by

$$K(r) = \frac{\sum_{i \neq j} B_i B_j \mathcal{I}\{\|X_i - X_j\| \leq r\} A}{(\sum_{i=1}^{N} B_i)^2} \tag{3.4}$$

where $B_i$ are independent binary variables following a Bernoulli distribution with mean $\alpha$. For a given set of positions $\{X_1, X_2, \ldots, X_N\}$ and a given sampling probability $\alpha$, we analytically compute expressions for the expected value and variance of $K(r)$, by using the binomial theorem. The details of the derivation are given in Text S1. The corresponding values in $L(r) - r$ can be approximately computed from the $K(r)$ function obtained.

### 3.4.3 Exact computation of $K$-function in the presence of localization uncertainty

In the presence of measurement error (localization uncertainty), the observed position of a point is a perturbed version of its true position. Let $X'_i$ denote the observed position of the $i$-th point whose true position was at $X_i$. Thus $W_i = X'_i - X_i$ is the corresponding measurement error. The $K$-function estimate obtained by using the observed positions is thus given by

$$K'(r) \quad = \quad \frac{\sum_{i \neq j} \mathcal{I}\{\|X_i - X_j + W_i - W_j\| \leq r\}/N}{N/A} \tag{3.5}$$

For a given set of true positions and given distribution of the observation errors, the expected value of $K'(r)$ can be calculated. A derivation of an analytical expression for this expected value, under an assumption of independent normal distributions for measurement errors, is given in Section 3.5.

### 3.4.4 Estimating true locations of molecules and true $L(r) - r$ function

In order to correct for measurement errors, we employ a technique to estimate the true locations of the points given the variance in their observed locations. We ignore clustering errors and separately estimate the locations of points within each cluster. Let $X'_1, X'_2, \ldots, X'_K$ be the observed locations of the points within a cluster containing $K$ points. Further, let $X'_i = (x'_i, y'_i)$ be the representation of the $i$-th point in terms of its $x$ and $y$ coordinates. We estimate the $x$ coordinates and $y$-coordinates of each point separately. Here we describe only the procedure for estimating the $x$-coordinates. The $y$-coordinates are estimated similarly. We model the true x-coordinates of all points in the cluster as i.i.d. random variables with an unknown mean $\mu_x$ and variance $\sigma_x^2$. Let $\sigma_{x,i}^2$ denote the measurement error variance in the $x$-coordinate of the $i$-th point. We first estimate the $x$-coordinate of the cluster center as

$$\overline{x} = \frac{1}{K} \sum_{i=1}^{K} x'_i, \tag{3.6}$$

and then compute an estimate of the mean error in the $x$-coordinates as

$$\overline{\sigma}_x^2 = \frac{1}{K} \sum_{i=1}^{K} \sigma_{x,i}^2. \tag{3.7}$$

Using this we estimate the true spread in the $x$-coordinates of the cluster. Let

$$\check{\sigma}_x^2 = \frac{1}{K-1} \sum_{i=1}^{K} (x'_i - \overline{x})^2 - \overline{\sigma}_x^2.$$

It is easy to verify that $\mathsf{E}\left[\check{\sigma}_x^2\right] = \sigma_x^2$ and thus $\check{\sigma}_x^2$ provides an unbiased estimate for the spread $\sigma_x^2$. However, since the estimate has to be non-negative we use a modified estimate:

$$\hat{\sigma}_x^2 = \begin{cases} \frac{1}{K-1} \sum_{i=1}^{K} (x'_i - \overline{x})^2 - \overline{\sigma}_x^2 & \text{if} \quad \frac{1}{K-1} \sum_{i=1}^{K} (x'_i - \overline{x})^2 > \overline{\sigma}_x^2 \\ \frac{1}{K-1} \sum_{i=1}^{K} (x'_i - \overline{x})^2 & \text{else.} \end{cases} \tag{3.8}$$

Finally we estimate the true $x$-coordinates of the points in the cluster as

$$\hat{x}_i = \overline{x} + \frac{\hat{\sigma}_x}{(\hat{\sigma}_x^2 + \sigma_{x,i}^2)^{\frac{1}{2}}}(x'_i - \overline{x}). \tag{3.9}$$

The justification for using this estimate is that the expectation of the pairwise squared distances between the estimated points remains the same as that of the true points (details in Section 3.5). Therefore, quantification measures based on distance metrics, computed based on the estimated true points, must also be accurate.

Finally, combining the estimates of both coordinates, we get estimates $\widehat{X}_i$ for the location of each molecule within the cluster. We separately apply this procedure to all observed clusters. Finally, we estimate the correct $K$-function using the estimated points as

$$K(r) = \frac{\sum_{i \neq j} \mathcal{I}\{\|\widehat{X}_i - \widehat{X}_j\| \leq r\}/N}{N/A}.$$

This procedure can be further refined by incorporating the differences in the variances of different points while estimating the x-coordinate of the cluster centre in Eq. (3.13).

### 3.4.5 Validation and simulation details

The demonstrative examples and *in silico* validation were done on “true points” (all label locations known with perfect accuracy), obtained either by simulation of point patterns or by setting the localizations obtained from a PALM experiment as the true points (Figure 3.1a). The latter is useful in that it provides a point pattern that more closely reflects a molecular spatial distribution in practice.

The clustered point patterns used for the simulations were obtained in the following way. Gaussian clusters with a set standard deviation $\sigma$ were generated in a $2\mu m$x$2\mu m$ area for different cluster densities (mean number of points that are clustered per unit area, values tested: 1000,100 and 10 $\mu m^{-2}$) and mean number of points per cluster (100, 30 and 10). A random point pattern is superimposed on the clustered points as background(“monomer fraction” of 30%). For Figure 3.6, the cluster size $\sigma$ was varied between 10nm and 100nm, and only the conditions of 10 and 100 molecules per cluster are displayed. For Figure 3.7, the cluster size ($\sigma$) was 5nm and 10nm, the number of molecules per cluster 2 and 4, and the density 10 and 1000 $\mu m^{-2}$. Examples of point patterns used for simulations are shown in Figure 3.11. The “true” $K(r)$ or $L(r) - r$ functions are then estimated using Eq. (3.3) and Eq. (3.2) (Figure 3.12).

Multiple realizations of the observed point patterns are then obtained by Monte Carlo simulations, based on the true points and the application of the effects of localization uncertainty and/or limited detection efficiency. For the observed points, the effect of subsampling corresponding to limited detection efficiency is added by generating a pseudo random number for each true point, sampled from a standard uniform distribution in $(0, 1)$, and the point is considered ”sampled” if the sampling ratio is greater than this value. The effect of localization uncertainty is added by sampling from a Gaussian uncertainty distribution centered at each true location, with the standard deviation sampled from a distribution corresponding to an exponential photon count model (Pertsinidis et al., 2013) (Figure 3.13). The $K(r)$ or $L(r) - r$ functions are then estimated. The estimations provided by the analytical methods presented are also computed on the basis of true points and the same error parameters used in simulations.

The relative mean squared error (MSE) or the relative standard deviation ($\sigma$) is then computed by dividing with the true $K(r)$ or $L(r) - r$ values. The results are either averaged over $r$ (Figure 3.5) or only the value at the true cluster radius (estimated from the maxima of $L_{true}(r) - r$ function) is used (other figures), and are then averaged over the different realizations of true point patterns for the same cluster condition (if the true points were obtained through simulations).

## 3.5 Supporting Information

### 3.5.1 Exact computation of variance of $K$-function due to random subsampling

The randomness in the estimate of $K(r)$ due to subsampling arises due to the Bernoulli random variables $B_1, B_2, \ldots, B_N$. The mean and variance of $K(r)$ can be estimated using the first and second moments of $K(r)$.

The first moment is

$$\mathsf{E}[K(r)] = \sum_{i \neq j} \mathsf{E}\left[\frac{B_i B_j}{(\sum_{i=1}^N B_i)^2}\right] \mathcal{I}\{\|X_i - X_j\| \leq r\} A \tag{3.10}$$

and the second moment is

$$\mathsf{E}[K(r)^2] = \sum_{i \neq j} \sum_{k \neq \ell} \mathsf{E}\left[\frac{B_i B_j B_k B_\ell}{(\sum_{i=1}^N B_i)^4}\right] \mathcal{I}\{\|X_i - X_j\| \leq r\} \mathcal{I}\{\|X_k - X_\ell\| \leq r\} A^2. \tag{3.11}$$

Since $B_i$ are i.i.d. and $B_i^2 = B_i$, in order to evaluate the expectations in Eq. (3.11) and Eq. (3.11), it is sufficient to compute $\mathsf{E}\left[\frac{B_1 B_2}{(\sum_{i=1}^N B_i)^2}\right]$, $\mathsf{E}\left[\frac{B_1 B_2 B_3}{(\sum_{i=1}^N B_i)^2}\right]$ and $\mathsf{E}\left[\frac{B_1 B_2 B_3 B_4}{(\sum_{i=1}^N B_i)^2}\right]$.

Let $\alpha = \mathsf{E}[B_1]$. We have

$$\begin{aligned}
\mathsf{E}\left[\frac{\prod_{j=1}^K B_j}{(\sum_{i=1}^N B_i)^2}\right] &= \sum_{k=1}^N \Pr\left\{\sum_{i=1}^N B_i = k\right\} \Pr\left\{\prod_{i=1}^K B_i = 1 | \sum_{i=1}^N B_i = k\right\} \frac{1}{k^2} \\
&= \sum_{k=1}^N \Pr\left\{\sum_{i=1}^N B_i = k\right\} \frac{\Pr\left\{\sum_{i=K+1}^N B_i = k-K\right\} \Pr\left\{\prod_{i=1}^K B_i = 1\right\}}{\Pr\left\{\sum_{i=1}^N B_i = k\right\}} \frac{1}{k^2} \\
&= \sum_{k=1}^N \Pr\left\{\sum_{i=K+1}^N B_i = k-K\right\} \Pr\left\{\prod_{i=1}^K B_i = 1\right\} \frac{1}{k^2} \\
&= \sum_{k=1}^N \binom{N-K}{k-K} \alpha^{k-K} (1-\alpha)^{N-k} \alpha^K \frac{1}{k^2} \\
&= \sum_{k=1}^N \binom{N-K}{k-K} \alpha^{k} (1-\alpha)^{N-k} \frac{1}{k^2}.
\end{aligned}$$

The last expression can be directly computed or approximated with an integral.

### 3.5.2 Exact computation of $K$-function in the presence of localization uncertainty

For example, if $W_i$ are assumed to be independently drawn zero mean Gaussian random vectors, the vector $X_i - X_j + W_i - W_j$ is a Gaussian random vector with mean $X_i - X_j$, and covariance equal to the sum of the covariances of $W_i$ and $W_j$, and hence $\|X_i - X_j + W_i - W_j\|^2$ is a non-central $\chi^2$ random variable, with known distribution. The expected value of

$K'(r)$ is given by

$$\begin{aligned}\mathsf{E}[K'(r)] &= \frac{\sum_{i\neq j}\mathsf{E}\left[\mathcal{I}\{\|X'_i - X'_j\| \leq r\}\right]/N}{N/A}\\ &= \frac{\sum_{i\neq j}\mathsf{E}\left[\mathcal{I}\{\|X_i - X_j + W_i - W_j\|^2 \leq r^2\}\right]/N}{N/A}.\end{aligned}$$

The expected value inside the summation is nothing but the complementary cumulative distribution function of a non-central $\chi^2$ random variable, which is easily computed using the Marcum Q-function.

### 3.5.3 Justification for the choice of estimator of true locations

In the Methods section of main text, the following estimators are defined.

$$\hat{x}_i = \overline{x} + \frac{\hat{\sigma}_x}{(\hat{\sigma}_x^2 + \sigma_{x,i}^2)^{\frac{1}{2}}}(x'_i - \overline{x}). \tag{3.12}$$

$$\overline{x} = \frac{1}{K}\sum_{i=1}^{K} x'_i, \tag{3.13}$$

$$\overline{\sigma}_x^2 = \frac{1}{K}\sum_{i=1}^{K} \sigma_{x,i}^2. \tag{3.14}$$

The estimate of Eq. (3.12) can be justified under the assumption that estimates of the x-coordinate of the cluster center in Eq. (3.13) and cluster spread of the x-coordinate in Eq. (3.14) are accurate. Let

$$\hat{x}_i = \mu_x + \frac{\sigma_x}{(\sigma_x^2 + \sigma_{x,i}^2)^{\frac{1}{2}}}(x'_i - \mu_x)$$

denote the estimate of Eq. (3.12) when the cluster center and spread are accurate. It is easy to verify that

$$\mathsf{E}\left[(\hat{x}_i - \hat{x}_j)^2 - (x_i - x_j)^2\right] = 0.$$

This suggests that by using the estimates of Eq. (3.12), the estimate of the squared distance between any pair of points in the cluster is unbiased, and thus the K-function computed using distances between the estimated points is expected to be accurate. This is the main reason for using the estimate of Eq. (3.12). It is to be noted here that if one were interested in minimising the squared error $\mathsf{E}[\|\widehat{X}_i - X_i\|^2]$ in the position of each molecule, then one would use the MMSE estimator of

$$\overline{x} + \frac{\hat{\sigma}_x^2}{\hat{\sigma}_x^2 + \sigma_{x,i}^2}(x'_i - \overline{x})$$

in Eq. (3.12). However, it was observed that in practice this leads to a shrinking of the reconstructed clusters. The current estimator does not have this drawback and has the added advantage of accurately approximating distances between points in the cluster.

### 3.5.4 Effect of clustering of localizations on reconstruction

The reconstruction method presented in the paper works on a cluster-by-cluster basis, and therefore the SMLM localizations must be first preprocessed by means of clustering algorithms like DBSCAN (Ester et al., 1996) or others (Rodriguez and Laio, 2014), before applying the method. The method presented assumes that the clustering errors are minimal. Example reconstructions after including clustering by DBSCAN is shown in Figure 3.8, which provided satisfactory results. The user is recommended to try out different clustering methods and parameters for a given dataset, so as to minimize the clustering errors. There are obvious limitations to this approach: in a case where the clusters are overlapping, it might be difficult for clustering algorithms to identify true clusters.

For the reconstruction method, since the X and Y coordinates are estimated separately, the method works best if the clusters are elliptical if not circular. As mentioned already, it is best if the clusters are well separated. Also, if a cluster with an arbitrarily complicated shape is clustered into multiple small symmetric clusters by the clustering algorithm, since the reconstruction method works on the basis of shrinking the clusters about a central point for each cluster, it might introduce artifacts, since each of the small clusters will be shrinked about their centers rather than the center of the true cluster. Therefore, the user must be careful to make sure that the clustering step does not introduce major errors or artifacts.

If the clusters are expected to have other specific parametric shapes, e.g., polygonal, helical etc., it might be possible to adapt the reconstruction method proposed in this paper to these alternate cluster shapes.

## 3.6 Other supporting information

File S1. MATLAB function to estimate the mean and the standard deviation of the subsampled $L(r) - r$ given true points. (Shivanandan et al., 2015)

File S2. MATLAB function implementing the reconstruction method.(Shivanandan et al., 2015)

## 3.7 Acknowledgments

The authors thank Dr. Paolo Annibale and Dr. Marco Scarselli for providing the PALM data that has been used in the paper. A. S. would like to thank Prof. Ivo F. Sbalzarini for early discussions and guidance, and Dr. Hendrik Deschout for discussions.

## 3.8 Author contributions

Designed the method and implemented the software: A. S. and J. U., performed the data analysis: A. S., wrote the paper: A. S., J. U. and A. R. All authors read and approved the final manuscript.

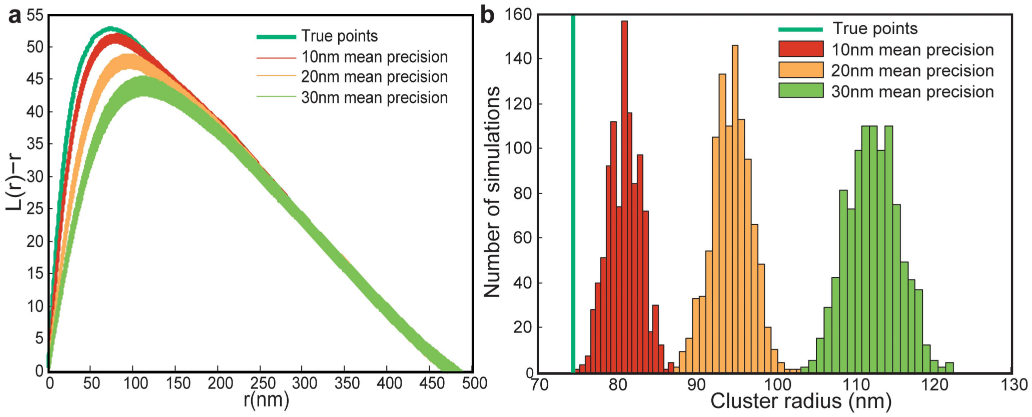

**Figure 3.4.** Propagation of localization error in cluster analysis with Ripley's $L(r) - r$ function.

$L(r) - r$ curves are plotted for a set of points obtained from a PALM experiment (shown in Figure 3.1 of main text), called true points, setting them as the true locations of molecules; and also for 1000 realizations of localizations estimated from these true points with a given estimation uncertainty model. (a) $L(r) - r$ curves corresponding to the true points (dark green) and 1000 realizations of the estimated localizations with different localization precisions (red: mean precision 10nm. orange: 20nm. green: 30nm). Details on the models for localization uncertainty and the distribution of localization precision can be found in Methods. (b) The cluster radius estimated from the maxima of different $L(r) - r$ curves. It can be seen that the $L(r) - r$ curves and the cluster radius corresponding to the estimated localizations is far off from the ones corresponding to true points, and the difference increases with worse localization precision. Also see Figure 3.10, for a method to predict the mean $L(r) - r$ curves given the true points and localization precisions.

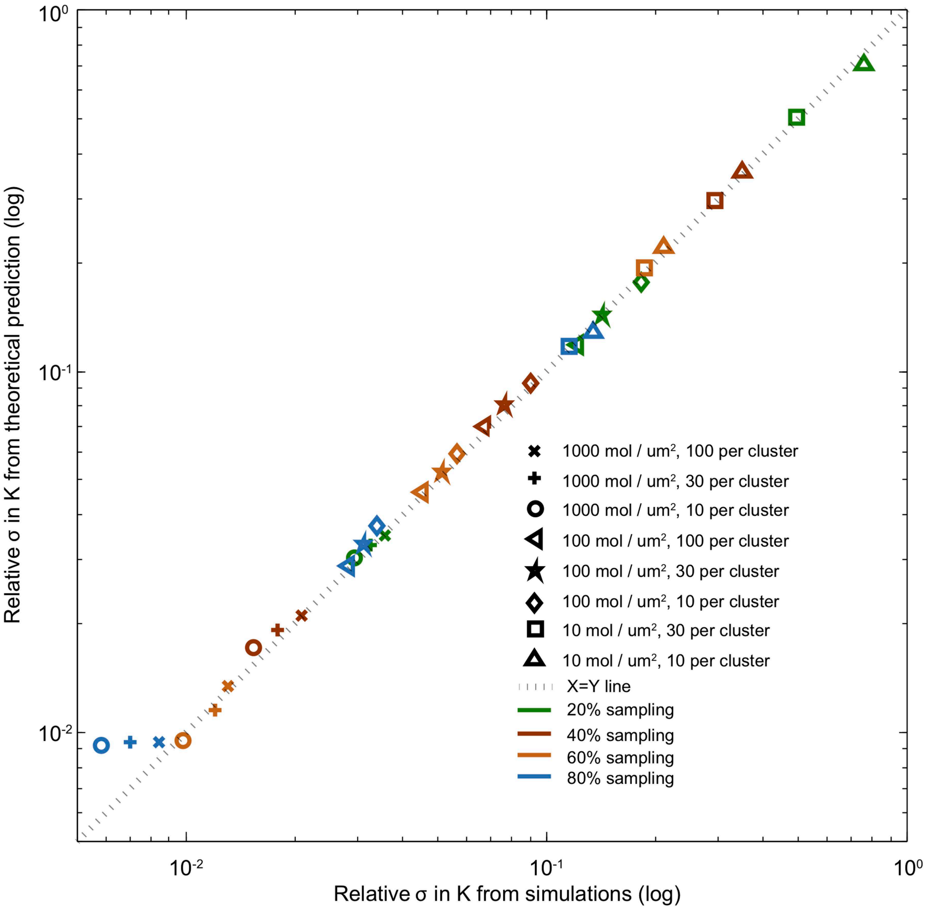

**Figure 3.5.** Validation of analytical method for estimating the variance in $K$-function due to subsampling.

Comparison of mean relative standard deviation in $K$-function due to subsampling (Relative $\sigma = \frac{\sigma_{K,subsampled}}{K_{true}}$), estimated by the theoretical method (section Exact computation of variance of $K$-function due to random subsampling in Methods), to that estimated from simulations (100 realizations of subsampling per point pattern). The comparison is done for different cluster conditions (denoted by different symbols) and subsampling ratios (colors), after averaging over $r$. It can be seen that the relation follows a linear pattern $y = x$ (note: plot is in log scale), i.e. the theoretical predictions match those from simulations. Details of the simulations can be found in Methods. The averaging was done over 10 point patterns per cluster condition.

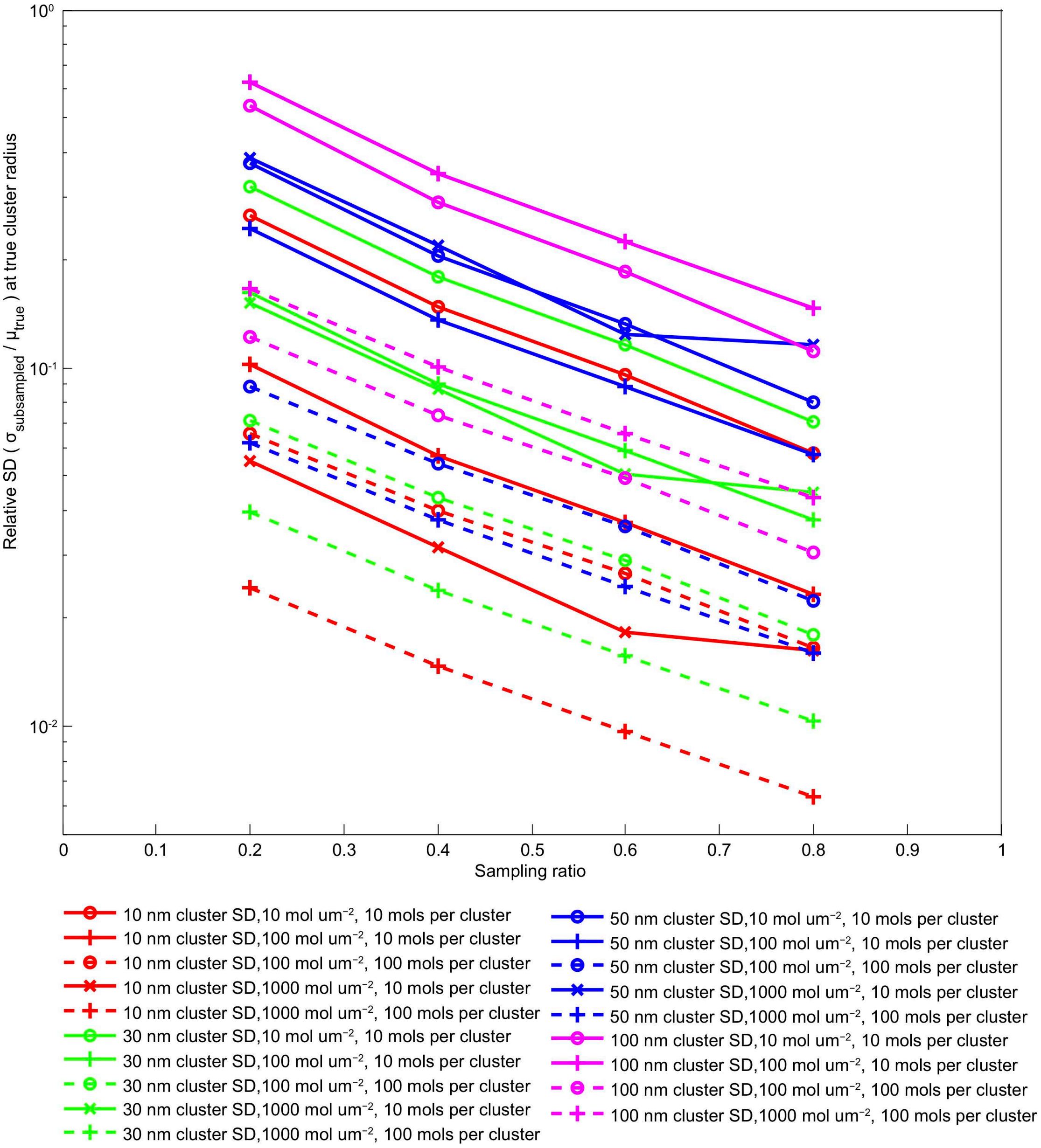

**Figure 3.6.** Characterization of relative standard deviation in $L(r) - r$ due to random subsampling, at $r = r_{true}$.

Relative $\sigma = \frac{\sigma_{subsampled}}{L_{true}(r)-r}$, $r = r_{true}$ is the true cluster radius estimated from $L_{true}(r) - r$. The comparison is on the basis for simulated points, with different cluster conditions (solid & broken lines: number of molecules per cluster; markers: density; color: cluster size (SD of Gaussian)) and subsampling ratios (x axis).

For all the clustering conditions presented, for 60% sampling, the relative $\sigma$ remained less than .25, with most obtaining a value less than .15. For a broad range of clustering conditions, the value remained less than .1 even for 20% sampling. It can be observed that the relative $\sigma$ increases with increasing cluster radius, other cluster conditions remaining same (that is, when clusters become less dense). Details of the cluster simulations can be found in Methods. The averaging was done over 10 point patterns per cluster condition.

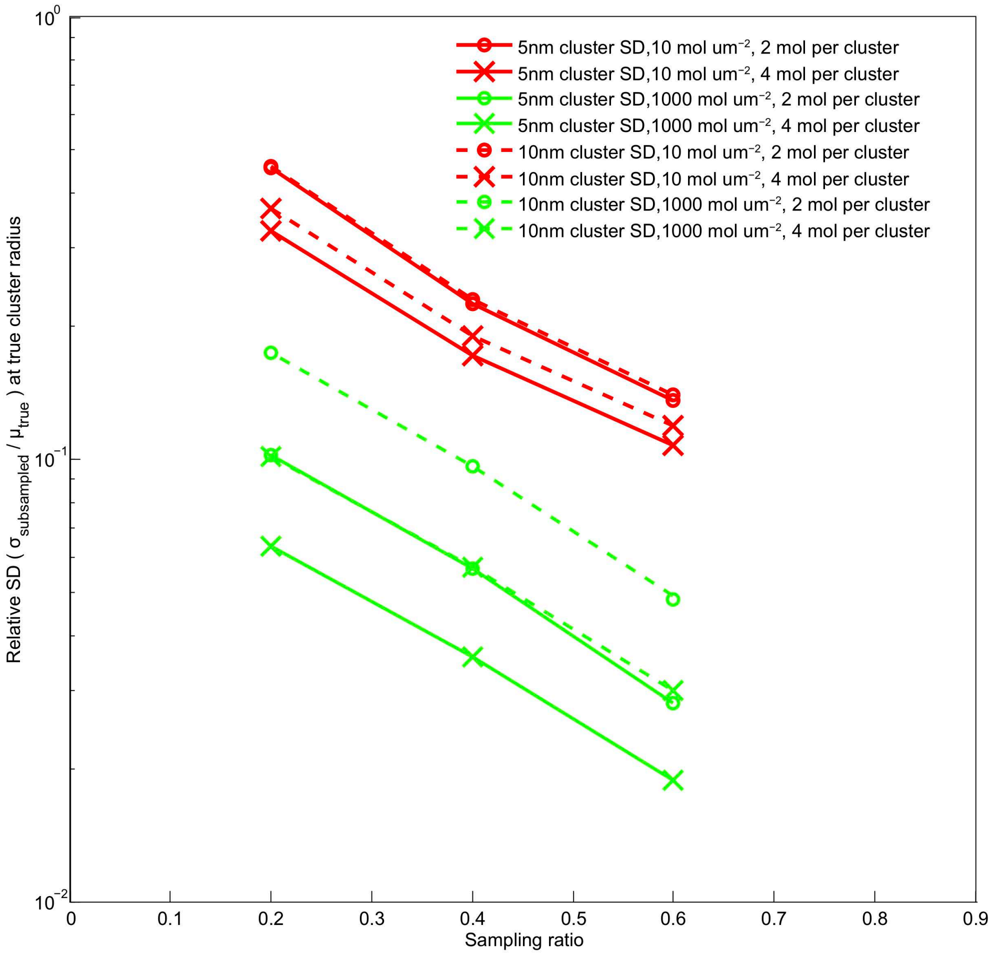

**Figure 3.7.** Characterization of relative standard deviation in $L(r) - r$ due to random subsampling, at $r = r_{true}$, in the case of dimers and tetramers.

Relative $\sigma = \frac{\sigma_{subsampled}}{L_{true}(r)-r}$. For sampling ratios of 60% or above, the relative $\sigma$ remained less than .15 for the clustering conditions tested. Details of the cluster simulations can be found in Methods. The averaging was done over 10 point patterns per cluster condition.

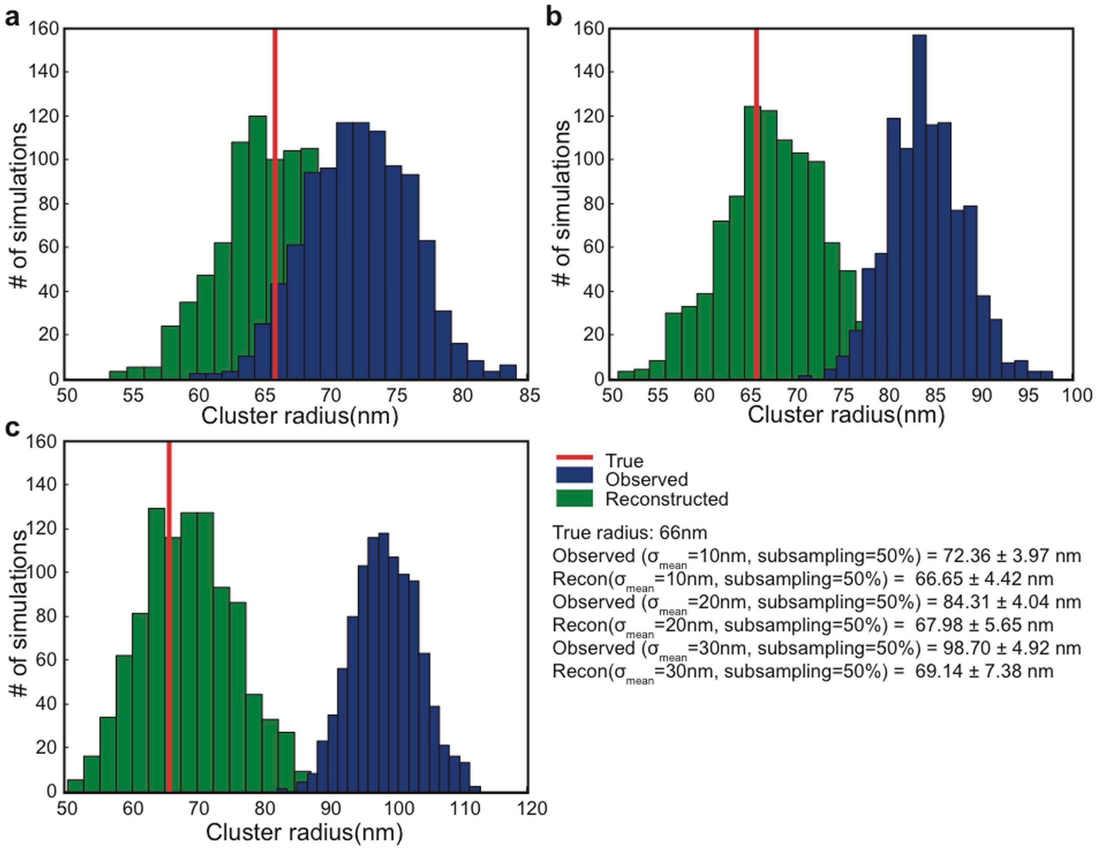

**Figure 3.8.** Application of reconstruction method on point locations from a PALM experiment as the true locations, and errors added artificially.

The point pattern used as true points is the same as the one in Figure 3.1 and Figure 3.4 and the errors applied to get observed points are: mean localization precision 10nm, 20nm, 30nm and 50% subsampling. The cluster radius corresponding to true, observed and reconstructed points, estimated from the maxima of $L(r) - r$ curves are displayed here. It can be seen that the ones corresponding to the reconstructed points are much closer to the true ones and its accuracy decreases with worse localization precision. The validation is important since it involves 1) a point pattern distributed as the one observed in a real PALM experiment rather than Gaussian clusters used in simulations, 2) the reconstruction also involves clustering, done by means of a clustering algorithm DBSCAN, rather than the perfect clustering (due to prior knowledge) used in simulations. A discussion on the importance of accurate clustering can be found in Section 3.5.

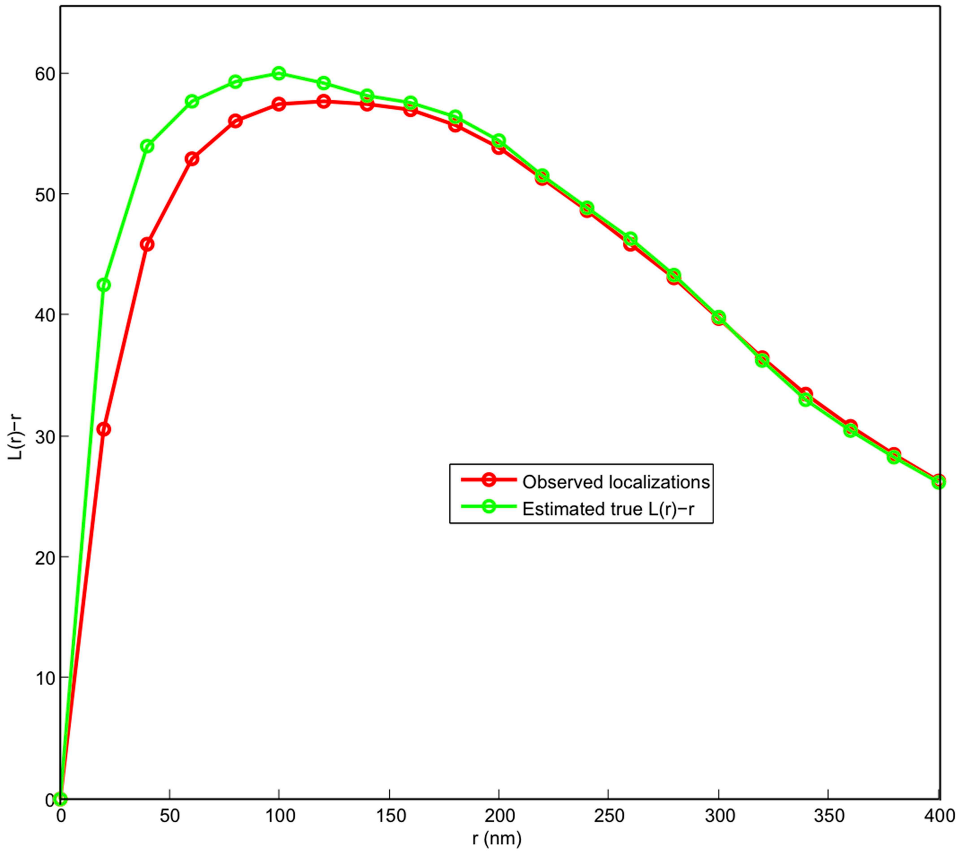

**Figure 3.9.** Example application of reconstruction method on previously published cluster analysis.
The method is applied on a previously published cluster analysis data, to note the extent of deviation between the $L(r) - r$ curves corresponding to the observed and the reconstructed data. The data is from the same experiment as that shown in Figure 3.1, published in Figure 3.2 of Scarselli et al. (2012). From the raw PALM localizations, localizations that appear multiple times are lumped together by setting a temporal threshold of 100 frames (of 10ms exposure). The localization precisions were computed with the expression provided in (Mortensen et al., 2010), for least squares fitting. All points that were localized with a precision that is better than 35nm was used for analysis, whether they are appearing in clusters or not. Clustering was performed for the reconstruction method using DBSCAN algorithm, with parameters $\varepsilon = 20nm$ and $minpts = 3$. The curve corresponding to the reconstructed points (estimated true points, green) deviates from that corresponding to the observed points (red).

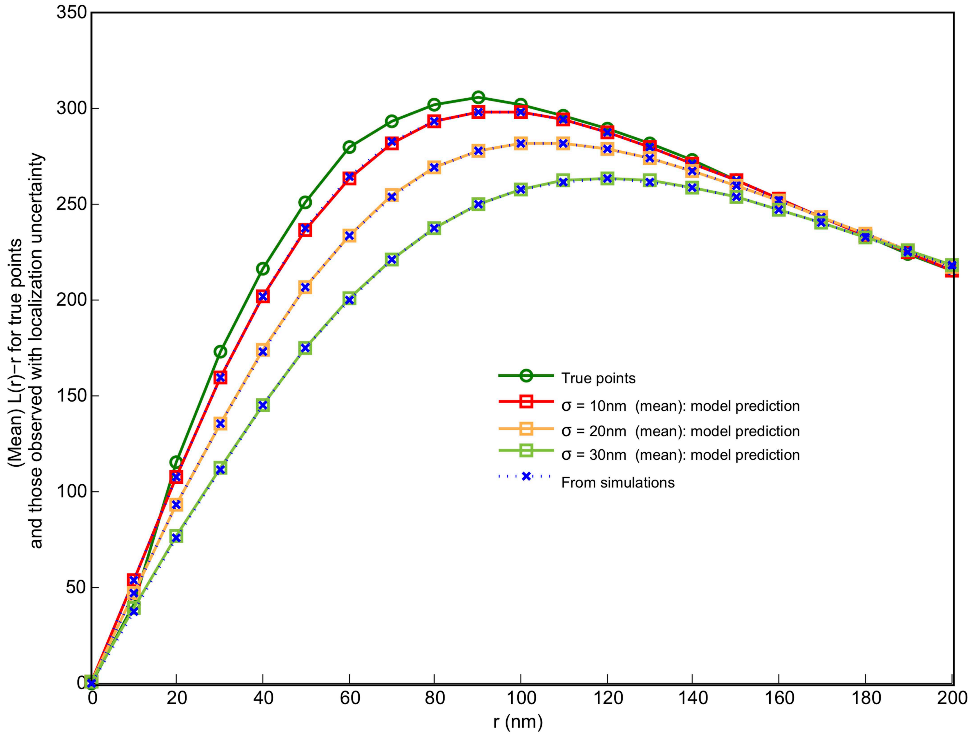

**Figure 3.10.** Demonstration of the method for the computation of $L$-function in the presence of localization uncertainty.

A Gaussian clustered point pattern (20 points per $\mu m^2$, 10 points per cluster, 30nm average cluster standard deviation) is observed with localization precision distributions similar to the ones shown in Figure 3.13, with mean precisions 10nm, 20nm and 30nm respectively. The $L(r) - r$ curves are plotted for the true points (dark green), and that for the mean corresponding to 1000 realizations of the observed points, sampling from the uncertainty distribution (blue broken lines). The approximate mean $L(r) - r$ as predicted by the presented method for the three cases is also plotted, computed from the exact $K$-function obtained, and can be seen as coinciding with those from the simulations.

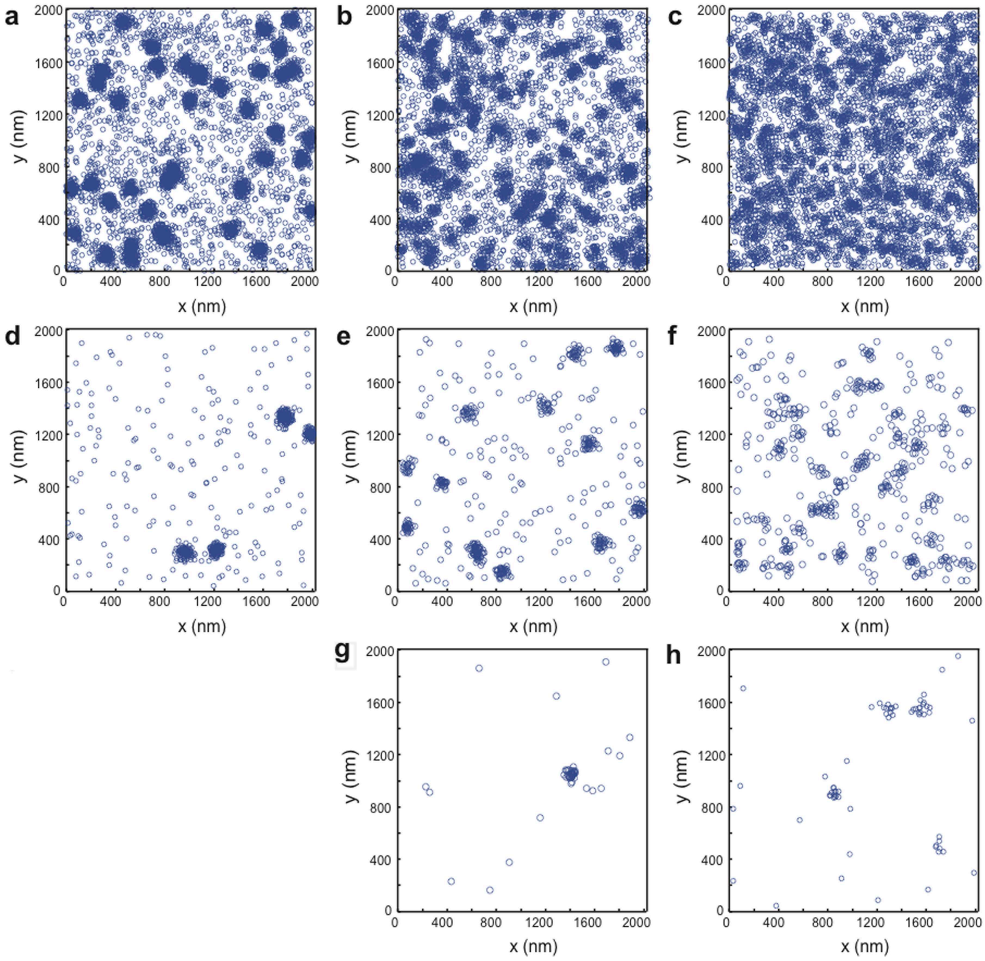

**Figure 3.11.** Example point patterns used in simulations.
Rows (top to bottom): Density of 1000 per $\mu m^2$ (a, b, c), 100 per $\mu m^2$ (d,e,f) and 10 per $\mu m^2$ (g,h). Columns (left to right): Molecules per cluster: 100 (a,d), 30 (b,e,g) and 10 (c,f,h). Example $L(r) - r$ functions estimated can be found in Figure 3.12.

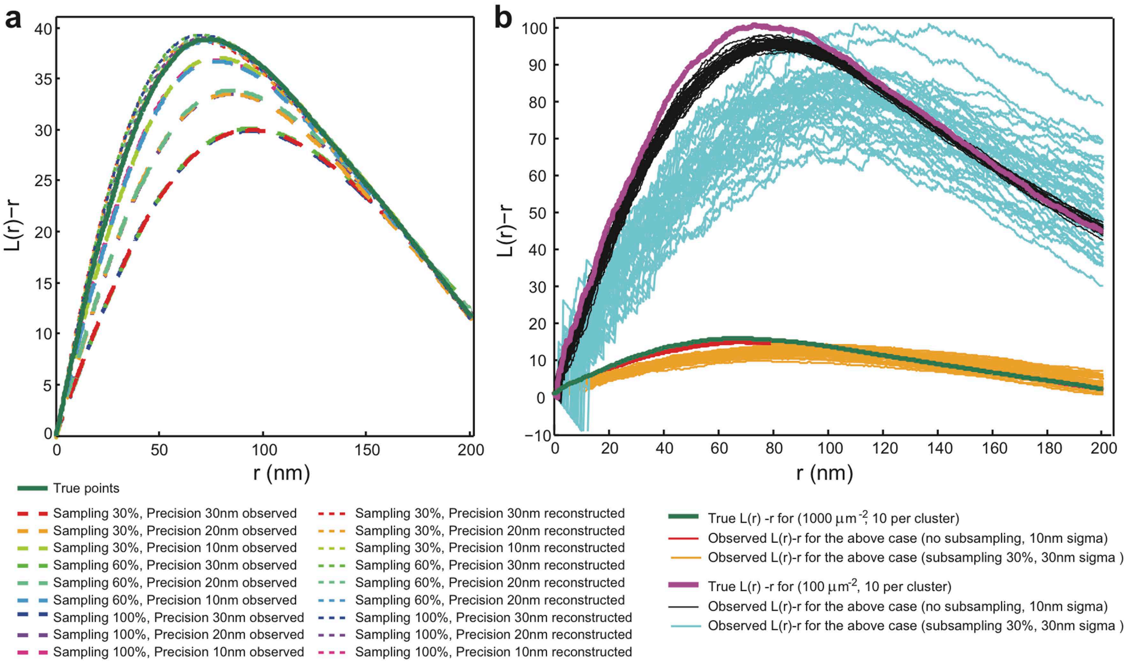

**Figure 3.12.** Example $L(r) - r$ curves used in simulations.

(a) Mean $L(r) - r$ functions (true, observed and reconstructed) corresponding to a particular cluster condition (density: 1000 per $\mu m^2$, 30 molecules per cluster). It can be noted that, in this case, the curves corresponding to the observed points with the same precision coincide approximately despite different subsampling ratios, as predicted by the invariance property of $L(r) - r$ to random subsampling. (b) Example $L(r) - r$ curves (true, observed) for the same number of molecules per cluster (10), but different density (1000 and 100 per $\mu m^2$). The relative effects of subsampling and localization uncertainty on the L(r)-r estimates can be observed. Also, even though the absolute variance ($\sigma_{observed}$) is higher for the point pattern with lower density (100 per $\mu m^2$) for the same error conditions, the relative variation ($\frac{\sigma_{observed}}{L_{true}(r)-r}$) can be higher for the case of higher density (1000 per $\mu m^2$), as found in other figures.

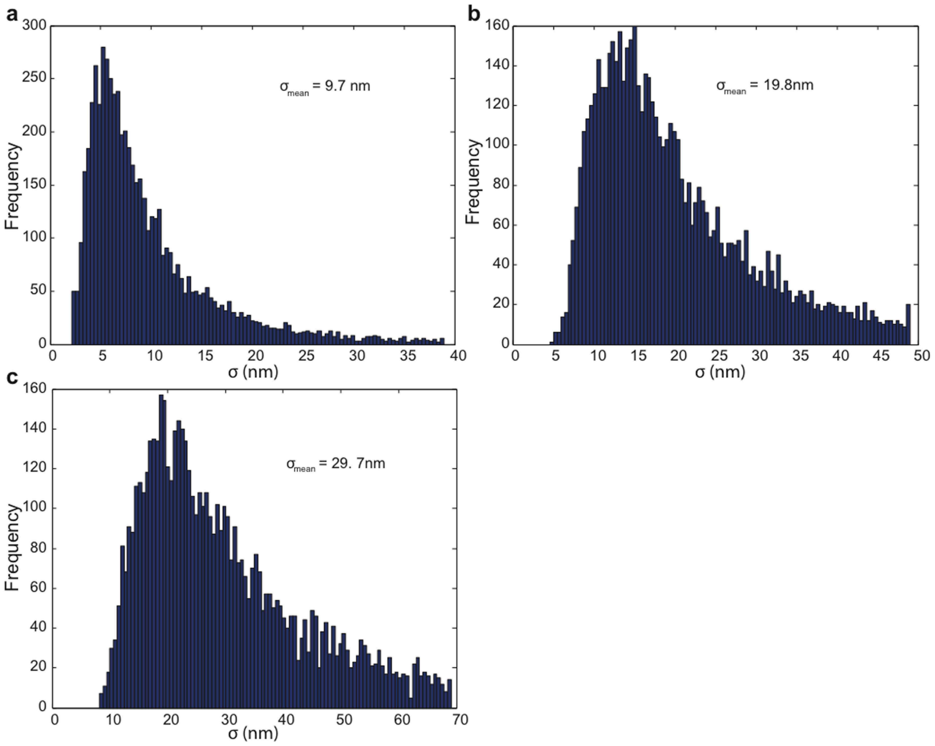

**Figure 3.13.** Distributions of localization precision used in the simulations. The distributions shown hereby, based on an exponential model for the photons collected, are the ones that were used for Figure 5a, b and c respectively.

## Chapter 4

# (More) Analytical and experimental approaches to quantification of spatial heterogeneity

*Manuscript(s) based on (verbatim) content provided in this chapter is under preparation, for submission to peer reviewed journals for publication.*

### 4.1 Introduction

In Chapter 3, we presented methods to account for two major sources of errors in quantitative spatial analysis with SMLM, that of a limited detection efficiency and localization precision. The methods were validated and errors characterized based on *in silico* approaches.

Biological clusters could be of different shapes, depending on the underlying physical mechanism( Veatch et al. (2012) and references therein). In the case of SMLM imaging, e.g., the clusters formed due to photoblinking has a Gaussian or Cauchy peak shape (Pertsinidis et al., 2010)), depending on the photon count distribution within the cluster. Therefore, cluster parameter estimation techniques must be evaluated for their dependencies on cluster shapes. Also, it is interesting if specific cluster models can be identified from (SMLM) data.

In this chapter, we generalize the methods developed in Chapter 3 for estimation of true point locations, given the locations observed with measurement error, to be applicable to different cluster models. Also, we present our results of the application of the methods described in Chapter 3 on experimental data from PALM experiments. Additionally, this chapter consists of some work on cluster model identification and parameter estimation – we theoretically evaluate a proposed estimator of cluster spatial size, and also, describe a method to identify cluster models from data.

### 4.2 General approach for estimation of true locations after accounting for localization uncertainty

The cluster reconstruction method presented in Chapter 3 is optimal in the case of Gaussian clusters. In the case of other cluster models, the same procedure can be adapted. In this section, we present a general approach based on the maximum likelihood estimation, that can be applied to any clusters which are i.i.d and the distribution is known. This estimator reduces to the estimator presented in chapter - in the case of Gaussian clusters. The approach can possibly be modified with non-parametric approaches, in case parameteric model for the clusters is not known. The adoption to other estimators, such as Minimum Mean Square Error (MMSE) estimator and others, such as the distance conserving estimator presented in 3.5.3, are straightforward.

Let the 2D vectors $X_1, X_2, \ldots, X_n$ be the true locations of the molecules within a cluster. We model them as being drawn i.i.d from some known distribution $F_X$. We observe $Y_i = X_i + W_i$ where $W_i$ are symmetric Gaussian noises with known variances (the method can be adapted for other error models). If $F_X$ follows a parametric model, the distribution of $Y$ can be found out with a 2D convolution of the Probability Density Functions (PDF) of $X$ and $W$. Then, we can

1. estimate the parameters of $F_X$ from the observations $Y_i$ based on some estimator. E.g. in the case of symmetric Gaussian shaped cluster, this will be the true cluster center and the true standard deviation of the cluster, and
2. with the estimated parameters, estimate $X_i' s$ from each $Y_i' s$ with the maximum likelihood approach.

E.g., in the case of Gaussian clusters, the formulation will be as follows. Let $X_i \sim \mathcal{N}(\mu, \Sigma)$ and $W_i \sim \mathcal{N}(0, \Sigma_i)$, where $\mu$ is a $2 \times 1$ vector representing the cluster center, and $\Sigma$ is a $2 \times 2$ matrix with diagonal entries equal to $\sigma^2$ and off-diagonal entries equal to 0 (similarly for $\Sigma_i$ – the diagonal entries being $\sigma_i^2$). $\Sigma_i$ is known from the experiment. Then, for $Y_i = X_i + W_i$,

$$P(Y_i) = \frac{1}{2\pi(\sigma^2 + \sigma_i^2)} \exp\left(\frac{-\|Y_i - \mu\|^2}{2(\sigma^2 + \sigma_i^2)}\right) \tag{4.1}$$

For $N$ independent observations of $Y_i$, the log likelihood will be

$$logP_\sigma(Y_1, Y_2, \ldots, Y_N) = \sum_{i=1}^{N} \left(-\log(\sigma^2 + \sigma_i^2) + \frac{-\|Y_i - \mu\|^2}{2(\sigma^2 + \sigma_i^2)}\right) + const. \tag{4.2}$$

The maximum likelihood will be at $\frac{d}{d\sigma} logP_\sigma = 0$, which gives

$$\sum_{i=1}^{N} \frac{-\|Y_i - \mu\|^2 + 2(\sigma^2 + \sigma_i^2)}{2(\sigma^2 + \sigma_i^2)^2} = 0. \tag{4.3}$$

It might be possible to evaluate this expression exactly given the values of $\sigma_i$, in order to find the maximum likelihood estimate for the true cluster standard deviation. In the general case, it might be practical to simply use a heuristic estimator, such as the solution of Eq. (4.3) in the case when $\sigma_i = \sigma_c = const \forall i$. In this case

$$\sigma_{ML}^2 = \frac{1}{2N} \sum_{i=1}^{N} \|Y_i - \mu\|^2 - \sigma_c^2, \tag{4.4}$$

which is similar to the estimator presented in Eq. (3.8).

The true locations $X_i$ can now be estimated by maximizing the likelihood of $Y_i$ as a function of estimated values of $\mu$ and $\sigma$. In the case of $F_X$ being Gaussian, the results are well known (Hajek, 2015, chap. 3), and reduces to the estimator presented in Eq. (3.12).

## 4.3 Estimating true locations from data with localization uncertainty: application on clusters due to blinking

The validation of the method presented in Section 3.2.2, to estimate the true point locations from the SMLM localizations in the presence of localization uncertainty, and generalized in Section 4.2, was mainly done on simulated data or errors. Here we apply the method on real data, and observe its performance.

A sample consisting of sparse, well separated distribution of photoswitching fluorophores is a system that can be studied with this method. E.g., Dronpa, the photoswitchable fluorophore, forms clusters in the PALM image, due to multiple localizations from a single fluorophore. The shape of such clusters can be approximated by a Gaussian (Section 4.6), and hence the method presented in Section 3.2.2 is directly applicable. Since the sample is sparse, we expect the identification of blink clusters can be done with negligible error, and also that the reconstruction algorithm will return much smaller clusters, tending towards single molecule size.

The application of the method indeed produced such a result, and can be seen in Figure 4.1. Sparse Dronpa single molecules immobilized on a coverslip were imaged, and the localizations were clustered using the DBSCAN algorithm. The standard deviation of the clusters belonging to the observed localization was $18.1 \pm 7.1$nm. After the estimation of true locations accounting for localization error as per Section 3.2.2, the standard deviation of clusters was reduced to $1.7 \pm 1.3$nm, as expected.

## 4.4 Theoretical $K$-function/PCF for cluster models: analytical framework

Exploratory spatial statistics tools such as Ripley $K$-function and Pair Correlation Function (PCF) have been commonly used to quantify spatial heterogeneity using SMLM. The most typical applications of these functions involve the test against Complete Spatial Randomness, or comparisons of empirical values of these functions for different experimental conditions. However, these functions have been also used for parameter estimation. The PC-PALM technique (Sengupta et al., 2011; Veatch et al., 2012), e.g., estimates various cluster process parameters based on fitting the empirical PCF to that of a theoretical one. Others (Kiskowski et al., 2009) have explored the use of the radius of maximal aggregation, the radius value at which $L(r) - r$ function is maximum, as an estimator of the cluster size. There is a need for such estimation tools to be analyzed or developed further, as will be made clear in the following sections. Prior to that, the framework used for this analysis will be elucidated in this section. The aim is to derive the theoretical functions corresponding to different cluster models, so that they can be used for estimation based on fitting, and to obtain the relationship between the radius of maximal aggregation and true cluster size.

It is useful to focus on a class of cluster processes, known as Poisson cluster processes, or Neyman-Scott processes, which are generated in the following way (Diggle, 2003; Illian et al., 2008). First, a set of *parent* points are created, following a spatial Poisson process (complete spatial randomness) with density (intensity) $\kappa$. Then, $S$ number of points are distributed around each *parent* point according to the i.i.d bivariate PDF $f(.)$, $S$ following some i.i.d distribution. These *offspring* points form the clustered point pattern.

Assuming $f(.)$ to be radially symmetric, let the PDF of the distance $r$ between two offspring points within a cluster is given by $h(r)$ and its Cumulative Distribution Function (CDF) by

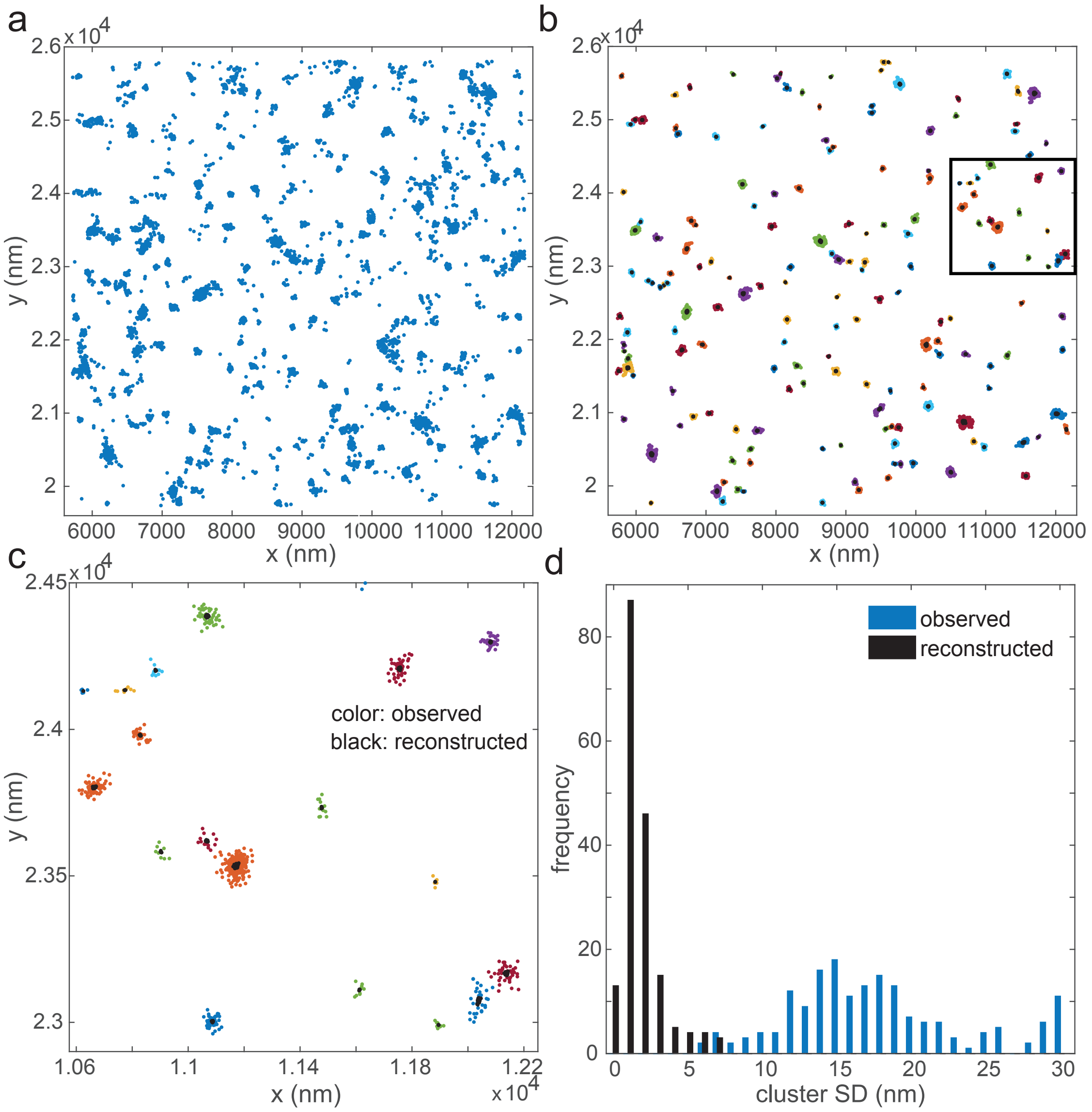

**Figure 4.1.** Estimation of true locations from data with localization uncertainty: application on clusters due to blinking.

**a** Raw localizations from *in vitro* Dronpa sample **b** after clustering with DBSCAN, with parameters $\varepsilon = 25$nm and minPts=4. **c** zoom in of inset in **b**. **d** histogram of cluster standard deviations, for the observed localizations and after reconstruction. It can be noted that the clusters shrink significantly, to a negligible size – from having an SD of 18.1 ± 7.1nm, it reduces to 1.7 ± 1.3nm.

$H(r)$. Then:

$$K_{clust}(r) = \pi r^2 + \frac{E[S(S-1)]}{\kappa\mu^2} H(r), \tag{4.5}$$

where the $\frac{E[S(S-1)]}{\kappa\mu^2} H(r)$ term is the expected contribution within each cluster, and $\pi r^2$ term represents the contribution from all other points(Diggle, 2003). The density of the point pattern will be $\mu\kappa$. When $S \sim Poiss(\mu)$, since $E[S(S-1)] = \mu^2$, Eq. (4.5) reduces to

$$K_{clust,Poisson}(r) = \pi r^2 + \frac{1}{\kappa} H(r). \tag{4.6}$$

The derivation in case of other distributions for points per cluster is straightforward.

$H$, being the CDF, is monotonic and non-decreasing. The corresponding PCF, $g(r) = \frac{K(r)'}{2\pi r}$ becomes:

$$g_{clust,Poisson}(r) = 1 + \frac{1}{2\pi\kappa}\frac{h(r)}{r} \tag{4.7}$$

This is the expression for purely cluster process, the next section describes ways to model a monomer fraction. The PCF and $K$-function for different cluster shapes are given in Table 4.1. We also add the physical Ising model to the compilation, since it is one of the models that has been proposed for membrane protein clustering (Veatch et al., 2012), even though it is not a Neyman-Scott process. We also note that the PCF of the variance gamma (VarGamma) model has the same shape as the Ising model, as $r \to \infty$(Jalilian et al., 2013). Also, the general exponential PCF mentioned in (Veatch et al., 2012), to be used as a model independent PCF to obtain model parameters, have the same shape as the VarGamma model in Table 4.1.

#### Monomer fraction

To model a monomer fraction or background, a spatial Poisson distributed monomer point pattern (density $\lambda$) can be superimposed to a purely clustered process. This is an approximate model as the superimposition can add points to the clusters as well. The resulting $K$-function and PCF can be obtained using the expression for superposition of two independent point processes (Diggle, 2003). In the case of a clustered process with $K(r) = \pi r^2 + \frac{1}{A}H(r)$, superposition with such a monomer process results in:

$$K(r) = K_{clust+monomer}(r) = \pi r^2 + \frac{1}{A_e}H(r) \tag{4.8}$$

$$g(r) = 1 + \frac{1}{2\pi A_e}\frac{h(r)}{r} \tag{4.9}$$

where $A_e = A/n^2$, $n$ being the purely clustered fraction. For the Poisson cluster process with $S \sim Poiss(\mu)$, $A = \kappa$ and $A_e = \kappa_e$, $n = \frac{\mu\kappa}{\mu\kappa+\lambda}$. It should be noted that the shape of the function remains the same as the purely clustered process, the change in parameter $A$ being the only change. That is, both $K(r)$ and PCF shapes are not unique for a particular model.

Another way to model a monomer fraction will be to use a bimodal distribution for $S$ (Illian et al., 2008, sec 6.7.2).

In the case of the constraint of no neighboring clusters within a distance of $r_{hard}$ from any cluster center, as in (Kiskowski et al., 2009) (where, for disk clusters with radius $R$, $r_{hard} = 4R$), for $r < 4R$, Eq. (4.5) will not have the $\pi r^2$ term, and, superposing the background results in:

$$K_{hard}(r) = \pi r^2(1 - m^2) + \frac{1}{\kappa_e}H(r) \tag{4.10}$$

$$g_{hard}(r) = (1 - m^2) + \frac{1}{2\pi\kappa_e}\frac{h(r)}{r}. \tag{4.11}$$

Such a formulation explains the results they obtain. Note that disk clusters contain points distributed uniformly at random within a circle (disk).

**Table 4.1. Cluster models used for analysis.**

| Model ($r_t$) | $g(r)-1$ | $K(r)-\pi r^2$ |
|---|---|---|
| Gaussian ($\sigma$)<br>(Illian et al., 2008) | $\frac{1}{4\pi\kappa\sigma^2}\exp(\frac{-r^2}{4\sigma^2})$ | $\frac{1}{\kappa}(1-\exp(\frac{-r^2}{4\sigma^2}))$ |
| Disk ($R$)<br>(Illian et al., 2008) | $\frac{2}{\pi^2 R^2\kappa}(\arccos(\frac{r}{2R})-\frac{r}{2R}\sqrt{1-\frac{r^2}{4R^2}})$ | $\frac{2}{\kappa\pi}\left(\frac{r^2\arccos(\frac{r}{2R})}{R^2}-\frac{r\sqrt{1-\frac{r^2}{4R^2}}(r^2+2R^2)}{4R^3}+\arcsin\left(\frac{r}{2R}\right)\right)$ |
| Cauchy $\alpha=1/2$ ($\omega$)<br>(Ghorbani, 2013) | $\frac{1}{8\pi\omega^2\kappa}(1+\frac{r^2}{4\omega^2})^{-3/2}$ | $\frac{1}{\kappa}(1-\frac{1}{\sqrt{1+\frac{r^2}{4\omega^2}}})$ |
| Variance Gamma $\nu=1/2$ ($\eta$)<br>(Jalilian et al., 2013) | $\frac{1}{2\pi\eta^2\kappa}\exp(-r/\eta)$ | $\frac{1}{\kappa}\left(1-e^{-\frac{r}{\eta}}\left(1+\frac{r}{\eta}\right)\right)$ |
| Ising<br>(Veatch et al., 2012) | $ar^{-1/4}\exp(-r/\xi)$ | $2\pi a\xi^{7/4}\left(\Gamma\left(\frac{7}{4}-\Gamma\left(\frac{7}{4},\frac{r}{s}\right)\right)\right)$ |

## 4.5 Estimation of cluster size from maxima of $L(r)-r$: a theoretical study

Accurate quantification of spatial heterogeneity requires accurate estimation methods. One of the key parameters in spatial distribution studies is the size of the cluster in space. Not only that this parameter provides information on cluster expansion or shrinkage to perturbations, but also the estimation of other parameters such as cluster density could be dependent on accurate estimation of the cluster size.

The radius of maximal aggregation $r_a$, the radii at which the $L(r)-r$ function of a spatial point pattern attains maxima, has been reported as an estimator for the true cluster size $r_t$ (Kiskowski et al., 2009; Antoku et al., 2015; Roy et al., 2013; Pezzarossa and Natuurwetenschappen, 2012; Malkusch et al., 2013; Lagache et al., 2013; Parton and Hancock, 2004; Deschout et al., 2014a; Shivanandan et al., 2015). Kiskowski et al. (2009) studied the relation between the $r_t$ and $r_a$ by means of simulations, and derived important insights – such as $r_t <= r_a <= 2r_t$. However, since the study was based on simulations, with a limited set of parameters and models (only disk clusters, e.g., so $r_t = R$, radius of the cluster), the understanding is limited, and the possibilities of generalization are not clear. Also, cluster shapes in biology could be very different from disk shape, and the performance of this estimator in such cases must be studied. The effect of other parameters, such as cluster shape, size, density, on this estimator is also not clear. Lagache et al. (2013) performed a theoretical analysis of a similar estimator, for disk shaped clusters, and reported a simpler, constant linear relation $r_a/r_t = 1.3$, which fails to systematically explain the more complex relationship observed by Kiskowski et al. (2009).

In this work, we explore, with mathematical rigor, the relation between $r_a$ and $r_t$, for different cluster shapes and conditions. Note that $r_t$ is defined differently for different cluster models: for a disk cluster, $r_t = R$, the true cluster radius, whereas for Gaussian clusters, we set $r_t = \sigma$, the true standard deviation (the full list can be found in Table 4.1), and hence are not meant to be directly comparable between different models. We find that, in general, for a large class of clustered point patterns, the ratio $p$ of the radius of maximal aggregation and the true cluster size ($p = r_a/r_t$) can be derived as an implicit function of two cluster parameters: $r_t$ and the number of clusters per unit area ($\kappa$). We also find that it possible to derive a theoretical lower bound for $p$, given a cluster model. We validate the theoretical results with simulations. The extension for more complicated cluster models are straightforward.

### 4.5.1 Radius of maximum aggregation vs true radius: theory

Here we analyze the relationship between the radius of maximum aggregation, defined as $r_a = \arg\max_r L(r) - r$, $L(r) = \sqrt{\frac{K(r)}{\pi}}$, as a function of true cluster parameters, for the class of clustered point patterns with $K$-functions of the form

$$K(r) = \pi r^2 + \frac{1}{A} H(r) \tag{4.12}$$

where $h(r) = H'(r)$ and $A > 0$, such as the ones introduced in Section 4.4 and Table 4.1. Then, $L'(r_a) - 1 = 0$, $L'(r_a) = 1 \implies K'(r_a)^2 = 4\pi K(r_a)$. Substituting in Eq. (4.12), we obtain

$$A = \frac{h(r_a)}{4\pi(H(r_a) - r_a h(r_a))}. \tag{4.13}$$

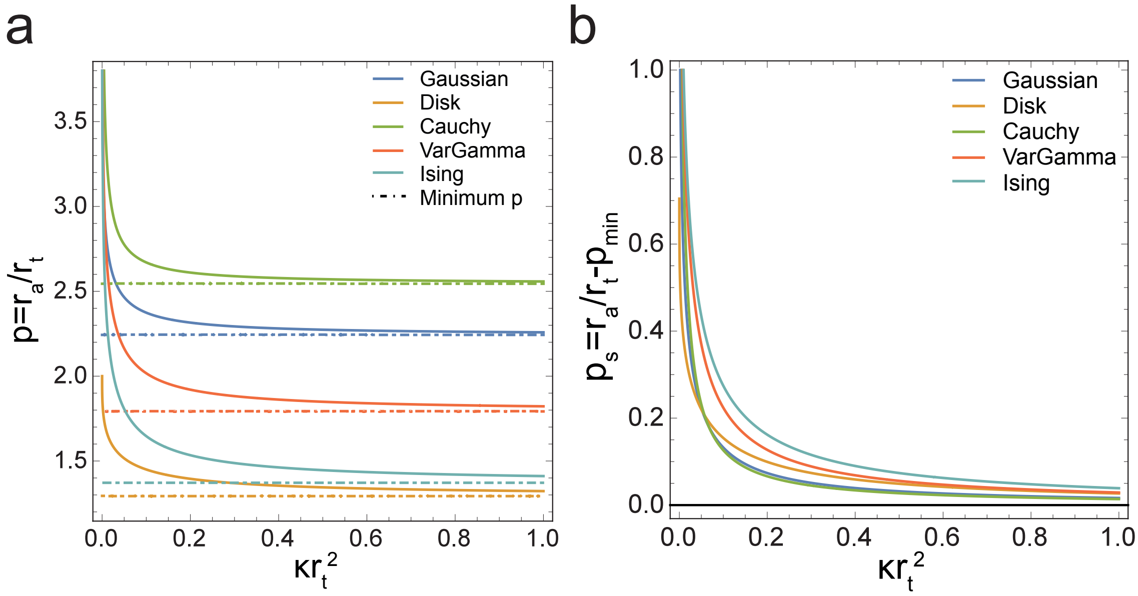

**Figure 4.2.** Relation between the radius of maximal aggregation and true cluster size. **a** For different cluster models, the relation between the ratio of radius of maximal aggregation $r_a$ and true cluster size $r_t$, as a function of the number of clusters per unit area $\kappa$ and true cluster size. It can be seen that the relationships are model dependent, while following a power law like shape. For the disk model, $1.29564 < r_a < 2$, whereas, e.g., for Gaussian model, $2.24181 < r_a < \infty$. The minimum $p$ value is obtained by exploiting the singularity in Eq. (4.13), given in Table 4.2 **b** Plots in **a** after translating by the minimum $p$.

Eq. (4.13) can be used to a relation between $p = \frac{r_a}{r_t}$ for all the processes listed in Table 4.1, where $r_t$ is the true size of the cluster. The results are given in Table 4.2. In fact, the singularity at $H(r_a) - r_a h(r_a) = 0$ provides a minimum bound for $p$ for all the models analyzed, and is also shown in Table 4.2. The lower bound so obtained is a fundamental characteristic of the cluster model's theoretical $L(r) - r$ functions.

It can be seen that the relationship $p = r_a/r_t$ is model dependent. For the disk model, e.g., $1.29564 < p < 2$, whereas, for Gaussian model, $2.24181 < p < \infty$. Also, with this approach, we could improve the accuracy of minimum $p$ from the value 1 obtained through simulation studies (Kiskowski et al., 2009) to 1.29564. This theoretical lower bound also coincides with the constant $p = 1.3$ reported by Lagache et al. (2013). By establishing a systematic relationship between $p, \kappa$ and $r_t$, the estimation approach becomes more accurate. On the

**Table 4.2. Exact expressions for the radius of maximal aggregation $r_a$ for different cluster models.**

| Cluster model | Expression for $\kappa r_t^2 = f(p = r_a/r_t)$ | Theoretical lower bound for $p$ (to 5 digits) |
|---|---|---|
| Gaussian ($p = r_a/\sigma$) | $\kappa\sigma^2 = \frac{e^{-\frac{p^2}{4}} p^2}{8\pi\left(-p^2+2e^{\frac{p^2}{4}}-2\right)}$ | 2.24181 |
| Disk ($p = r_a/R$) | $\kappa R^2 = \frac{p^2\left(p\sqrt{4-p^2}-4\arccos\left(\frac{p}{2}\right)\right)^2}{\pi^2\left(\sqrt{4-p^2}(3p^2-2)p-8p^2\arccos\left(\frac{p}{2}\right)+8\arcsin\left(\frac{p}{2}\right)\right)}$ | 1.29564 |
| Cauchy($p = r_a/\omega$) | $\kappa\omega^2 = \frac{p^2}{\pi(p^2+4)^{3/2}\left((p^2+4)^{3/2}-4p^2-8\right)}$ | 2.54404 |
| VarGamma ($p = r_a/\eta$) | $\kappa\eta^2 = \frac{p^2}{4\pi(\exp(2p)-\exp(p)(p^2+p+1))}$ | 1.79328 |
| Ising ($p = r_a/\xi$) | $\frac{1}{2\pi}a^{-1}\xi^{1/4} = \frac{\exp(-2p)p^{3/2}}{4\pi\left(-\exp(-p)p^{7/4}-\Gamma\left(\frac{7}{4},p\right)+\Gamma\left(\frac{7}{4}\right)\right)}$ | 1.37220 |

other hand, this approach means that unless the cluster models are known *a priori*, relating the radius of maximal aggregation to the true cluster size is not obvious. The dependency of $p$ on other cluster parameters and the cluster model means that the estimator could be a poor choice as a comparison tool between different experiments, if there is a possibility that the cluster model, $\kappa$ or $r_t$ are different.

### 4.5.2 Comparison with simulations

To establish the validity of the theoretical derivation obtained in Section 4.8 and Table 4.2 we performed a Monte Carlo simulation study. Clustered point patterns, belonging to either Gaussian or Disk clusters, were simulated in a unit square, for varying $\kappa$ and $r_t$. The theoretical value of $p$ for a given $\kappa$ and $r_t$ were obtained by solving the analytical expressions in Table 4.2, and was compared to $\hat{p} = \hat{r}_a/r_t$. $\hat{r}_a$ was obtained from the empirical maximum of the $L(r) - r$ curves. The results are shown in Figure 4.3. The mean value of $\hat{p}$ from simulations broadly agree with the theoretical results, though the deviation increases with increasing $\kappa r_t^2$. This is the result of increasing number of clusters per unit area (increasing $\kappa$) or having larger clusters within the unit square used in the simulations (increasing $r_t$), both resulting in overlapping clusters, resulting in deviations from theoretical framework based on a particular cluster model. In fact, the deviation is most influenced by increasing radius(Figure 4.3, bottom). We conclude that our theoretical analysis is valid for the conditions where the estimator $r_a = \arg\max_r L(r) - r$ has a reliable behavior.

## 4.6 Identification of cluster models: model selection and parameter estimation

A common approach in spatial statistics to estimate the cluster parameters is by fitting the theoretical function corresponding to a cluster model, such as the ones elucidated in Section 4.4, to data to obtain the parameters(Diggle, 2003; Illian et al., 2008). The PC-PALM method, which proposed to identify the cluster parameters after accounting for blinking, followed this approach, by fitting the empirical PCF to a model corresponding to an exponential decay, assumed to represent no particular cluster shape(Sengupta et al., 2011; Veatch et al., 2012; Sengupta et al., 2013; Tobin et al., 2014), while acknowledging other possible cluster models (Veatch et al., 2012). For example, in the case of membrane proteins, it has been proposed that the underlying processes could be an Ising or disk cluster process (Veatch et al., 2012).

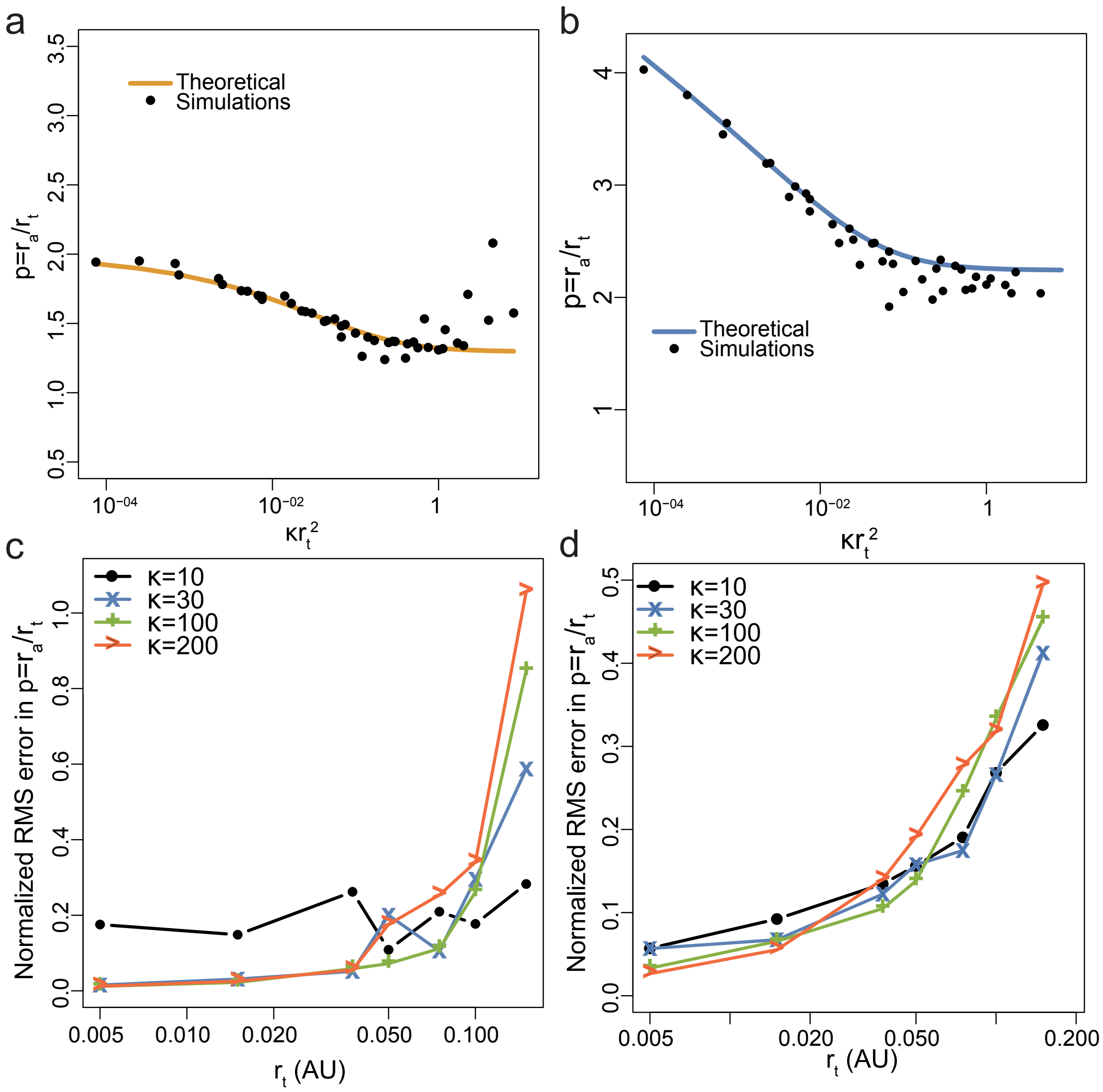

**Figure 4.3.** Comparison of theoretical results on $p = r_a/r_t$ with that from simulations **a,b** Results from theory (solid curve) as well as simulations (dots), for disk and Gaussian clusters respectively. Only the mean value from 100 simulations are shown. It can be seen that in both cases, the mean values from simulations deviate from the theoretical values with increasing $\kappa r_t^2$. **c,d** The root mean squared error, normalized by the theoretical value, for disk and Gaussian clusters respectively, plotted against $r_t$. The colors denote different $\kappa$ values. It can be seen that the error values are highly influenced by $r_t$.

As we have shown in Section 4.4, the exponential PCF shape is indistinguishable from that corresponding to a VarGamma model. Also, it may not be accurate to compare the estimated parameters corresponding to the generic exponential decay PCF as in the PC-PALM method, between say a true Gaussian process and a true disk process, as the parameters need not be mapped one-one. Instead, the model must be inferred from data.

However, as discussed in Section 4.4, the theoretical PCF is not unique for a cluster model, and its shape is not sufficient to identify the models(Figure 4.4). Model selection based on Monte Carlo (MC) rank tests – ranking the empirical statistic among the statistics from MC simulations based on estimated parameters – based on PCF or the related $K$ statistic is not sound, if the same statistic was used for parameter estimation(Diggle, 2003). The standard method in this case is to perform MC rank tests with a statistic that is different from the

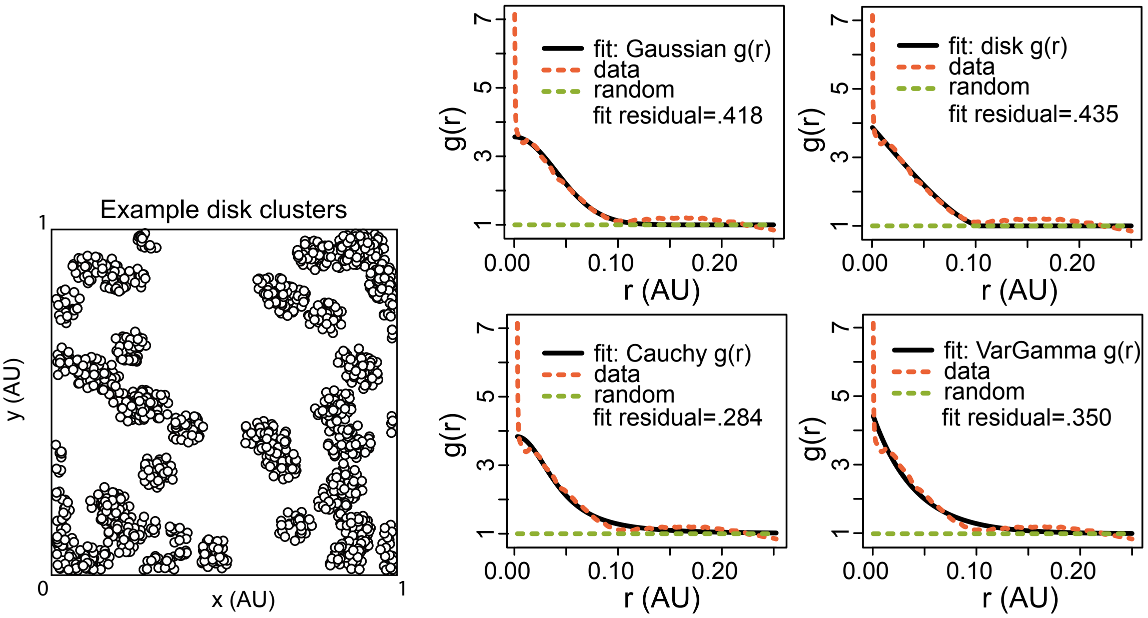

**Figure 4.4.** Demonstrative example of fitting model PCFs to the PCF of a disk point pattern The empirical PCF of the point pattern in the left is computed, and is fit to the theoretical PCFs of various cluster processes. Fit results $(\hat{\kappa}, \hat{r_t}, \hat{\Delta})$, $\hat{\Delta}$ being the value of the objective function at the estimated parameters, called fit residual: Gaussian $(38.11, .028, .418)$, disk $(40.64, .052, .435)$, Cauchy $(21.55, .051, .284)$, var gamma $(27.86, .040, .350)$), whereas the true values of the disk point pattern are $(\kappa = 50, r_t = R = .05)$. The Cauchy distribution is found to have the best fitness, whereas the disk one has the worst. The $p = r_a/r_t$ corresponding to disk distribution, with the estimated parameters above is $\hat{p} = 1.44$. The maxima of $L(r) - r$ is at $\hat{r}_a = 0.072$, providing a $\hat{r}_t = \hat{r}_a/p = .050$.

one that was used for parameter estimation, e.g., the nearest neighbor distribution function. However, the approach is known to have low statistical power (Illian et al., 2008), and we too had similar experience during preliminary attempts to identify the cluster models from SMLM data (results not shown).

An alternative to the summary statistic approach to perform an ensemble model selection is to use model selection at the cluster level. After clustering by a shape independent clustering algorithm (such as DBSCAN), each cluster can be fit to candidate models. Model selection can then be obtained, by comparing the Akaike Information Criterion(AIC). AIC, which uses both the goodness of fit (log likelihood) as well as model complexity (number of estimated parameters), provides a measure of the information lost when a particular model is selected to explain data. A preferred model among several candidates will have a lowest AIC.

An example application of this approach is shown in Figure 4.5. Clusters following Cauchy distributions in a unit square are identified using DBSCAN, and the x (and y) coordinates of points in each cluster are fit to 1 dimensional normal and Cauchy distributions (candidate models) using maximum likelihood estimation. The difference in the AIC values for each cluster in the x and y direction are shown. It can be seen that for all clusters, the AIC values are lower for the Cauchy fit, and hence Cauchy distribution has been (correctly) identified. It can also be noted that this identification technique is prone to edge effects, as the clusters close to the edge have much lower difference in AIC values between the two candidate models. Also, choosing optimal DBSCAN parameters could be a challenge, and could involve a tradeoff between accuracy and completeness of clustering.

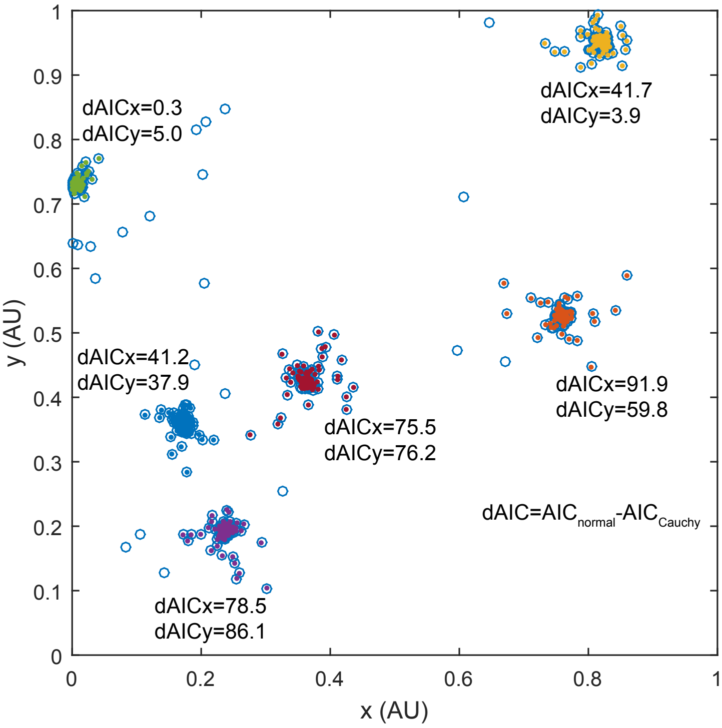

**Figure 4.5.** Demonstration of cluster model selection approach.
For the Cauchy clustered point pattern, after identifying the clusters with DBSCAN,are fit to both Gaussian and Cauchy distributions, cluster-by-cluster, in both axis. The difference in AIC between the model fits are shown. The Cauchy model was selected for all the clusters. Empty circles denote the true points, whereas filled dots denote points detected by DBSCAN.

We applied this technique to identify the cluster models for the Dronpa *in vitro* dataset shown in Figure 4.1. There are at least two valid candidate models for the clustering due to blinking of a photoswitchable flourophore: a Gaussian distribution or one with a Cauchy peak shape (Pertsinidis et al., 2013), depending on the distribution of photon counts between the points in a cluster. The results of analysis are shown in Figure 4.6. The vast majority of clusters (more than 98%) were found to fit a Gaussian distribution better.

## 4.7 Spatial distribution of fluorophore detection efficiency and influence on second-order properties

### 4.7.1 Background

To recapitulate the challenge of imperfect detection efficiency to quantitative PALM: It has been observed that only about 80% of the GFP molecules present in the sample emit a fluorescent signal(Ulbrich and Isacoff, 2007), and in the case of photo-activable fluorophores, the corresponding value (henceforth referred to as *detection efficiency* of the fluorophore, represented by $p$) is 40-60% depending on the fluorophore, with the popular mEos2 exhibiting about 50-60%(Annibale et al., 2012; Puchner et al., 2013; Durisic et al., 2014b). The limited detection efficiency at the single fluorophore level has been modeled as a case of independent Bernoulli sampling, with constant probability $p$. E.g., in step-wise photobleaching experiments, by fusing each monomer molecule of the protein of interest with a fluorescent protein molecule, the signal count (i.e, the number of steps in fluorescence signal before

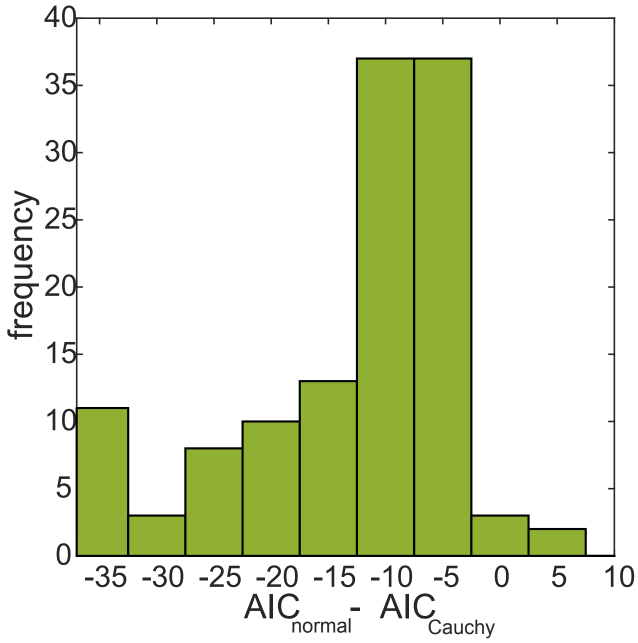

**Figure 4.6.** Model selection: application to Dronpa blinking cluster
The results of application of the AIC approach to the dataset in Figure 4.1. Normal distribution is preferred for vast majority of clusters.

photobleaching) from the protein complex, composed of possibly multiple monomers, can be identified. The distribution of such counts for the whole experiment can be fit to a binomial distribution(Ulbrich and Isacoff, 2007) or a hyper-geometric distribution, to estimate $p$ and the subunit count or stoichiometry of the protein complex. Such approaches have provided estimates of detection efficiencies of various PA-FPs (Puchner et al., 2013; Durisic et al., 2014b). While this model – independent Bernaulli trials for each molecule with constant retention probability $p$ for the whole experiment, or $p$-thinning – appears to be valid for first-order properties such as counting, its effect on estimates of second-order properties such as clustering and co-localization quantification, key in the analysis of spatial organization, needs to be investigated theoretically, and validated experimentally. E.g., in the case of a true single molecule co-localization of 100%, and with a detection efficiency of .5 for both fluorophores, the expected observed co-localization is 25%, and not accounting for the detection efficiency will result in erroneous conclusions.

In our work (Shivanandan et al., 2015), we dealt with second-order properties in the case of limited detection efficiency (and also localization precision) that is observed in the context of SMLM/PALM. One of the major ideas presented in our paper was: if limited detection efficiency in a PALM experiment can be considered as random subsampling (by means of independent Bernaulli trials, or $p$-thinning) of the true set of label molecules present in the sample, a class of second-order summary statistics functions commonly used in SMLM, such as the Ripley's $K$-function, $L(r) - r$ function and the Pair Correlation Function (PCF) is *invariant* to this subsampling. This *invariance to independent p-thinning* is a well known property in spatial statistics. Also, these functions are routinely used in SMLM analysis, both for clustering and co-localization quantification.

For the estimation of these summary statistics from data, this means that, the function (say, $L(r) - r$) corresponding to each realization of subsampling (a PALM experiment provides just one), $L_{subsampling}(r) - r$, is sampled from an i.i.d distribution (approximated by a normal distribution), centered at the function value corresponding to the true points ($L_{true}(r) - r$).

Our paper provides a method to estimate the variance of the this distribution analytically, given the true set of points and the sampling ratio. In the paper, we validated the methods (both the invariance property and variance estimation) through simulations, of both Gaussian clusters as well as applying errors artificially on PALM images. While the methods were found to perform well in these scenarios, the applicability of these methods in actual experiments needs to be demonstrated. Specifically, this involves the applicability of the assumptions of the $p$-thinning model: a constant retention probability $p$ per molecule for the whole experiment, independent of molecules and their location.

### 4.7.2 Identification strategy: data from redundant labeling experiments

Ideally, the validation should be done on independent, preferably correlative measurements. For example, if *single molecule resolution* AFM or TEM data are available of a field of view imaged by PALM, with perfect detection efficiency and negligible registration errors, then the effect of imperfect detection efficiency in PALM on both first and second-order properties can be studied. However, it appears such data is difficult to obtain in practice. However, redundant labeling of the target protein allows use the same estimation strategy used in step-wise photobleaching experiments, to study spatial organization of detection efficiency. E.g., if a protein is fused with 2 fluorophores (called 2x condition) per molecule (Figure 4.7), we can identify the spatial locations of molecules where both molecules emit signals (referred to as 2 signals case, or 2s), or those where only one out of the two emit a signal (1 signal case, 1s). These locations can be further analyzed, to identify the relationship between the second order properties of 1s, 2s and 1s+2s point patterns. The data used in Durisic et al. (2014b) provide a platform for this, and we study the spatial distribution of detection efficiency using these data.

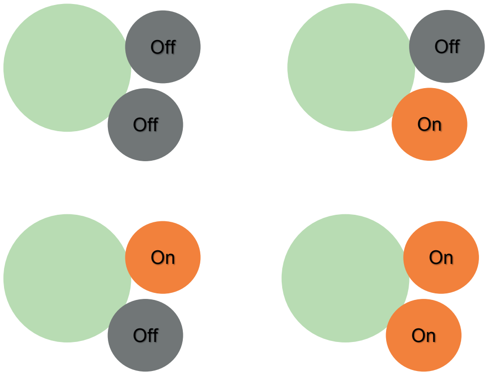

**Figure 4.7.** Redundant labeling approach
A target protein fused to two fluorophores (2x). There are four possibilities of detection – (off,off), (on,off),(off,on), (on,on). States (on,off) and(off,on) are referred to as 1s case, and (on,on) as 2s case.

Note that the redundant labeling strategy in PALM can at least be of two types: the fusion protein can have either one label attached per monomer in an oligomer, or multiple labels per monomer for a non-oligomeric protein. Either case, we use the same notation: an experiment with a redundancy of 3 fluorophores is called 3x experiment (and similarly for 2x, and the experiment with no redundancy is called 1x experiment). The point patterns identified, categorized by the number of fluorophores emitting a signal per fusion protein (after accounting for multiple fluorescent bursts from the same fluorophore), is referred to as 1s,2s and 3s, corresponding to signal count per fluorescent protein, for the 3x experiment.

Figure 4.7 makes this clear, in the case of 2x fusion protein.

The analysis strategy is explained in the cartoon figure Figure 4.8. Let 1s and 2s represent the point patterns corresponding to 1 and 2 signal counts, in the 2x case. We can compare the second-order properties (e.g. $L(r) - r$) corresponding to 2s ($L_{2s}(r) - r$) with that of the whole imaged population (those which emitted 1 signal *or* 2 signal, 1s+2s), represented by $L_{1s+2s}(r) - r$. It is a case of subsampling of the 1s+2s point pattern, with $p = \frac{\#2s}{\#1s+\#2s}$, # representing the counts. In case the assumption of *p-thinning* are valid, the 2s pattern should have second-order properties within the bounds ($\sigma_{true,subsampling}(r, p))$) predicted by the method presented for *p-thinning*(Figure 4.8). If the spatial distribution of 2s is different from the 1s+2s pattern – say, due to some spatial effect such as varying illumination or pH – the $L(r) - r$ curve for 2s case could be outside the bounds. The same approach can be used to compare the distribution of 1s (with 1s+2s, with $p = \frac{\#1s}{\#1s+\#2s}$).

The identification strategy for 2x can be summerized as follows:

1. Identify the 1s and 2s point patterns from a 2x PALM experiment
2. Estimate the $L(r) - r$ function corresponding to
    a) 1s+2s: $\hat{L}_{1s+2s}(r) - r$
    b) 1s: $\hat{L}_{1s}(r) - r$
    c) 2s: $\hat{L}_{2s}(r) - r$
    d) $\hat{\sigma}_{1s}$ of $L(r) - r$ of $p$-thinning 1s+2s with $\hat{p} = \frac{\#1s}{\#1s+\#2s}$
    e) $\hat{\sigma}_{2s}$ of $L(r) - r$ of $p$-thinning 1s+2s with $\hat{p} = \frac{\#2s}{\#1s+\#2s}$
3. Estimate the z score $\hat{z}_{.}(r) = \frac{\hat{L}_{.}(r) - \hat{L}_{1s+2s}(r)}{\hat{\sigma}_{.}}$. The null hypothesis of $p$-thinning is rejected at 95% if $|\hat{z}_{.}(r)| > 1.96$.

### 4.7.3 Application to data from Durisic et al

In (Durisic et al., 2014b), the researchers tagged the human glycine receptor (GlyR) complex in Xenpus oocytes with a redundant-labelling strategy. The receptor has 2 $\beta$ subunits and 3 $\alpha$ subunits. For PALM experiments with mEos2, they co-expressed the $\beta$ subunits with mEos2 (forming 2x labelling) and the $\alpha$ subunits with mCherry, in order to have a correlative reference and only the spots co-localizing with the green channel in the maximum intensity projection images were used for analysis. Using this strategy, the identified the detection efficiency of mEos2 to be $\approx .61$.

#### Processing details

We used ThunderSTORM (Ovesný et al., 2014), with the wavelet filter (peak intensity threshold =1.5 times the standard deviation of first wavelet)(Figure 4.9). Localizations with outlier PSFs (less than 30nm or greater than 600nm) were removed, as were the ones with uncertainty greater than 100nm. Since a correlative image in the green channel (mCherry) was available(Figure 4.9), to remove noise, only those localizations that colocalized with the green channel image (after thresholding) was used for analysis(Figure 4.9). The localizations were then blink corrected by merging spatio-temporal clusters within a distance=pixel size (157nm) and a dark time of 82 frames (4.1 seconds) as done in the original paper. Then, for each localization, the neighbors within a distance $r_t = 100nm$ are identified, and those with 1 neighbor merged to get the 2s point pattern, and those without a neighbor to get 1s point pattern, which were used for further analysis(Figure 4.10). $r_t$ was identified by plotting the detection efficiency corresponding to different $r_t$ values, and taking the value when the detection efficiency did not change any more. Once the point patterns were identified, the $L(r) - r$ functions were estimated, and the $\sigma_{subsampling}$ were identified with methods presented in Section 3.2.1.

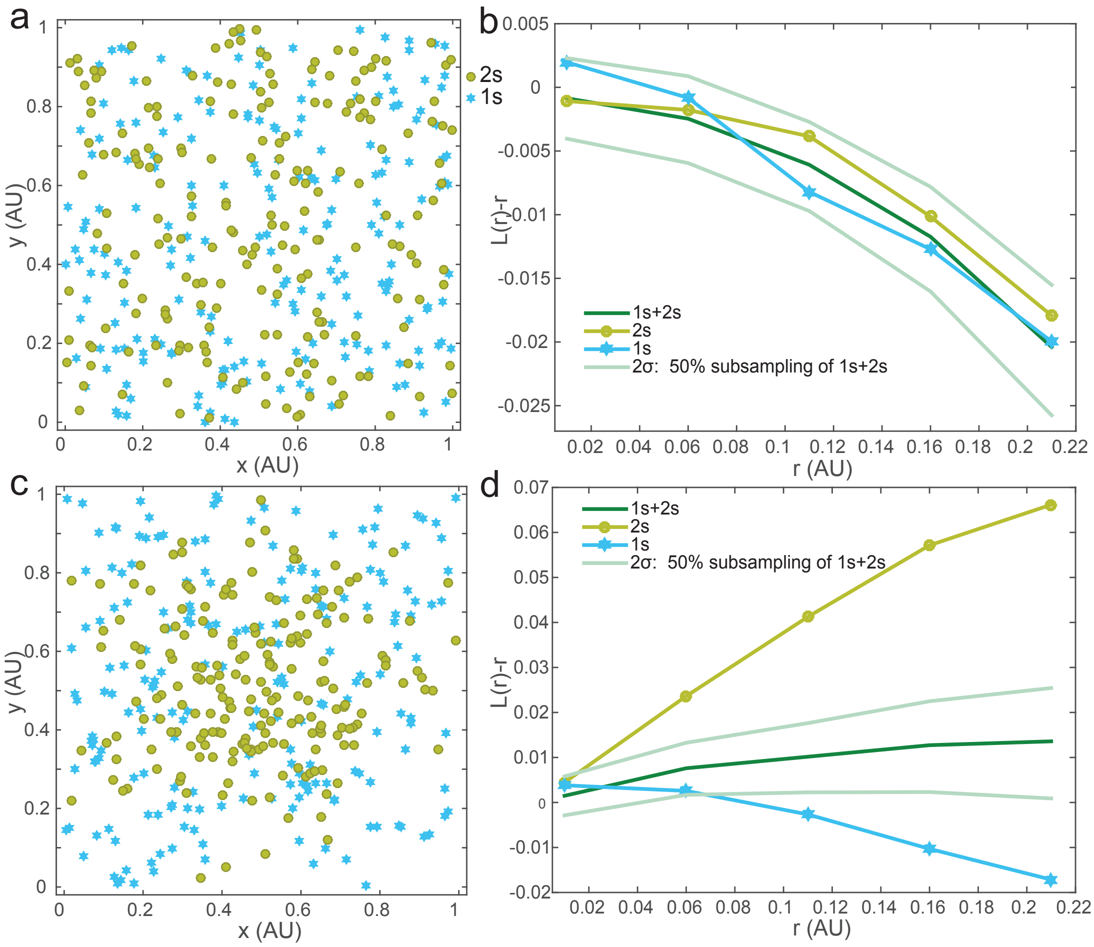

**Figure 4.8.** Identifying the applicability of random subsampling model,in the 2-redundant labeling sample (2x)

**a,c** Demonstrative point patterns corresponding to those proteins where only one fluorophore emits signal (1s, blue hexagons) and both emit signals (2s, green circles). **a** when both 1s and 2s are $p$-thinned subsamples of the same spatial distribution, **b** a case in which when they are not. In **a**, both point patterns are distributed uniformly at random, and in **b**, the 1s points are distributed uniformly at random, with the 2s points forming a Gaussian distribution in space. All four point patterns have same density (100 points in 1x1 $AU^2$ space). **b,d** L(r)-r functions corresponding to 1s, 2s and superimposition of 1s and 2s (1s+2s), along with the $2\sigma$ bounds corresponding to the subsampling of 1s+2s with a sampling factor .5, corresponding to a detection efficiency of .66. In the case when both are p-thinned subsamples of same point pattern the $L(r)-r$ values of 1s/2s point patterns are expected to lie within the $2\sigma$ bounds (with ≈ 95% probability), whereas in the case when they form different spatial distributions, the *p-thinning* assumption is not valid, and the $L(r)-r$ values could be outside the $2\sigma$ bounds. Note that the $L(r)-r$ values are estimated without an edge correction, for the ease of computation of $\sigma$, and hence the $L(r)-r$ values at large $r$ could be underestimated.

### Results and Discussion

The results of analysis can be found in Figure 4.12. The $L(r)-r$ function corresponding to both 1s and 2s point patterns fall within the bounds of p-thinning 1s+2s by $p = \frac{\#1s}{\#1s+\#2s}$ and $p = \frac{\#2s}{\#1s+\#2s}$ respectively, and the respective z-scores are within the bounds for a significance level of 5%. Therefore, the null hypothesis that the detection efficiency can be modeled as

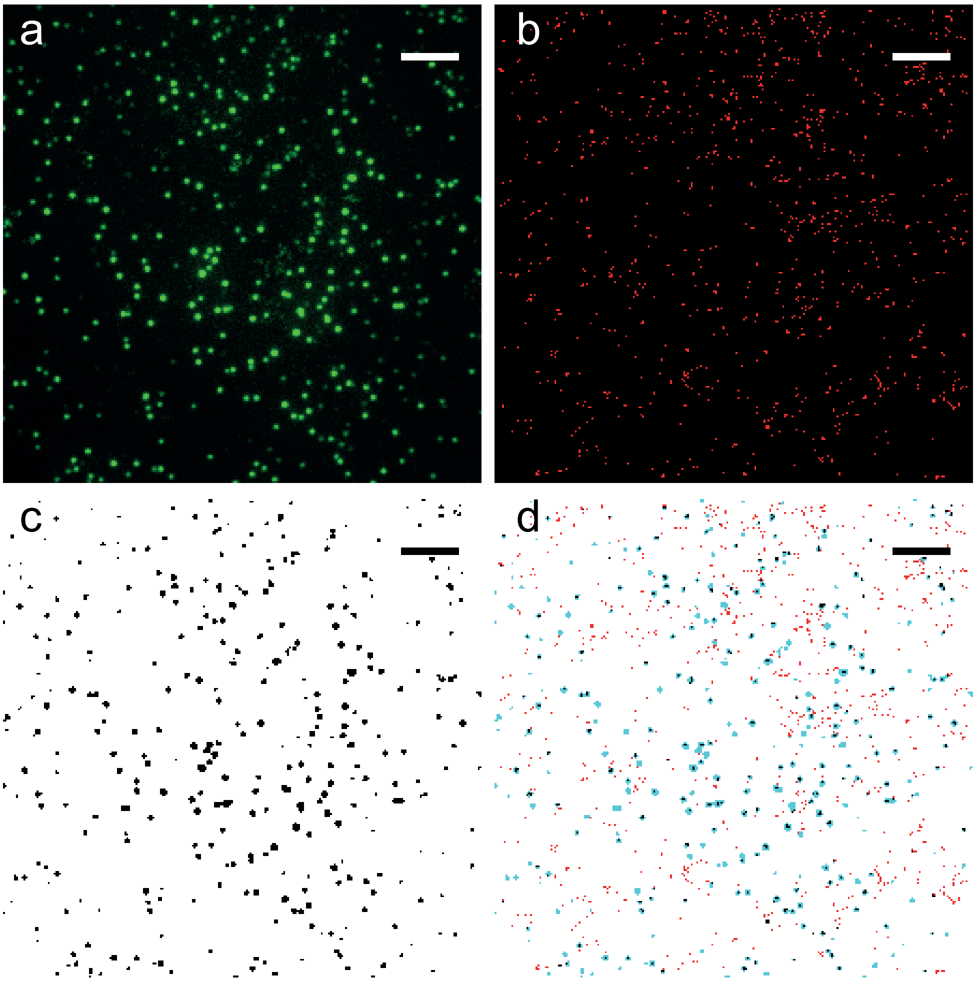

**Figure 4.9.** Green/red channel images of GlyR receptor complex
**a** On the green channel, the $\alpha$ subunits of GlyR are labelled with mCherry, and **b** on the red channel, the $\beta$ subunits labelled with mEos2 (scatter plot of PALM localizations). **c** Thresholded green channel image **d** co-localization (black) of thresholded mCherry image (cyan) and mEos2 localizations (red). Only the co-localized localizations were used for further analysis. Scale bar: 5um.

$p$-thinning cannot be rejected at this significance level. The spatial distribution of detection efficiency at the single fluorophore level appears to be soundly modeled with the $p$-thinning, i.e, the random, independent subsampling model.

While this points to the applicability of this assumption in the context of PALM imaging, and that of the methods described in Section 3.2.1, the validation approach using redundant labeling should be considered critically. The crucial source of error in such analysis is the accuracy in the identification of 1s and 2s point patterns. Errors due to fluorophore blinking, sample drift and single molecule diffusion, and spurious localizations due to low signal-to-noise ratio (SNR) or high background could be significant in the use of redundant labeling approach as a tool for single molecule level quantitative validation. In the datasets analyzed in the above sections, the effect due to blinking was minimized by applying the spatial-temporal threshold method. Errors due to sample drift and SM diffusion are also limited by the relatively short imaging time and also the use of the reference image in the green channel. The latter approach also helps minimizing the errors due to spurious localizations, along with the use of carefully tuned localization algorithm parameters, in

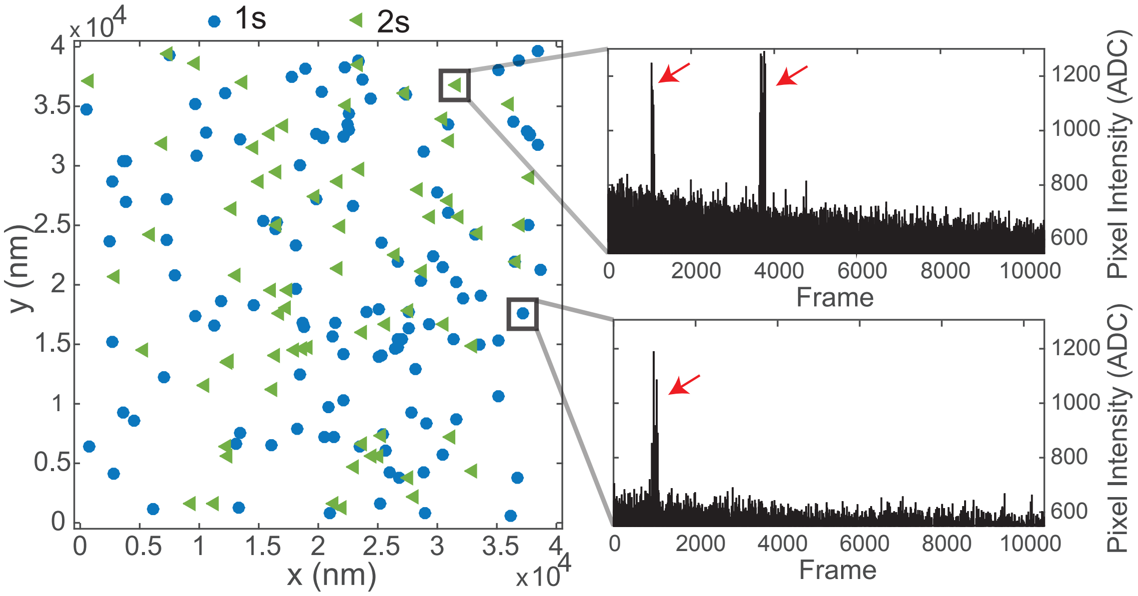

**Figure 4.10.** Identification of 1s and 2s point patterns
The localizations that co-localize with green channel image are further processed, and localizations with 1 or no neighbors within a radius $r_t$ =100nm are identified (and merged in the case of a neighbor) to get 2s(green arrows) and 1s(blue circles) point patterns respectively. The intensity in raw red channel image of sample point locations of identified point patterns corresponding to 1s and 2s point patterns are shown. The signals can be seen to be well separated in time.

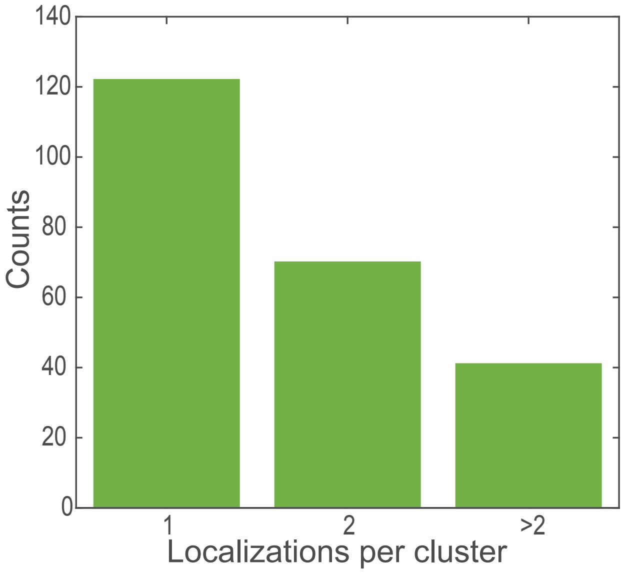

**Figure 4.11.** Histogram of counts
The histogram of counts corresponding to localizations with no neighbor (1s), with 1 neighbor (2s) and more than 1 neighbor within a distance of 100nm is shown.

the case when the density of localizations in the PALM dataset is relatively low.

Another possible source of error in such an approach is the algorithm used for categorization of the localizations into 1s and 2s datasets. The problem becomes complicated if the density of localizations is high – it becomes difficult to correctly choose subsets (with 1 or

2 members) of localizations and their membership in the categories, as multiple solutions are possible. The development and application of specialized, sophisticated classification algorithms, with notions of confidence intervals, can tackle this problem; along with the use of valid experimental controls.

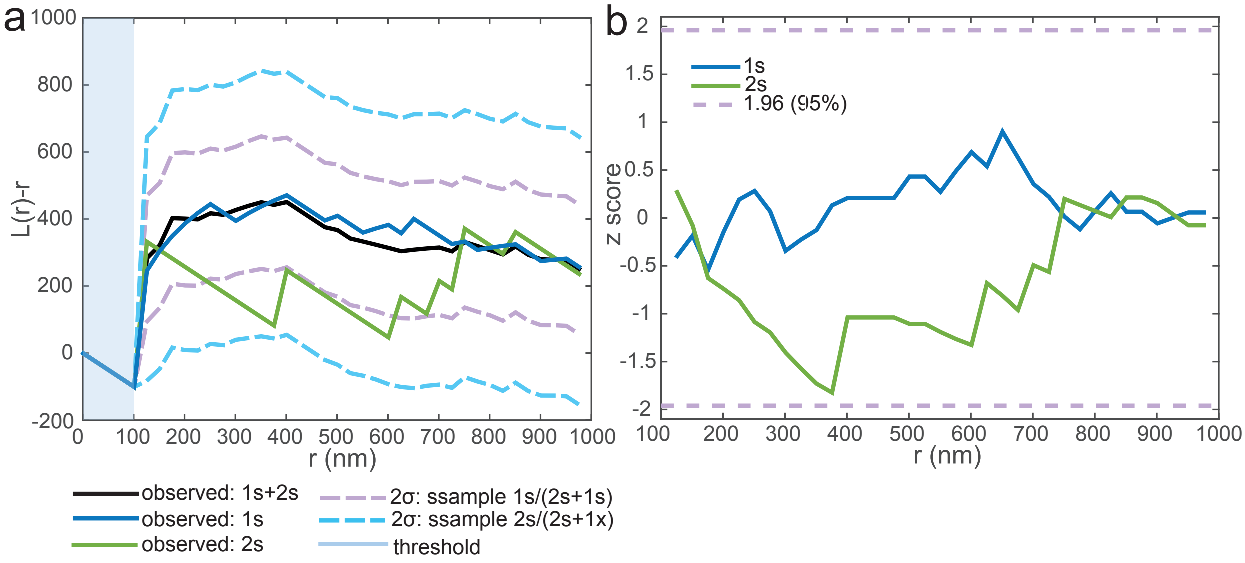

**Figure 4.12.** Comparison of $L(r) - r$ and z-score for 1s and 2s point patterns
It can be seen that the $L(r) - r$ curves for 1s/2s point patterns fall well within the bounds predicted for $p$-thinning of the 1s+2s point pattern, and the z-scores fall within the bounds for 95% confidence interval. Therefore, the null hypothesis of $p$-thinning cannot be rejected.

## 4.8 Conclusions

In this chapter, a mélange of analytical methods as well as applications to SMLM data were described, in the context of accurate quantitative spatial analysis. The work developed in this chapter clarifies several issues that are involved in quantitative cluster analysis of membrane proteins with SMLM, and provides solutions to some of them.

Section 4.2 describes a general framework for the estimation of true fluorophore locations from the clustered localizations with measurement error, given the true cluster model, in the lines of the method presented in Section 3.2.2. The method presented in Section 3.2.2 is exact in case the true clusters follow a Gaussian distribution, and is valid if such an approximation is sound. In the case of other cluster distributions (and localization uncertainty models), the framework in Section 4.2 provides the corresponding exact estimator.

While the method provides exact estimators given a true cluster model, and can be easily be applied in cases when such a model is available, such as in the case of single fluorophore blinking, and e.g., that of proteins internalized in a spherical shaped compartment, where a hard-core (i.e distributed uniformly at random in a sphere, whose radius is the hard-core) distribution could be plausible, it also prompts the question about the importance of the information about the true cluster model in this approach, especially because in several instances in the case of membrane proteins a simple spatial distribution cannot be expected to model the protein clusters accurately. This indeed is a very valid question, and is relevant to other methods that have been developed in the SMLM field, such as the PC-PALM method discussed in Section 4.6.

In general, if the underlying physical processes lead to specific spatial patterns that can be described by spatial models, such as in the case of SM fluorophore blinking or internalization in spherical shaped organelles, the methods developed can be easily adopted. The methods can be adapted in the case of continuum models as well. The approach could also be valid in case the empirically observed clusters can be described by robust spatial distribution models – even if a mechanistic explanation is absent. Such models could be identified, e.g., with the approach presented in Section 4.6, which can be developed further. Also, it might be possible to model the clusters with more complex spatial models, such as mixture models or non-parametric models, which can not only account for biological complexity, but also errors in the application of clustering algorithms in case of overlapping clusters. Models that describe a system with a stochastic distribution of parameters, such as cluster size, could also be applied. The validity and power of such approaches depend on the complexity of the system under hand. Significance tests, and confidence intervals for estimated parameters, could prove important in accurate identification of models and parameters. The methods, hereby described for 2D imaging, could be modified to the 3D case. 3D imaging ideally solves the problems associated with 2D projection of 3D structures: another approach would be to account for membrane undulations in the 2D models used.

The methods described in Section 4.2 and 4.6 is also predicated on accurate clustering of the observed data, so that clustering algorithm preserves the structure of the observed clusters. E.g., in the case of a long-tailed cluster distribution, inaccurate clustering might miss the (sparse) localizations occuring at the long tails, and this might bias the identification process. The challenge is lesser in the case if all competing distributions are short-tailed.

The analysis of the theoretical $r_a = \arg\max_r L(r) - r$ function in Section , which is an estimator of true cluster size described in membrane protein analysis literature, studies its dependency on the membrane protein models and its parameters. The study concluded that such dependencies might limit its applicability as an estimator, as it could be biased by the models and the parameters involved.

On the other hand, the work on limited detection efficiency and the summary statistics functions, described in Section 4.7 is independent of the true cluster models: it instead is concerned with the spatial distribution of probability of detection with SMLM, given a specific system. The results point to the applicability of the methods described in Section 3.2.1.

## 4.9 Acknowledgements

We thank Paolo Annibale for kindly providing the Dronpa data, Jayakrishnan Unnikrishnan for guidance and discussions and Melike Lakadamyali for providing the data on redundant labeling.

## Chapter 5

# High resolution correlative microscopy: Bridging the gap between Single Molecule Localization Microscopy and Atomic Force Microscopy

*This is a verbatim copy of an article that has been published in a peer reviewed journal: P. D. Odermatt, A. Shivanandan, H. Deschout, R. Jankele, A. P. Nievergelt, L. Feletti, M. W. Davidson, A. Radenovic, and G. E. Fantner. High resolution correlative microscopy: Bridging the gap between Single Molecule Localization Microscopy and Atomic Force Microscopy.* Nano Lett, *2015.* Published.

### Abstract

Nanoscale characterization of living samples has become essential for modern biology. Atomic Force Microscopy (AFM) creates topological images of fragile biological structures from biomolecules to living cells in aqueous environment. However, correlating nanoscale structure to biological function of specific proteins can be challenging. To this end we have built and characterized correlated SMLM (Single Molecule Localization Microscope)/AFM that allows localizing specific labelled proteins within high-resolution AFM images in a biologically relevant context. Using direct Stochastic Optical Reconstruction Microscopy (dSTORM)/AFM, we directly correlate and quantify the density of localizations using both imaging modalities along (F-) actin cytoskeletal filaments. In addition, using Photo Activated Light Microscopy (PALM)/AFM, we provide correlative images of bacterial cells in aqueous condition. Moreover, we report first correlated AFM/PALM imaging of live mammalian cells. The complementary information provided by the two techniques opens a new dimension for structural and functional nanoscale biology.

## 5.1 Correlative SMLM-AFM

Observing nanoscale structural changes associated with many cellular processes is essential for understanding the complex mechanisms underlying biomolecular function. Performing the experiments in aqueous environments is essential for maintaining cellular integrity. At the nanoscale, the two imaging modalities Atomic Force Microscopy (AFM) and Single Molecule Localization Microscopy (SMLM), fulfil the requirement of concomitant assessment of structure and dynamics under close to physiological conditions. AFM has long since provided nanoscale structural information on living cells (Henderson et al., 1992;

Dufrene et al., 1999; Rotsch et al., 1997). Recent advances in high-speed AFM have even been successfully used to directly visualize the dynamics of molecular machinery such as protein motors (Kodera et al., 2010; Ando, 2012). In addition, newly emerged Single Molecule Localization Microscopy (SMLM) techniques extended all the advantages of fluorescence microscopy beyond its diffraction limited spatial resolution of about 200 nm (Betzig et al., 2006; Rust et al., 2006; Hess et al., 2006) and provided new important insights into structural organization (Xu et al., 2013; Szymborska et al., 2013), dynamics (Shroff et al., 2008) and quantification (Annibale et al., 2011b, 2012; Durisic et al., 2014a) of biomolecules. Both techniques by themselves have proven to be very powerful for research in nanoscale structural biology. However, in SMLM, biomolecules themselves are invisible and one observes/localizes only the fluorophores. In addition, translating the SMLM localization precision, typically between 10 and 25 nm, into spatial resolution is still very challenging due to a number of complicating factors (Nieuwenhuizen et al., 2013). Therefore, early on, the validation of SMLM has been carried out with correlative imaging using Transmission Electron Microscopy (TEM) (Betzig et al., 2006). Yet, in the case when SMLM is correlated either with TEM (Betzig et al., 2006; Chang et al., 2014) or Scanning Electron Microscopy (SEM) (Kopek et al., 2013; Monserrate et al., 2014), sample preparation conditions are far from physiological prohibiting the observation of live processes. Structural artefacts might as well be introduced unless one performs experiments on vitrified samples as Chang et al (Chang et al., 2014).

AFM on the other hand has proven to obtain sub-molecular resolution on membrane proteins in solution (Muller et al., 1995), but it fails at providing biomolecular specificity. In combination, AFM and SMLM hold promise for doing correlated nanoscale biomolecular and structural characterization on living samples in physiological conditions.

Nevertheless, the first attempts to correlate AFM with SMLM (Monserrate et al., 2014) have not fully exploited this opportunity. For example, Monserrate et al. (2014) performed AFM imaging of DNA in air dried down on a mica substrate. While this approach allows a nice comparison of the two techniques, it does not allow for the two techniques to complement each other to learn new things about structure-function relationships in living systems. In addition, the presence of the thin mica sheet on the glass coverslip deteriorated the Point Spread Function (PSF) and compromised the performance of SMLM. Although Chacko et al. (2013) employ both modalities in physiological conditions, their samples were chemically fixed.

In order to exploit the full potential of high-resolution correlative AFM/SMLM imaging, one has to maintain optimal performance in both imaging modalities. This requires careful design of experimental procedures so that the two methods do not deteriorate each other's performance. In particular, during AFM imaging, maintaining low imaging forces is essential to ensure minimal damage to the soft biological samples in fluid. At the same time, one has to maintain a low level of noise that should not be compromised by the integration with the SMLM optical microscope. To this end, we have built a mechanical support structure to hold the AFM in place without it mechanically contacting the microscope body( Figure 5.1). Simultaneously, in SMLM it is important that the fluorescent labelling strategy minimally affects the 3D structure of the sample. Due to this requirement, from the plethora of labelling/imaging strategies we have chosen dSTORM (direct stochastic optical reconstruction microscopy) and Photo Activated Light Microscopy (PALM). In dSTROM, the light-induced reversible photoswitching of organic fluorophores is obtained in the presence of millimolar concentrations of reducing thiol compounds such as dithiothreitol (DTT), glutathione (GSH), or mercaptoethylamine (MEA), but without requiring the presence of an activator fluorophore in aqueous buffer (Heilemann et al., 2008). In particular, using fusion proteins or intercalating small molecules such as fluorescently labelled phalloidin, allowed us to completely avoid antibodies that would have otherwise significantly altered the sample's 3D structure. Also, after ensuring that the laser used by the AFM to detect the cantilever motion does not overlap with the fluorophore excitation spectra, only a sub-set of fluorophores is available for correlated microscopy. The purpose of correlated AFM-dSTORM microscopy can be twofold; first to compare and validate the resolutions of the one technique with the other, and second to provide complementary information about two different aspects of the same biological sample. To establish accurate correlation and measurement protocols, we chose F-actin as a first test sample, since high-resolution images of F-actin have been reported in both imaging modalities. Monomers in actin filaments are very weakly bound since they have to be dynamically assembled and disassembled in the cell. Even after stabilization by phalloidin they are very delicate. AFM imaging of actin filaments in physiological buffer therefore requires excellent force control to image at high resolution without destroying them (Schmitz et al., 2010). This makes them an excellent test sample to ensure high quality AFM performance. Actin is also one of the best studied structures with SMLM both in vitro (Metcalf et al., 2013) as in vivo (Xu et al., 2012). For direct comparison of the two techniques we imaged polymerized actin filaments on a glass cover slip. The sample preparation procedure was designed to meet the requirements of both techniques. Fluorescently labelled phalloidin was used to prepare the sample for SMLM as well as for AFM, although not strictly required in the latter case. The glass coverslip was functionalized with APTES ((3-Aminopropyl)triethoxysilane) to adhere the actin filaments as required for AFM and SMLM imaging. Both imaging modes were performed in buffer, however each technique requires its own. While the SMLM experiment requires a buffer optimized for blinking of the corresponding fluorescent dye, the AFM requires a buffer which ensures structural integrity and stability. The best image quality by AFM was obtained using soft cantilevers (BL-AC40TS-C2 cantilevers (Olympus)) with a nominal spring constant of 0.09 N/m operated in peak force tapping keeping the force setpoint below 100 pN to not destroy the filament. Figure 5.2a shows a high resolution AFM image of the F-actin revealing the 36 nm periodicity of the single left handed generic helix (Dominguez and Holmes, 2011). The spacing of the individual G-actin monomers can be seen in the cross section (Figure 5.2c), which is equivalent to the highest resolution AFM images of F-actin published thus far (Schmitz et al., 2010). The height of F-actin as obtained by AFM was as expected between 6-8 nm and a crossection revealed a full width at half maximum (FWHM) height of about 10 nm (Figure 5.2d). This result demonstrates that the performance of the AFM is not deteriorated by the fact that it was recorded on the combined SMLM/AFM system.

To assess the image quality obtained by SMLM on this combined system, we imaged F-actin labelled with phalloidin-alexa647, since alexa647 dye has been reported to give optimal SMLM image quality (Dempsey et al., 2011). Figure 5.2e shows a dSTORM image with a mean photon count of about 5500 (Figure 5.6a) and a mean localization precision of 12.5 nm, comparable to the values reported in the literature(Dempsey et al., 2011). Actin filaments that have a cross-section profile with a full width half maximum (FWHM) of ≈ 24nm are visible (Figure 5.2e-g). Our measurements demonstrate that a high image quality is obtainable by both techniques individually even when performed on the combined instrument.

The procedure for correlated image acquisition is depicted in Figure 5.3a through h. Since alexa647 emission deteriorates after exposure to the AFM laser (Figure 5.7a-c) phalloidin-atto488 was used instead to label F-actin for the correlative experiment. This significantly reduced the bleaching of the dye, although some bleaching still occurs (compare Figure 5.3b & e), but also reduced the photon count and therefore the ultimately achievable localization precision. We recorded the AFM image before recording the dSTORM image, since the dSTORM seemed to degrade the structural integrity of the actin filaments (for details see Figure 5.15). By minimizing the AFM peak forces to as low as 50 pN, the sample remained intact for the subsequent dSTORM image acquisition, which is a prerequisite for recording correlative images. After the AFM image was recorded, the buffer was exchanged and phalloidin-atto488 was forced into a triplet state by means of the chemical reducing agent NaBH4 (Figure 5.3f). Subsequently, the reducing agent was washed and the buffer exchanged with the dSTORM imaging buffer containing an oxide scavenging system to ensure optimal blinking behaviour. Then, the dSTORM image was acquired (Figure 5.3h). Figure 5.3i through k show the resulting AFM images and the dSTORM image, with the squares in Figure 5.3i & j indicating the areas where AFM images were taken. Similar results are displayed in Figure 5.8. The effects of various forms of aberrations, primarily spherical aberrations in SMLM (Annibale et al., 2012), are minimized by performing accurate transformation and overlay (detailed in the Supporting information and Figure 5.9). The correlative images allow comparison as well as provide complimentary information about the sample. Comparing the width of the actin bundles as measured by AFM and by dSTORM, we find that dSTORM provides comparable values to AFM. On the ability to distinguish two diverging bundles of filaments, AFM provides clearer information than dSTORM (Figure 5.4a-c). The height and width of the actin filament bundles measured by AFM was 14 nm and 65 nm FWHM respectively. The FWHM of dSTORM was 94 nm and of TIRF 271 nm for the filament bundles. In addition to direct comparison, the two techniques provide complimentary information about the sample. The dSTORM image reveals a non-homogeneous intensity along the filament which is often attributed to local differences in labelling along the filament. The correlated AFM measurements however suggest that the fluctuation in localization densities is partially due to the presence of actin bundles rather than single filaments. The tendency of F-actin filaments to bundle up(Ikawa et al., 2007) therefore likely contributes to the local differences of localizations recorded by dSTORM along the filament (Figure 5.4h). We indeed observe a correlation between the height of the F-actin and the number of localizations recorded at that particular location (Figure 5.4i). Along a single filament with a height of around 8 nm about 8 localizations are detected per line scanned by AFM (corresponding to 12 nm in length). On the other hand, in areas where an increased height was measured ( 12-14 nm) the number of dSTORM localizations is 1.5 times higher than observed on a single filament.

After correlation protocols have been established we used the combination of the AFM and SMLM to extract complementary information about two different aspects of one and the same biological sample. For this we extended our method to samples including chemically fixed bacterial cells (Figure 5.4j) and mammalian cells (Figure 5.11). *Escherichia coli* (*E. coli*) expressing the fusion protein RNP-mEos2 was measured by AFM and subsequently by PALM. We chose PALM over dSTORM for these experiments since PALM can be performed with lower laser power, which is better suited for eventually extending the technique to live cell imaging. The AFM provides the 3D morphology of the bacteria, while PALM provides the expression level and the 2D projection of the spatial distribution of the fusion protein. Interestingly, one of the bacteria showed no presence of the fusion protein in part of the PALM image. The AFM image clearly shows the fact that this bacterium is situated slightly on top of two other bacteria. We hypothesize therefore that the fusion proteins of this particular bacteria were not mapped because the bacterium was out of the illumination volume covered in TIRF conditions. This is a good example where the combination of the two techniques yields a clearer interpretation of the microscopy data than PALM alone. However, the conventional PALM we use, does not provide 3D information of the location of the fluorescence signals with respect to the morphology of the cell. Recent advancements in 3D PALM(York et al., 2011) would further leverage the power of the correlated technique.

The same technique can be applied to correlated AFM/PALM measurements on mammalian cells. Figure 5.11 shows a fixed mouse embryonic fibroblast expressing the fusion protein paxillin-mEos2, which is part of the focal adhesion complexes that form contact with the substrate. Performing SMLM and AFM measurements co-localized within biologically relevant media not only allows for direct comparison of the two techniques, but also allows us to learn more about each individual technique and to augment the weaknesses of one with the strength of the other. In the case of the actin filaments, AFM provided a reference for the location and height of the filaments that could be directly compared to the labelling density fluctuations along the filaments as observed by SMLM. This showed that the labelling fluctuations originate partially from the presence of double and triple filaments (Figure 5.4h & i), and is therefore not solely due to insufficient labelling as it was incorrectly assumed. On the other hand, in areas along the filament revealed by AFM to be a single filament, the fluctuations can now be unequivocally attributed to insufficient binding of tagged phalloidin. This dual information makes the comparison between different labelling protocols much more effective and accurate. On the other hand, the fact that the number of localizations per scan-line correlates well with the AFM height (and therefore the number of filaments), suggests that the localization intensity could eventually be used for quantifying the number of actin filaments in a bundle in situations where no AFM information can be obtained such as in whole cell imaging.

Thus far, we have chosen our sample so that a direct comparison of the two techniques is possible and we also showed the potential of revealing complementary information in fixed bacteria and mammalian cells. Now that the correlation between the two techniques has been established, they can be reliably used to complement each other in applications where the protein specific SMLM information has to be put in a 3D cellular or mechanical context. This will be especially important for the recent and on-going developments in 3D SMLM (Huang et al., 2008; Pavani et al., 2009; Shtengel et al., 2009; Abrahamsson et al., 2013). Since we perform our AFM experiments in physiological solution, it is even possible to perform live cell imaging and nanomechanical stimulation using the AFM cantilever. Using the combination of live cell AFM (Rotsch et al., 1999; Colom et al., 2013; Dufrene et al., 2013) and live cell SMLM (Shim et al., 2012), one could observe the reaction of the cells to nanomechanical stimuli with unprecedented resolution. A major concern for live cell imaging is the image acquisition speed of both SMLM and AFM, as they both traditionally require 10s of minutes to obtain a high quality image. With the development of high speed AFM by Ando et al. (Kodera et al., 2010) and the pioneering work in high-speed SMLM by Zhang et al. (Shim et al., 2012; Jones et al., 2011), real time nanoscale imaging of living cells is within reach. Our combined AFM-SMLM system is already capable of such experiments since live cell PALM has already been reported11, and the AFM we used is capable of imaging live cells within a minute or less (Slade and Minne, 2014). Figure 5.5 shows such time resolved AFM and PALM image sequences of live CHO-K1 cells in physiological environment. From the whole cell shown in Figure 5.5a, we chose the leading edge (upper corner) for time resolved analysis (Figure 5.5b & c). AFM images (Figure 5.5b) were recorded at 1-minute intervals showing filopodia already extended with subsequent following of the lamellipodium. PALM images shown in Figure 5.5c were recorded directly after AFM imaging and the cell edge from the last image in the AFM sequence is shown for reference in the PALM images. Fluorescent frames were recorded at a rate of 20 frames/s and processed 5000 at a time with a “running average” of 1000 frames to create each PALM image (see methods, Figure 5.16 and Supporting movie 1 for details). Figure 5.5d-g show zoom-ins of regions depicting paxillin clusters in focal adhesions. In d and e a paxillin cluster disappears at one place while in f and g new ones appear.

The dynamic changes we observed in both the AFM and PALM images and the complementary information they provide demonstrate the potential of correlated AFM/PALM imaging of live cells. It should be noted that in these experiments the AFM and PALM data were recorded in a correlated fashion, but not simultaneously. A better integration of the AFM operating software with the PALM acquisition software would allow for truly simultaneous imaging. While many of the experimental conditions for routine experiments still have to be worked out, we expect this to become a truly enabling method in the study of mechanobiology and mechanotransduction (Ingber, 2006; Wang et al., 2008).

## 5.2 Materials and methods

### 5.2.1 Choice of labelling strategy

What fluorescent labelling strategy is best suited for the experiment depends on the kind of correlated experiment that is performed. In the case of the actin filaments we imaged the same aspect of a sample with both modalities. In that case it is imperative that the fluorescent labelling does not interfere with the sample structure as measured by AFM. In such a case it is preferential to use a small intercalating dye such as fluorescently labelled phalloidin. When one images different aspects of a sample with the two techniques (such as we did in the combined imaging of cells), a broader choice of labelling strategies is available such as antibody labelling or genetic expression of fluorescent fusion proteins. We chose the latter for live cell imaging as it allows for labelling of intracellular structures without permeabilizing the cell membrane. In all cases, it is essential however that the AFM laser does not bleach the flurophores.

### 5.2.2 F-actin

F-actin has been polymerized from G-actin following the manufacturer's protocol (BK003, Cytoskeleton, Inc.) and stored on ice subsequently. Then, 5 ul of G-actin aliquot (200 uM) 45 ul pre-chilled general actin buffer was added, ending up with 20 uM G-actin in 5 mM Tris-HCl pH 8.0, 50 mM KCl, 0.2 mM CaCl2. Next, 5 ul of 10x polymerization buffer was added, resulting in a final concentration of 50 mM KCl, 2mM MgCl2, 1 mM ATP, and incubated at room temperature to polymerize for 2 hours before storing on ice. Actin was stored up to one month.

### 5.2.3 E.coli

*E. coli* bacteria expressing RNA polymerase labelled with mEos2 (Endesfelder et al., 2013) are kindly provided by Dr. Mike Heilemann. The bacteria were grown in lysogeny broth (LB) medium supplemented with ampicillin (0.1 mg/ml) at 37 ° C in an orbital shaker overnight. Then, 100 ul of bacteria solution was added to 4 ml fresh medium and incubated again for 3 hours. Subsequently, 1 ml was pelleted by centrifugation and the supernatant was discarded. The pellet was resuspended in deionized water and the washing step was repeated once more. The pellet was eventually resuspended in 400 ul deionized water and used for subsequent sample preparation on the prepared glass coverslip.

### 5.2.4 Glass coverslip

25mm diameter round glass coverslips (72225-01, Electron Microscopy Sciences) were cleaned by piranha etch (H2SO4 and H2O2 at a ratio of 2:1) on a heating plate for at least 20 minutes and then left to cool down. Then, the coverslips were thoroughly rinsed with water and blown dry by a nitrogen stream. On coverslips prepared for the F-actin sample, 500 ul water (milliQ) containing 0.5% (v/v) APTS (440140, Sigma-Aldrich, Switzerland) was deposited and incubated for 10 minutes before rinsing with water. Coverslips were then dried at 65 ° C for 1 hour in vertical position. Coverslips were prepared fresh on the day of the experiment. Cleaned coverslips used to deposit *E. coli* were immersed for 10 minutes in a solution containing 0.05 mg/ml poly-L-lysine hydrobromide (Sigma, P1524) and

10 mM Tris at pH 8. Coverslips were then dried in a vertical position at room temperature overnight and used within a week. Cleaned and coated coverslips were glued into a custom made holder before the respective sample was deposited.

### 5.2.5 Sample deposition and Imaging Buffers

F-actin samples were prepared as follows: 3 ul phalloidin-alexa647 (A22287, Life Technologies) or phalloidin-atto488 (49409, Sigma-Aldrich, Switzerland) and 1 ul polymerized F-actin was added to 45 ul Buffer A (2 mM MgCl2, 1 mM EGTA, 20 mM Imidazole-HCl, pH 7.6) and incubated in darkness for 10 minutes. Then 100 ul Buffer A was added and 50 ul of this were deposited on a coverslip. Another 150 ul Buffer A was added to the sample and incubated for 5 minutes. Additionally, up to 1 ml of Buffer A was added for AFM experiments. *E. coli* samples were prepared as follows. A drop of concentrated bacteria solution was deposited onto the coated coverslip and bacteria were left to adhere for 30 minutes before the coverslip was gently washed with water. After imaging by AFM, the sample was washed with PHEM buffer (60 mM Pipes, 25 mM HEPES, 10 mM EGTA, and 2 mM MgCl2 at pH 6.9) and fixed with 4% paraformaldehyde in PHEM buffer for 30 minutes without changing the position of the sample. Subsequently, the sample was washed with PHEM buffer 3 times and PALM images were acquired.

### 5.2.6 CHO-K1 cells

CHO-K1 cells were grown in an incubator at 37 ° C, 5% CO2 in DMEM-F12 supplemented with 10% (vol/vol) FBS and 1% antibiotics to 70% confluency prior to transfection. 4 x 105 cells were transfected with 2 ug of plasmid DNA containing the paxillin-meos2 sequence with the Neon electroporation system. Cells were then seeded in a 6 well plate with DMEM supplemented with FBS only. The following day they were transferred onto plasma cleaned fibronectin coated 25 mm diameter glass coverslips and grown for another 2 to 24 hours. Prior to the experiment the cells on the coverslip were transferred on a home-built coverslip heater shown in Figure 5.14 to keep them at 37 ° C and the medium was exchanged to DMEM without phenol red buffered with 25 mM Hepes. As imaging took less than 35 minutes it was not necessary to have a controlled CO2 environment. For longer term imaging we suggest putting a CO2 cage around the sample including the AFM, or use the commercially available perfusion chamber for the FastScan Bio AFM.

### 5.2.7 AFM

AFM experiments were conducted with a Dimension FastScan (Bruker, USA) mounted on a custom-built support structure on top of an inverted optical microscope (IX71, Olympus, Japan). BL-AC40TS-C2 cantilevers (Olympus, Japan) with a nominal spring constant of 0.09 N/m and a resonance frequency of 110 kHz were used to image the F-actin samples. Images were taken in PeakForce QNM mode at a maximal force ¡ 100 pN, at a resolution of 512 x 256 pixels. *E. coli* samples were imaged using Scanasyst-Fluid cantilevers (Bruker) with a nominal spring constant of 0.7 N/m and a resonance frequency of 150 kHz. For the live-cell experiment on CHO-K1 cells Fastscan-D cantilevers (Bruker) with a nominal spring constant of 0.25 N/m and a typical resonance frequency in water of 110 kHz were used. Images were taken in tapping mode at a resolution of 512 x 128 and a frame rate of 1 min-1. AFM data was processed with standard SPM software. Figure 5.12 displays 2D AFM height images of the 3D representations shown in the main figures. The reconstruction of the tip used in Figure 5.3 as obtained by the software Nanoscope Analysis (Bruker, USA) is shown in Figure 5.13. More details are provided in the text of the Supporting material.

### 5.2.8 dSTORM

For the imaging with alexa-647, the sample was imaged in the buffer conditions described in Olivier et al. (2013). 2 ml of buffer (pH 7.5) was composed of: 1.685 ml PBS, 200 ul Tris (100 mM pH 7.4), 20 ul of 1M mercaptoethylamine stock pH 8 (MEA, Sigma; pH adjusted with glacial acetic acid 100%), $\beta$-mercaptoethanol 7 ul (M6250, Sigma), 20 ul of 200 mM cyclooctatetraene (COT) stock made of 1.27 ml of DMSO and 30 ul of COT (Sigma), 50 ul of 100 mM protocatechuic acid (PCA, Sigma) at pH 9 (adjusted with KOH) and 20 ul of 5 uM protocatechuic dioxygenase (PCD, Sigma) stock stored in 50% glycerol in 50 mM KCl, 1 mM EDTA and 100 mM Tris-HCl pH 8. For the correlative imaging with ATTO-488, the following protocol was used. After AFM imaging, the sample was washed 3x with PBS, leaving 300 ul PBS. 600 ul PBS containing 0.5 mg/ml NaBH4 was added to a final concentration of 10 mM NaBH4 and incubated for at least 5 minutes or until the fluorescence was quenched. Then the sample was washed with Tris / Trolox buffer pH 8 (100 mM Tris, 1 mM Trolox), leaving 250 ul buffer on the sample. Next, 750 ul buffer containing glucose, catalase and glucose oxidase was added, resulting in a final concentration of 0.5 mg/ml glucose oxidase, 40 ug/ml catalase and 5% (w/v) glucose. Additionally, 3 ul of 100 nm fluorescent beads (Tetraspeck, Life technologies) was added to the sample. The dSTORM measurements were performed with a TIRF objective (APON 60X TIRF, Olympus, after a further magnification of 2X, yielding a pixel size of 133 nm) and appropriate optical filters (Dichroic: F73-866; Emission filter: F72-866, AHF Analysetechnik AG, Germany). Illumination was provided by a monolithic laser combiner (MLC400B, Agilent, UK) and the optical fiber output of the MLC400B was coupled into an optical system (TIRFM Illuminator, Olympus, Japan) in order to generate TIRF illumination. Images were recorded with an iXon Ultra 897 (Andor) EMCCD camera. The power of the 488nm laser at the fiber output was set to 80 mW and that of the 647 nm laser at a maximum of 140 mW, the gain of the EMCCD camera was set to 200 and images were taken at an exposure time of 20 ms.

### 5.2.9 PALM

The fixed MEF cells were imaged in PHEM buffer at room temperature. The live CHO-K1 cells were imaged in 25mM Hepes buffered DMEM at 37 ° C. More details can be found in the Supporting material. The PALM measurements were performed with the same set-up as described in the dSTORM section. The emission light coming from mEos2 was separated from the illumination light using a combination of a dichroic mirror (493/574 nm BrightLine, Semrock) and an emission filter (405/488/568 nm StopLine, Semrock). An optical system (DV2, Photometrics) equipped with a dichroic mirror (617/73 nm BrightLine, Semrock) was placed between the EMCCD camera and the microscope frame. The DV2 splits the emission light from the on- and off-state of the mEos2, and sends each colour to a separate half of the EMCCD camera chip. In order to find a cell in the sample, the mEos2 in the off-state was visualized in the green channel by excitation of 488 nm with 5 mW power at the MLC400B output. Before imaging of the mEos2 in the on-state, fiduciary beads (100 nm gold nanospheres, Corpuscular) were added to the sample. The gold beads that did not sediment after 5 min are removed by washing 1x with PHEM for the MEF cell experiment. Imaging of the mEos2 in the on-state was performed in the red channel by excitation of 561 nm with 30 mW power at the MLC400B output. During imaging, the mEos2 in the off-state was activated by 405 nm with a gradually increasing power at the MLC400B output, ranging for 0 mW to 2 mW. The gain of the EMCCD camera was 200 and the exposure time was 50 ms.

### 5.2.10 Reconstruction

The estimation of the single molecule positions from the images and the rendering as a probability map were done by the code (MATLAB, MathWorks) kindly provided by Dr. Eric Betzig, using the same algorithm described in Betzig et al. (2006). The localization precision was estimated by means of the expression provided in Mortensen et al. (2010), also incorporating the precision loss due to the use of the EMCCD camera. The factor to convert ADC values to photon counts was calibrated as explained elsewhere (Janesick, 2001). The drift during imaging was corrected using either fiducial marker traces or using the correlation between frames (Ovesný et al., 2014). The dSTORM image displayed in Figure 5.2 was obtained from 16000 frames of imaging, and the one in Figure 5.3 & Figure 5.4 from 60000 frames. For Figure 5.2, only localizations with a precision between 2 nm and 30 nm, and a photon count between 300 and 50000 were considered. For Figure 5.3 & Figure 5.4, a localization precision cut-off of 50 nm and a minimum photon count of 100 were used. The PALM image displayed in Figure 5.4j was obtained from 62000 frames of imaging, and that in Figure 5.11 from 27000 frames. Localizations in both images were plotted if the corresponding mEos2 image contained at least 100 photons and if the localization precision was between 3 and 30 nm. The PALM time sequence (Figure 5.5c & Supporting movie 1) was obtained from 14000 frames of imaging, with each individual PALM image in the sequence obtained from a subset of 5000 frames. The time sequence was obtained by shifting 1000 (Supporting movie 1) frames of imaging between each PALM image (for details see Figure 5.16). In Figure 5.5c selected frames of the sequence are shown. Only mEos2 localizations with a precision between 2 and 40 nm and a photon count of at least 100 were plotted.

### 5.2.11 Overlay

Overlay between the AFM image and the STORM localizations was done by estimating an affine transformation matrix between the two by minimizing a cost function based on the overlap between the two images. More details are provided in the text of the Supporting material.

## 5.3 Acknowledgements

This work was financially supported by FNS grants No. 200021–125319, No. 20021–132206, No. 205321-134786 and No. 205320-152675 as well as the European Union's Seventh Framework Program FP7/2007-2011 under grant agreement 286146 and FP7/2007-2013/ERC grant agreement 307338. A. Shivanandan was funded by a PhD fellowship grant from NCCBI. We thank Dr. P. Annibale for initial help with the instrument. We thank Lina Carlini for discussion, Prof. Mike Heilemann on the generous gift of bacterial strain expressing mEos2-RNAP and Prof. Nicolas Mermod for providing CHO-K1 cells.

## 5.4 Author contributions

A.R. and G.E.F. conceived the project. P.D.O. with the help of G.E.F. and A.P.N built the instrument. L.F prepared the in vivo specimens. A.P.N. designed and built the coverslip heating holder. R.J. and P.D.O. developed the protocol for actin filament sample preparation. A.S optimized the STORM imaging protocol and implemented and performed the dSTORM/AFM overlay. P.D.O and A.S. performed the dSTORM/AFM imaging experiments and analysed the data. P.D.O and H.D performed the PALM/AFM imaging experiments and analysed the data. P.D.O., A.R., and G.E.F. wrote the manuscript with inputs from A.S and H.D.

## 5.5 Supporting Information

### 5.5.1 MEF cell sample preparation

The mouse embryonic fibroblast (MEF) cells are kindly provided by Dr. Luca Scorrano, and the mEos2-paxillin-22 vector is kindly provided by Dr. Michael Davidson. The MEF cells are grown in DMEM supplemented with 10% fetal bovine serum, 1% penicillin-streptomycin, 1% non-essential amino acids and 1% glutamine, at 37 ° C with 5% CO2. A 25 mm diameter round cover slip (# 1.5, Electron Microscopy Sciences) is prepared by first treating it with an oxygen plasma for 5 min and then incubating it with PBS containing 50 ug/ml fibronectin (bovine plasma fibronectin, Invitrogen) for 30 min at 37 ° C. To remove the excess of fibronectin, the cover slip is washed 1x with PBS. The cells are transfected by electroporation (Neon Transfection System, Invitrogen). The electroporation is performed on ≈500,000 cells using 2 ug of DNA, using 1 pulse of 1350 V with a width of 35 ms. The transfected cells are seeded on the cover slip and grown in DMEM supplemented with 10% fetal bovine serum, 1% non-essential amino acids and 1% glutamine, at 37 ° C with 5% CO2. At least 24 h after transfection, the cells are washed 1x with PHEM (60 mM Pipes, 25 mM HEPES, 10 mM EGTA, and 2 mM MgCl2 at pH 6.9) and fixed by incubating them in PHEM with 4% paraformaldehyde at 37 ° C for 30 min. After removing the fixative, the cells are again washed 3x with PHEM and the cover slip is glued into a custom made holder that is positioned on the microscope stage.

### 5.5.2 Imaging procedure

AFM images were then recorded using the Dimension Icon head (Bruker) in peak force tapping mode. Lever A of a Hydra-All-G cantilever (AppNano) with a nominal spring constant of 0.292 N/m was used. Images were recorded at a line rate of 0.5 Hz and a pixel resolution of 512x256.

### 5.5.3 Overlay between AFM and STORM images

Both AFM and STORM imaging can involve various forms of aberrations. This is especially pronounced in the case the optical aberrations in STORM imaging. Correlative imaging therefore should account for these. Additionally, since the images are not necessarily of exactly the same size and of the same region (our STORM images typically cover a larger field of view than the AFM image), accurate overlay also involves the matching of structures in the image. We approximate the net effect of these as an affine transformation of STORM localizations. We then estimate the transformation parameters from data to obtain the more accurate overlay. The 2D affine transformation can be described as $x' = Ax + By + T_x$ and $y' = Cx + Dy + T_y$, where $x'$ and $y'$ are the coordinates obtained by the transformation of the original $x$ and $y$ coordinates (STORM localizations); $A, B, C$ and $D$ are lumped parameters that can cause scale, shear and rotation operations; and $T_x$ and $T_y$ are translation parameters. We estimate these parameters by the optimization of the overlap between the structures in the STORM and AFM images. The cost function for optimization is computed based on the total number of the affine-transformed STORM localizations with a signal in the corresponding pixel of the AFM image. The optimization and parameter estimation are then done by means of generic algorithm. An example of the estimation process is shown in Figure 5.9 which shows the overlays before and after the estimation. For the overlay figures (Figure 5.9g and Figure 5.8c), since the probability map rendering of the dSTORM localizations involved the shifting of the origin estimated by the overlay algorithm to accommodate the localization error distributions, an additional manual translation operation was performed.

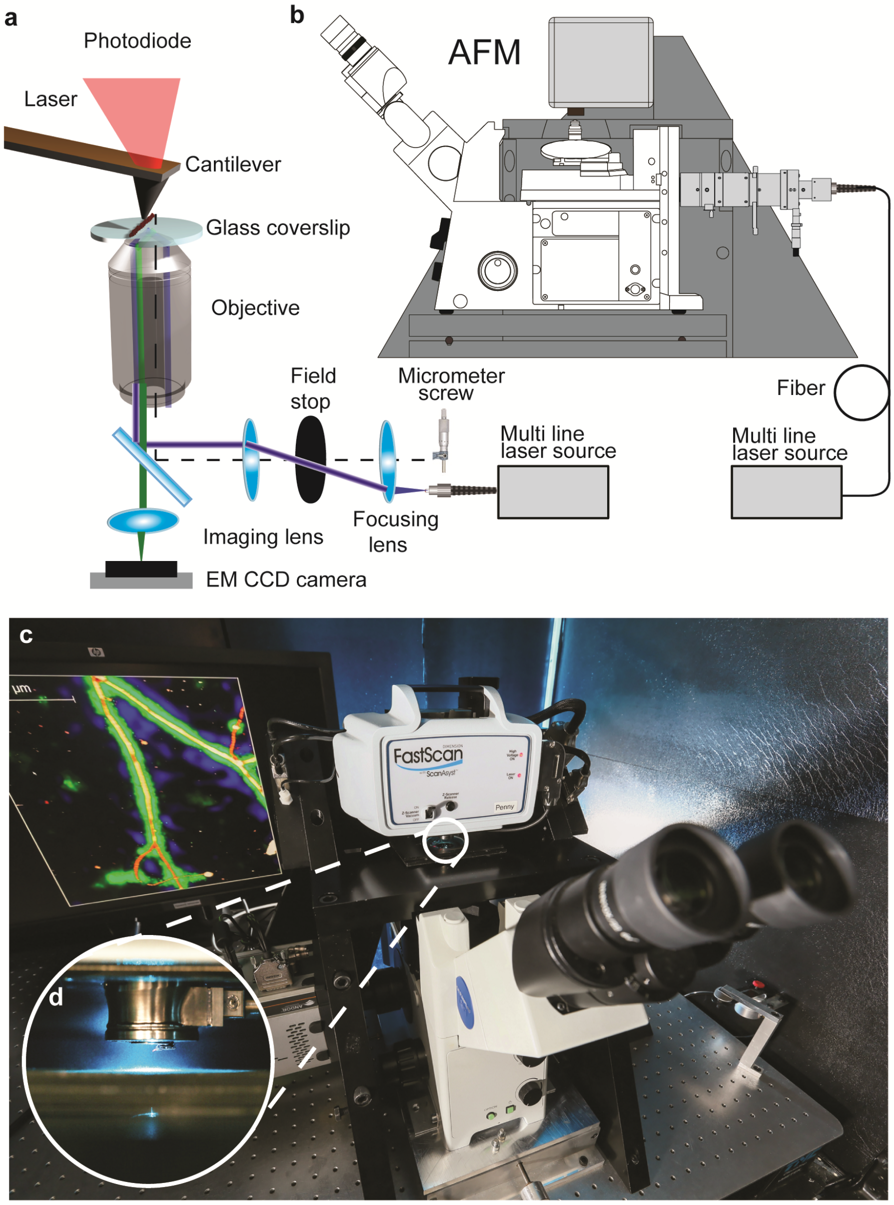

**Figure 5.1.** Correlative AFM-SMLM: instrument setup.
(a) Schematic of aligned optical light path with AFM cantilever. By laterally translating the incoming laser beam using a micrometre screw, the TIRF illumination condition is enabled. The AFM cantilever is centred in the field of view by adjusting the position of the inverted optical microscope mounted on an x / y-translation stage (as shown in b & c). (b) Mechanical integration of an inverted optical microscope and the AFM. The inverted optical microscope is mounted on an x / y-translation stage. Around it a mechanical support structure is built to hold the AFM in place without mechanically contacting the microscope body. The whole instrument is placed on a vibration isolation platform inside an acoustic isolation box. (c) Photograph of the instrument, (d) zoom in to the AFM cantilever aligned to the optical axis.

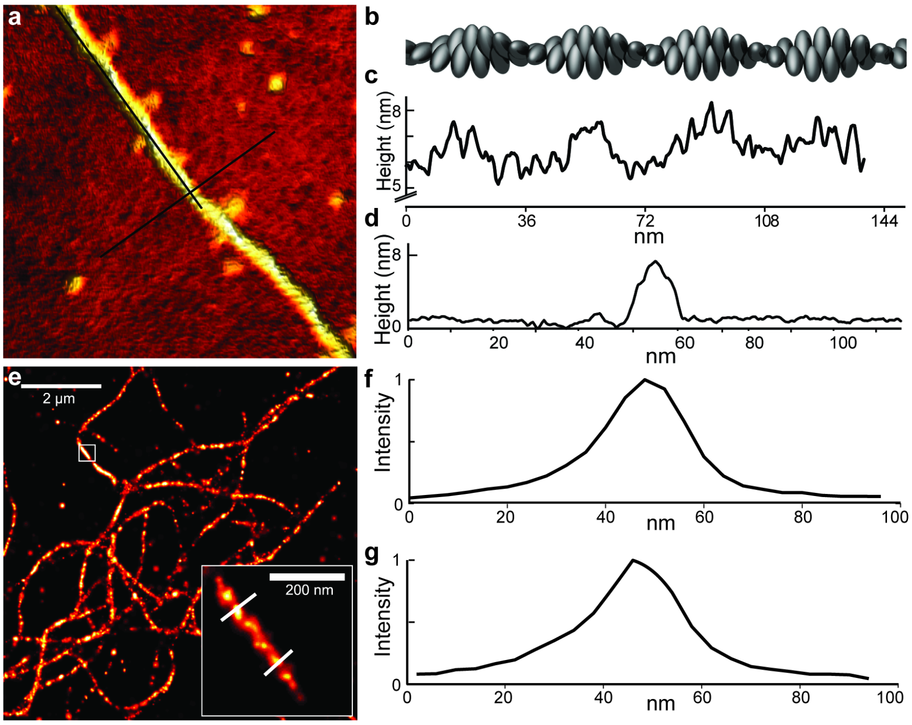

**Figure 5.2.** Independent performance of AFM and dSTORM on the combined AFM/SMLM system.

(a) AFM image of F-actin deposited on an APTES coated glass coverslip (200 nm x 200 nm). (b) 3D model of F-actin showing its apparent helical structure, which is observed by AFM as well. (c) Height profile of F-actin extracted from AFM data, along the filament (profile line indicated in (a)). The length of one helical turn is 37 nm. (d) Profile perpendicular to the F-actin having a full width at the base of $< 15$ nm. (e) Probability map of F-actin labelled with phalloidin-alexa647 imaged with dSTORM, with a selected filament zoomed in (inset). Pixel size full image: 10nm, inset: 4nm. (f & g) Intensity profiles corresponding to the lines in the inset, normalized to the maximum intensity in the profile. The FWHM of the profiles are $\approx$24nm.

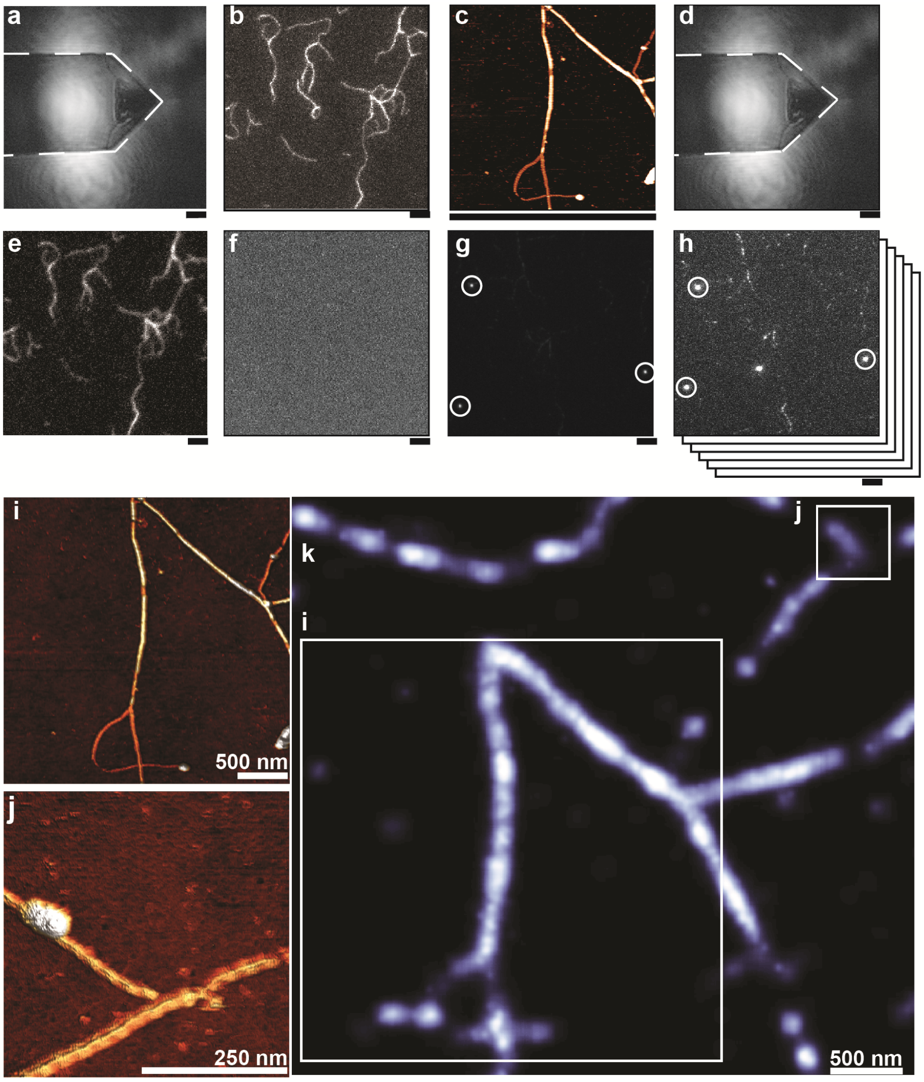

**Figure 5.3.** Experimental procedure and representative correlated AFM-dSTORM images. Experimental procedure (a-h): (a) The AFM cantilever is centered in the optical field of view of the camera by translating the inverted microscope in x- & y-direction. (b) The sampled is moved and a region of interest is selected. (c) The AFM image is acquired. (d) To determine the center of the scan another optical image is taken to account for an applied offset during AFM image acquisition. (e) Then, another TIRF image of the sample was taken and the illumination condition was optimized. (f) The fluorescent labels (Phalloidin-atto488) are quenched chemically and forced into a dark state by exchanging the buffer containing 10 mM NaBH4. (g) The buffer of the sample is exchanged with optimal dSTORM buffer and beads are added to be used as fiducial markers during the image reconstruction. (h) dSTORM images are acquired. Scale bars below images (a-h) are 3 um. (i & j) AFM images, (k) reconstructed dSTORM image in probability map representation. (i & j) Areas correlated with AFM.

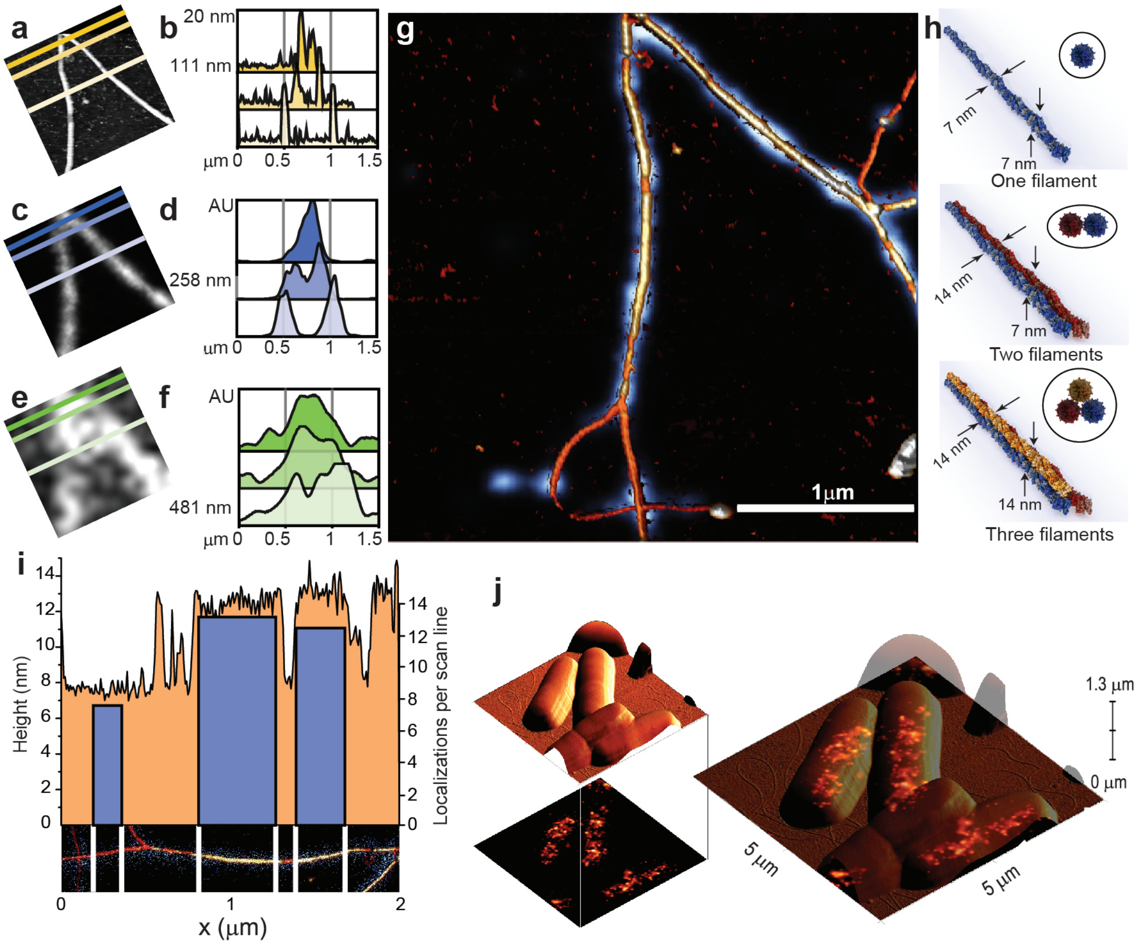

**Figure 5.4.** Comparison of AFM, dSTORM and TIRF imaging resolution from correlative imaging.
( a, c & e) AFM, dSTORM and TIRF images respectively (1.5 um x 1.5 um) of correlated filaments. Lines and colors indicate the location of profiles shown in (b, d & f). (g) Overlay of dSTORM probability map (blue) and 3D rendered AFM image (yellow-brown-). (h) Different F-actin arrangements suggested based on the AFM data. (i) Orange: Maximum height projection of the AFM section showed below the plot. Blue: Number of localizations detected in regions between the white lines per line scan of the AFM. In higher areas more localizations are observed. (j) Correlative AFM/PALM image of *E. coli* bacteria expressing RNA polymerase-mEos2.

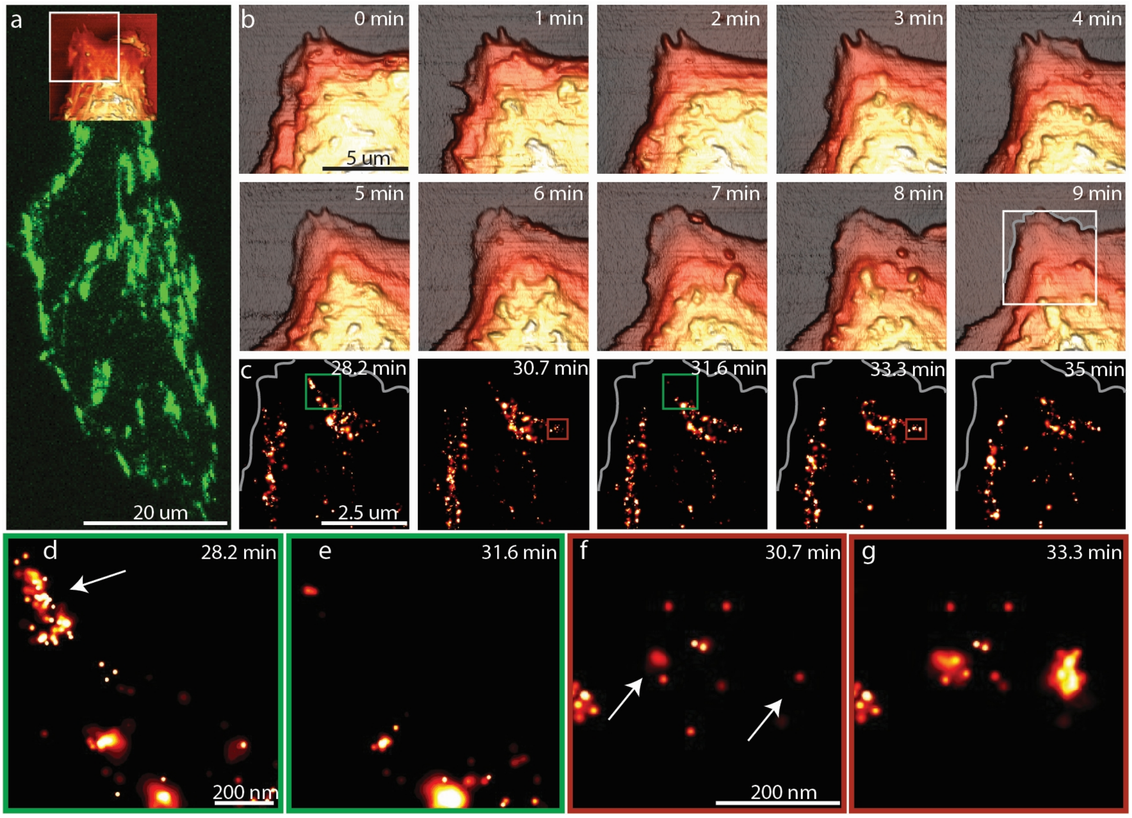

**Figure 5.5.** Live-cell time-resolved AFM/PALM on mammalian cell.
(a) CHO-K1cell transiently expressing a paxillin-mEos2 construct imaged in its off-state under TIRF illumination. Overlaid is an AFM overview image from the upper part of the cell. The white square outlines the area zoomed in for the AFM time-series shown in (b). (b) Time-resolved AFM sequence of the leading edge of the cell, showing the normal cell behavior of filopodia protrusion with subsequent lamellopodia extension. The frame rate is 1 min-1. The white square in the AFM image recorded after 9 min marks the area of subsequent PALM images shown in (c). (c) Live-cell PALM time series showing the reorganization of the paxillin-mEos2 clusters. (d) Zoom in of the green square outlined in c at 28.2 min. (e) The same area as in d at 31.6 min. (f) Zoom of the area outlined in red in (c) in the image taken at 30.7 min. (g) Zoom of the same area as in f at 33.3 min. While the AFM images show the dynamics of the cell membrane the PALM series monitors the changes in the paxillin-mEos2 clusters. In (d & e) paxillin clusters disappear from the top left corner (arrow). New paxillin clusters are formed within 3 minutes at the site shown in (f & g) (arrows).

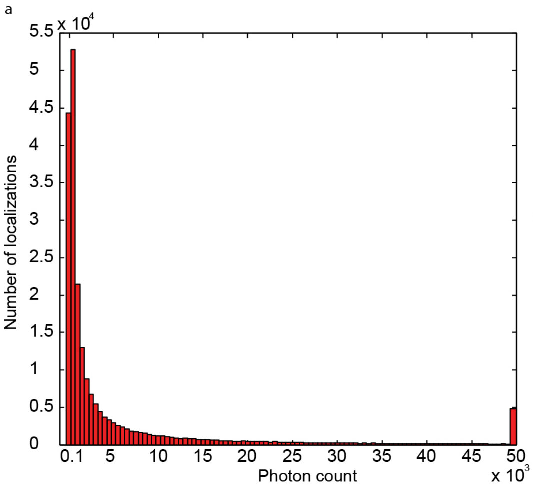

**Figure 5.6.** Photon count histograms of STORM images.
(a) corresponding to Figure 5.2e (with alexa647) and (b) Figure 5.3 (ATTO488).

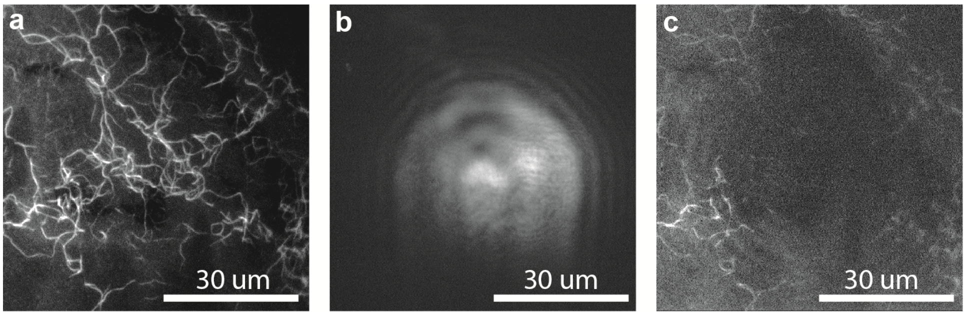

**Figure 5.7.** Bleaching effect of AFM laser on alexa647.
TIRF images of F-actin labelled with phalloidin-alexa647 exposed to the laser of the AFM. (a-c) and effect of dSTORM on F-actin structure. (a) TIRF image taken of a fresh sample of F-actin labelled with phalloidin-alexa647 deposited on glass coverslip. (b) The AFM tip was then brought close to the sample surface by false engaging without scanning and kept at this position for 30 minutes. (c) The fluorescence in the area where the cantilever was positioned was substantially bleached after 30 minutes of exposure to the laser of the AFM, making a subsequent dSTORM image impossible. Therefore for correlated AFM/dSTORM atto488 was used.

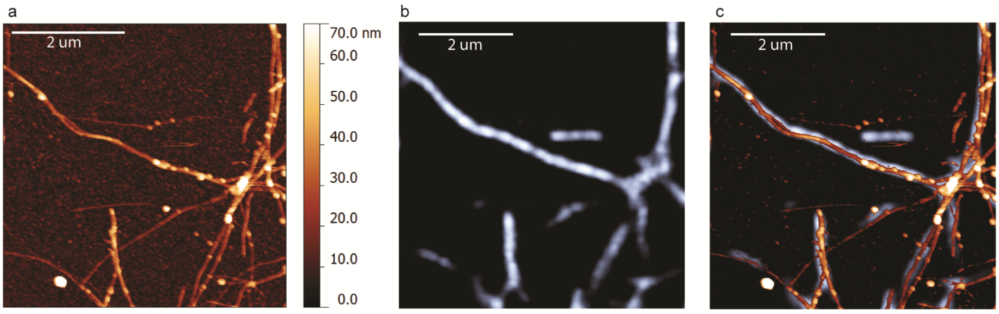

**Figure 5.8.** Additional correlated AFM/dSTORM on F-actin.
F-actin labelled with phalloidin-atto488 imaged by AFM and dSTORM. (a) AFM height image (b) dSTORM image of the same area (c) Overlay of a and b. Details to the overlay is shown in Figure 5.9b.

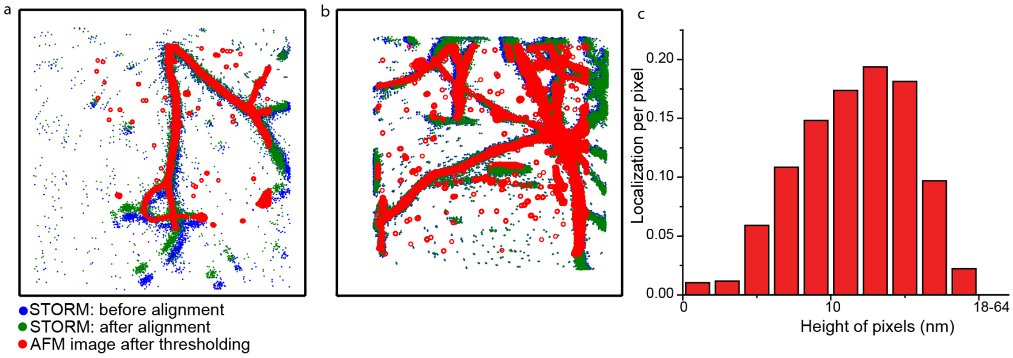

**Figure 5.9.** Alignment process for correlated AFM/STORM.
Alignment process for STORM images of Figure 5.3k (a) and Figure 5.8 (b) The localizations obtained from STORM imaging (blue) is transformed by a 2D affine transform to obtain the coordinates (green) that are better aligned with the structure in the AFM image (red). The parameters of the transform are estimated by the procedure mentioned in the Supporting material text. (c) Histogram showing the distribution of localizations per area of a particular height as measured by AFM. By correlating dSTORM data and AFM data as shown in Figure 5.4g, a height value was assigned to pixels of the dSTORM image. The sum of localizations occurring within a bin (bin size 2 nm) was divided by the total number of pixels falling into that particular bin size. Most localizations relative to the number of pixels appeared at heights between 8 nm - 14 nm, which corresponds to the measured physical height of F-actin, while very few localizations were detected on the level of the substrate (0 - 2 nm). This histogram is a quantitative representation of the correlation of dSTORM and AFM data.

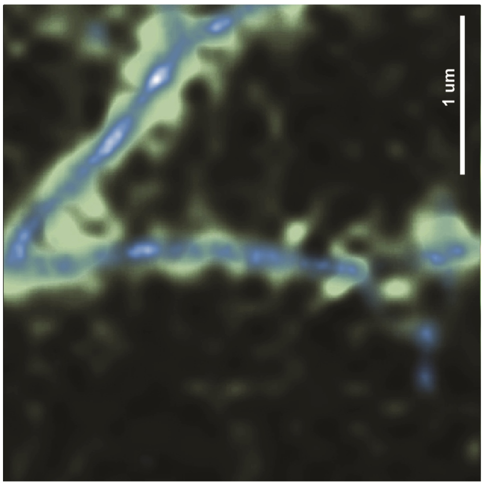

**Figure 5.10.** Overlay of dSTORM and TIRF.
Overlay of dSTORM (blue) image and total internal reflection fluorescence (TIRF) image (green) of the same area as shown in Figure 5.4g. The TIRF image shown here was used for the analysis in Figure 5.4e& f.

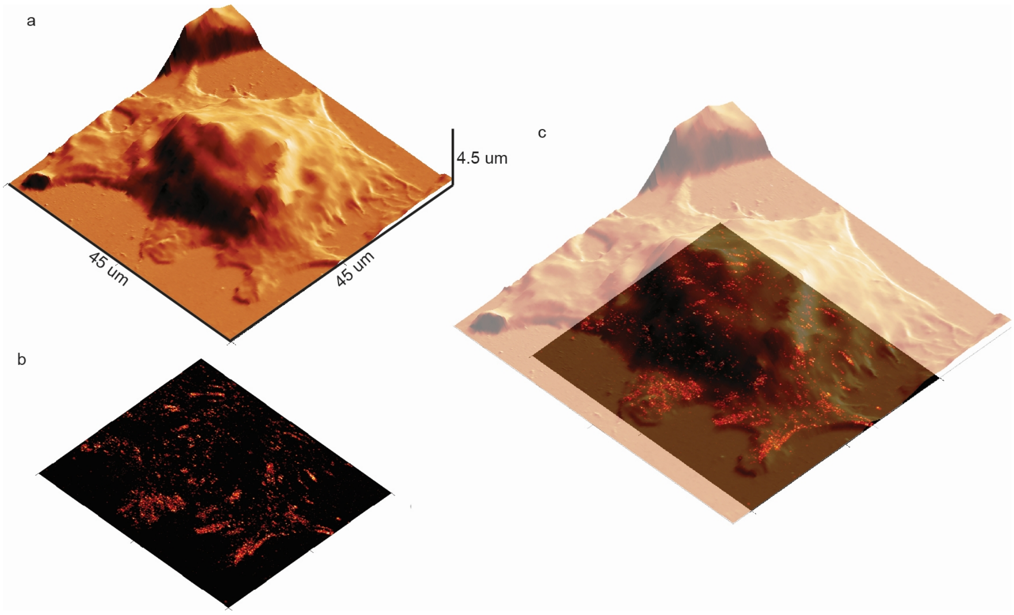

**Figure 5.11.** Correlative AFM/PALM image of MEF cell.
Correlative AFM/PALM image of a fixed mammalian cell (mouse embryonic fibroblast (MEF) cell) expressing the fusion protein paxillin-mEos2. (a) 3D render of AFM image with error channel as mask. (b) PALM image. (c) Correlated AFM and PALM image. Details describing the sample preparation are discussed in the text of the Supporting material.

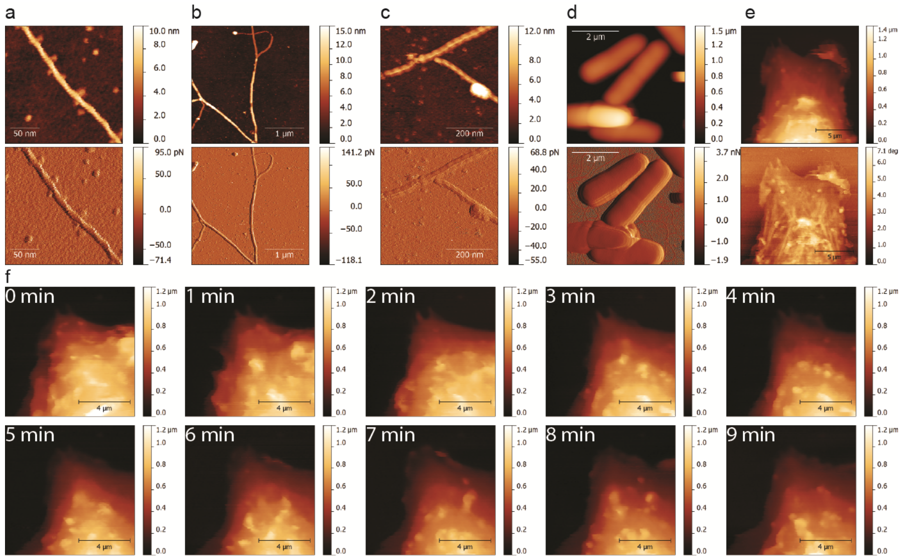

**Figure 5.12.** 2D AFM images of 3D representations shown in main figures.
2D AFM height images of 3D representations shown in main figures. (a) Corresponds to AFM image shown in Figure 5.2a. (b) Corresponds to AFM image shown in Figure 5.3i& 5.4g. (c) Corresponds to AFM image shown in Figure 5.3j. (d) Corresponds to AFM image shown in Figure 5.4j. (a-d) Top height image, bottom peak force error image. (e) Corresponds to AFM image shown in Figure 5.5a. Top height image, bottom phase image. (f) Corresponds to AFM time-resolved images shown in Figure 5.5b.

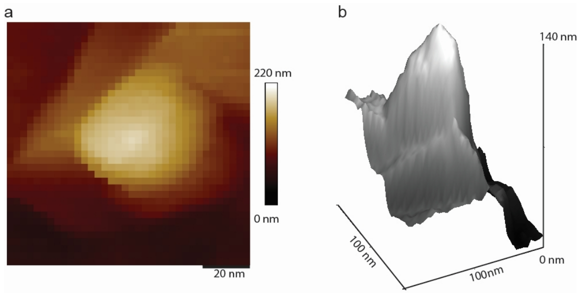

**Figure 5.13.** Reconstruction of tip used for AFM for Figure 5.3 and 4.
Tip reconstruction as obtained by Nanoscope Analysis software of the AFM tip used for imaging F-actin filaments shown in Figure 5.3 & Figure 5.4. The tip shape was reconstructed from an image of a tip characterization sample. (a) 2D height image. (b) 3D representation of tip reconstruction.

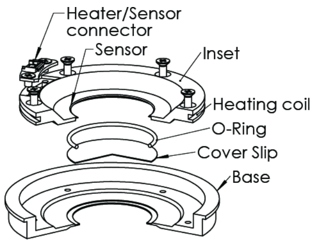

**Figure 5.14.** Glass coverslip heating holder used for live-cell experiment.
Schematic of the home-built glass coverslip holder used to keep the live-cell CHO-K1 sample at 37 ° C. The temperature was controlled with TC-2-80-15 (Bioscience Tools).

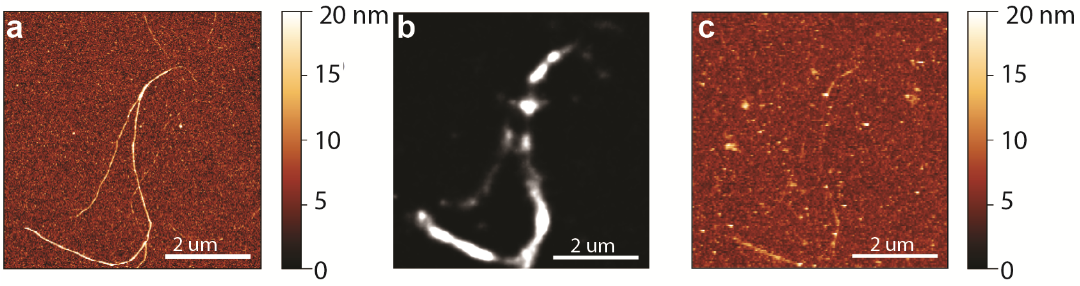

**Figure 5.15.** Effect of dSTORM measurement on structural integrity of actin filament.
Effect of dSTORM measurement on actin filament interity. (a) AFM image of F-actin labelled with phalloidin-atto488 before dSTORM. (b) dSTORM image acquired as described in the methods. Reconstruction was done using the software thunderSTORM without drift-correction. (c) After dSTORM image was acquired another AFM was recorded. Parts of actin filaments disintegrated.

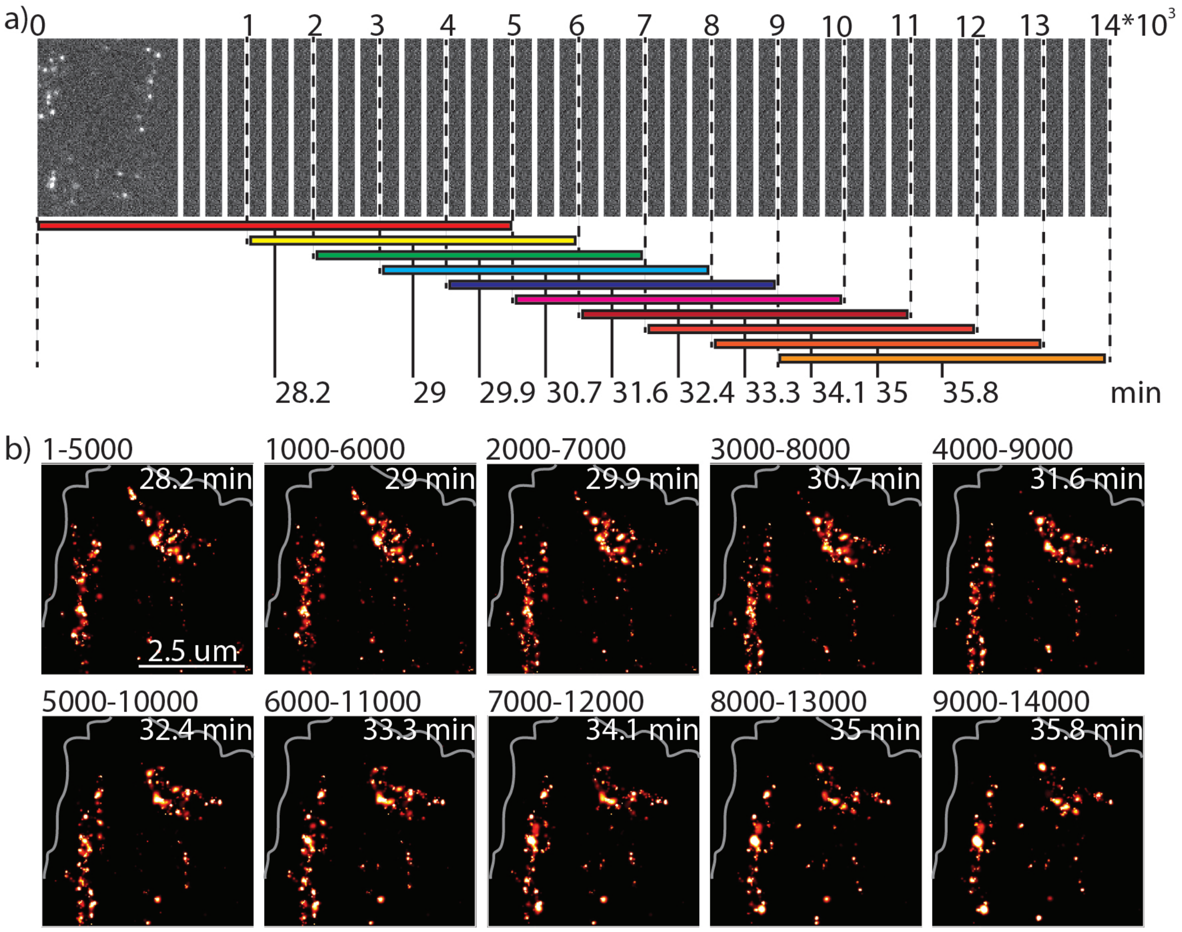

**Figure 5.16.** Schematic of PALM image reconstruction and time-sequence. Time-resolved PALM images constructed from 5000 frames with a running average approach. (a) Schematic showing the time-resolved PALM image reconstruction. Each PALM image is a reconstruction out of 5000 frames. Between each consecutive PALM image there is an offset of 1000 frames. The time reported indicates the time at which the middle frame of the respective PALM frame has been acquired. (b) Time-resolved PALM series. On top of each PALM image the number of frames used for its reconstruction is indicated. The outline of the cell is marked in gray. This time-sequence was used for the Supporting movie 1.

# Chapter 6

# MosaicIA: An ImageJ/Fiji plugin for spatial pattern and interaction analysis

*This is a verbatim copy of an open access peer reviewed publication A. Shivanandan, A. Radenovic, and I. F. Sbalzarini. MosaicIA: an ImageJ/Fiji plugin for spatial pattern and interaction analysis.* BMC Bioinformatics, *14(1):349, 2013.*

## Abstract

**Background:** Analyzing spatial distributions of objects in images is a fundamental task in many biological studies. The relative arrangement of a set of objects with respect to another set of objects contains information about potential interactions between the two sets of objects. If they do not "feel" each other's presence, their spatial distributions are expected to be independent of one another. Spatial correlations in their distributions are indicative of interactions and can be modeled by an effective interaction potential acting between the points of the two sets. This can be used to generalize co-localization analysis to spatial interaction analysis. However, no user-friendly software for this type of analysis was available so far.

**Results:** We present an ImageJ/Fiji plugin that implements the complete workflow of spatial pattern and interaction analysis for point-like objects. The plugin detects objects in images, infers the interaction potential that is most likely to explain the observed pattern, and provides statistical tests for whether an inferred interaction is significant given the number of objects detected in the images and the size of the space within which they can distribute. We benchmark and demonstrate the present software using examples from confocal and PALM single-molecule microscopy.

**Conclusions:** The present software greatly simplifies spatial interaction analysis for point patterns, and makes it available to the large user community of ImageJ and Fiji. The presented showcases illustrate the usage of the software.

## Keywords

spatial pattern analysis, microscopy, co-localization analysis, interaction analysis, PALM, ImageJ, Fiji, image analysis

## 6.1 Background

We present a software plugin to analyze and quantify spatial patterns of objects in images using the free open-source image-processing platform ImageJ (Abramoff et al., 2004) or its distribution Fiji (Schindelin et al., 2012). The spatial arrangement of objects relative to each other is a rich source of phenotypic information. This ranges from spatial patterns of sub-cellular structures or proteins, to the spatial patterns formed by cells in tissues, to spatial patterns of organisms in ecosystems. The mathematical framework of spatial statistics allows quantifying and analyzing such patterns, comparing them with each other, and performing statistical tests on them (Mecke and Stoyan, 2000; Diggle, 2003; Moller and Waagepetersen, 2004). This for example allows testing whether the distribution of a set of objects is significantly different from random, or whether the objects in one set are distributed independently of the objects in another set. Significant deviations from spatial randomness are indicative of interactions (of some sort) between the objects, as formalized in the framework of spatial interaction analysis (Helmuth et al., 2010).

Biology has long relied on co-localization analysis in order to quantify the spatial distribution of one set of objects with respect to another one. This includes pixel-based and object-based co-localization analysis methods (Bolte and Cordelières, 2006). Pixel-based methods typically use a correlation measure between the pixel intensities in different images in order to quantify the degree of overlap or co-localization between the object distributions represented in the images. Object-based methods first detect and delineate the objects of interest in the images and then quantify their degree of co-localization using an overlap measure. While pixel-based measures are easy to compute, they are difficult to interpret. They are also sensitive to blurring and noise in the image. Moreover, in some observations, like those from Photo-Activation Localization Microscopy (PALM) and STochastic Optical Reconstruction Microscopy (STORM) (Betzig et al., 2006; Rust et al., 2006; Hess et al., 2006), it is not obvious what constitutes an image (Baddeley et al., 2010), as these methods provide locations and localization uncertainties of individual molecules. Pixel-based methods are hence not directly applicable, unless one first renders a synthetic image from the observed point locations. This, however, leads to a loss of information as nearby molecule detections fuse into one blob in the rendered image. Object-based methods are more intuitive to interpret, as they directly work with locations of objects. However, they depend on prior object detection and segmentation. It is also not clear when two object should be considered "overlapping". This requires defining a distance threshold, which typically is $\approx$200 nm for diffraction-limited data (Lachmanovich et al., 2003). Single-molecule imaging, like PALM and STORM, directly provides point locations, rendering a separate object-detection step unnecessary.

While co-localization analysis captures the amount of overlap between objects, it is not sufficient to describe spatial patterns and interactions (Helmuth et al., 2010). Also, co-localization measures do not account for the fact that accidental overlap occurs even in randomly distributed objects and becomes more frequent as the object density increases. This typically leads to a density bias in the final co-localization score.

### 6.1.1 Spatial interaction analysis

Helmuth et al. (Helmuth et al., 2010) have generalized co-localization analysis to interaction analysis, which corrects for accidental overlaps, is robust against imaging noise and image-processing errors, does not require defining a distance threshold, and is able to capture patterns also at larger length scales than just immediate overlap. They used a nearest-neighbor interaction model based on spatial Gibbs statistics, which characterizes an observed pattern by an interaction potential. This is the potential that is most likely to produce the observed distribution of nearest-neighbor (NN) distances between objects if the objects interact pair-wise according to this potential.

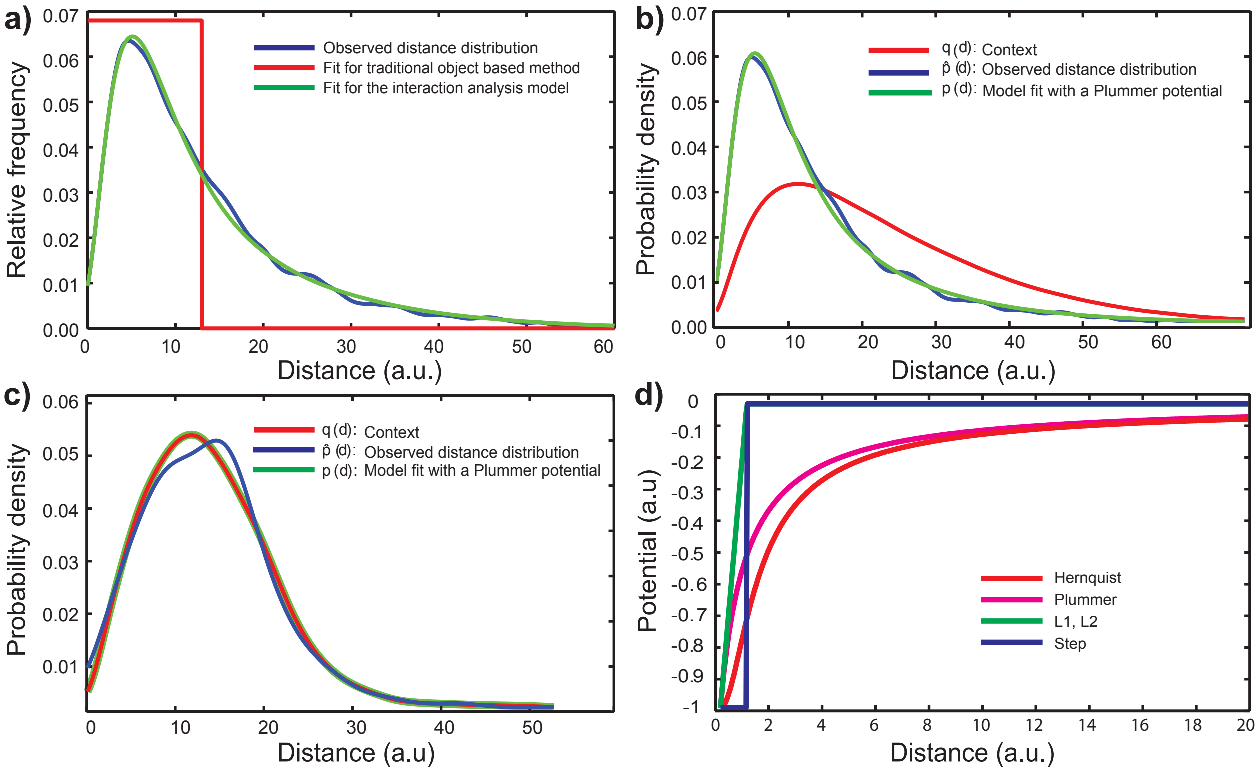

**Figure 6.1.** Interaction analysis with smooth potentials and context correction. (**a**) Example comparison of fits to data (blue) using traditional, uncorrected object-based co-localization analysis (red) and using the context-corrected method used in MosaicIA (green). The plots show the nearest-neighbor (NN) distance distribution between two arbitrary point patterns. (**b,c**) Sample fits corresponding to interacting and non-interacting point patterns, respectively. In the case of the non-interacting point pattern, the model fit (green) to the observed NN distribution (blue) coincides with the context (red). In the presence of an interaction, the NN distance distribution (blue) is different from the context (red). The difference is explained by an interaction potential, leading to the green model fit. (**d**) Shapes of different potentials provided by MosaicIA. Parameters: $\sigma = 1$, and $t = 0$ for all except step potential, where $\sigma = t = 1$.

Compared to object-based co-localization analysis, the interaction analysis model uses additional information that is present in the data, namely nearest-neighbor distance distributions also between non-overlapping objects. The model is hence able to better fit an observed distance distribution than a co-localization score would be (see Fig. 6.1a). The method also provides standardized ways to (1) correct for the influence of the distribution of points within one set onto the distance distribution to another set; (2) infer parameters of the interaction potential, such as the strength and length scale of the interaction; (3) perform statistical hypothesis tests for the presence of an interaction.

The notion of “interaction” used here is purely geometric. We say that two sets of objects interact if the spatial distribution of one set is not independent of the distribution of the other set (see Fig. 6.1b). The objects do not interact if the distribution of one set can be explained by a random distribution that does not depend on the other, the reference set (see Fig. 6.1c). These interactions or spatial patterns need not imply causal interactions.

### 6.1.2 The Interaction analysis model

Let the two sets of objects be represented by their spatial positions $X = \{\mathbf{x}_i\}_{i=1}^{N}$ and $Y = \{\mathbf{y}_j\}_{j=1}^{M}$. Further let $D = \{d_i\}_{i=1}^{N}$ be the set of distances from any point in $X$ to its nearest neighbor (NN) in the reference set $Y$. The context $q(d)$ is the probability density function (p.d.f.) of NN distances if the objects in $X$ were distributed uniformly at random and independently of the distribution of the objects in $Y$. We call this the *context* because it corrects for how the objects in $Y$ are distributed and for the shape of the space within which the objects in $X$ can distribute. The p.d.f. of the observed NN distances is then modeled as (Helmuth et al., 2010):

$$p(D|q) = Z^{-N} \prod_{i=1}^{N} q(d_i) \exp\left(-\varphi(d_i)\right) , \tag{6.1}$$

where $Z$ is the normalization constant (partition function), and $\varphi(d)$ the unknown distance-dependent interaction potential. The role of the potential is to "deform" the context in order to explain the distribution of $X$ with respect to $Y$ as a result of the points in $X$ interacting with their nearest neighbors in $Y$ through the potential $\varphi$ (see Fig. 6.1b,c).

The potential $\varphi(d)$ can be of any shape, including a step function for which a context-corrected version of traditional threshold-based co-localization measure is recovered (Helmuth et al., 2010). Often, we use a parametric potential of the form $\varphi(d) = \varepsilon f((d-t)/\sigma)$, where $\varepsilon$ is the interaction strength, $\sigma$ the length scale of the interaction, and $t$ a threshold closer than which objects are considered overlapping. The function $f$ defines the shape of the potential. If the shape $f$ is unknown, a piece-wise linear non-parametric function is used. Plots of the different parametric potential shapes provided by the plugin are shown in Fig. 6.1d.

## 6.2 Implementation

The plugin is written in Java. It uses the open-source Java library Weka (Hall et al., 2009) for efficiently computing NN distances using *kd*-trees and for kernel density estimation of probability distributions. The plugin further uses CMA-ES (the Covariance Matrix Adaptation Evolution Strategy) (Hansen and Ostermeier, 2001) for parameter optimization. This optimizer is less prone to get stuck in local optima than the simplex method used in the original publication (Helmuth et al., 2010). The plugin has been tested with both ImageJ and Fiji on Windows, MacOS X, and Linux. It should run on any platform where Java and ImageJ are available. Running a complete analysis using the present plugin takes between a few seconds and a few minutes, depending on the number of objects present in the image.

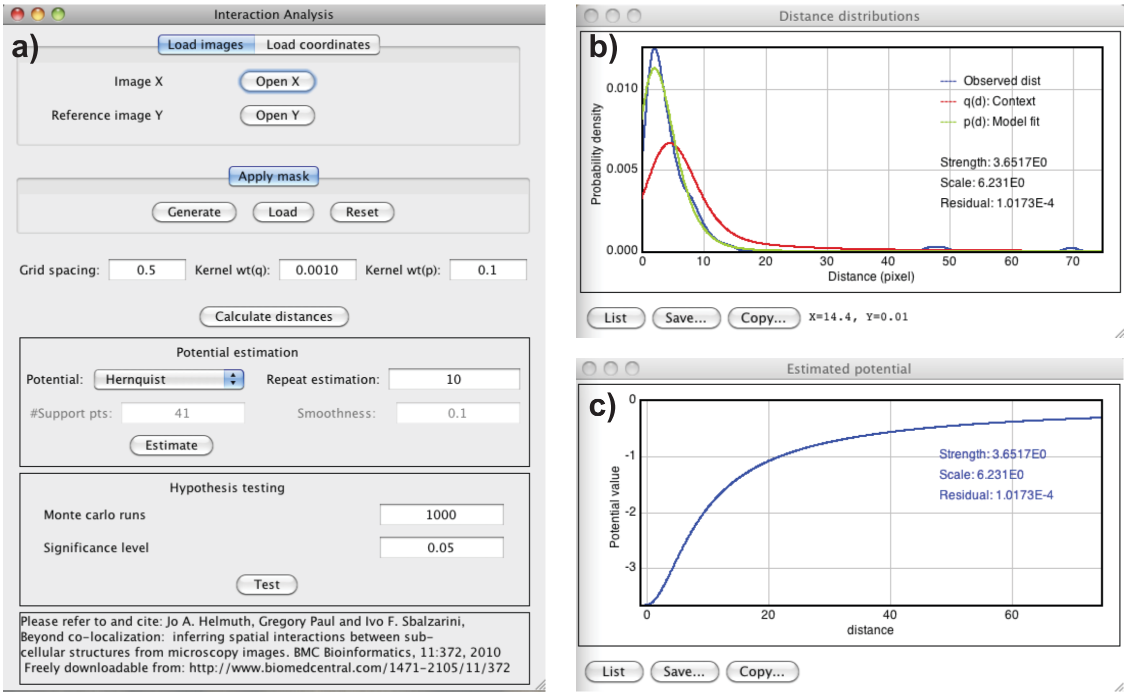

Grid spacing: 0.5 Kernel wt(q): 0.0010 Kernel wt(p): 0.1

Potential: Hernquist Repeat estimation: 10

#Support pts: 41 Smoothness: 0.1

Monte carlo runs 1000

Significance level 0.05

Please refer to and cite: Jo A. Helmuth, Gregory Paul and Ivo F. Sbalzarini, Beyond co-localization: inferring spatial interactions between sub-cellular structures from microscopy images. BMC Bioinformatics, 11:372, 2010
Freely downloadable from: http://www.biomedcentral.com/1471-2105/11/372

**Figure 6.2.** The graphical user interface of the plugin.
(**a**) The main mask of MosaicIA where the parameters are entered. (**b,c**) Windows showing example results of an analysis. The measured and fitted NN distance distributions, along with the context, are shown in (**b**). The interaction potential leading to the displayed fit is shown in (**c**)

The user interface of MosaicIA is shown in Fig. 6.2. Its workflow is explained in the flowchart in Fig. 6.3. The plugin reads either images (2D or 3D), or comma-separated text files containing the coordinates of objects. The user can create or load a mask to restrict the analysis to a certain region of interest, if necessary. If the analysis is based on images, bright points in the images are first detected using the feature-point detector by Sbalzarini and Koumoutsakos (Sbalzarini and Koumoutsakos, 2005), which is also available in Java as an ImageJ plugin and processes both 2D and 3D images. Then, the NN distance distribution $D$ between the two point sets is computed and the context $q(d)$ estimated using grid sampling (Helmuth et al., 2010). This means that $q(d)$ is approximated by computing the NN distance from each point on a regular Cartesian lattice to the nearest neighbor in $Y$. The grid resolution has to be set by the user. Finer grids lead to more accurate results, but require more computer time. Smooth representations of the observed (empirical) NN distance distribution $\hat{p}(d)$, and of the sampled context $q(d)$ are obtained by kernel density estimation. The estimator kernel widths are set by the user, but the software provides an initial guess calculated with Silverman's rule (Silverman and Green, 1986).

The plugin currently works with point objects only, even though the interaction analysis framework generalizes to extended objects, too (Helmuth et al., 2010). In order to work with non-point objects in the present plugin, they can be segmented using other software, e.g. the Region Competition plugin for ImageJ (Cardinale et al., 2012), and their centers of mass can be read into the present plugin. Representing extended objects by their centers of mass does not significantly change the result of the interaction analysis, as shown in the PALM example below.

The type of the potential function can be selected from a drop-down menu. Both parametric

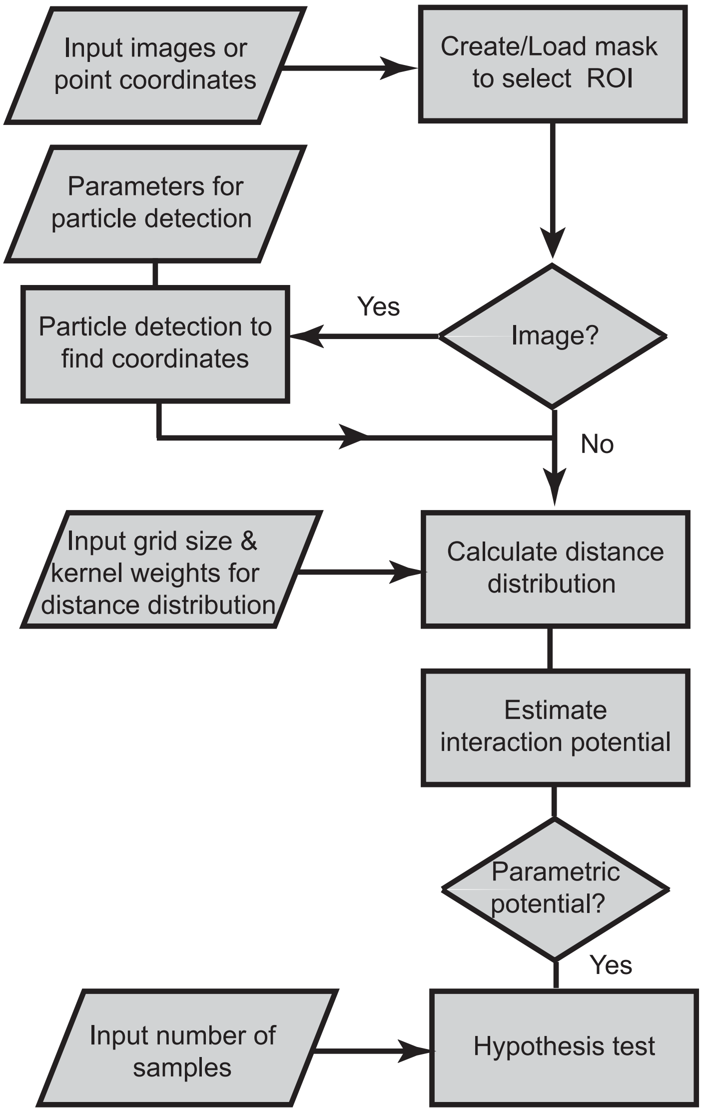

**Figure 6.3.** Workflow of interaction analysis with MosaicIA. See main text for details and examples.

and non-parametric functions are provided. The plugin then estimates the potential or its parameters from the data by minimizing the $\ell^2$ difference $\|\hat{p}(d) - p(d)\|_2$ between the observed NN distance distribution $\hat{p}(d)$ and the one predicted from the interaction model $p(d)$ (see Appendix B). The results, including the residual fitting error, are then shown along with a plot of $\hat{p}(d)$, $p(d)$, and $q(d)$, as shown as in Fig. 6.2b,c.

The plugin also provides hypothesis tests to check whether the estimated interaction is statistically significant. The test statistic is computed from $K$ Monte Carlo samples of point distributions corresponding to the null hypothesis of “no interaction”. The test statistic from the actually observed distribution is ranked against these $K$ random samples. If it ranks higher than $\lceil(1-\alpha)K\rceil$-th, the null hypothesis of “no interaction” is rejected on the significance level $\alpha$ (Helmuth et al., 2010).

### 6.2.1 List of parameter inputs to the plugin

The plugin has six parameters that the user can set to control its behavior. These parameters and their typical values are described below.

#### Parameters for particle detection

The following parameters control the image-processing part of the plugin. The algorithm used to detect bright particles in the images and extract their location is described in Ref. (Sbalzarini and Koumoutsakos, 2005). See this reference for a more in-depth discussion of these parameters and for illustrations of how they affect particle detection.

- **Radius**: Approximate radius of the particles in the images in units of pixels. This value should be slightly larger than the visible particle radius, but smaller than the smallest inter-particle separation.
- **Cutoff**: The score cut-off for false-positive rejection. The larger the cutoff, the more conservative the algorithm becomes to only select particles that look alike.
- **Percentile**: Determines how bright a spot has to be in order to be considered a particle. All local intensity maxima in the given upper percentile of the image intensity histogram are considered candidate particles.

#### Parameters for computing distance distributions

Once the particles have been detected in both images, or their coordinates have been read from files, the following parameters can be used to control interaction inference:

- **Grid spacing**: The grid spacing controls how finely the context $q(d)$ is sampled in units of pixels It should ideally be less than half of shortest possible interaction that can be detected with the available data. For an image without sub-pixel particle detection, 0.5 (pixel) is hence sufficient. In cases where finer resolution is needed, the user can try successively smaller values until the context $q(d)$ does not change any more. Grid sampling the context $q(d)$ is the most time-consuming part of the analysis. Adjusting the grid size hence significantly influences the computational time.
- **Kernel wt(q)**: This is the weight parameter used by the kernel density estimator to estimate the smooth context p.d.f. $q(d)$ from the grid samples. Since the number of grid points is usually large, a small kernel weight of 0.001 should be sufficient to produce smooth results. This parameter usually does not need to be changed.
- **Kernel wt(p)**: This is the weight parameter used by the kernel density estimator to estimate the smooth NN distance distribution $\hat{p}(d)$. The value of this parameter is critical, and a rough estimate for it is computed using Silverman's rule (Silverman and Green, 1986). The resulting value is shown as a suggestion. This parameter should be carefully tuned so that the resulting distribution contains all relevant information from the histograms, without overfitting them. A larger value for this parameters leads to a more fine-grained, less smooth fit.

### 6.2.2 List of potentials provided

The plugin provides both parametric and non-parametric potentials that can be used to describe an interaction. The non-parametric potential is more flexible and does not require the user to assume anything about the functional shape of the interaction. However, it requires more computer time to be estimated and does not support statistical tests for the significance of an interaction. Parametric potentials offer an intuitive interpretation of an interaction by its strength and length scale. Frequently, one first estimates a non-parametric potential in order to get an idea of the rough shape of the interaction. Then, one selects the parametric potential most similar to it and repeats the estimation.

#### Parametric potentials

Potentials are parameterized as $\varphi(d) = \varepsilon f((d-t)/\sigma)$ with interaction strength $\varepsilon$, length scale $\sigma$, and a hard core $t$. For the step potential, $\sigma = 1$. For all other potentials, $t = 0$. The shapes $f(\cdot)$ of the various potentials are:

- Step potential:

$$f^{\mathrm{st}}(r) = \begin{cases} -1 & \text{if } r < 0 \\ 0 & \text{else} \end{cases} . \tag{6.2}$$

- Hernquist potential:

$$f^{\mathrm{he}}(r) = \begin{cases} -\left(r+1\right)^{-1} & \text{if } r > 0 \\ -(1-r) & \text{else} \end{cases} . \tag{6.3}$$

- Linear potential, type 1:

$$f^{\mathrm{l1}}(r) = \begin{cases} 0 & \text{if } r > 1 \\ -(1-r) & \text{else} \end{cases} . \tag{6.4}$$

- Linear potential, type 2:

$$f^{\mathrm{l2}}(r) = \begin{cases} 0 & \text{if } r > 1 \\ -1 & \text{if } r < 0 \\ -(1-r) & \text{else} \end{cases} . \tag{6.5}$$

- Plummer potential:

$$f^{\mathrm{pl}}(r) = \begin{cases} -\left(r^2+1\right)^{-0.5} & \text{if } r > 0 \\ -1 & \text{else} \end{cases} . \tag{6.6}$$

Plots of these potentials are shown in Fig. 6.1d. In principle, other potentials can be implemented, too.

#### Non-parametric potential

The non-parametric potential does not assume any specific shape and can be used to gain an approximate idea of the shape of an unknown interaction. It is defined as a weighted sum of linear kernel functions centered on $P$ support points (defined in the #**support pts** field). The more support points are used, the finer the potential is resolved, but the more costly and unstable the estimation becomes. The smoothness of the estimated potential is controlled by the **smoothness** parameter, which penalizes differences between adjacent support points. Larger smoothness parameters lead to smoother potentials, but may miss or average out interesting interactions. Therefore, this parameter should be used with caution.

### 6.2.3 Working with coordinates instead of images

It is possible to directly use MosaicIA on localization data. This is useful when working with imaging modalities like PALM and STORM that provide point coordinates rather than images. It is also useful when working with objects that are not point-like, or for which the point-detection step of the plugin does not work well. These objects can then be detected and segmented using any other tool, e.g. the Region Competition plugin for ImageJ (Cardinale et al., 2012), and their coordinates stored in a file. A comma-separated text file of coordinates can be read into the plugin by clicking ***load coordinates*** instead of ***load images***. Each line in the file should contain the coordinates of one object in the format $x$, $y$, ($z$). The spatial boundaries of the point patterns (they must be identical for both $X$ and $Y$) are entered in the fields provided. For objects detected in a $400 \times 400$ pixel image, the boundaries are $(0, 399)$ in both directions.

### 6.2.4 Interpreting the results

The estimated interaction potentials and parameters can be used to quantitatively compare spatial distributions across different samples and conditions (e.g., perturbations). Comparisons based on interaction strengths and length scales, however, should only be done for results obtained with the same potential shape.

The strength of an interaction, $\varepsilon$, is equal to zero for independent, i.e. non-interacting, point patterns. However, due to noise and random overlap in the data, the strength may be slightly greater than zero even in the case of no interaction. A hypothesis test is therefore provided in order to check whether an estimated interaction is statistically significant given the amount and quality of the data used to infer it.

The hard core of an interaction, $t$, is akin to the distance threshold in classical object-based co-localization analysis. If two objects are closer to each other than this hard core, they are considered overlapping.

The length scale of an interaction, $\sigma$, quantifies over how many units of length the potential is scaled. It hence provides information about the length scale of organization between the two point patterns. The unit of length is pixels if the objects are detected from images. If coordinates are read from a file, the unit of length is as defined in that file.

## 6.3 Results and Discussion

We validated and tested the plugin on synthetically generated point distributions in the presence and absence of interactions and confirmed that interactions were correctly detected (results not shown). We show here the application of the plugin to two real-world cases: interactions between viruses and endosomes in HER-911 cells as inferred from fluorescence confocal microscopy images, and clathrin–GPCR interactions as inferred from PALM super-resolution data in HeLa cells.

### 6.3.1 Application to virus–endosome interaction from confocal images

We apply the plugin to analyze the interactions between human adenoviruses of serotype 2 (Ad2), stained with ATTO-647, and Rab5-EGFP-stained endosomes in HER-911 cells (image data: Greber lab, University of Zurich). Similar data has also been used in Ref. (Helmuth et al., 2010). The results are shown in Fig. 6.4. Figure 6.4a shows the image $X$ of the virus particles after particle detection in the plugin. The image $Y$ of the endosomes after particle detection is shown in Fig. 6.4b. Fig. 6.4c shows the observed NN distance distribution (blue curve), the expected distribution if viruses were distributed at random and independently of the endosomes, i.e., the context (red curve), and the best fit (green curve) with the Plummer potential shown in Fig. 6.4e. Figure 6.4d shows the results when using the step potential shown in Fig. 6.4f, corresponding to a context-corrected object-based co-localization count. The residual fitting error when using the Plummer potential is about 4-fold lower than when using the step potential, even though the latter also corrects for the context. The improvement stems from using continuous distance information. The error when using classical co-localization analysis without correcting for the context would be even larger.

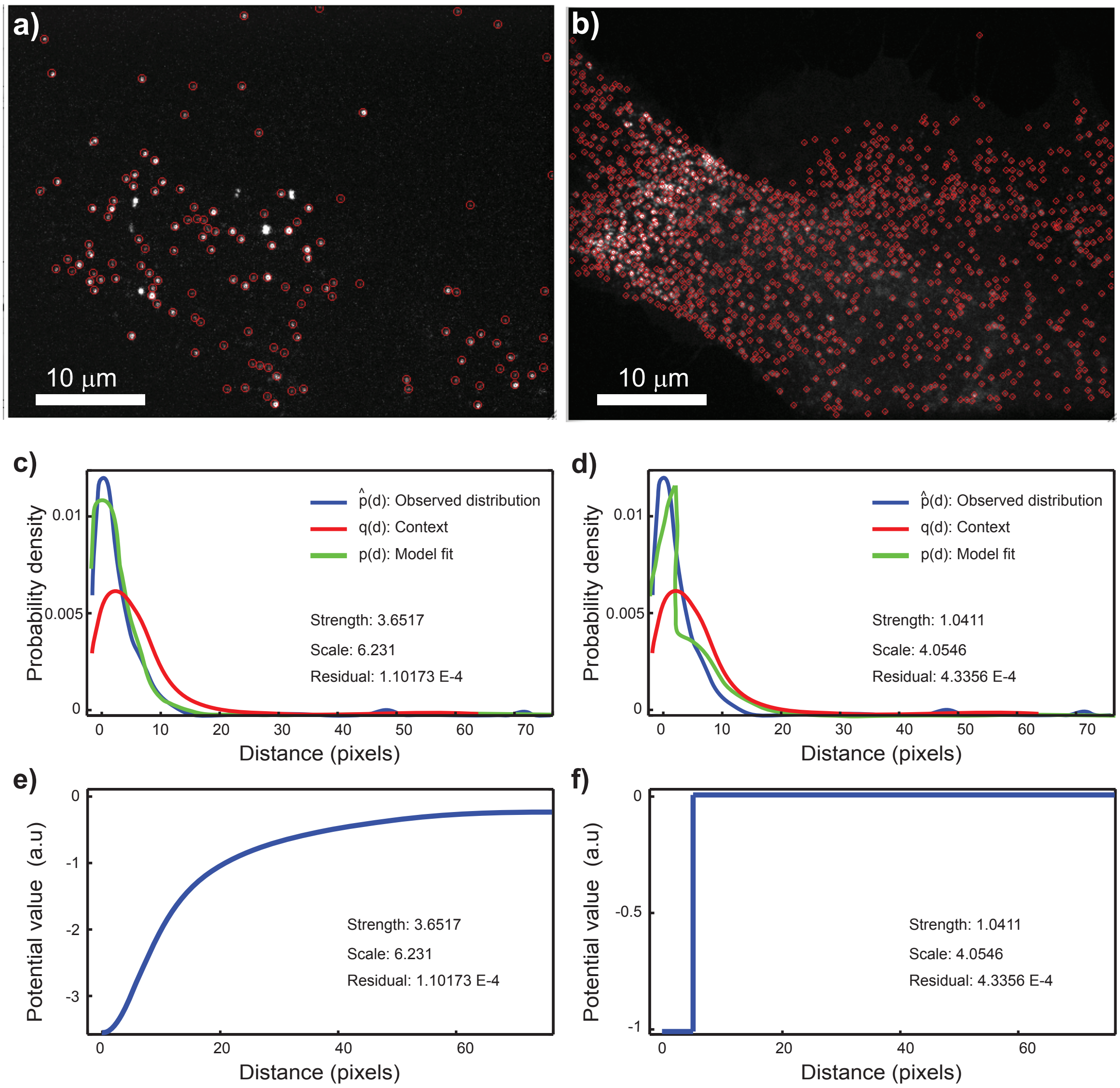

**Figure 6.4.** Results of applying the plugin to virus–endosome data from confocal microscopy.
(**a**) Image $X$ of the red channel showing adenovirus serotype 2 (Ad2) tagged with ATTO-647. (**b**) Image $Y$ of the green channel showing Rab5-EGFP, a marker for endosomes. The results from particle detection using MosaicIA are shown as overlaid red circles. Only a single 2D image is used here, and no $z$-stack. (**c,d**) Distance distributions obtained after fitting the data with a Plummer and step potential model, respectively. (**e,f**) The corresponding estimated interaction potentials. The Plummer potential leads to a 4-fold lower fitting error than the step potential.

### 6.3.2 Application to GPCR–clathrin interaction from PALM data

Super-resolution microscopy techniques such as PALM and STORM do not provide images, but produce point clouds by measuring the coordinates of individual fluorophores and their localization uncertainties. Directly working with these position data provides more information than first rendering an artificial image from them and then working with that image (Baddeley et al., 2010).

G-protein-coupled receptors (GPCRs) are important signaling proteins that are transported in clathrin-coated vesicles. The sizes of these vesicles are typically below the resolution limit of classical microscopy, rendering them a good system to be studied with super-resolution techniques like PALM and STORM.

We analyze the prototypical GPCR $\beta$2-adrenergic receptor ($\beta$2-AR) and its internalization in clathrin-coated vesicles post stimulation with the agonist isoproterenol in HeLa cells (Annibale et al., 2012). $\beta$2-AR is labelled with PSCFP2, and clathrin light chains are labeled with PAMCherry1 (Annibale et al., 2012). Figure 6.5a shows an exemplary rendered probability map from dual-color PALM after setting a clustering threshold to remove localized molecules that are not within a cluster of at least the threshold size (Annibale et al., 2012). The estimated locations of these individual fluorescent molecules are shown as dots in Fig. 6.5b, without the localization uncertainty distributions. Circles mark clusters of fluorophores with the cluster centers given by the crosses.

We can either analyze the interactions between the individual molecules in one color channel with those in the other channel, or we may exploit the biological knowledge that the actual interaction acts at the organelle level rather than the molecular level. For the latter, we hence analyze the interactions between the centers of the detected clusters across the two color channels. For the sake of simplicity, we do not explicitly model localization uncertainty, registration errors, and limited detection efficiency.

The results corresponding to the parametric potential that provided the best fit (in this case an L1 linear potential) are shown in Fig. 6.5. Figures 6.5c,d show the results of the analysis based on cluster centers, Figs. 6.5e,f those based on individual molecules. In both cases, the residual fitting error is 5-fold lower than when using a step potential. Figures 6.5g,h show controls obtained by randomly scrambling the cluster-center locations. We see that: (1) the plugin correctly infers an interaction (estimated $\varepsilon = 1.85$) in the data with cluster centers, but detects no interaction in the randomized control ($\varepsilon = 0.6$; the null hypothesis of no interaction has rank 512 of 1000 and cannot be rejected). (2) The results when applying the analysis to individual molecules or to cluster centers are similar, with the former estimating $\varepsilon = 2.0$, indicating that the analysis is robust against clustering effects and correctly identifies the length scale of the interaction. A randomization control based on individual molecules yields $\varepsilon = 0.3$ (data not shown), and the null hypothesis of no interaction cannot be rejected (rank 202 of 1000). This indicates that analyzing interactions between organelles by considering their cluster centers, rather than individual molecules, may be sufficient to distinguish an interacting pattern from a non-interacting one. Analysis with other potential shapes provided similar results.

## 6.4 Conclusions

We presented MosaicIA, an ImageJ/Fiji plugin for spatial point pattern and interaction analysis. The plugin takes as an input two 2D or 3D images showing the spatial distributions of two sets of bright, point-like objects, or it reads the coordinates of two sets of objects from files. It then uses a nearest-neighbor Gibbs interaction model from spatial statistics in order to infer the pair-wise interaction potential that is most likely to create the observed distribution of objects. Compared to classical pixel-based or object-based co-localization analysis, this makes better use of the information present in the image and hence provides superior statistical detection power (Helmuth et al., 2010). The analysis also accounts for the context created by the shape of the space within which the objects are distributed and by the object distribution within the reference set. Estimating interaction models is more robust against imaging noise and image-processing errors than classical co-localization analysis (Helmuth, 2010). Statistical tests are provided by the plugin in order to check the significance of an interaction. The estimated interaction parameters provide a quantitative way of comparing spatial patterns across different samples, conditions, and perturbations.

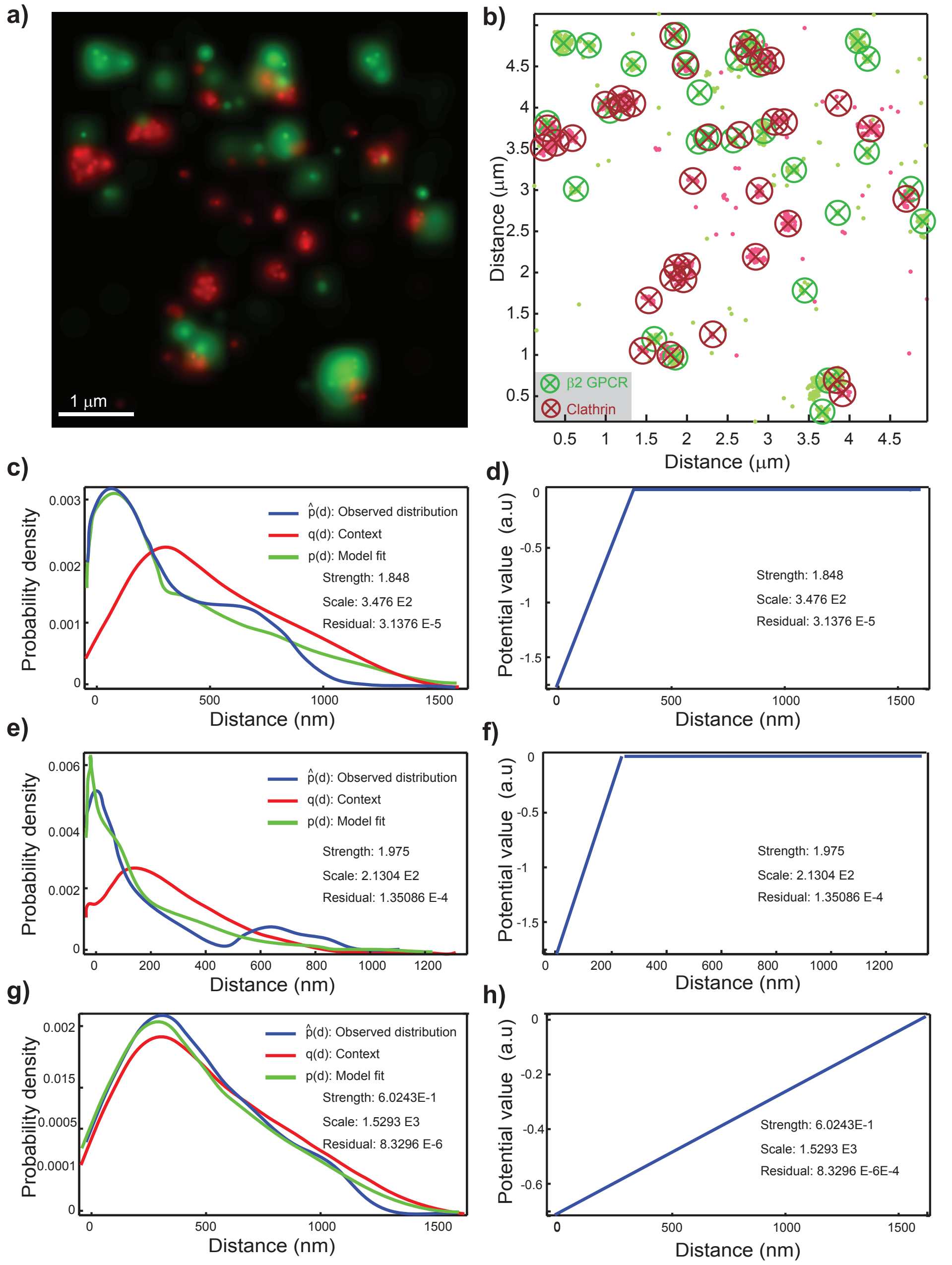

**Figure 6.5.** Results of applying the plugin to clathrin–$\beta$2-AR data from single-molecule PALM.

MosaicIA applied to PALM super-resolution imaging in fixed HeLa cells: The green channel ($X$) shows the GPCR protein $\beta$2-AR labelled with PSCFP2. The red channel ($Y$) shows Clathrin Light Chain-PAMCherry1. (**a**) Rendering of the PALM image as a probability map showing only molecules that localized into clusters of a given threshold size. (**b**) These molecules displayed as points without their corresponding localization uncertainty. Clusters of molecules are visualized by circles with × marking the cluster centers. (**c,e,g**) Distance distributions obtained after fitting the model with a linear L1 potential. (**c,d**) Fit and estimated interaction potential when using only cluster centers for the analysis. (**e,f**) Fit and estimated interaction potential when only using all individual molecules. (**g,h**) Randomization control using a randomly shuffled point pattern $X$ with the same number of points as in **c**.

The plugin has been tested on both synthetic and real-world data. We demonstrated its application to virus trafficking data obtained with confocal fluorescence microscopy and to PALM super-resolution data of the interaction between clathrin and $\beta$2-AR. In the latter case, we compared the results from applying the analysis to individual points with the results obtained from cluster centers. In all tested cases, the best interaction potential explained the data 4 to 5-fold better than a step potential, i.e., than context-corrected object-based co-localization analysis. Without context correction, the fits would be even worse.

Despite the fact that we have here only demonstrated the plugin for fluorescence microscopy and PALM data, it can be applied to distributions of any type of objects (organelles, cells, organisms), as long as their positions can be extracted from images or read from files. For example, in the case of cells in tissue, it can be applied with the help of segmentation methods that can provide the spatial location that best fits a cell (Qu et al., 2011). Comparing the model fits obtained with different parametric potentials can also be used to test and compare hypothetical interaction mechanisms directly on the data.

Future work includes extending the plugin to also handle extended objects that are not point-like, and to explicitly account for localization uncertainties and registration (aberration) errors. Other useful extensions could be testing for spatial randomness within a single set of objects, and automatic estimation of algorithm parameters from the data.

## 6.5 Author contributions

Designed the method and the software: IFS and AS, implemented the software: AS, performed the data analysis: AS and AR, wrote the paper: AS, IFS, and AR. All authors read and approved the final manuscript.

## Chapter 7

# Conclusions and outlook

This thesis started with a broad discussion of the challenges in using SMLM for quantitative studies(Section 1.2 and detailed review in Section 2.2). It was elucidated that the errors due to imperfect labeling, detection efficiency and localization precision, overcounting due to photoblinking, sample drift, fixation artifacts, and registration could significantly affect quantitative studies. Tools that account for these errors are therefore required.

The effect of imperfect localization precision and detection efficiency could be accounted for in quantitative analysis of spatial clustering by means of analytical tools that incorporate these sources of errors (Chapter 3). It was demonstrated (Section 3.2.1) that the popularly used spatial statistics tools in quantitative SMLM, the second order properties such as Ripley's $K$-function, $L(r) - r$ function and the PCF are *invariant* to $p$-thinning or independent subsampling, i.e., modeling the detection of a point as independent Bernaulli trials with a constant probability $p$, which is independent of spatial location. The estimators of these second order properties of the subsampled points are stochastic, due to the stochasticity in subsampling, with its mean being an unbiased estimator of the true value of the respective second order property. It was shown that the variance in the subsampled statistic can be analytically expressed as a function of true points and the sampling factor(the result is exact in the case of $K$-function). The methods were validated and the errors due to subsampling characterized using simulations. The results imply that for a large range of cluster conditions, the variance of the subsampled function is low for the detection efficiencies that are relevant to PALM. The applicability of the *invariance* result to limited detection efficiency in real experiments was also explored(Section 4.7), with positive results. The results are also applicable for two type second order properties such as cross correlation function, i.e. in co-localization analysis as well. The methods developed is not only limited to SMLM or microscopy, they are general results regarding these second-order properties that are widely used in spatial statistics.

The analytical method to estimate the variance given the true points, currently developed in exact form for one-type $K$-function and in the approximate form for one-type $L(r) - r$ function, can be extended to one type PCF and also for the two-type second order properties. Edge correction, e.g., proposed by Ohser (1991), can also be incorporated to this approach. Also, currently, one has to depend on simulations of true points to estimate the variance, since the true points are not known (only one realization of the subsampled points is known). It will be useful if the relation between the sampling factor and the variance due to subsampling can be established, perhaps as a function of observed points. Computational statistics approaches, such as bootstrapping, might be used for this purpose (Loh and Stein, 2004; Loh, 2008).

A framework to estimate the true locations of points that are imaged with imperfect localization precision was also proposed (Section 3.2.2 and 4.2). Such an approach can not only provide accurate estimates of true locations, but also improve the quantification of parameters such as cluster size, density, shape, strength etc. The estimator involves a three step procedure: first the localizations are clustered using a clustering algorithm, then the true cluster radius is estimated by means of some estimator for each cluster, and then the true point locations in each cluster estimated based on the observed localizations and the estimate of true cluster radius, using the maximum likelihood approach. This approach was observed to provide excellent results, when tested with simulations on Gaussian shaped clusters. The method was applied on real data – the clusters formed by photoblinking, and could provide results as expected( Section 4.3). It should be noted that purely for the characterization of true cluster sizes, step 3 (estimation of true locations) is not necessary. Also, an analytical method to estimate the second order properties given the true points and the localization precision for each point was developed (Section 3.4.3).

The estimator (of true locations)'s reliance on cluster-by-cluster analysis means that errors due to clustering could become significant. Performing informed clustering and selection of clustering parameters, and possibly the use more sophisticated parametric models (e.g. mixture models), or an extension based on nonparametric models, could help in this regard. It might be possible to also incorporate imperfect detection efficiency to improve this approach, e.g., by using Expectation Maximization (EM) algorithm (Dempster et al., 1977).

The clusters observed in biology can be of different structure and shapes, depending on the physical processes involved. It is important to identify the cluster model from data, not only with the aim of identifying the physical processes involved, but also for accurate estimation of cluster parameters(Section 4.4). Cluster parameter estimation could be a complicated problem. We studied the theoretical properties of an estimator that has been proposed to estimate the cluster size – the radius of maximum aggregation, obtained from the maxima of $L(r) - r$ function – for a variety of cluster processes (Section 4.5), and concluded that the relation between it and the true cluster size is crucially dependent on the true cluster radius as well as the number of clusters per unit area, and also on the cluster model. Previously, this relation was not clear, and our findings lead to more accurate parameter estimation.

As discussed in detail in Section 4.8, the estimators presented – whether for estimating true locations of clustered points observed with measurement error, or estimating true cluster parameters – are in general dependent on cluster shapes, and information about this becomes important in analysis, either from mechanistic formulations or identification from empirical data. Mechanistic formulations are more obvious in the case of certain systems (e.g., fluorophore blinking or simple internalizations). If such models are not available, robust spatial models that can describe the clusters, if possible, must be identified from data. In these lines, we also described a method in Section 4.6 to identify cluster models, based on clustering by a shape independent clustering algorithm, followed by the comparison of the Akaike Information Criteria (AIC) for the fits of each cluster to competing cluster models. Again, as mentioned above, it is important to perform careful and informed clustering, and more sophisticated (e.g. mixture models) or detailed models (non-parameteric ones, e.g.,) or improved models that account for errors due to clustering might help. Such a development in the context of more realistic biophysical models of clustering, and its application on SMLM experiments on membrane proteins in order to identify cluster models from data would be a very interesting future work.

One obvious and useful extension of the methods that account for localization uncertainty is to account for the errors in labeling as well. Use of label-linker structures of finite size, often in the 10nm range or more, especially in the case of immunolabelling, and possibly in an arbitrary orientation, could significantly affect quantitative analysis (Section 2.3.1, and Figure 2.3). True protein cluster model distributions, or approximations thereof, can be combined with realistic stochastic models for labeling, to obtain better quantitative information about the true structure.

The analytical methods described in this thesis is focused on the specific problem faced in spatial distribution analysis of membrane proteins in fixed cells. However, these methods are also valid in the case of live cell imaging, though other sources of errors associated with live imaging, such as in accurate single particle (molecule) tracking and location estimation (Sibarita, 2014), probably are the crucial limiting problems in such a case. Also, the reformulation of these methods, currently in 2D form, for 3D data, or by introducing provisions for membrane undulations etc, would lead to more accurate analysis.

Validation with relevant experimental tools, such as correlative microscopy involving both SMLM and AFM, can also aid the development of quantitative SMLM. Moreover, such correlative microscopy can provide complementary information: SMLM providing single molecule localization of specific species, while AFM providing high resolution information about its spatial context – cell morphology, membrane undulations, etc. Furthermore, the possibility of obtaining mechanical properties with AFM, or its use as a nanomanipulation tool, can be exploited. Chapter 5 discusses a correlative microscopic tool that was used to image actin filaments *in vitro* using STORM, and bacterial cells and live mammalian cells with PALM. We could identify that the density of localization in SMLM is correlated with the height information from AFM, and hence, attribute part of the localization inhomogeneities to physical differences in actin filaments (i.e., presence of single or multiple filaments), instead of labeling inaccuracies. The approach promises to be not only a useful validation tool, but also a new microscopy modality that can provide complementary information about the sample, which specifically designed experiments can take advantage of.

An important step in making quantitative SMLM a regular tool for biological experiments is the availability of easy to use, efficient software that can hide the complexity of correct but tedious computational methods under its hood. The MATLAB code for methods presented in Section 3.2.1 and Section 3.2.2 are available online (Shivanandan et al., 2015). An ImageJ plugin that incorporates these methods along with general spatial analysis tools relevant to SMLM, in an efficient, parallelized manner, is under development. Chapter 6 describes an ImageJ/Fiji plugin that implements a spatial interaction analysis framework that extends the concept of co-localization by using concepts from spatial statistics. The framework models spatial interactions between two-type (dual-color) point patterns as a nearest neighbour Gibbs function of an interaction potential. The interaction potential can be of different shapes (Figure 6.1), in contrast with the standard step-function in classical object based co-localization, improving statistical power for the test for interaction. The model also corrects for cellular context and provides a hypothesis test for interaction and a framework for model selection, and was shown to be robust against imaging noise. The plugin is not limited to SMLM localization data – it can also work with images, i.e., it works also with conventional FM. Section 6.3 describes the application of the plugin to virus-endosome confocal microscopy data and GPCR protein-clathrin PALM data.

In conclusion, the work presented in the thesis has identified many of the challenges faced in performing accurate quantitative SMLM. It has addressed some of these challenges, focusing on some of the most important ones, thus contributing to improved quantitative SMLM. In this endeavor, it has produced results that are not only applicable to SMLM, but often are more general, e.g., the analytical results and software are applicable to the vast domain of spatial statistics, or systems involving spatial point patterns.

# Appendix A

# Progress in quantitative single-molecule localization microscopy

*This is a verbatim copy of an article that has been published in a peer reviewed journal: H. Deschout, A. Shivanandan, P. Annibale, M. Scarselli, and A. Radenovic. Progress in quantitative Single Molecule Localization Microscopy.* Histochem Cell Biol*, 142(1):5–17, 2014a*

## A.1 Introduction

With the invention of single-molecule localization microscopy (SMLM) techniques (Betzig et al., 2006; Rust et al., 2006; Hess et al., 2006), it has become possible to image intracellular proteins with high contrast at a hitherto unprecedented resolution in conditions that resemble their natural environment. Nowadays, SMLM is starting to be used routinely for imaging of biological samples in 2D and 3D, in fixed and live cells, and in multiple colors (Oddone et al., 2014; Klein et al., 2014).

SMLM techniques can be used for quantitative studies, e.g., counting proteins in a single cell, analyzing the spatial organization of proteins, or estimating co-localization between organelles that are smaller than the optical diffraction limit or even between single molecules. SMLM can also be used for other types of quantitative measurements, for instance in single-particle tracking (SPT) mode (Manley et al., 2008; Persson et al., 2013). The high labeling specificity offered by fusion proteins, and the relatively low chance of overcounting caused by repeated imaging of the same fluorophore due to the phenomenon of photoblinking, makes photoactivated localization microscopy (PALM), among the different SMLM techniques, a relatively better choice for quantitative imaging.

However, to use SMLM/PALM for quantitative measurements, a number of issues have to be overcome. Since these techniques provide localizations of individual fluorescent molecules rather than a single image, the tools required for quantitative analysis are often different from these in conventional fluorescence microscopy. Also, imaging with PALM involves multiple sources of errors, such as: overcounting of commonly used fluorescent proteins in the range of 100 % due to photoblinking (Annibale et al., 2010; Lee et al., 2012), limited detection efficiency in the range of 40–60 % related to incomplete photoconversion (Annibale et al., 2012; Durisic et al., 2014b); uncertainty in the localization of molecules in the order of 15–50 nm caused by, among other factors, a limited number of detected photons (Mortensen et al., 2010; Thompson et al., 2002); and sample drift during the long imaging time in the order of 50 nm (Betzig et al., 2006). In the case of co-localization analysis using PALM, additional challenges exist in the form of the limited number of available spectrally separate fluorescent proteins for multi-color imaging, and that of accurately overlaying the images from the two-color channels (Annibale et al., 2012). It must also be mentioned that the computational methods used in SMLM, i.e., the image processing and localization algorithms, can be another source of error in quantification (Deschout et al., 2014b; Small and Stahlheber, 2014).

Here, we review the recently reported efforts toward solving some of the problems that affect quantitative SMLM measurements. In particular, we focus on PALM and its commonly reported applications: counting single molecules, analyzing protein organization, and measuring co-localization on the single-molecule level.

## A.2 Single-molecule counting with PALM

Several important cellular functions involve low-copy number proteins that are not detectable by conventional measurement techniques (Ghaemmaghami et al., 2003). Also, studies dealing with the stochastic nature of gene expression and its importance in biology (Elowitz et al., 2002; Raj and van Oudenaarden, 2008) require accurate and precise single-molecule counting. while omics-scale abundance data with single-molecule sensitivity can be obtained from conventional fluorescence microscopy (Taniguchi et al., 2010), the spatial resolution is limited due to the diffraction of light. PALM, with the possibility of single-molecule resolution counting in sub-diffraction limit voxels, therefore clearly offers interesting prospects in this field.

In order to use PALM for counting, the ideal scenario would be that each fluorescent protein present is counted once and only once. However, there are at least two critical issues that result in counting errors - under-counting due to a limited detection efficiency and overcounting due to multiple appearances of the same fluorophore. Due to the limited detection efficiency inherent to fluorescence microscopy, resulting from misfolding and incomplete maturation of the fluorescent proteins, only a fraction of the molecules can be imaged. In conventional fluorescence microscopy, this fraction is about 80% for GFP (Ulbrich and Isacoff, 2007). In PALM, even lower fractions are observed, because of the limited photoconversion efficiency. A fraction of 53-60% has been reported for the relatively bright mEos2 (Annibale et al., 2012; Durisic et al., 2014b), and many other fluorescent proteins perform even worse.

Various methods have been developed to work around this obvious limitation. Diffraction-limited protein subunit stoichiometry estimation can be performed by observing the bleaching steps of individual fluorophores attached to the subunit molecules. This method was used to estimate the subunit stoichiometry of membrane proteins (specifically, NMDA receptors) in live cells, composed of two different subunits, by means of labeling with GFP (Ulbrich and Isacoff, 2007). The detection efficiency of GFP was estimated by fitting the observed number of bleaching steps to a binomial model for detection. A similar approach was used to estimate the subunit stoichiometry of heteromeric glycine-gated channels (GlyRs) (Durisic et al., 2012). In the context of SMLM, the stoichiometry of the asialoglycoprotein receptor complex in rat hepatic lectin 1 (RHL1) and rat hepatic lectin 2 (RHL2) was estimated by single-molecule counting (Renz et al., 2012). The problem of limited detection efficiency was avoided by focusing on the ratio of detected molecules. First, the relative detection efficiency of paGFP/paCherry was characterized, by performing dual-color PALM on a 1:1 fusion construct. Subsequently, dual-color PALM was used to investigate the homo/hetero-association, by determining the ratio between the counts of paGFP-RHL1/paCherry-RHL1 pairs and paGFP-RHL1/paCherry-RHL2 pairs, respectively. In another work, the expected ratio between monomers and dimers of pamCherry1 for a given detection efficiency was modeled, and was fit to data to estimate the detection efficiency (Nan et al., 2013).

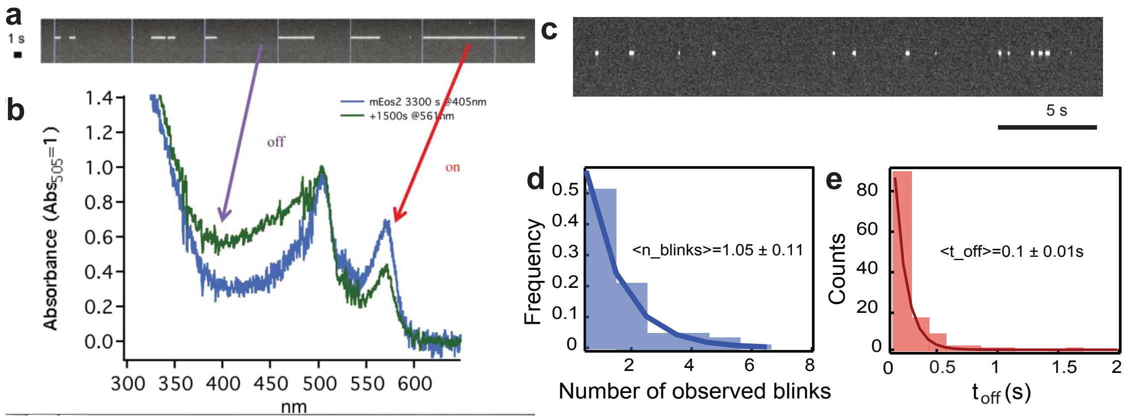

**Figure A.1.** Photoblinking: on/off times.
a A single-molecule kymograph of an individual mEos2 molecule, upon pulsed 405 nm irradiation (blue vertical lines). Taken from Annibale (2012). b The spectral evolution of partially photoconverted mEos2 upon 561 nm irradiation, displaying an increase in 405 nm absorbance, corresponding to the protonated form of the red fluorescent state. Taken from Annibale (2012). c The photoblinking phenomenon exists even at continuous activation. A typical kymograph of an mEos2 molecule embedded in a polymer gel, upon continous 405 nm irradiation at low intensity. Taken from Annibale et al. (2011a). d A histogram of the number of times a single mEos2 molecule undergoes photoblinking (nblink) before definitive photobleaching. Experimental values based on a single exponential best fit are shown, the 1/e decay values indicate a mean of nblink = 1.05 ± 0.11. Taken from Annibale et al. (2011b). e A histogram of the measured dark times showing a mean of toff = 0.10 ± 0.01 s. Taken from Annibale et al. (2011b).

Another phenomenon that critically affects counting in SMLM is that of overcounting due to photoblinking. In one of the first quantitative studies involving PALM, the photo-blinking behavior of the fluorophore (i.e., tdEos) was not taken into account (Greenfield et al., 2009). In the case of its monomeric form mEos2, the phenomenon of photoblinking was investigated by systematic inspection of the fluorophore traces of immobilized molecules in polymer gels (Annibale et al., 2010). Similar to the long-lived dark state of GFP (Dickson et al., 1997), it was found that the activated and excited mEos2 (i.e., on-state) might reversibly go to a long-lived dark state instead of getting photobleached, and later come back to the bright state, as illustrated in Figure A.1a–c. This means that, due to this "blinking" phenomenon, the same molecule might be counted multiple times by a localization algorithm that does not correct for it. In vitro experiments on gels showed that roughly half of the mEos2 molecules are reactivated at least once (Figure A.1d), making it possible that the molecules are overcounted by a factor of 2. In the case of paGFP, the number of reactivations is lower, and for a photoswitchable fluorescent protein such as Dronpa, the number is higher, as shown in Figure A.3b (Annibale et al., 2011b). Similar photophysical behavior has been reported for the photoconvertible fluorescent protein mMaple (McEvoy et al., 2012). Since the time spent in the dark state (toff) is orders of magnitude lower than the duration of the experiment, photoblinking will form small clusters in a time series plot of the localizations for the whole duration of the experiment, as illustrated Figure A.2. This immediately suggests a method to account for photoblinking: by using a threshold in time (td) and in space, it is possible to partition these traces in spatial-temporal clusters, and to assign each cluster to one molecule. This apparently simple method was found to be highly effective in correcting for photoblinking (Figure A.2) Annibale et al. (2011a).

How to select the optimal td? By collecting the localizations within a set spatial radius that depends on labeling density and localization uncertainty, and within a time interval td,

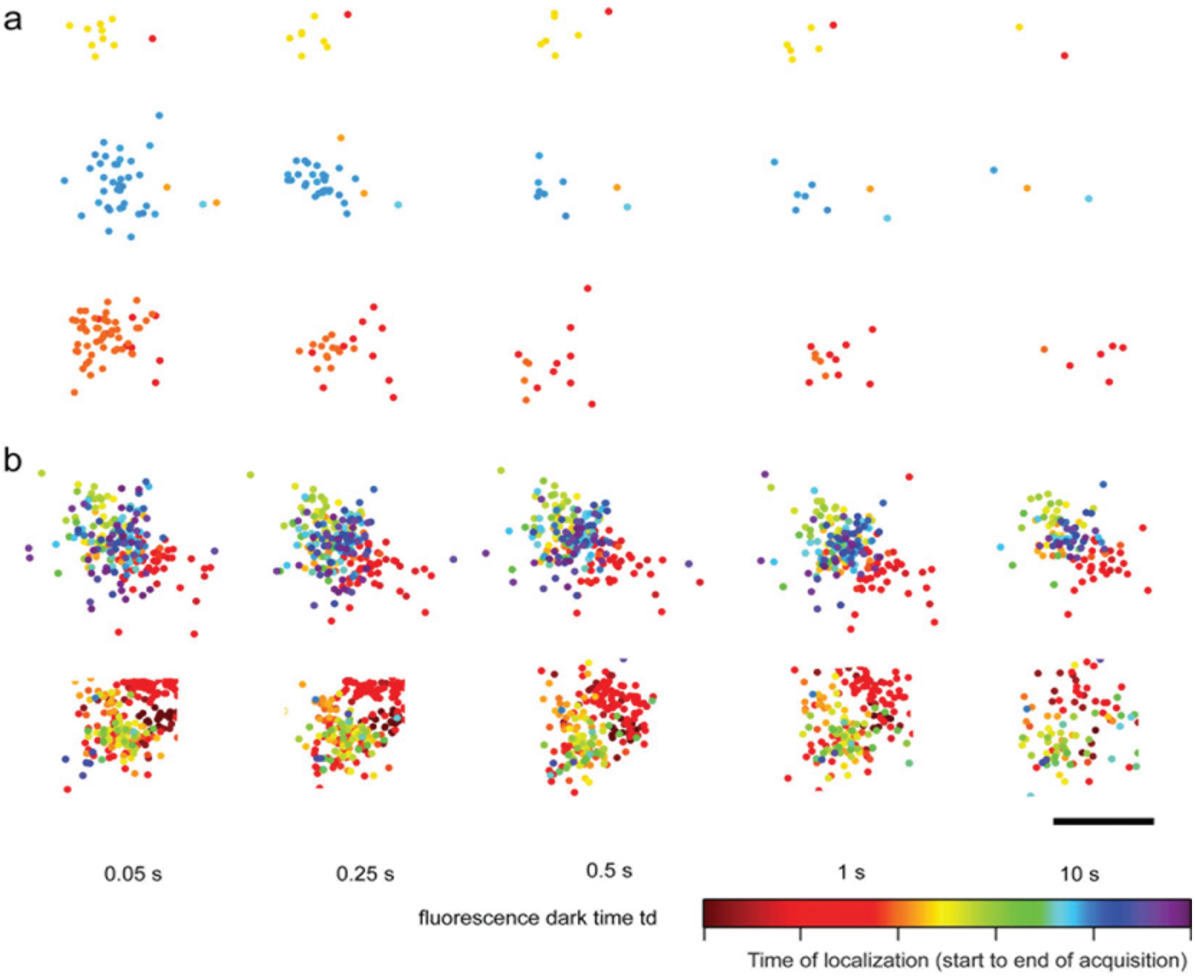

**Figure A.2.** Clusters due to photoblinking: effect of dark time td.
Snapshots of clusters formed by localizations of membrane proteins in fixed HeLa cells. Markers represent single-molecule localizations and their color represents the time of localization. a Representative images of three artifact spatial-temporal clusters of SrcN15-mEos2 (a negative control for clustering) and their evolution for increasing values of the allowed fluorescence dark time threshold td. b Representative images of two $\beta$2-mEos2 clusters and their evolution with the fluorescence dark time threshold td. A temporal artifact component (red sub-cluster) is also visible in the second cluster. The estimated location of the molecules changes slightly from one td value to another since the number of collected photons and their spatial distribution attributed to each localized molecule changes. Scale 100 nm. Taken from Annibale et al. (2011b).

and counting them as one localization after performing weighted averaging, it is possible to compute the number of molecules N(td) counted for different values of td. It was found that the empirical N(td) curve obtained in this way fits well to a negative exponential function, as shown in Figure A.3a. That is, for larger values of td, the improvement in counting accuracy becomes asymptotically lower. Also, setting a too high value for this parameter might result in missed localizations, i.e., localizations corrresponding to different molecules getting grouped together as one. Therefore, depending on the nature of the application, the value of td should be selected so as to minimize the errors coming from both the multiple counting of a photo- blinking molecule and the missed localizations, or a conservative value of td should be chosen so that the observed count is a lower bound, see Figure A.3a (Annibale et al., 2011b).

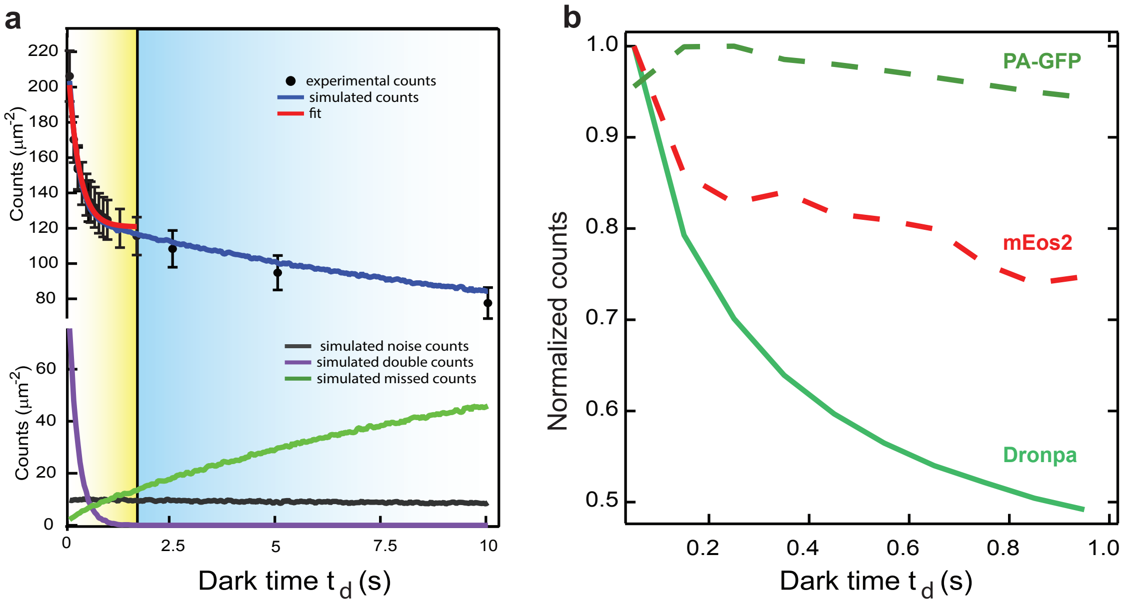

**Figure A.3.** Schematic of PALM image reconstruction and time-sequence. a The experimental (markers) and simulated (blue curve) counts of mEos2 molecules localized as a function of the dark time threshold td, together with the simulated counts ascribed to missed counts (green), multiple counts (violet), and noise (black). For all samples, the duration of the acquisition is 20,000 frames x 50 ms. The red curve shows the best fit to the data for td values between 0.05 and 2 s. If no missed counts were to occur, the asymptote of the decaying curve of the observed counts would converge to the effective number of molecules present in the sample. Fitting to a negative exponential model yielded a mean of toff = 0.260 s and a mean of nblink = 0.760, consistent with what was shown in Figure A.1d and e respectively. The fit yielded N = 121 ± 6 molecules/um2, whereas the total density of the simulated sample was 135 molecules/um2 including noise counts, resulting in a 10 % error. Taken from Annibale et al. (2011b). b Comparison of the normalized estimates for counts of localized molecules as a function of td, for three different fluorescent proteins: paGFP, Dronpa and mEos2. Taken from Annibale et al. (2011b).

Lee et al. (2012) introduced a more detailed model for N(td), and, based on its photobleaching and blinking behavior, proposed Dendra2 as a better alternative to meos2 for counting purposes. Additionally, an imaging strategy called Fermi photoactivation was proposed, which improves the temporal separation in the activation of different molecules, thus helping to overcome under- counting due to the overlapping of molecules in the initial frames of imaging, which might occur when using a fixed activation power during the whole imaging time (Lee et al., 2012). On the other hand, by assuming that the probability of activating a molecule remains constant over time, a relationship between the cumulative number of localizations and the imaging time was found (Gunzenhäuser et al., 2012). Such a relationship can provide a stopping criterion for imaging, given a target accuracy in counting. The method was applied to imaging the HIV structural protein Gag labeled with tdEos and also with mEos2.

Alternatively, a method based on Kalman filtering has been proposed, in order to scan and group photoblinking molecules (Lando et al., 2012). A very different approach, based on the spatial pair correlation function (PCF), was inspired by the special case of spatial cluster analysis of membrane proteins and utilizes the difference between the spatial signature of the multiple appearances of the same molecule due to photoblinking and that of the true protein clusters (Sengupta et al., 2011). Another method was proposed to estimate the average number of localizations per molecule in samples that form definite spatial structures (e.g., microtubules or actin filaments), mainly in the context of stochastic optical reconstruction microscopy (STORM) (Nieuwenhuizen et al., 2013). This approach, based on Fourier ring correlation analysis, can also be used to estimate the resolution obtained in SMLM images, although only samples with definite spatial structures were investigated. Others have reported a similar measure to estimate the resolution in SMLM (Banterle et al., 2013).

## A.3 Quantitative analysis of heterogeneity in protein spatial organization

One of the niche areas in cell imaging that SMLM appeals to is the study of spatial heterogeneity in protein organization; e.g., that of membrane proteins appearing as micro-or nanodomains rather than individual molecules diffusing freely along the membrane, and its function in, for instance, signaling. In addition to membrane proteins, other systems with spatial heterogeneity can also be studied with SMLM. Indeed, SMLM has been used to study protein spatial organization in various systems including signaling receptors in the Escherichia Coli chemotaxis signaling network (Greenfield et al., 2009), signaling proteins in T-cells (Rossy et al., 2013; Williamson et al., 2011), GPI-anchored proteins (Sengupta et al., 2011), G protein-coupled receptors (GPCRs) (Scarselli et al., 2012), SNAP receptor (SNARe) complexes (Pertsinidis et al., 2013), and RNAP in E. coli (Endesfelder et al., 2013). while most of these studies have focused on the characterization of heterogeneity in spatial organization and its dependence on different conditions, some have even used the estimated parameters to fit biophysical models(Greenfield et al., 2009; Hess et al., 2007). A brief discussion of some of the questions and studies in this field can be found elsewhere (Lang and Rizzoli, 2010; Owen and Gaus, 2013).

Various clustering and cluster analysis techniques have been used for the analysis of spatial heterogeneity in SMLM images, in particular the quantification of nanodomain properties and their comparison at different conditions. These approaches can be divided into two broad categories: (1) exploratory analysis tools from spatial statistics that have been used for similar problems in electron microscopy (Parton and Hancock, 2004; Zhang et al., 2006), such as PCF and Ripley's $L(r) - r$ function, or the nearest neighbor distance distribution (Endesfelder et al., 2013) and (2) clustering by means of algorithms such as density-based spatial clustering of applications with noise (DBSCAN) (Ester et al., 1996), followed by analysis of the obtained clusters by various methods to estimate cluster parameters, e.g., by averaging or by fitting each cluster to a normal distribution to estimate the cluster radius.

An introduction to the first approach can be found elsewhere (Diggle, 2003; Gould et al., 2012). Briefly, the Ripley's $K(r)$ function is the ratio of the average number of extra localizations within distance r of a randomly chosen point and the density of localization in the area of analysis, and $L(r)$ is the transformation $K(r)$ with certain convenient properties. For instance, $L(r) - r$, by definition, is equal to zero for a point pattern that is distributed completely at random, i.e., complete spatial randomness (CSR). $L(r) - r$ is greater than zero if the points are clustered and is less than zero if the point pattern shows regularity. The magnitude of $L(r) - r$ is a measure for the degree of clustering and can be used for comparison between different conditions. The value of $r$ corresponding to the maximum of $L(r) - r$ gives an estimate of the average cluster radius in the point pattern. The PCF $g(r)$ is a closely related measure, $K(r)$ being the integral of $2prg(r)$, and it can also provide estimates of parameters like the ones mentioned above. These measures can also be used to estimate other parameters such as the number of localizations per cluster (Parton and Hancock, 2004; Zhang et al., 2006; Sengupta et al., 2011), and the effective potential of the mean force between the localized molecules (Veatch et al., 2012). The $L(r) - r$ function has an advantage when compared to the PCF in that, since $L(r) - r$ is based on an integration over the radius $r$, it is less influenced by noise. On the other hand, this also means it is less sensitive and that systematic errors such as overcounting due to photoblinking are accumulated over $r$. Therefore, when this measure is used, photoblinking artifacts must be accounted for by one of the methods mentioned in the section on counting.

The first approach, i.e., exploratory tools such as PCF or Ripley's function, has been extended to account for some error sources inherent to SMLM. In a technique called pair correlation PALM (PC-PALM), the PCF approach is extended by means of a model to differentiate the artifact clusters due to fluorophore photoblinking from true proteins clusters (Sengupta et al., 2011). Modifications of the $L(r) - r$ function have been suggested to incorporate membrane curvature characteristics, since 2D imaging of proteins in undulating membranes can cause clustering artifacts (Owen et al., 2013). This work also shows the applicability of Ripley's function in the case of 3D localization data. while this approach is promising, it uses $L(r) - r$ only to identify clusters (Owen et al., 2010), rather than as an exploratory statistical tool to be used for inference and comparison (Hess et al., 2007; Lillemeier et al., 2009; Scarselli et al., 2013).

The nearest neighbor approach as an exploratory tool involves finding the nearest neighbor distance distribution within a point pattern and comparing it to one that corresponds to a point pattern distributed by CSR. The contrast between the nearest neighbor distance method and correlation methods such as $L(r) - r$ or PCF is that, since the former looks at nearest neighbors only, it focuses on information on the short scale, whereas the latter gives information on a variety of scales.

It should be noted that Ripley's function and PCF are defined for a stationary, spatially homogeneous point process only, i.e., the average density within the point pattern is assumed to be independent of the spatial location. If the point process is spatially inhomogeneous, e.g., due to a spatial gradient in protein locations, other extensions must be used in order to be statistically more accurate (Baddeley et al., 1998). Also, the inevitable choice of limiting the analysis to a window results in the exclusion of the points near the borders, often resulting in a significantly biased estimation. various edge correction methods are available to correct for this bias (Haase, 1995).

In the case of the second approach, i.e., clustering followed by parameter inference, various algorithms are used for the clustering part. The DBSCAN algorithm is the most popular one (Annibale, 2012; Endesfelder et al., 2013; Nan et al., 2013; Pertsinidis et al., 2013), although other methods have also been used (Gunzenhäuser et al., 2012; Lelek et al., 2012; Owen et al., 2010). DBSCAN works by exploiting the density difference between clusters and the background, i.e., the density in the neighborhood of a point must exceed a threshold in order to be identified as part of a cluster. This method has several advantages over other commonly available clustering algorithms, including that it does not need an a priori number of clusters to be provided as input, that it can identify clusters of arbitrary shapes, and that it can account for background noise (and for a monomer fraction). An algorithm based on DBSCAN to account for errors in clustering due to the presence of localization uncertainty in PALM was used to study RAF multimer formation and signaling (Nan et al., 2013). However, identifying the parameters required by DBSCAN is another problem, which is often solved empirically (Annibale, 2012; Endesfelder et al., 2013; Pertsinidis et al., 2013), even though some have used the heuristic suggestions of the original DBSCAN paper on how to set the parameters (Bar-On et al., 2012). extensions such as OPTICS that do not need these parameters as input might also be useful (Ankerst et al., 1999).

The choice between the two above-mentioned approaches depends on the problem at hand. In general, the first approach (i.e., exploratory tools such as PCF or $L(r) - r$) is less arbitrary than the second one (i.e., clustering followed by characterization). However, since PCF or Ripley's function estimate an ensemble parameter, e.g., cluster radius, for the whole area of analysis rather than for individual clusters, they may not be the ideal tool if the parameters show significant variation between clusters. Similar problems might arise if the cluster shapes are elliptical or asymmetric and the study of the shape parameters is important. In such cases, the approach of clustering followed by parameter estimation for individual clusters might be more suitable.

Protein assemblies such as nuclear pore complexes (NPCs) are ideal systems for the application of SMLM, due to their fixed protein stoichiometry and structure. Systematic labeling of different NPC components combined with averaging of thousands of corresponding SMLM images allowed the creation of a human NPC scaffold structure model with a localization uncertainty well below 1 nm (Szymborska et al., 2013). In this study, imaging with both immunolabeling as well as fusion protein/nanobody labeling were done separately, and in the case of many proteins, the former was found to systematically overestimate the NPC radius by around 7 nm (about 15 %), possibly due to the larger size of primary and secondary antibodies. Prior work on NPCs with a similar averaging approach had also achieved major improvements in resolution (Loschberger et al., 2012). Integrated targeted proteomics and PALM were used by Ori et al. (2013). to determine the absolute stoichiometry of the NPC, which was found to vary across different human cell lines (Ori et al., 2013).

## A.4 Toward quantitative co-localization with dual-color SMLM

Having reviewed in the previous two sections the SMLM-based methods for counting single molecules and investigating protein spatial heterogeneity, we will now discuss the ability of dual-color SMLM to measure co-localization on the single-molecule level. Fluorescence microscopy in general is an excellent tool to probe potential interactions between cellular objects by measuring their co-localization. This requires labeling of the different objects with spectrally separate fluorophores and subsequent recording of an image in each of the corresponding color channels. The co-localization between the objects can then be visualized by simply overlaying the images. Quantification is also possible, for instance, by estimating the correlation between the pixel values in the overlaid images (Bolte and Cordelières, 2006; Dunn et al., 2011; Zinchuk et al., 2007). while the resolution in diffraction-limited microscopy usually restricts the interpretation of co-localization to the level of organelles or other objects of similar size, far more detailed information is offered by SMLM. In theory, these techniques even allow to investigate the co-localization between individual molecules. As a consequence, SMLM techniques are already being embraced by biologists that aim to unravel the mechanisms that govern protein-protein interactions (Lehmann et al., 2011; Lubeck and Cai, 2012; Sherman et al., 2011; Winckler et al., 2013). In the following sections, we will review the practical problems that are present in using dual-color SMLM for quantitative experiments and discuss the recent approaches to solve those problems.

### A.4.1 Image registration

One key requirement for co-localization analysis is a sufficiently precise overlay of the images in the different color channels. This is especially challenging for SMLM-based co-localization, since the images are rendered from single fluorophore locations that are usually determined with an uncertainty in the order of 15–50 nm (Mortensen et al., 2010; Thompson et al., 2002). The procedure for aligning the images, i.e., the image registration, starts with localizing fiducials that are visible in the different color channels. This results in a list of positions for each color channel that should be identical after alignment, allowing to estimate a function that maps one channel onto another one (Goshtasby, 1988). Different

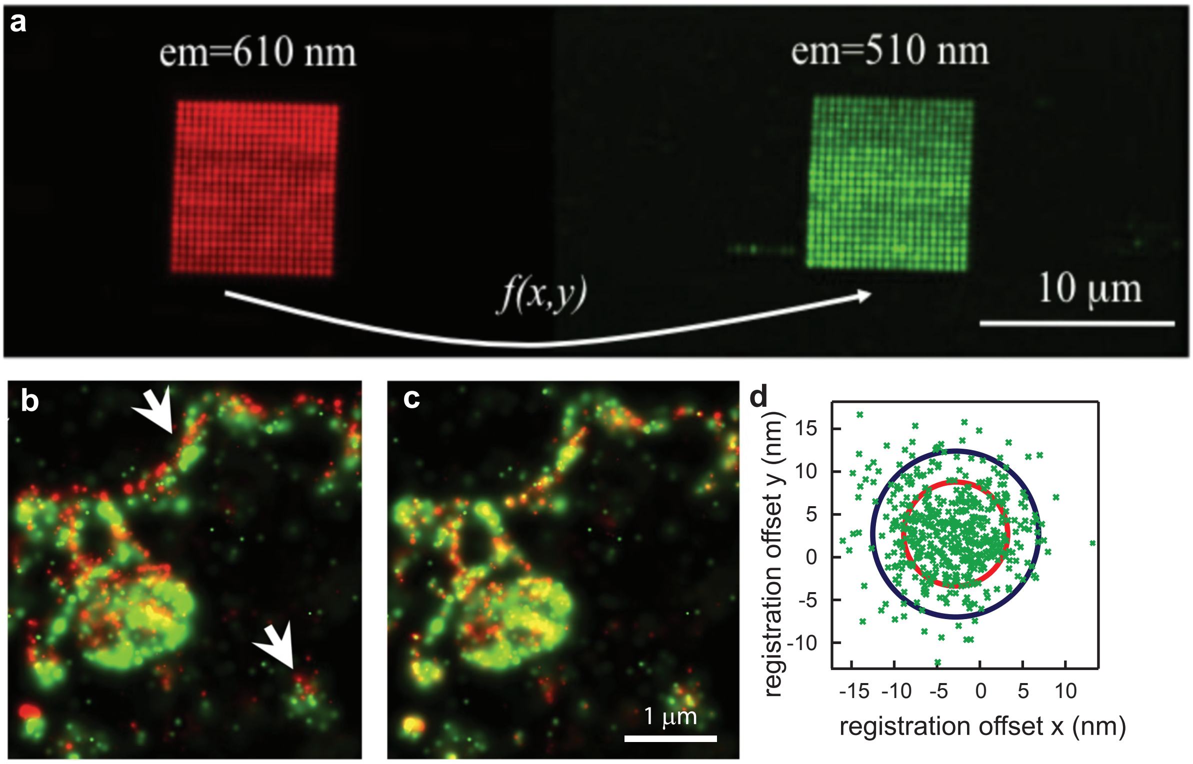

**Figure A.4.** An illustration of the image registration procedure to align images from different color channels.

a An image obtained by integrating the images in the green and red channel of a fiducial scanned across a square grid with a size of ≈ 10 um. b An overlay of the red and green PALM images of a membrane patch of a cell that expressed the protein SrcN labeled with a fusion construct of psCFP2 and mEos2, prior to image registration and c after image registration. d A scatter plot of the residual offset $x_g - x_r$ and $y_g - y_r$, with $x_g$ and $x_r$ being the x-coordinates in the green and red channel respectively, and $y_g$ and $y_r$ being the y-coordinates in the green and red channel respectively. The blue circle has a radius of 10 nm, the red circle has a radius given by $\sigma_g^2 + \sigma_r^2 + TRE$, with $\sigma_g$ and $\sigma_r$ being the localization precisions in the green and red channel respectively. The residuals were extracted from the trajectory of a fluorescent bead with 100 nm diameter, immobilized on the coverslip and imaged during a time lapse movie. Adapted from Annibale et al. (2012) and Annibale (2012).

types of fiducials have been reported, such as a lattice that contains optical holes in a grid with known spacing (Koyama-Honda et al., 2005; Pertsinidis et al., 2013) or a geometrical structure inside the sample itself, such as the center of the ring-shaped nuclear pore complex (Loschberger et al., 2012). A more popular type of fiducials that do not require special manufacturing or prior knowledge of the sample are beads that are fluorescent in both color channels (Baddeley et al., 2011; Bates et al., 2012; Churchman et al., 2005; Lehmann et al., 2011). In order to illustrate the importance of image registration, dual-color PALM was performed on a fusion construct of psCFP2 and mEos2 attached to the cell membrane protein SrcN (Annibale et al., 2012). An isolated bead was used as a fiducial, and it was moved in the field of view along a grid pattern, using a piezo stage, and at each grid position an image was recorded in both color channels, as illustrated in Figure A.4a. It is clear that a correct overlay was obtained only after image registration, as can be seen in Figure A.4b and c.

In order to properly interpret the measured co-localization, it is necessary to quantify the precision of the image registration procedure. One often used measure for this precision is the target registration error (TRE), which can be interpreted as the mean offset between the positions of the fiducials in both color channels after image registration (Churchman et al., 2005; Cohen and Ober, 2013). TRE values below 10 nm are typically reported (Annibale et al., 2012; Bates et al., 2012; Churchman et al., 2005; Malkusch et al., 2012; Pertsinidis et al., 2013), and one study even achieved a TRe below 1 nm within a single pixel, by accounting for pixel response non-uniformities and mechanically stabilizing the microscope with an active feedback system (Pertsinidis et al., 2010). The evolution of the image registration precision over time was investigated by recording a time lapse movie of a bead, while using an axial stability feedback system(Annibale et al., 2012). During acquisition, the bead followed a trajectory determined by the lateral drift of the setup. while the TRe was 4.5 nm, the mean of the differences between the positions of the bead between both color channels after registration had a larger value of 6.7 nm, possibly due to long-term mechanical instabilities, as shown in Figure A.4d.

### A.4.2 Fluorescent protein pairs

If the detection efficiency for the label in one channel is $x$, and that in the other channel is $y$, then the estimated co-localization underestimates the true co-localization by a factor $xy$, assuming a linear relation to the co-localization measure used. In other words, the correct estimation of co-localization in dual-color PALM experiments is possible only if the fraction of fluorescent proteins that did not photoconvert to the on-state is accounted for. Several investigations have been undertaken to measure the photoconversion efficiency of different fluorescent proteins, for instance, by monitoring the change in the absorbance spectrum of a solution upon irradiation with 405 nm light (Annibale et al., 2012; Wiedenmann et al., 2004). However, the photoconversion efficiency of a fluorescent protein in this in vitro environment might be altered with respect to the cellular environment. One recent study has, therefore, attempted to measure the photoconversion efficiency inside cells, by counting either the photoconversion or the photobleaching events corresponding to individual fluorescent proteins that are attached to the subunits of the cell membrane receptor GlyR (Durisic et al., 2014b). Among several other fluorophores, they found a photoconversion efficiency of 60 % for mEos2 50 % for pamCherry. Multiplication of these values can be used as an estimate of the efficiency with which the co-localization between the corresponding fluorophores can be observed.

However, such an estimate might not reflect the true co-localization efficiency, as it is determined from single-color PALM experiments, while the illumination procedure in a dual-color PALM experiment can increase the rate at which fluorescent proteins photobleach before being photoconverted to the on-state. Dual-color PALM experiments performed on 1:1 fusion constructs of both fluorescent proteins, for instance inside a polymer gel or attached to a membrane protein, provide a solution (Annibale et al., 2012; Renz et al., 2012). Since one observes the same fluorophore pattern in both color channels, the measured fraction of co-localized fluorophores provides an alternative estimate of the co-localization efficiency. This fraction was measured for fusion constructs of three pairs, namely: psCFP2-pamCherry, Dronpa-mEos2 and psCFP2-mEos2 (Annibale et al., 2012). For the latter pair, virtually no co-localization was found, probably due to photobleaching of psCFP2 during activation of mEos2. The other two pairs gave rise to a 15 % co-localization fraction, which can partially be explained by the photoconversion efficiencies of the fluorophores. Although mEos2 has a superior photon yield, psCFP2 and pamCherry are arguably the most suitable pair for dual-color PALM, since pamCherry is not fluorescent in the off-state and therefore allows simultaneous image acquisition in both color channels.

### A.4.3 Co-localization analysis

The output of an SMLM experiment can be represented as a pixelated image, for instance, by giving each pixel a value that scales linearly with the number of localized fluorophores inside the area that corresponds to that pixel. This means that intensity-based co-localization methods that rely on quantifying the correlation between the pixel values of images in different color channels (Bolte and Cordelières, 2006; Dunn et al., 2011; Zinchuk et al., 2007) can in principle be applied. However, such correlations are challenging to interpret, as they are highly susceptible to overestimation caused by noise and bleed-through(Bolte and Cordelières, 2006). One recent study reports a method that allows correcting for bleed-through in the context of SMLM (Kim et al., 2013).

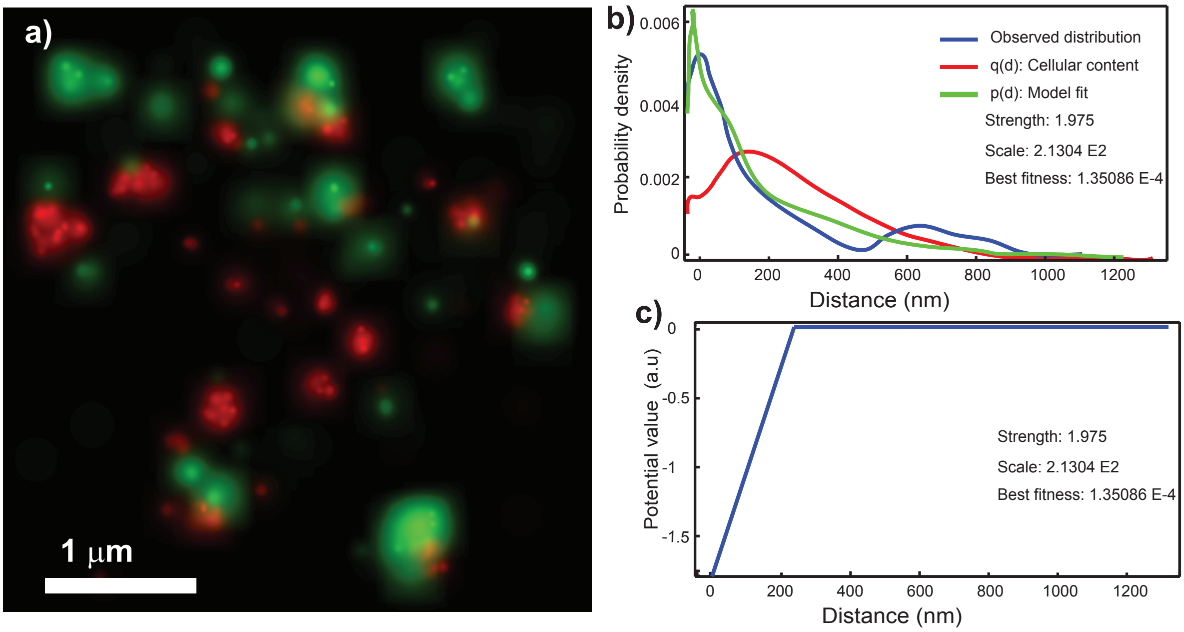

**Figure A.5.** Spatial interaction analysis of dual-color PALM images.
The method uses a nearest neighbor spatial interaction model based on Gibbs statistics, which characterizes an interaction by means of a potential (Helmuth et al., 2010). a Dual-color PALM data represented as probability maps. The green channel shows the GPCR protein $\beta$2- adrenergic receptor labeled with psCFP2, and the red channel shows clathrin light chain labeled with pamCherry (Annibale et al., 2012) and (Annibale, 2012). b Results of interaction analysis: the observed nearest neighbor distance distribution between the two channels (blue); the result of fitting the spatial interaction model with a linear L1 potential to this distribution (green); the curve corresponding to the null hypothesis of “no interaction”, estimated by accounting for the intra-point pattern distance distribution (red). The method also returns the inferred parameters (i.e., strength and scale) that can be used for comparison. c The inferred interaction potential. Adapted from (Shivanandan et al., 2013).

Since raw SMLM data consist of locations of individual fluorophores, object-based co-localization methods (Bolte and Cordelières, 2006) can be used without any prior data processing. Usually, co-localization between objects in different color channels is investigated by calculating the distance between their positions and comparing it to a predefined threshold. However, it is challenging to define an optimal value for this threshold, and sometimes a rather arbitrary value of 200 nm based on the diffraction-limited resolution is used. An object-based method was, therefore, recently developed that can estimate the threshold value from the data, by modeling the nearest neighbor distance distribution in a spatial statistics framework that estimates a spatial interaction potential between the objects in the different color channels (Bolte and Cordelières, 2006; Helmuth et al., 2010). In addition to this feature, the method also extends the classical threshold-based co-localization by providing other interaction "potentials" apart from the threshold function, and also incorporates in the model the spatial distribution of objects within a point pattern. The latter corrects for the fact that estimates of spatial interaction, e.g., co-localization, depend on the intra-object spatial distribution. This method was found to be robust against errors in the identification of the objects by image processing. In the context of PALM, this method was applied to investigate the co-localization between pamCherry-labeled clathrin-coated vesicles and psCFP2-labeled GPCRs during internalization (Shivanandan et al., 2013), as illustrated in Figure A.5. Another solution for the dependency of co-localization on the intra-object distribution has recently been reported by taking into account the spatial distribution of the objects (Malkusch et al., 2012). This object-based method has the extra advantage that it corrects for photoblinking. Another approach that is frequently reported in the context of SMLM-based co-localization is the spatial cross-correlation analysis which uses the bivariate version of the PCF, called the cross-correlation function (CCF) (Gunewardene et al., 2011; Pertsinidis et al., 2013; Sengupta et al., 2011; Veatch et al., 2012).

## A.5 Conclusion and outlook

We have reviewed recent developments in SMLM for counting single molecules, analyzing the heterogeneity of the spatial distribution of proteins and measuring co-localization on the single-molecule level. As quantitative SMLM-based methods for these purposes have only recently been reported, there are still several problems and difficulties that need to be addressed. For instance, any study that uses SMLM for quantitative analysis must have stringent negative and positive controls, since artifacts in the imaging or analysis methods can give rise to wrong inferences. Also, the data must be corrected for sample drift by means of fiducial markers, or by correlative or statistical approaches based on the data itself (Geisler et al., 2012; Mlodzianoski et al., 2011). working with the localizations directly rather than image representations such as histograms or probability maps is better for quantitative analysis, as the latter involves a loss of information. A challenge remains in identifying well-accepted standard methods for the quantitative analysis of SMLM, which would allow researchers to perform the correct comparison between reported results.

An important issue, especially in analyzing the spatial heterogeneity or co-localization of proteins, is the effect of localization uncertainty (Deschout et al., 2014b; Mortensen et al., 2010; Thompson et al., 2002). Not incorporating this effect into the analysis might result in incorrect estimates. For instance, in the case of cluster analysis, the presence of localization uncertainty, equivalent to sampling from a circular or elliptical Gaussian distribution (Thompson et al., 2002), will result in deformed if not enlarged clusters being imaged. Also, the uncertainty in position estimates results in an uncertainty in distances computed from them and hence affects object-based co-localization (Ruprecht et al., 2010). Measures that do not account for the localization uncertainty might result in a wrong interpretation in both cases. The PC-PALM technique that accounts for photoblinking artifacts also incorporates a localization uncertainty model in the analysis, but only through the average uncertainty of all molecule localizations, and its effect was not studied systematically. Defining a cutoff value for the localization uncertainty distribution to select only the more precise molecular localizations can result in artifacts, especially if the localization uncertainty is not homogeneously distributed in space. This problem was investigated in the case of the CCF, which is used to study inter-protein interactions in dual-color PALM, from a purely empirical perspective, with rather mixed results (Sherman et al., 2011).

Besides accounting for the localization uncertainty, progress is required on other issues as well in order to achieve quantitative co-localization on the single-molecule level. The community would benefit from a uniform measure of the registration error, allowing comparison between co-localization results from different studies. An important limitation toward single-molecule level co-localization in the context of PALM is the low co-localization efficiency of current fluorescent protein pairs, necessitating the search for more promising candidates (Bourgeois and Adam, 2012).

Artifacts in the sample can also pose challenges to quantitative SMLM. Many of the studies reported in this review were done on fixed samples, although it has been observed that fixation can introduce artifacts in the protein spatial configuration (Annibale et al., 2012; Tanaka et al., 2010). A rigorous investigation of different fixation techniques will therefore be helpful. Also, it has been noticed that SMLM images of organelles such as mitochondria (Betzig et al., 2006), microtubules, or clathrin-coated pits have localization densities that are spatially inhomogeneous, often resulting in spurious structures, e.g., clathrin-coated pits with poor symmetry (Lang and Rizzoli, 2010). It will be useful to study this phenomenon in more detail, perhaps by means of correlative microscopy, i.e., by imaging the same structure with other high-resolution imaging techniques such as transmission electron microscopy (TEM) or atomic force microscopy (AFM). Such studies might also provide validations about localization uncertainty and detection efficiency.

# Appendix B

# Analysis of the MLE in the interaction analysis method

The Maximum Likelihood Estimator (MLE) in the interaction analysis method presented in Helmuth et al. (2010) is biased towards detecting interactions, i.e., in the case of true "no interaction", the maxima of the likelihood need not correspond to the interaction strength parameter $\varepsilon = 0$. An elementary analysis of this estimator that demonstrates this is provided below.

Also, for this reason, we use the Least Squares estimator in the implementation in Chapter 6.

We show that for $D$ corresponding to a non-interacting point pattern, if $L_1$ is the likelihood corresponding to 'no-interaction' parameters, and if $L_2$ is the likelihood corresponding to some interaction with strength $\varepsilon$, then the likelihood ratio $\frac{L_1}{L_2}$ is not strictly greater than one. It is instead a function of $\varepsilon, \sigma$ and the number of points $N$ and can be less than 1.

The likelihood for the interaction analysis model, $L(\varphi|D, q)$, hereafter represented by $L$, is given by:

$$L = \prod_{i=1}^{N} p(d_i|q, \varphi)$$

where

$$p(d_i|q, \varphi) = \frac{1}{Z} q(d_i) \exp(-\varphi(d_i)),$$

and

$$Z = \int_{-\infty}^{\infty} q(d) \exp(-\varphi(d)) \partial d.$$

In the case of no interaction, the strength of interaction parameter $\varepsilon$ is $\approx 0$, and for some observed $D$, the likelihood

$$L_1 = \frac{1}{Z_1^N} \prod_{i=1}^{N} q(d_i), \quad Z_1 = \int_{-\infty}^{\infty} q(d) \partial d, \tag{B.1}$$

since $\exp(-\varphi(d_i)) = 1 \; \forall d_i$, as $\varphi(d) = \varepsilon f(d, \sigma) = 0$.

Now, consider a different set of parameters $(\varepsilon_2, \sigma_2) = (u, min(D))$ representing an interaction(i.e., $u > 0$). The results hold also for any $\sigma_3 \in [min(D), max(D)]$ (not shown). Then, e.g., in the case of a step potential, Eq. (6.2)), denoting the hard-core parameter with $\sigma$:

$$\varphi_2(d) = \begin{cases} 0, & \forall d > \sigma_2 \\ -u, & \forall d \leq \sigma_2 \end{cases}$$

For simplicity, assume that one and only one $d_i \in D = \sigma_2$.

In this case,

$$p(d) = \begin{cases} \frac{1}{Z_2} v q(d), & \forall d \leq \sigma_2 \\ \frac{1}{Z_2} q(d), & \forall d > \sigma_2 \end{cases}$$

where $v = \exp(u) > 1$ as $u > 0$, and $Z_2 = Z_1 + \Delta Z$, where

$$\begin{aligned} \Delta Z &= Z_2 - Z_1 \\ &= \int_{-\infty}^{\infty} (\exp(-\varphi_2(d)) - \exp(-\varphi_1(d))) q(d) \partial d \\ &= \int_{-\infty}^{\sigma_2} (v-1) q(d) \partial d + \int_{\sigma_2+}^{\infty} (1-1) q(d) \partial d \\ &= (v-1) \int_{-\infty}^{\sigma_2} q(d) \partial d. \end{aligned}$$

And the likelihood

$$\begin{aligned} L_2 &= \frac{1}{Z_2^N} \prod_{i=1, d_i \leq \sigma_2}^{N} v q(d_i) \prod_{i=1, d_i > \sigma_2}^{N} q(d_i) \\ &= \frac{1}{Z_2^N} v q(\sigma_2) \prod_{i=1, d_i > \sigma_2}^{N} q(d_i) \\ &= \frac{1}{Z_2^N} v \prod_{i=1}^{N} q(d_i). \end{aligned}$$

Substituting Eq. (B.1), and using $Z_2 = Z_1 + \Delta Z$:

$$L_2 = \frac{v}{\left(1 + \frac{\Delta Z}{Z_1}\right)^N} L_1. \tag{B.2}$$

Let $f = \frac{v}{\left(1+\frac{\Delta Z}{Z_1}\right)^N}$ be the ratio of likelihoods, then $L_2 = f L_1$, substituting for $\Delta Z$ and $Z_1$:

$$f = \frac{v}{\left(1 + (v-1)\frac{\int_{-\infty}^{\sigma_2} q(d)}{\int_{-\infty}^{\infty} q(d)}\right)^N}. \tag{B.3}$$

To get the correct estimate corresponding to "no interaction" i.e $\varepsilon \approx 0$ by maximizing the likelihood, $L_1$ must be strictly greater than $L_2$, i.e.,

$$f < 1. \tag{B.4}$$

The expression in Eq. (B.3) as such provides no such guarantees.

# Bibliography

S. Abrahamsson, J. J. Chen, B. Hajj, S. Stallinga, A. Y. Katsov, J. Wisniewski, G. Mizuguchi, P. Soule, F. Mueller, C. D. Darzacq, X. Darzacq, C. Wu, C. I. Bargmann, D. A. Agard, M. Dahan, and M. G. L. Gustafsson. Fast multicolor 3d imaging using aberration-corrected multifocus microscopy. *Nature Methods*, 10(1):60–U80, 2013.

M. D. Abramoff, P. J. Magelhaes, and S. J. Ram. Image processing with ImageJ. *Biophotonics Int*, 11(7):36–42, 2004.

T. Ando. High-speed atomic force microscopy coming of age. *Nanotechnology*, 23(6):062001, 2012.

M. Ankerst, M. M. Breunig, H.-P. Kriegel, and J. Sander. Optics: ordering points to identify the clustering structure. In *ACM Sigmod Record*, volume 28, pages 49–60. ACM, 1999.

P. Annibale. *Investigating the impact of single molecule fluorescence dynamics on photo activated localization microscopy experiments*. PhD thesis, EPFL, 2012.

P. Annibale, M. Scarselli, A. Kodiyan, and A. Radenovic. Photoactivatable fluorescent protein meos2 displays repeated photoactivation after a long-lived dark state in the red photoconverted form. *The Journal of Physical Chemistry Letters*, 1(9):1506–1510, 2010.

P. Annibale, S. Vanni, M. Scarselli, U. Roetlisberger, and A. Radenovic. Identification of clustering artifacts in photo activated localization microscopy. *Nat Methods*, 8:527–528, 2011a.

P. Annibale, S. Vanni, M. Scarselli, U. Rothlisberger, and A. Radenovic. Quantitative photo activated localization microscopy: Unraveling the effects of photoblinking. *PLoS One*, 6 (7):e22678, 07 2011b.

P. Annibale, M. Scarselli, M. Greco, and A. Radenovic. Identification of the factors affecting co-localization precision for quantitative multicolor localization microscopy. *Optical Nanoscopy*, 1(9), 2012.

Y. Antoku, P. Dedecker, P. S. Pinheiro, T. Vosch, and J. B. Sørensen. Spatial distribution and temporal evolution of DRONPA-fused SNAP25 clusters in adrenal chromaffin cells. *Photochem. Photobiol. Sci.*, 2015.

M. Baday, A. Cravens, A. Hastie, H. Kim, D. E. Kudeki, P. Y. Kwok, M. Xiao, and P. R. Selvin. Multicolor super-resolution dna imaging for genetic analysis. *Nano Lett*, 12(7): 3861–6, 2012.

A. Baddeley. *Analysing Spatial Point Patterns in R*. CSIRO, Canberra, Australia, 2008.

A. J. Baddeley, J. Møller, and R. Waagepetersen. *Non-and semi-parametric estimation of interaction in inhomogeneous point patterns*. University of Aarhus. Centre for Mathematical Physics and Stochastics (MaPhySto)[MPS], 1998.

D. Baddeley, M. B. Cannell, and C. Soeller. Visualization of localization microscopy data. *Microscopy and Microanalysis*, 16(01):64–72, 2010.

D. Baddeley, D. Crossman, S. Rossberger, J. E. Cheyne, J. M. Montgomery, I. D. Jayasinghe, C. Cremer, M. B. Cannell, and C. Soeller. 4D super-resolution microscopy with conventional fluorophores and single wavelength excitation in optically thick cells and tissues. *PLoS ONE*, 6(5):e20645, 05 2011.

N. Banterle, K. H. Bui, E. A. Lemke, and M. Beck. Fourier ring correlation as a resolution criterion for super-resolution microscopy. *Journal of structural biology*, 183(3):363–367, 2013.

D. Bar-On, S. Wolter, S. van de Linde, M. Heilemann, G. Nudelman, E. Nachliel, M. Gutman, M. Sauer, and U. Ashery. Super-resolution imaging reveals the internal architecture of nano-sized syntaxin clusters. *J Biol Chem*, 287(32):27158–67, 2012.

M. Bates, G. T. Dempsey, K. H. Chen, and X. Zhuang. Multicolor super-resolution fluorescence imaging via multi-parameter fluorophore detection. *ChemPhysChem*, 13(1):99–107, 2012.

E. Betzig. Proposed method for molecular optical imaging. *Opt. Lett.*, 20(3):237–239, Feb 1995.

E. Betzig, G. H. Patterson, R. Sougrat, O. W. Lindwasser, S. Olenych, J. S. Bonifacino, M. W. Davidson, J. Lippincott-Schwartz, and H. F. Hess. Imaging Intracellular Fluorescent Proteins at Nanometer Resolution. *Science*, 313(5793):1642–1645, 2006.

S. Bolte and F. P. Cordelières. A guided tour into subcellular colocalization analysis in light microscopy. *Journal of Microscopy*, 224(3):213–232, Dec. 2006.

D. Bourgeois and V. Adam. Reversible photoswitching in fluorescent proteins: a mechanistic view. *IUBMB life*, 64(6):482–491, 2012.

J. Cardinale, G. Paul, and I. F. Sbalzarini. Discrete region competition for unknown numbers of connected regions. *IEEE Trans. Image Process.*, 21(8):3531–3545, 2012.

J. V. Chacko, F. C. Zanacchi, and A. Diaspro. Probing cytoskeletal structures by coupling optical superresolution and afm techniques for a correlative approach. *Cytoskeleton*, 70 (11):729–40, 2013.

Y. W. Chang, S. Y. Chen, E. I. Tocheva, A. Treuner-Lange, S. Loebach, L. Sogaard-Andersen, and G. J. Jensen. Correlated cryogenic photoactivated localization microscopy and cryo-electron tomography. *Nature Methods*, 11(7):737–U179, 2014.

L. S. Churchman, Z. Okten, R. S. Rock, J. F. Dawson, and J. A. Spudich. Single molecule high-resolution colocalization of Cy3 and Cy5 attached to macromolecules measures intramolecular distances through time. *Proceedings of the National Academy of Sciences of the United States of America*, 102(5):1419–1423, 2005.

S. L. Churchman, H. Flyvbjerg, and J. A. Spudich. A non-gaussian distribution quantifies distances measured with fluorescence localization techniques. *Biophysical Journal*, 90(2): 668–671, Jan. 2006.

E. A. Cohen and R. J. Ober. Analysis of point based image registration errors with applications in single molecule microscopy. *Signal Processing, IEEE Transactions on*, 61(24): 6291–6306, 2013.

A. Colom, I. Casuso, F. Rico, and S. Scheuring. A hybrid high-speed atomic force-optical microscope for visualizing single membrane proteins on eukaryotic cells. *Nature Communications*, 4, 2013.

A. Dani, B. Huang, J. Bergan, C. Dulac, and X. Zhuang. Superresolution imaging of chemical synapses in the brain. *Neuron*, 68(5):843–56, 2010.

H. De Jong. Modeling and simulation of genetic regulatory systems: a literature review. *Journal of computational biology*, 9(1):67–103, 2002.

G. T. Dempsey, J. C. Vaughan, K. H. Chen, M. Bates, and X. Zhuang. Evaluation of fluorophores for optimal performance in localization-based super-resolution imaging. *Nat Methods*, 8(12):1027–36, 2011.

A. P. Dempster, N. M. Laird, and D. B. Rubin. Maximum likelihood from incomplete data via the em algorithm. *Journal of the royal statistical society. Series B (methodological)*, pages 1–38, 1977.

H. Deschout, A. Shivanandan, P. Annibale, M. Scarselli, and A. Radenovic. Progress in quantitative Single Molecule Localization Microscopy. *Histochem Cell Biol*, 142(1):5–17, 2014a.

H. Deschout, F. C. Zanacchi, M. Mlodzianoski, A. Diaspro, J. Bewersdorf, S. T. Hess, and K. Braeckmans. Precisely and accurately localizing single emitters in fluorescence microscopy. *Nat Methods*, 11(3):253–66, 2014b.

R. E. Dickson, A. B. Cubitt, R. Y. Tsien, and W. E. Moerner. On/off blinking and switching behaviour of single molecules of green fluorescent protein. *Nature*, 388(6640):355–358, 1997.

P. J. Diggle. *Statistical Analysis of Spatial Point Patterns*. Arnold, London, 2003.

R. Dominguez and K. C. Holmes. Actin structure and function. *Annual Review of Biophysics*, 40(1):169–186, 2011.

Y. F. Dufrene, C. Boonaert, P. Gerin, M. Asther, and P. Rouxhet. Direct probing of the surface ultrastructure and molecular interactions of dormant and germinating spores ofphanerochaete chrysosporium. *Journal of Bacteriology*, 181(17):5, 1999.

Y. F. Dufrene, D. Martinez-Martin, I. Medalsy, D. Alsteens, and D. J. Muller. Multiparametric imaging of biological systems by force-distance curve-based afm. *Nature Methods*, 10(9): 847–854, 2013.

K. W. Dunn, M. M. Kamocka, and J. H. McDonald. A practical guide to evaluating colocalization in biological microscopy. *American Journal of Physiology-Cell Physiology*, 300(4): C723–C742, 2011.

N. Durisic, A. G. Godin, C. M. Wever, C. D. Heyes, M. Lakadamyali, and J. A. Dent. Stoichiometry of the human glycine receptor revealed by direct subunit counting. *The Journal of Neuroscience*, 32(37):12915–12920, 2012.

N. Durisic, L. Laparra-Cuervo, A. Sandoval-Alvarez, J. S. Borbely, and M. Lakadamyali. Single-molecule evaluation of fluorescent protein photoactivation efficiency using an in vivo nanotemplate. *Nat Meth*, 11(2):156–162, Feb. 2014a.

N. Durisic, L. Laparra-Cuervo, A. Sandoval-Alvarez, J. S. Borbely, and M. Lakadamyali. Single-molecule evaluation of fluorescent protein photoactivation efficiency using an in vivo nanotemplate. *Nat Meth*, 11(2):156–162, Feb. 2014b.

M. B. Elowitz, A. J. Levine, E. D. Siggia, and P. S. Swain. Stochastic gene expression in a single cell. *Science*, 297(5584):1183–1186, 2002.

J. Enderlein, E. Toprak, and P. R. Selvin. Polarization effect on position accuracy of fluorophore localization. *Opt. Express*, 14(18):8111–8120, Sep 2006.

U. Endesfelder, K. Finan, S. Holden, P. Cook, A. N. Kapanidis, and M. Heilemann. Multiscale spatial organization of rna polymerase in escherichia coli. *Biophysical journal*, 105:10, 2013.

J. Engelhardt, J. Keller, P. Hoyer, M. Reuss, T. Staudt, and S. W. Hell. Molecular orientation affects localization accuracy in superresolution far-field fluorescence microscopy. *Nano Lett*, 11(1):209–213, 2011.

M. Ester, H.-P. Kriegel, J. Sander, and X. Xu. A density-based algorithm for discovering clusters in large spatial databases with noise. In *Second International Conference on Knowledge Discovery and Data Mining*, pages 226–231. AAAI Press, 1996.

N. A. Frost, H. E. Lu, and T. A. Blanpied. Optimization of cell morphology measurement via single-molecule tracking palm. *PLoS One*, 7(5):e36751, 2012.

C. Geisler, T. Hotz, A. Schonle, S. W. Hell, A. Munk, and A. Egner. Drift estimation for single marker switching based imaging schemes. *Opt Express*, 20(7):7274–89, 2012.

S. Ghaemmaghami, W.-K. Huh, K. Bower, R. W. Howson, A. Belle, N. Dephoure, E. K. O'Shea, and J. S. Weissman. Global analysis of protein expression in yeast. *Nature*, 425 (6959):737–741, 2003.

M. Ghorbani. Cauchy cluster process. *Metrika*, 76(5):697–706, 2013. ISSN 0026-1335.

A. Goshtasby. Image registration by local approximation methods. *Image and Vision Computing*, 6(4):255 – 261, 1988.

T. J. Gould, S. T. Hess, and J. Bewersdorf. Optical nanoscopy: from acquisition to analysis. *Annu Rev Biomed Eng*, 14:231–54, 2012.

D. Greenfield, A. L. McEvoy, H. Shroff, G. E. Crooks, N. S. Wingreen, E. Betzig, and J. Liphardt. Self-organization of the ¡italic¿escherichia coli¡/italic¿ chemotaxis network imaged with super-resolution light microscopy. *PLoS Biol*, 7(6):e1000137, 06 2009.

M. S. Gunewardene, F. V. Subach, T. J. Gould, G. P. Penoncello, M. V. Gudheti, V. V. Verkhusha, and S. T. Hess. Superresolution imaging of multiple fluorescent proteins with highly overlapping emission spectra in living cells. *Biophysical Journal*, 101(6):1522 – 1528, 2011.

J. Gunzenhäuser, N. Olivier, T. Pengo, and S. Manley. Quantitative super-resolution imaging reveals protein stoichiometry and nanoscale morphology of assembling hiv-gag virions. *Nano Letters*, 12(9):4705–4710, 2012.

M. G. Gustafsson. Surpassing the lateral resolution limit by a factor of two using structured illumination microscopy. *Journal of microscopy*, 198(2):82–87, 2000.

M. G. L. Gustafsson. Nonlinear structured-illumination microscopy: Wide-field fluorescence imaging with theoretically unlimited resolution. *PNAS*, 102(37):13081–13086, Sept. 2005.

P. Haase. Spatial pattern analysis in ecology based on ripley's k-function: introduction and methods of edge correction. *Journal of vegetation science*, pages 575–582, 1995.

B. Hajek. *Random Processes for Engineers*. Cambridge University Press, 2015. ISBN 9781107100121.

M. Hall, E. Frank, G. Holmes, B. Pfahringer, P. Reutemann, and I. H. Witten. The weka data mining software: an update. *SIGKDD Explor. Newsl.*, 11(1):10–18, Nov. 2009.

N. Hansen and A. Ostermeier. Completely derandomized self-adaptation in evolution strategies. *Evolutionary Computation*, 9(2):159–195, June 2001.

N. C. Hartman and J. T. Groves. Signaling clusters in the cell membrane. *Curr. Opin. Cell Biol.*, 23(4):370–376, Aug 2011.

M. Heilemann, S. van de Linde, M. Schuttpelz, R. Kasper, B. Seefeldt, A. Mukherjee, P. Tinnefeld, and M. Sauer. Subdiffraction-resolution fluorescence imaging with conventional fluorescent probes. *Angewandte Chemie-International Edition*, 47(33):6172–6176, 2008.

S. W. Hell. Far-field optical nanoscopy. *Science*, 316(5828):1153–1158, 2007.

S. W. Hell and J. Wichmann. Breaking the diffraction resolution limit by stimulated emission: stimulated-emission-depletion fluorescence microscopy. *Opt. Lett.*, 19(11):780–782, Jun 1994.

J. Helmuth, G. Paul, and I. Sbalzarini. Beyond co-localization: inferring spatial interactions between sub-cellular structures from microscopy images. *BMC Bioinformatics*, 11(1):372, 2010.

J. A. Helmuth. *Computational Methods for Analyzing and Simulating Intra-Cellular Transport Processes*. PhD thesis, Diss. ETH No. 19190, ETH Zürich, 2010.

E. Henderson, P. Haydon, and D. Sakaguchi. Actin filament dynamics in living glial cells imaged by atomic force microscopy. *Science*, 257(5078):3, 1992.

S. T. Hess, T. P. Girirajan, and M. D. Mason. Ultra-High Resolution Imaging by Fluorescence Photoactivation Localization Microscopy. *Biophys J*, 91(11):4258 – 4272, 2006.

S. T. Hess, T. J. Gould, M. V. Gudheti, S. A. Maas, K. D. Mills, and J. Zimmerberg. Dynamic clustered distribution of hemagglutinin resolved at 40 nm in living cell membranes discriminates between raft theories. *Proceedings of the National Academy of Sciences*, 104(44): 17370–17375, 2007.

S. J. Holden, T. Pengo, K. L. Meibom, C. Fernandez Fernandez, J. Collier, and S. Manley. High throughput 3d super-resolution microscopy reveals caulobacter crescentus in vivo z-ring organization. *Proceedings of the National Academy of Sciences*, 111(12):4566–4571, 2014.

B. Huang, W. Q. Wang, M. Bates, and X. W. Zhuang. Three-dimensional super-resolution imaging by stochastic optical reconstruction microscopy. *Science*, 319(5864):810–813, 2008.

F. Huang, T. M. Hartwich, F. E. Rivera-Molina, Y. Lin, W. C. Duim, J. J. Long, P. D. Uchil, J. R. Myers, M. A. Baird, W. Mothes, et al. Video-rate nanoscopy using scmos camera-specific single-molecule localization algorithms. *Nature methods*, 10(7):653–658, 2013.

A. Ianoul, D. D. Grant, Y. Rouleau, M. Bani-Yaghoub, L. J. Johnston, and J. P. Pezacki. Imaging nanometer domains of $\beta$-adrenergic receptor complexes on the surface of cardiac myocytes. *Nature chemical biology*, 1(4):196–202, 2005.

T. Ikawa, F. Hoshino, O. Watanabe, Y. L. Li, P. Pincus, and C. R. Safinya. Molecular scale imaging of f-actin assemblies immobilized on a photopolymer surface. *Physical Review Letters*, 98(1), 2007.

J. Illian, A. Penttinen, H. Stoyan, and D. Stoyan. *Statistical analysis and modelling of spatial point patterns*, volume 70. John Wiley & Sons, 2008.

D. E. Ingber. Cellular mechanotransduction: putting all the pieces together again. *Faseb Journal*, 20(7):811–827, 2006.

A. Jalilian, Y. Guan, and R. Waagepetersen. Decomposition of Variance for Spatial Cox Processes. *Scandinavian Journal of Statistics*, 40(1):119–137, Mar. 2013.

J. R. Janesick. *Scientific charge-coupled devices*. SPIE Publications, 2001. ISBN 0819436984.

S. Jones, S. H. Shim, J. He, and X. Zhuang. Fast, three-dimensional super-resolution imaging of live cells. *Nature Methods*, 8(6):499–505, 2011.

D. Kim, N. M. Curthoys, M. T. Parent, and S. T. Hess. Bleed-through correction for rendering and correlation analysis in multi-colour localization microscopy. *Journal of Optics*, 15 (9):094011, 2013.

M. A. Kiskowski, J. F. Hancock, and A. K. Kenworthy. On the Use of Ripley's K-Function and Its Derivatives to Analyze Domain Size. *Biophys J*, 97(4):1095–1103, Aug. 2009.

T. Klein, S. Proppert, and M. Sauer. Eight years of single-molecule localization microscopy. *Histochemistry and Cell Biology*, 141(6):561–575, 2014. doi: 10.1007/s00418-014-1184-3.

N. Kodera, D. Yamamoto, R. Ishikawa, and T. Ando. Video imaging of walking myosin v by high-speed atomic force microscopy. *Nature*, 468(7320):72–+, 2010.

B. G. Kopek, G. Shtengel, J. B. Grimm, D. A. Clayton, and H. F. Hess. Correlative photoactivated localization and scanning electron microscopy. *Plos One*, 8(10), 2013.

I. Koyama-Honda, K. Ritchie, T. Fujiwara, R. Iino, H. Murakoshi, R. S. Kasai, and A. Kusumi. Fluorescence imaging for monitoring the colocalization of two single molecules in living cells. *Biophysical journal*, 88(3):2126–2136, 2005.

E. Lachmanovich, D. E. Shvartsman, Y. Malka, C. Botvin, Y. I. Henis, and A. M. Weiss. Colocalization analysis of complex formation among membrane proteins by computerized fluorescence microscopy: application to immunofluorescence co-patching studies. *Journal of Microscopy*, 212(2):122–131, 2003.

T. Lagache, G. Lang, N. Sauvonnet, and J.-C. Olivo-Marin. Analysis of the Spatial Organization of Molecules with Robust Statistics. *PLoS ONE*, 8(12):e80914, Dec. 2013.

D. Lando, U. Endesfelder, H. Berger, L. Subramanian, P. D. Dunne, J. McColl, D. Klenerman, A. M. Carr, M. Sauer, R. C. Allshire, M. Heilemann, and E. D. Laue. Quantitative single-molecule microscopy reveals that CENP-ACnp1 deposition occurs during g2 in fission yeast. *Open Biol*, 2(7), July 2012.

T. Lang and S. O. Rizzoli. Membrane protein clusters at nanoscale resolution: more than pretty pictures. *Physiology*, 25(2):116–124, Apr 2010.

S.-H. Lee, J. Y. Shin, A. Lee, and C. Bustamante. Counting single photoactivatable fluorescent molecules by photoactivated localization microscopy (PALM). *Proceedings of the National Academy of Sciences*, Oct. 2012.

M. Lehmann, S. Rocha, B. Mangeat, F. Blanchet, H. Uji-i, J. Hofkens, and V. Piguet. Quantitative multicolor super-resolution microscopy reveals tetherin hiv-1 interaction. *PLoS Pathog*, 7(12):e1002456, 12 2011.

M. Lelek, F. Di Nunzio, R. Henriques, P. Charneau, N. Arhel, and C. Zimmer. Superresolution imaging of hiv in infected cells with flash-palm. *Proc Natl Acad Sci U S A*, 109(22): 8564–9, 2012.

B. F. Lillemeier, J. R. Pfeiffer, Z. Surviladze, B. S. Wilson, and M. M. Davis. Plasma membrane-associated proteins are clustered into islands attached to the cytoskeleton. *Proc Natl Acad Sci U S A*, 103(50):18992–18997, Dec 2006.

B. F. Lillemeier, M. A. Mörtelmaier, M. B. Forstner, J. B. Huppa, J. T. Groves, and M. M. Davis. TCR and lat are expressed on separate protein islands on t cell membranes and concatenate during activation. *Nat Immunol*, 11(1):90–96, Dec. 2009.

J. Loh and M. Stein. Bootstrapping a spatial point process. *Statistica Sinica*, 14(1):69–102, 2004.

J. M. Loh. A valid and fast spatial bootstrap for correlation functions. *The Astrophysical Journal*, 681(1):726, 2008.

A. Loschberger, S. van de Linde, M. C. Dabauvalle, B. Rieger, M. Heilemann, G. Krohne, and M. Sauer. Super-resolution imaging visualizes the eightfold symmetry of gp210 proteins around the nuclear pore complex and resolves the central channel with nanometer resolution. *Journal of Cell Science*, 125(3):570–575, 2012.

E. Lubeck and L. Cai. Single-cell systems biology by super-resolution imaging and combinatorial labeling. *Nature methods*, 9(7):743–748, 2012.

H. D. MacGillavry, Y. Song, S. Raghavachari, and T. A. Blanpied. Nanoscale scaffolding domains within the postsynaptic density concentrate synaptic ampa receptors. *Neuron*, 78(4):615–22, 2013.

S. Malkusch, U. Endesfelder, J. Mondry, M. Gelleri, P. Verveer, and M. Heilemann. Coordinate-based colocalization analysis of single-molecule localization microscopy data. *Histochemistry and Cell Biology*, 137(1):1–10, Jan. 2012.

S. Malkusch, W. Muranyi, B. Müller, H.-G. Kräusslich, and M. Heilemann. Single-molecule coordinate-based analysis of the morphology of hiv-1 assembly sites with near-molecular spatial resolution. *Histochemistry and Cell Biology*, 139(1):173–179, 2013. doi: 10.1007/s00418-012-1014-4.

S. Manley, J. M. Gillette, G. H. Patterson, H. Shroff, H. F. Hess, E. Betzig, and J. Lippincott-Schwartz. High-density mapping of single-molecule trajectories with photoactivated localization microscopy. *Nature Methods*, 5(2):155–157, 2008.

A. L. McEvoy, H. Hoi, M. Bates, E. Platonova, P. J. Cranfill, M. A. Baird, M. W. Davidson, H. Ewers, J. Liphardt, and R. E. Campbell. mmaple: A photoconvertible fluorescent protein for use in multiple imaging modalities. *PLoS ONE*, 7(12):e51314, 12 2012.

K. R. Mecke and D. Stoyan. *Statistical Physics and Spatial Statistics : the Art of Analyzing and Modeling Spatial Structures and Pattern Formation*. Springer-Verlag, 2000.

D. J. Metcalf, R. Edwards, N. Kumarswami, and A. E. Knight. Test samples for optimizing storm super-resolution microscopy. *Journal of visualized experiments : JoVE*, (79), 2013.

M. J. Mlodzianoski, J. M. Schreiner, S. P. Callahan, K. Smolkova, A. Dlaskova, J. Santorova, P. Jezek, and J. Bewersdorf. Sample drift correction in 3d fluorescence photoactivation localization microscopy. *Opt Express*, 19(16):15009–19, 2011.

J. Møller and R. Waagepetersen. *Statistical Inference and Simulation for Spatial Point Processes*. Chapman and Hall/CRC, Boca Raton, 2004.

J. Moller and R. P. Waagepetersen. *Statistical Inference and Simulation for Spatial Point Processes*. Taylor Francis Group, 2004.

A. Monserrate, S. Casado, and C. Flors. Correlative atomic force microscopy and localization-based super-resolution microscopy: revealing labelling and image reconstruction artefacts. *Chemphyschem : a European journal of chemical physics and physical chemistry*, 15(4):647–50, 2014.

K. I. Mortensen, L. S. Churchman, J. A. Spudich, and H. Flyvbjerg. Optimized localization analysis for single-molecule tracking and super-resolution microscopy. *Nat Methods*, 7(5): 377–381, 2010.

D. J. Muller, F. A. Schabert, G. Buldt, and A. Engel. Imaging purple membranes in aqueous solutions at sub-nanometer resolution by atomic force microscopy. *Biophysical journal*, 68 (5):1681–6, 1995.

X. Nan, E. A. Collisson, S. Lewis, J. Huang, T. M. Tamguney, J. T. Liphardt, F. McCormick, J. W. Gray, and S. Chu. Single-molecule superresolution imaging allows quantitative analysis of raf multimer formation and signaling. *Proc Natl Acad Sci U S A*, 110(46): 18519–24, 2013.

R. P. Nieuwenhuizen, K. A. Lidke, M. Bates, D. L. Puig, D. Grunwald, S. Stallinga, and B. Rieger. Measuring image resolution in optical nanoscopy. *Nature Methods*, 10(6):557–62, 2013.

A. Oddone, I. V. Vilanova, J. Tam, and M. Lakadamyali. Super-resolution imaging with stochastic single-molecule localization: Concepts, technical developments, and biological applications. *Microscopy Research and Technique*, 77(7):502–509, 2014.

P. D. Odermatt, A. Shivanandan, H. Deschout, R. Jankele, A. P. Nievergelt, L. Feletti, M. W. Davidson, A. Radenovic, and G. E. Fantner. High resolution correlative microscopy: Bridging the gap between Single Molecule Localization Microscopy and Atomic Force Microscopy. *Nano Lett*, 2015. *Published.*

J. Ohser. On estimation of pair correlation functions. *Res Informatics*, 4:147–152, 1991.

N. Olivier, D. Keller, P. Gonczy, and S. Manley. Resolution doubling in 3d-storm imaging through improved buffers. *Plos One*, 8(7), 2013.

A. Ori, N. Banterle, M. Iskar, A. Andrés-Pons, C. Escher, H. K. Bui, L. Sparks, V. Solis-Mezarino, O. Rinner, P. Bork, et al. Cell type-specific nuclear pores: a case in point for context-dependent stoichiometry of molecular machines. *Molecular systems biology*, 9(1): 648, 2013.

M. Ovesný, P. Křížek, J. Borkovec, Z. Švindrych, and G. M. Hagen. Thunderstorm: a comprehensive imagej plug-in for palm and storm data analysis and super-resolution imaging. *Bioinformatics*, 30(16):2389–2390, 2014.

D. M. Owen and K. Gaus. Imaging lipid domains in cell membranes: the advent of super-resolution fluorescence microscopy. *Frontiers in plant science*, 4, 2013.

D. M. Owen, C. Rentero, J. Rossy, A. Magenau, D. Williamson, M. Rodriguez, and K. Gaus. Palm imaging and cluster analysis of protein heterogeneity at the cell surface. *Journal of biophotonics*, 3(7):446–454, 2010.

D. M. Owen, D. J. Williamson, L. Boelen, A. Magenau, J. Rossy, and K. Gaus. Quantitative analysis of three-dimensional fluorescence localization microscopy data. *Biophysical journal*, 105(2):L05–L07, 2013.

R. G. Parton and J. F. Hancock. Lipid rafts and plasma membrane microorganization: insights from Ras. *Trends in Cell Biology*, 14(3):141–147, 2004.

S. R. P. Pavani, M. A. Thompson, J. S. Biteen, S. J. Lord, N. Liu, R. J. Twieg, R. Piestun, and W. E. Moerner. Three-dimensional, single-molecule fluorescence imaging beyond the diffraction limit by using a double-helix point spread function. *Proceedings of the National Academy of Sciences of the United States of America*, 106(9):2995–2999, 2009.

C. F. Pereira, J. Rossy, D. M. Owen, J. Mak, and K. Gaus. Hiv taken by storm: super-resolution fluorescence microscopy of a viral infection. *Virol J*, 9:84, 2012.

F. Persson, M. Lindén, C. Unoson, and J. Elf. Extracting intracellular diffusive states and transition rates from single-molecule tracking data. *Nature Methods*, 10(3):265–269, 2013.

A. Pertsinidis, Y. Zhang, and S. Chu. Subnanometre single-molecule localization, registration and distance measurements. *Nature*, 466(6306):647–651, 2010.

A. Pertsinidis, K. Mukherjee, M. Sharma, Z. P. Pang, S. R. Park, Y. Zhang, A. T. Brunger, T. C. Südhof, and S. Chu. Ultrahigh-resolution imaging reveals formation of neuronal SNARE/Munc18 complexes in situ. *Proc Natl Acad Sci U S A*, 110(30):E2812–E2820, July 2013.

A. Pezzarossa and F. d. W. e. Natuurwetenschappen. Imaging plasma membrane domains in signal-transduction pathways, Mar. 2012.

J. L. Ptacin, S. F. Lee, E. C. Garner, E. Toro, M. Eckart, L. R. Comolli, W. E. Moerner, and L. Shapiro. A spindle-like apparatus guides bacterial chromosome segregation. *Nat Cell Biol*, 12(8):791–8, 2010.

E. M. Puchner, J. M. Walter, R. Kasper, B. Huang, and W. A. Lim. Counting molecules in single organelles with superresolution microscopy allows tracking of the endosome maturation trajectory. *Proceedings of the National Academy of Sciences*, 110(40):16015–16020, 2013.

L. Qu, F. Long, X. Liu, S. Kim, E. Myers, and H. Peng. Simultaneous recognition and segmentation of cells: application in c.elegans. *Bioinformatics*, 27(20):2895–2902, 2011.

A. Raj and A. van Oudenaarden. Nature, nurture, or chance: stochastic gene expression and its consequences. *Cell*, 135(2):216–226, 2008.

M. Renz, B. R. Daniels, G. Vamosi, I. M. Arias, and J. Lippincott-Schwartz. Plasticity of the asialoglycoprotein receptor deciphered by ensemble fret imaging and single-molecule counting palm imaging. *Proceedings of the National Academy of Sciences of the United States of America*, 109(44):E2989–E2997, 2012.

A. Rodriguez and A. Laio. Clustering by fast search and find of density peaks. *Science*, 344 (6191):1492–1496, 2014.

J. Rossy, D. M. Owen, D. J. Williamson, Z. Yang, and K. Gaus. Conformational states of the kinase lck regulate clustering in early t cell signaling. *Nat Immunol*, 14(1):82–9, 2013.

C. Rotsch, F. Braet, E. Wisse, and M. Radmacher. Afm imaging and elasticity measurements on living rat liver macrophages. *Cell Biology International*, 21(11):685–696, 1997.

C. Rotsch, K. Jacobson, and M. Radmacher. Dimensional and mechanical dynamics of active and stable edges in motile fibroblasts investigated by using atomic force microscopy. *Proceedings of the National Academy of Sciences of the United States of America*, 96(3):921–926, 1999.

N. H. Roy, J. Chan, M. Lambelé, and M. Thali. Clustering and Mobility of HIV-1 Env at Viral Assembly Sites Predict Its Propensity To Induce Cell-Cell Fusion. *J. Virol.*, 87(13): 7516–7525, July 2013.

V. Ruprecht, J. Weghuber, S. Wieser, and G. J. Schütz. *Chapter Two - Measuring Colocalization by Dual Color Single Molecule Imaging: Thresholds, Error Rates, and Sensitivity*, volume Volume 12, pages 21–40. Academic Press, 2010.

M. J. Rust, M. Bates, and X. Zhuang. Sub-diffraction-limit imaging by stochastic optical reconstruction microscopy (STORM). *Nat Methods*, 3(10):793–796, 2006.

I. F. Sbalzarini and P. Koumoutsakos. Feature point tracking and trajectory analysis for video imaging in cell biology. *J. Struct. Biol.*, 151(2):182–195, 2005.

M. Scarselli, P. Annibale, and A. Radenovic. Cell type-specific b2-adrenergic receptor clusters identified using photoactivated localization microscopy are not lipid raft related, but depend on actin cytoskeleton integrity. *J Biol Chem*, 287(20):16768–16780, May 2012.

M. Scarselli, P. Annibale, C. Gerace, and A. Radenovic. Enlightening g-protein-coupled receptors on the plasma membrane using super-resolution photoactivated localization microscopy. *Biochemical Society Transactions*, 41:191–196, 2013.

J. Schindelin, I. Arganda-Carreras, E. Frise, V. Kaynig, M. Longair, T. Pietzsch, S. Preibisch, C. Rueden, S. Saalfeld, B. Schmid, J.-Y. Y. Tinevez, D. J. J. White, V. Hartenstein, K. Eliceiri, P. Tomancak, and A. Cardona. Fiji: an open-source platform for biological-image analysis. *Nature methods*, 9(7):676–682, July 2012.

S. Schmitz, I. A. Schaap, J. Kleinjung, S. Harder, M. Grainger, L. Calder, P. B. Rosenthal, A. A. Holder, and C. Veigel. Malaria parasite actin polymerization and filament structure. *The Journal of biological chemistry*, 285(47):36577–85, 2010.

P. Sengupta, T. Jovanovic-Talisman, D. Skoko, M. Renz, S. L. Veatch, and J. Lippincott-Schwartz. Probing protein heterogeneity in the plasma membrane using PALM and pair correlation analysis. *Nat Methods*, 8(11):969–975, 2011.

P. Sengupta, T. Jovanovic-Talisman, and J. Lippincott-Schwartz. Quantifying spatial organization in point-localization superresolution images using pair correlation analysis. *Nature protocols*, 8(2):345–354, 2013.

E. Sherman, V. Barr, S. Manley, G. Patterson, L. Balagopalan, I. Akpan, C. K. Regan, R. K. Merrill, C. L. Sommers, J. Lippincott-Schwartz, and L. E. Samelson. Functional nanoscale organization of signaling molecules downstream of the t cell antigen receptor. *Immunity*, 35(5):705–720, 2011.

S. H. Shim, C. L. Xia, G. S. Zhong, H. P. Babcock, J. C. Vaughan, B. Huang, X. Wang, C. Xu, G. Q. Bi, and X. W. Zhuang. Super-resolution fluorescence imaging of organelles in live cells with photoswitchable membrane probes. *Proceedings of the National Academy of Sciences of the United States of America*, 109(35):13978–13983, 2012.

A. Shivanandan, A. Radenovic, and I. F. Sbalzarini. MosaicIA: an ImageJ/Fiji plugin for spatial pattern and interaction analysis. *BMC Bioinformatics*, 14(1):349, 2013.

A. Shivanandan, H. Deschout, M. Scarselli, and A. Radenovic. Challenges in quantitative Single Molecule Localization Microscopy. *FEBS Lett*, 588(19):3595–3602, 2014.

A. Shivanandan, J. Unnikrishnan, and A. Radenovic. Accounting for limited detection efficiency and localization precision in cluster analysis in Single Molecule Localization Microscopy. *PLOS ONE*, 10(3):e0118767, 2015.

H. Shroff, C. G. Galbraith, J. A. Galbraith, and E. Betzig. Live-cell photoactivated localization microscopy of nanoscale adhesion dynamics. *Nature Methods*, 5(5):417–423, 2008.

G. Shtengel, J. A. Galbraith, C. G. Galbraith, J. Lippincott-Schwartz, J. M. Gillette, S. Manley, R. Sougrat, C. M. Waterman, P. Kanchanawong, M. W. Davidson, R. D. Fetter, and H. F. Hess. Interferometric fluorescent super-resolution microscopy resolves 3d cellular ultrastructure. *Proceedings of the National Academy of Sciences of the United States of America*, 106 (9):3125–3130, 2009.

J.-B. Sibarita. High-density single-particle tracking: quantifying molecule organization and dynamics at the nanoscale. *Histochemistry and cell biology*, 141(6):587–595, 2014.

J. J. Sieber, K. I. Willig, C. Kutzner, C. Gerding-Reimers, B. Harke, G. Donnert, B. Rammner, C. Eggeling, S. W. Hell, H. Grubmuller, and T. Lang. Anatomy and dynamics of a supramolecular membrane protein cluster. *Science*, 317(5841):1072–1076, Aug 2007.

B. W. Silverman and P. J. Green. *Density Estimation for Statistics and Data Analysis*. Chapman and Hall, London, 1986.

K. Simons and E. Ikonen. Functional rafts in cell membranes. *Nature*, 387(6633):569–572, Jun 1997.

A. Slade and S. C. Minne. Time-resolved nanometer scale afm imaging of antimicrobial peptide activity on live escherichia coli cells. *Microscopy and Microanalysis*, 20(SupplementS3): 2074–2075, 2014.

A. Small and S. Stahlheber. Fluorophore localization algorithms for super-resolution microscopy. *Nat Methods*, 11(3):267–79, 2014.

K. A. Sochacki, B. T. Larson, D. C. Sengupta, M. P. Daniels, G. Shtengel, H. F. Hess, and J. W. Taraska. Imaging the post-fusion release and capture of a vesicle membrane protein. *Nat Commun*, 3:1154, 2012.

S. Stallinga and B. Rieger. Accuracy of the gaussian point spread function model in 2d localizationmicroscopy. *Opt. Express*, 18(24):24461–24476, Nov 2010.

A. Szymborska, A. de Marco, N. Daigle, V. C. Cordes, J. A. G. Briggs, and J. Ellenberg. Nuclear pore scaffold structure analyzed by super-resolution microscopy and particle averaging. *Science*, 341(6146):655–658, 2013.

K. A. K. Tanaka, K. G. N. Suzuki, Y. M. Shirai, S. T. Shibutani, M. S. H. Miyahara, H. Tsuboi, M. Yahara, A. Yoshimura, S. Mayor, T. K. Fujiwara, and A. Kusumi. Membrane molecules mobile even after chemical fixation. *Nature Methods*, 7(11):865–866, 2010.

Y. Taniguchi, P. J. Choi, G.-W. Li, H. Chen, M. Babu, J. Hearn, A. Emili, and X. S. Xie. Quantifying e. coli proteome and transcriptome with single-molecule sensitivity in single cells. *Science*, 329(5991):533–538, 2010.

R. E. Thompson, D. R. Larson, and W. W. Webb. Precise nanometer localization analysis for individual fluorescent probes. *Biophysical Journal*, 82(5):2775 – 2783, 2002.

S. J. Tobin, E. E. Cacao, D. W. W. Hong, L. Terenius, V. Vukojevic, and T. Jovanovic-Talisman. Nanoscale effects of ethanol and naltrexone on protein organization in the plasma membrane studied by photoactivated localization microscopy (palm). *PloS one*, 9(2):e87225, 2014.

M. H. Ulbrich and E. Y. Isacoff. Subunit counting in membrane-bound proteins. *Nature methods*, 4(4):319–321, 2007.

S. L. Veatch, B. B. Machta, S. A. Shelby, E. N. Chiang, D. A. Holowka, and B. A. Baird. Correlation functions quantify super-resolution images and estimate apparent clustering due to over-counting. *PloS one*, 7(2):e31457, 2012.

S. Wang, J. R. Moffitt, G. T. Dempsey, X. S. Xie, and X. Zhuang. Characterization and development of photoactivatable fluorescent proteins for single-molecule–based superresolution imaging. *Proceedings of the National Academy of Sciences*, 111(23):8452–8457, 2014.

W. Wang, G. W. Li, C. Chen, X. S. Xie, and X. Zhuang. Chromosome organization by a nucleoid-associated protein in live bacteria. *Science*, 333(6048):1445–9, 2011.

Y. X. Wang, J. Y. J. Shyy, and S. Chien. Fluorescence proteins, live-cell imaging, and mechanobiology: Seeing is believing. *Annual Review of Biomedical Engineering*, 10:1–38, 2008.

J. Wiedenmann, S. Ivanchenko, F. Oswald, F. Schmitt, C. Röcker, A. Salih, K.-D. Spindler, and G. U. Nienhaus. Eosfp, a fluorescent marker protein with uv-inducible green-to-red fluorescence conversion. *Proceedings of the National Academy of Sciences of the United States of America*, 101(45):15905–15910, 2004.

D. J. Williamson, D. M. Owen, J. Rossy, A. Magenau, M. Wehrmann, J. J. Gooding, and K. Gaus. Pre-existing clusters of the adaptor lat do not participate in early t cell signaling events. *Nat Immunol*, 12(7):655–662, June 2011.

P. Winckler, L. Lartigue, G. Giannone, F. De Giorgi, F. Ichas, J.-B. Sibarita, B. Lounis, and L. Cognet. Identification and super-resolution imaging of ligand-activated receptor dimers in live cells. *Scientific reports*, 3, 2013.

K. Xu, H. P. Babcock, and X. W. Zhuang. Dual-objective storm reveals three-dimensional filament organization in the actin cytoskeleton. *Nature Methods*, 9(2):185–188, 2012.

K. Xu, G. S. Zhong, and X. W. Zhuang. Actin, spectrin, and associated proteins form a periodic cytoskeletal structure in axons. *Science*, 339(6118):452–456, 2013.

L. Yang, A. R. Dun, K. J. Martin, Z. Qiu, A. Dunn, G. J. Lord, W. Lu, R. R. Duncan, and C. Rickman. Secretory vesicles are preferentially targeted to areas of low molecular snare density. *PLoS One*, 7(11):e49514, 2012.

A. G. York, A. Ghitani, A. Vaziri, M. W. Davidson, and H. Shroff. Confined activation and subdiffractive localization enables whole-cell palm with genetically expressed probes. *Nat Meth*, 8(4):327–333, 2011.

J. Zhang, K. Leiderman, J. R. Pfeiffer, B. S. Wilson, J. M. Oliver, and S. L. Steinberg. Characterizing the topography of membrane receptors and signaling molecules from spatial patterns obtained using nanometer-scale electron-dense probes and electron microscopy. *Micron*, 37(1):14 – 34, 2006.

L. Zhu, W. Zhang, D. Elnatan, and B. Huang. Faster storm using compressed sensing. *Nat Methods*, 9(7):721–3, 2012.

V. Zinchuk, O. Zinchuk, and T. Okada. Quantitative colocalization analysis of multicolor confocal immunofluorescence microscopy images: pushing pixels to explore biological phenomena. *Acta histochemica et cytochemica*, 40(4):101, 2007.

# ARUN SHIVANANDAN

**PRESENT ADDRESS**
EPFL STI/SV - IBI - LBEN
BM 2138, Station 17
CH-1015 Lausanne, Switzerland
Office: +41 (0)21 693 1162

**PERMANENT ADDRESS**
Pulari, MG Nagar
Punkunnam PO, Thrissur
Kerala, India - 680002
`arun.shivanandan@gmail.com`

## ACADEMIC PROFILE

**PhD Student** Jul 2011– Ongoing
Doctoral Program in Biotechnology and Bioengineering
École Polytechnique Fédérale de Lausanne,
Lausanne, Switzerland
Primary supervisor: Prof. Aleksandra Radenovic

**Master of Science in Informatics** Sep 2009– Jun 2011
Université Joseph Fourier/ENSIMAG, Grenoble, France

**Bachelor of Technology in Mechanical Engineering** Aug 2002– Apr 2006
National Institute of Technology, Calicut, India

## PRIOR RESEARCH EXPERIENCE

**Research Intern** IBIS Group, Nov 2009– Jun 2011
INRIA, Grenoble-Rhône-Alpes
France

## INDUSTRY EXPERIENCE

**Software Programmer** IBM Jun 2006– Aug 2009
Bangalore, India

## RESEARCH PROJECTS

- **Doctoral thesis: Analytical Methods, Correlative Microscopy and Software Tools for Quantitative Single Molecule Localization Microscopy**
  Supervised by Prof. Aleksandra Radenovic, EPFL (primary)
  and Prof. Ivo F. Sbalzarini, MPI-CBG, Dresden
  The focus area of my work is quantitative analysis of Single Molecule Localization Microscopy (SMLM) data. SMLM can provide high specificity images of proteins in conditions resembling their natural conditions, with single molecule resolution. However, it has several sources of errors, limiting its utility for quantitative measurements. I worked on three different but related projects to develop methods that address these errors, from all the three angles: analytical, experimental and software. They include:

  1. Quantitative cluster analysis methods that corrects for the errors introduced by the limited detection efficiency and localization precision that are inherent in the SMLM technique. The work is in the context of quantification of spatial organization structures of membrane proteins.
  2. Another collaborative project (LBNI lab, EPFL) on developing an SMLM-AFM correlated microscopic tool, so that the SMLM data can be validated with high resolution AFM data, and its various errors characterized. The complementary information provided by this tool can be used for innovative experiments. The tool was used to image *in vitro* actin filaments, bacteria and live mammalian cells.
  3. Development of a software framework to infer protein-protein spatial interaction parameters from dual color microscopy data, including SMLM. It has hence been released as an open source plugin in the ImageJ/Fiji framework.

- **Masters thesis: Stochastic Modeling and Identification of Arabinose Uptake Network in Escherichia coli** (2011)
  Supervised by Dr. Eugenio Cinquemani, INRIA Grenoble-Rhône-Alpes, France
  I worked on the identification of stochastic models of single cell gene regulation network. Specifically, we built a model of arabinose uptake network in *E. coli*, and data from fluorescence microscopy. We used methods based on Finite State Projection (FSP) and its variants to solve the Chemical Master Equation.

## PUBLICATIONS

1. **A. Shivanandan**, *Stochastic modelling and identification of arabinose uptake network in Escherichia coli*, Master thesis, Université Joseph Fourier, 2011.
2. **A. Shivanandan**, A. Radenovic, and I. F. Sbalzarini. *MosaicIA: an ImageJ/Fiji plugin for spatial pattern and interaction analysis.* BMC Bioinformatics, 14(1):349, 2013
3. H. Deschout, **A. Shivanandan**, P. Annibale, M. Scarselli, and A. Radenovic. *Progress in quantitative single-molecule localization microscopy.* Histochem Cell Biol, 142(1):517, 2014
4. **A. Shivanandan**, H. Deschout, M. Scarselli, and A. Radenovic. *Challenges in quantitative single molecule localization microscopy.* FEBS Lett, 588(19):3595-3602, 2014
5. **A. Shivanandan**, J. Unnikrishnan, and A. Radenovic. *Accounting for limited detection efficiency and localization precision in cluster analysis in single molecule localization microscopy.* PLOS ONE, 10(3):e0118767, 2015
6. P. D. Odermatt, **A. Shivanandan**, H. Deschout, R. Jankele, A. P. Nievergelt, L. Feletti, M. W. Davidson, A. Radenovic, and G. E. Fantner. *High resolution correlative microscopy: Bridging the gap between single molecule localization microscopy and atomic force microscopy.* Nano Lett (just published)

## ORAL PRESENTATIONS

- *Analytical methods and tools for single molecule localization microscopy*, Single Molecule Localization Microscopy Symposium, King's College, London, UK, August 27-29, 2014.
- *Super-resolution imaging and image analysis of protein-protein interactions in membranes*, Mats Gustafsson Memorial Symposium on High Resolution Imaging, Janelia Farm Research Campus, VA, USA, May 20-23, 2012 (with travel grant)

## TEACHING EXPERIENCE

- Teaching assistant for Advanced Bioengineering Methods Laboratories (EPFL, 2013)

## PAST PROJECTS

- **Qualitative analysis of steady state interactions in gycolytic network of *Escherichia coli* using computer algebra tools** (2010)
  Supervised by Dr. Hidde de Jong, INRIA
  I studied the effects of qualitative perturbations of enzyme concentrations on the quasi-steady state values of metabolites in the carbon assimilation network in *E. coli* by resolving the signs of interactions (i.e huge equations) using computer algebra tools. This work was submitted to the University as a Travail d'Etude et de Recherche (TER) project.
- ***Luv_lena*: a general purpose image processing software** (2010)
  Done as a month long programming project as part of Masters, Grades obtained: 18/20
  Designed and developed a software in C++/Qt, that can do basic image processing (crop, resize, rotate, scale, contrast, histogram, sharpen, blur, line detection), custom convolution, FFT etc. We also implemented advanced functionalities like context aware resizing and intelligent scissors based on latest research papers. The code is available in the public domain at: `http://code.google.com/p/luvlena/`
- **Internet based control and tele-operation of a mobile rover** (2006)
  Undergraduate Thesis project, Grades : 10/10 (midterm), 10/10 (final)
  Designed and fabricated a four wheeled mobile robot. Designed electronics for actuator/ sensor/ computer interfacing and control. Tele-operation via wireless Internet was implemented through a chat based algorithm and real-time video streaming.

- **Design, fabrication and control of a bipedal mechanism based on penguin walking** (2004)
  "Best design" award, Tathva Technical Festival, NIT Calicut.
  The design mimicked the waddling motion of penguins, making use of the research in this area that side-to-side waddling of a penguin can cause additional energy conservation in the Inverted Pendulum model of walking, causing more efficient motion in the case of a very high loads. The biped was designed to walk, turn, climb stairs, manage slopes, stand and flip over a leg.
- **Design, fabrication and control of a bipedal mechanism with series elastic actuators, based on human walking**(2004)
  "Third prize" , Tathva Technical Festival,NIT Calicut.
  The biped had hip, knee and ankle joints. Elastic Belt Actuation (EBA) technique was an attempted extention of "Series Elastic Actuation", implemented in order to satisfy the "compliance factor" in the Spring Loaded Inverted Pendulum(SLIP) model of running."
- **An inexpensive can crushing mechanism that saves the waste removing cost of junk cola cans by 90 percent** (2005)
  Mechanical Engineering project, Grade - 10/10
  A can crusher which can be attached to a vending machine was designed and developed. The mechanism was based on a simple slider crank, with the long crank acting as a second-class lever and a few modifications in the cylinder to reduce friction.

## PROJECTS IN INDUSTRY

- **Development of an interactive Knowledge Management System (KMS)**
  While at IBM (2008–09), I worked on developing a KMS application with wikis, blogs, forums, feeds, bug tracking systems and several other features, with Java based technologies (Spring, Hibernate, Velocity, etc). We also worked on applying machine learning and search algorithms on trouble resolution data to categorize new trouble tickets.
- **Development of a web application for telecommunication systems**
  At IBM (2006–08), I worked on developing and maintaining a web based enterprise application for applications in the telecommuncations industry. The application had interfaces with several other software systems, and hence several middleware. I worked on Java and several middleware and SOA technologies while in this project.

## HONORS

- Grenoble Institute of Technology (INPG) Scholarship of Excellence 2010
- Travel grant for microscopy symposium at Janelia Farm (2012)
- Top .3% rank in the Engineering Entrance Examination, Kerala, India
- Promoted as a Functional Lead at the end of first year at IBM.
- Awards for robotics projects: Best design award for the penguin inspired biped and third prize for biped based on serial elastic activation, Tathva 04, a technical festival organized by NITC
- Second best paper in symposium conducted by Larsen and Toubro Ltd for a paper on a heuristic algorithm based on Ant Colony Optimization (2005)

## COMPUTER SKILLS

- *Programming* : Java, C, C++, Unix shell scripting, MATLAB, R
- *Tools* : MATLAB, ImageJ/Fiji, Mathematica
- *Misl* : GIT, Eclipse, Jira

## REFERENCES

On request.